
**UNIVERSIDADE ESTADUAL DE CAMPINAS**
**Faculdade de Engenharia Mecânica**

**Edson Jansen Pedrosa de Miranda Junior**

# Dynamic Analysis of Phononic Crystals and Elastic Metamaterials Using Semi-Analytical and Numerical Approaches

## *Análise Dinâmica de Cristais Fonônicos e Metamateriais Elásticos Utilizando Abordagens Semi-Analíticas e Numéricas*

CAMPINAS
2018

**Edson Jansen Pedrosa de Miranda Junior**

# Dynamic Analysis of Phononic Crystals and Elastic Metamaterials Using Semi-Analytical and Numerical Approaches

# *Análise Dinâmica de Cristais Fonônicos e Metamateriais Elásticos Utilizando Abordagens Semi-Analíticas e Numéricas*

Doctoral Thesis presented to the School of Mechanical Engineering of the University of Campinas in partial fulfillment of the requirements for the degree of Doctor in Mechanical Engineering, in the Area of Solid Mechanics and Mechanical Design.

*Tese de Doutorado apresentada à Faculdade de Engenharia Mecânica da Universidade Estadual de Campinas como parte dos requisitos exigidos para obtenção do título de Doutor em Engenharia Mecânica, na Área de Mecânica dos Sólidos e Projeto Mecânico.*

Orientador: Prof. Dr. José Maria Campos dos Santos

ESTE EXEMPLAR CORRESPONDE À VERSÃO FINAL DA TESE DEFENDIDA PELO ALUNO EDSON JANSEN PEDROSA DE MIRANDA JUNIOR, E ORIENTADO PELO PROF. DR. JOSÉ MARIA CAMPOS DOS SANTOS.

**CAMPINAS**
**2018**

**Agência(s) de fomento e nº(s) de processo(s):** FAPEMA, BM E BD-02591/15
**ORCID:** https://orcid.org/0000-0003-1100-9169

Ficha catalográfica
Universidade Estadual de Campinas
Biblioteca da Área de Engenharia e Arquitetura
Luciana Pietrosanto Milla - CRB 8/8129

M672d

Miranda Junior, Edson Jansen Pedrosa de, 1988-
Dynamic analysis of phononic crystals and elastic metamaterials using semi-analytical and numerical approaches / Edson Jansen Pedrosa de Miranda Junior. – Campinas, SP : [s.n.], 2018.

Orientador: José Maria Campos dos Santos.
Tese (doutorado) – Universidade Estadual de Campinas, Faculdade de Engenharia Mecânica.

1. Cristais fonônicos. 2. Metamateriais. 3. Vibração - Controle. 4. Ondas elásticas - Propagação. 5. Diagramas de bandas. I. Santos, José Maria Campos dos, 1953-. II. Universidade Estadual de Campinas. Faculdade de Engenharia Mecânica. III. Título.

Informações para Biblioteca Digital

**Título em outro idioma:** Análise dinâmica de cristais fonônicos e metamateriais elásticos utilizando abordagens semi-analíticas e numéricas
**Palavras-chave em inglês:**
Phononic crystals
Metamaterials
Vibration - Control
Elastic waves - Propagation
Band diagrams
**Área de concentração:** Mecânica dos Sólidos e Projeto Mecânico
**Titulação:** Doutor em Engenharia Mecânica
**Banca examinadora:**
José Maria Campos dos Santos [Orientador]
José Roberto de França Arruda
Vitor Rafael Coluci
Carlos De Marqui Junior
Leopoldo Pisanelli Rodrigues de Oliveira
**Data de defesa:** 01-03-2018
**Programa de Pós-Graduação:** Engenharia Mecânica

**UNIVERSIDADE ESTADUAL DE CAMPINAS**

**FACULDADE DE ENGENHARIA MECÂNICA**

**COMISSÃO DE PÓS-GRADUAÇÃO EM ENGENHARIA MECÂNICA**

**DEPARTAMENTO DE MECÂNICA COMPUTACIONAL**

**TESE DE DOUTORADO**

# Dynamic Analysis of Phononic Crystals and Elastic Metamaterials Using Semi-Analytical and Numerical Approaches

## *Análise Dinâmica de Cristais Fonônicos e Metamateriais Elásticos Utilizando Abordagens Semi-Analíticas e Numéricas*

Autor: Edson Jansen Pedrosa de Miranda Junior

Orientador: José Maria Campos dos Santos

A Banca Examinadora composta pelos membros abaixo aprovou esta Tese:

**Prof. Dr. José Maria Campos dos Santos, Presidente**
**DMC - Faculdade de Engenharia Mecânica - UNICAMP**

**Prof. Dr. José Roberto de França Arruda**
**DMC - Faculdade de Engenharia Mecânica - UNICAMP**

**Prof. Dr. Vitor Rafael Coluci**
**LaSCADo - Faculdade de Tecnologia - UNICAMP**

**Prof. Dr. Carlos De Marqui Junior**
**SAA - Escola de Engenharia de São Carlos - USP**

**Prof. Dr. Leopoldo Pisanelli Rodrigues de Oliveira**
**SEM - Escola de Engenharia de São Carlos - USP**

A Ata da defesa com as respectivas assinaturas dos membros encontra-se no processo de vida acadêmica do aluno.

Campinas, 01 de março de 2018.

# Dedication

*I dedicate this thesis to my saviour, Jesus Christ, and to my daughter Helena that will born in 2018.*

*Eu dedico essa tese ao meu salvador, Jesus Cristo, e à minha filha Helena que nascerá em 2018.*

# Acknowledgements

Firstly, I thank God for giving me the strength necessary to complete this thesis.

I would like to thank my wife and my family for the support, patience and motivation during the last four years.

I wish to express my sincere thanks to my supervisor Prof. Dr. José Maria Campos dos Santos for his support, discussions, challenges, motivation and patience during this research.

I am also thankful to Prof. Dr. José Roberto de França Arruda for his discussions and suggestions about this research. His course of Introduction to Structural Acoustics helped so much in this research.

I would like to thank the external members of the jury for coming to my defence and contribute with their experienced advices to improve this thesis. I am also thankful to Prof. Dr. Carlos De Marqui Junior, Prof. Dr. José Roberto de França Arruda, Prof. Dr. Leopoldo Pisanelli Rodrigues de Oliveira and Prof. Dr. Vitor Rafael Coluci, members of the jury, for valuable discussions during this thesis and for their suggestions.

I also thank the Faculty of Mechanical Engineering at UNICAMP, in special, the Department of Computational Mechanics, for providing me the facilities necessary to the development of this thesis.

I wish to express my sincere gratefulness to my friends and fellow labmates, in special, Anderson Ferreira, Edilson Dantas, Danilo Beli, Edgar Andres, Guilherme Paiva, Daniela Damasceno, Lucas Cóser, Wendell Diniz, Helio Vitor, Luis Filipe, Rayston Werner, Helder Daiha, Fernando Ortolano and Vinicius Dias. Our discussions, hours of hard work, and all the fun we have had contributed to make things easier.

I am thankful to FAPEMA, through process numbers BM E BD-02591/15, APEC-04259/16, and APEC-00155/17 for providing me the financial support necessary to the development of this thesis.

I also thank Federal Institute of Maranhão – IFMA, for providing me the financial support necessary to the development of this thesis.

Finally, I would like to thank all who in one way or another contributed to the completion of this thesis.

*The God of the Bible is also the God of the genome. He can be worshipped in the cathedral or in the laboratory. His creation is majestic, awesome, intricate, and beautiful.*

Francis Collins

*O Deus da Bíblia é também o Deus do genoma. Ele pode ser adorado na catedral ou no laboratório. Sua criação é majestosa, incrível, complexa, e bonita.*

Francis Collins

# Resumo

Nesta tese, os métodos de expansão em ondas planas (PWE), expansão em ondas planas melhorado (IPWE) e expansão em ondas planas estendido (EPWE) são utilizados para obter a estrutura de banda de cristais fonônicos (PnCs) e de metamateriais elásticos (EMs) uni- (1D) e bi-dimensionais (2D), isto é, estruturas artificiais projetadas para criarem bandas proibidas de Bragg e/ou localmente ressonantes. Estas estruturas periódicas estão sendo aplicadas em vários ramos da ciência e possuem diversas aplicações – controle passivo/ativo de vibração, filtros/barreiras acústicas, metamateriais para captação de energia, guias de onda, dentre outras. A principal aplicação considerada nesta tese é o controle passivo de vibração. Primeiro, as formulações do PWE, IPWE e EPWE são apresentadas para alguns casos e vantagens e limitações são discutidas. Os casos considerados são PnCs 1D de barra, cristais sônicos 2D e EMs 1D de viga de Euler-Bernoulli. Posteriormente, alguns exemplos de propagação de ondas mecânicas nestas estruturas periódicas são abordados através da análise da estrutura de banda. Em seguida, algumas aplicações dos PnCs e EMs para controle passivo de vibração são discutidas em artigos anexados. Inicialmente, a estrutura de banda e a resposta forçada harmônica de um PnC simples de viga de Euler-Bernoulli são calculadas. Vários métodos são aplicados e os resultados simulados podem localizar a posição e a largura das bandas proibidas de Bragg próximas dos resultados experimentais. Posteriormente, é considerada a formação de bandas proibidas de ondas de flexão em um PnC de placa com diferentes inclusões em redes quadrada e triangular, considerando-se a teoria de Mindlin-Reissner. O melhor desempenho é encontrado para a inclusão com seção transversal circular em uma rede triangular. Em seguida, a estrutura de banda de ondas elásticas se propagando em PnCs com nanoestruturas de carbono e em nanocristais fonônicos piezoelétricos com diferentes tipos de rede e inclusão são calculadas. Bandas proibidas totais entre os modos XY e Z são observadas para todos os tipos de inclusão. A piezoeletricidade influencia significativamente as bandas proibidas para inclusão circular vazada em frequências mais baixas. Posteriormente, um PnC magnético-elétrico-elástico 2D é considerado. Diferentes tipos de rede e de inclusão também são considerados. A piezoeletricidade e o piezomagnetismo influenciam significativamente as bandas proibidas. Finalmente, são considerados EMs 1D de viga de Euler-Bernoulli e 2D de placa fina. A influência de ressonadores de um grau de liberdade e de múltiplos graus de liberdade periodicamente conectados nas células unitárias do EM de viga de Euler-Bernoulli e EM 2D de placa fina são investigadas. Diferentes configurações da distribuição dos ressonadores são consideradas para investigar os mecanismos de formação das bandas proibidas, isto é, ressonância local e espalhamento de Bragg.

*Palavras-chave*: Cristais fonônicos, Metamateriais elásticos, Bandas proibidas, Expansão em ondas planas, Controle passivo de vibração.

# Abstract

In this thesis, plane wave expansion (PWE), improved plane wave expansion (IPWE) and extended plane wave expansion (EPWE) methods are used in order to obtain the band structure of one- (1D) and two-dimensional (2D) phononic crystals (PnCs) and elastic metamaterials (EMs), *i.e.*, artificial structures designed to open up Bragg-type and/or locally resonant band gaps. Such periodic structures are being applied in many branches of science, and have many applications – passive/active vibration control, acoustic barriers/filters, metamaterials-based enhanced energy harvesting, waveguides, among others. The main application considered in this thesis is passive vibration control. First, PWE, IPWE and EPWE formulations are presented for some cases and advantages and drawbacks are discussed. The cases regarded are 1D PnC rods, 2D sonic crystals and 1D EM Euler-Bernoulli beams. Afterwards, some examples of mechanical wave propagation in these periodic structures are addressed by means of band structure analysis. Next, some applications of PnCs and EMs for passive vibration control are discussed in attached papers. Initially, the band structure and harmonic forced response of a simple 1D PnC Euler-Bernoulli beam are carried out. Several approaches are applied and the simulated results can localize the Bragg-type band gap position and width close to the experimental results. Next, it is considered the formation of flexural wave band gaps in a PnC plate with different inclusions in square and triangular lattices, considering Mindlin-Reissner theory. The best performance is found for circular cross section inclusion in a triangular lattice. Afterwards, the band structure of elastic waves propagating in carbon nanostructure PnCs and nano-piezoelectric PnCs with different types of lattice and inclusion are calculated. Full band gaps between XY and Z modes are observed for all types of inclusions. Piezoelectricity influences significantly the band gaps for hollow circular inclusion in lower frequencies. After that, a magnetoelectroelastic 2D PnC is considered. Different types of lattice and inclusion are also addressed. Piezoelectricity and piezomagnetism influence significantly the band gaps. Finally, 1D EM Euler-Bernoulli beams and 2D EM thin plates are regarded. The influence of single degree of freedom and multiple degrees of freedom resonators periodically attached in unit cells of the EM Euler-Bernoulli beam and 2D EM thin plate are investigated. Different configurations of resonator distribution are carried out in order to investigate the band gap formation mechanisms, *i.e.*, local resonance and Bragg scattering.



*Keywords*: Phononic crystals, Elastic metamaterials, Band gaps, Plane wave expansion, Passive vibration control.

# List of Figures

# List of Abbreviations and Acronyms

***Matrices and Vectors***

| | | | |
|---|---|---|---|
| $\mathbf{A}$ | - | matrix of PWE eigenvalue problem | $[N/m]$ |
| $\bar{\mathbf{A}}$ | - | matrix of PWE eigenvalue problem | $[N/m]$ |
| $\mathbf{B}$ | - | matrix of PWE eigenvalue problem | $[N/m]$ |
| $\mathbf{C}$ | - | matrix of PWE eigenvalue problem | $[m^2/kg]$ |
| $\bar{\mathbf{C}}$ | - | matrix of PWE eigenvalue problem | $[m^2/kg]$ |
| $\mathbf{D}$ | - | matrix of PWE eigenvalue problem | $[m^2/N]$ |
| $\mathbf{I}$ | - | identity matrix | $[1]$ |
| $\mathbf{G}_1$ | - | diagonal matrix with coefficients $\delta_{mn} g_{1_m}$ | $[1/m]$ |
| $\mathbf{G}_2$ | - | diagonal matrix with coefficients $\delta_{mn} g_{2_n}$ | $[1/m]$ |
| $\mathbf{K}$ | - | matrix of PWE eigenvalue problem | $[-]$ |
| $\mathbf{M}$ | - | matrix of PWE eigenvalue problem | $[-]$ |
| $\mathbf{P}$ | - | matrix with coefficients $\rho^{-1}_{\bar{m}-m,\bar{n}-n}$ | $[m^3/kg]$ |
| $\mathbf{X}_i$ | - | matrices with coefficients $X_{i_{m\tilde{m}}}$ | $[1]$ |
| $\mathbf{\Gamma}_1$ | - | diagonal matrix with coefficients $\Gamma_{1_{mn}}$ | $[1/m]$ |
| $\mathbf{\Gamma}_2$ | - | diagonal matrix with coefficients $\Gamma_{2_{mn}}$ | $[1/m]$ |
| | | | |
| $\mathbf{a}_i$ | - | primitive vectors in real space | $[m]$ |
| $\mathbf{b}_i$ | - | reciprocal primitive vectors | $[1/m]$ |
| $\mathbf{e}_i$ | - | basis vectors in real space | $[1]$ |
| $\mathbf{g}$ | - | reciprocal lattice vector for Fourier series expansion of displacement | $[1/m]$ |
| $\mathbf{g}_{m,n}$ | - | 2D reciprocal lattice vector for Fourier series expansion of displacement | $[1/m]$ |
| $\mathbf{g}_{\bar{m},\bar{n}}$ | - | 2D reciprocal lattice vector for Fourier series expansion of displacement | $[1/m]$ |
| $\mathbf{g}_{\tilde{m},\tilde{n}}$ | - | 2D reciprocal lattice vector for Fourier series expansion of displacement | $[1/m]$ |

| | | | |
|---|---|---|---|
| $\mathbf{k}$ | - | Bloch wave vector | $[1/m]$ |
| $\bar{\mathbf{k}}$ | - | reduced Bloch wave vector | $[1]$ |
| $\mathbf{p}$ | - | vector containing Fourier series coefficients $p_{m,n}$ | $[N/m^2]$ |
| $\bar{\mathbf{r}}$ | - | lattice vector | $[m]$ |
| $\mathbf{r}$ | - | 2D spatial vector | $[m]$ |
| $\mathbf{u}$ | - | elastic displacement vector | $[m]$ |
| $\tilde{\mathbf{u}}$ | - | vector containing Fourier series coefficients $u_{3_m}$ and $w_i$ | $[m]$ |
| $\mathbf{u}_i$ | - | vectorial components of $\mathbf{u}$ | $[m]$ |
| $\bar{\mathbf{u}}_1$ | - | vector containing Fourier series coefficients $u_{1_m}$ | $[m]$ |
| $\bar{\mathbf{u}}_3$ | - | vector containing Fourier series coefficients $u_{3_m}$ | $[m]$ |
| $\mathbf{w}$ | - | resonator displacement vector | $[m]$ |
| $\boldsymbol{\sigma}$ | - | unit vector | $[1]$ |
| $\boldsymbol{\phi}$ | - | vector for EPWE formulation | $[m/s^2]$ |
| $\bar{\boldsymbol{\phi}}$ | - | vector for EPWE formulation | $[m/s^2]$ |
| $\boldsymbol{\psi}$ | - | eigenvector of the eigenvalue problem $\mathbf{k}(\omega)$ | $[-]$ |

***Superscripts***

| | | |
|---|---|---|
| $H$ | - | vector conjugate transpose |

***Subscripts***

| | | |
|---|---|---|
| $A$ | - | relative to inclusion |
| $B$ | - | relative to matrix |
| $C$ | - | relative to unit cell |
| $l$ | - | wave mode index |
| $s$ | - | wave mode index |

***Latin Letters***

| | | | |
|---|---|---|---|
| $a$ | - | lattice parameter | $[m]$ |
| $a_1$ | - | lattice parameter for rectangular lattice on *x* direction | $[m]$ |
| $a_2$ | - | lattice parameter for rectangular lattice on *y* direction | $[m]$ |
| $A_{m\bar{m}}$ | - | coefficient of matrix $\mathbf{A}$ | $[N/m]$ |
| $\bar{A}_{m\bar{m}}$ | - | coefficient of matrix $\bar{\mathbf{A}}$ | $[N/m]$ |
| $B_{m\bar{m}}$ | - | coefficient of matrix $\mathbf{B}$ | $[N/m]$ |
| $c_{11}$ | - | elastic constant using Voigt notation | $[N/m^2]$ |
| $c_{11_{\bar{m},\bar{n}}}$ | - | Fourier series coefficient of $c_{11}$ | $[N/m^2]$ |
| $c_{11_{\bar{m}-m,\bar{n}-n}}$ | - | Fourier series coefficient of $c_{11}$ | $[N/m^2]$ |
| $c_{11_{\tilde{m}-m,\tilde{n}-n}}$ | - | Fourier series coefficient of $c_{11}$ | $[N/m^2]$ |
| $c_{12}$ | - | elastic constant using Voigt notation | $[N/m^2]$ |
| $c_{44}$ | - | elastic constant using Voigt notation | $[N/m^2]$ |
| $c_{66}$ | - | elastic constant using Voigt notation | $[N/m^2]$ |
| $c_l$ | - | longitudinal speed of sound | $[m/s^2]$ |
| $c_t$ | - | transverse speed of sound | $[m/s^2]$ |
| $C_{m,\bar{m},n,\bar{n}}$ | - | inverse coefficient of matrix $\mathbf{C}$ | $[m^2/kg]$ |
| $\bar{C}_{m,\bar{m},n,\bar{n}}$ | - | inverse coefficient of matrix $\bar{\mathbf{C}}$ | $[m^2/kg]$ |
| $D_i$ | - | dynamic stiffness of the *i*th resonator | $[N/m]$ |
| $D_{m,\bar{m},n,\bar{n}}$ | - | inverse coefficient of matrix $\mathbf{D}$ | $[m^2/N]$ |
| $E$ | - | Young's modulus | $[N/m^2]$ |
| $f$ | - | frequency | $[Hz]$ |
| $\bar{f}$ | - | filling fraction | $[1]$ |
| $f_i$ | - | natural frequency of the *i*th resonator | $[Hz]$ |
| $f_{B_1}$ | - | first Bragg-frequency | $[Hz]$ |

| | | | |
|---|---|---|---|
| $g_m$ | - | absolute value of 1D reciprocal lattice vector | $[1/m]$ |
| $g_{\bar{m}}$ | - | absolute value of 1D reciprocal lattice vector | $[1/m]$ |
| $g_{\tilde{m}}$ | - | absolute value of 1D reciprocal lattice vector | $[1/m]$ |
| $g_{1_m}$ | - | component of 2D reciprocal lattice vector on $x$ direction | $[1/m]$ |
| $g_{1_{\bar{m}}}$ | - | component of 2D reciprocal lattice vector on $x$ direction | $[1/m]$ |
| $g_{1_{\tilde{m}}}$ | - | component of 2D reciprocal lattice vector on $x$ direction | $[1/m]$ |
| $g_{2_n}$ | - | component of 2D reciprocal lattice vector on $y$ direction | $[1/m]$ |
| $g_{2_{\bar{n}}}$ | - | component of 2D reciprocal lattice vector on $y$ direction | $[1/m]$ |
| $g_{2_{\tilde{n}}}$ | - | component of 2D reciprocal lattice vector on $y$ direction | $[1/m]$ |
| $I$ | - | second moment of area | $[m^4]$ |
| $j$ | - | imaginary unit $\sqrt{-1}$ | [1] |
| $k$ | - | absolute value of Bloch wave vector | $[1/m]$ |
| $k_1$ | - | component of Bloch wave vector on *x* direction | $[1/m]$ |
| $k_2$ | - | component of Bloch wave vector on *y* direction | $[1/m]$ |
| $k_3$ | - | component of Bloch wave vector on *z* direction | $[1/m]$ |
| $\hat{k}$ | - | absolute value of Bloch wave vector multiplied by unit cell length | [1] |
| $\tilde{k}_i$ | - | stiffness of the *i*th resonator | $[N/m]$ |
| $K_{m,\tilde{m},i}$ | - | coefficient of matrix $\mathbf{K}$ | $[-]$ |
| $m$ | - | integer number | [1] |
| $m_i$ | - | mass of the *i*th resonator | $[kg]$ |
| $\bar{m}$ | - | integer number | [1] |
| $\tilde{m}$ | - | integer number | [1] |
| $M$ | - | integer number | [1] |
| $M_{m,\tilde{m},i}$ | - | coefficient of matrix $\mathbf{M}$ | $[-]$ |
| $n$ | - | integer number | [1] |
| $\bar{n}$ | - | integer number | [1] |
| $\tilde{n}$ | - | integer number or natural number | [1] |
| $N$ | - | number of resonators | [1] |
| $\mathbb{N}$ | - | set of natural numbers | [1] |
| $\hat{p}$ | - | acoustic pressure in time domain | $[N/m^2]$ |
| $p$ | - | acoustic pressure in frequency domain | $[N/m^2]$ |
| $p_{\mathbf{k}}$ | - | Bloch wave amplitude of $p$ | $[N/m^2]$ |
| $p_{m,n}$ | - | Fourier series coefficient of $p_{\mathbf{k}}$ | $[N/m^2]$ |
| $P$ | - | can be $\rho^{-1}$ or $c_{11}^{-1}$ | $[-]$ |
| $\bar{P}$ | - | can be $\alpha$ or $\gamma$ | $[-]$ |
| $P_{\bar{m},\bar{n}}$ | - | Fourier series coefficient of $P$ | $[-]$ |

| | | | |
|---|---|---|---|
| $\bar{P}_{\bar{m}}$ | - | Fourier series coefficient of $\bar{P}$ | $[-]$ |
| $q_i$ | - | force applied to the beam by the *i*th resonator spring | $[N]$ |
| $\mathbb{Q}$ | - | set of rational numbers | $[1]$ |
| $\mathbb{R}$ | - | set of real numbers | $[1]$ |
| $S$ | - | cross section area | $[m^2]$ |
| $S_A$ | - | inclusion cross section area | $[m^2]$ |
| $S_C$ | - | unit cell cross section area | $[m^2]$ |
| $t$ | - | time | $[s]$ |
| $\hat{u}_i$ | - | elastic displacement in time domain | $[m]$ |
| $u_i$ | - | elastic displacement in frequency domain | $[m]$ |
| $u_{i_m}$ | - | Fourier coefficient series of $u_{i_{\mathbf{k}}}$ | $[m]$ |
| $u_{i_{\tilde{m}}}$ | - | Fourier coefficient series of $u_{i_{\mathbf{k}}}$ | $[m]$ |
| $u_{i_{\mathbf{k}}}$ | - | Bloch wave amplitude of $u_i$ | $[m]$ |
| $\bar{u}$ | - | rational number | $[1]$ |
| $\bar{v}$ | - | rational number | $[1]$ |
| $x$ | - | real number | $[1]$ |
| $x_i$ | - | position of the *i*th resonator on $x$ direction | $[m]$ |
| $X_{i_{m\tilde{m}}}$ | - | coefficient of matrix $\mathbf{X}_i$ | $[1]$ |
| $w_i$ | - | displacement of the *i*th resonator on $y$ direction | $[m]$ |
| $y$ | - | real number | $[1]$ |
| $z_i$ | - | integer number | $[1]$ |
| $\mathbb{Z}$ | - | set of integer numbers | $[1]$ |

***Greek Letters***

| | | | |
|---|---|---|---|
| $\alpha$ | - | product of density and cross section area | $[kg/m]$ |
| $\alpha_{\bar{m}}$ | - | Fourier series coefficient of $\alpha$ | $[kg/m]$ |
| $\alpha_{\tilde{m}-m}$ | - | Fourier series coefficient of $\alpha$ | $[kg/m]$ |
| $\gamma$ | - | product of Young's modulus and cross section area | $[N]$ |
| $\gamma_{\bar{m}}$ | - | Fourier series coefficient of $\gamma$ | $[N]$ |
| $\gamma_{\tilde{m}-m}$ | - | Fourier series coefficient of $\gamma$ | $[N]$ |
| $\bar{\gamma}_1$ | - | ratio of resonator mass to the beam unit cell mass | $[1]$ |
| $\Gamma_{1_{mn}}$ | - | coefficient of matrix $\mathbf{\Gamma}_1$ | $[1/m]$ |
| $\Gamma_{2_{mn}}$ | - | coefficient of matrix $\mathbf{\Gamma}_2$ | $[1/m]$ |
| $\delta$ | - | Dirac delta function | $[1]$ |
| $\delta_{ij}$ | - | Kronecker delta | $[1]$ |
| $\delta_{\tilde{m}\bar{m}}$ | - | Kronecker delta | $[1]$ |
| $\delta_{\bar{m}m}$ | - | Kronecker delta | $[1]$ |

| | | | |
|---|---|---|---|
| $\delta_{\mathbf{g}_{\tilde{m},\tilde{n}}\mathbf{g}_{\bar{m},\bar{n}}}$ | - | Kronecker delta | [1] |
| $\delta_{\bar{m}}$ | - | Fourier series coefficients | [1] |
| $\Delta\omega$ | - | angular frequency increment | $[rad/s]$ |
| $\varepsilon_{ijk}$ | - | Levi-Civita symbol | [1] |
| $\lambda$ | - | wave length | $[m]$ |
| $\eta$ | - | structural damping | [1] |
| $\eta_i$ | - | structural damping of the *i*th resonator | [1] |
| $\theta$ | - | incident angle | $[rad]$ |
| $\mu_i$ | - | integer number | [1] |
| $\rho$ | - | density | $[kg/m^3]$ |
| $\rho_{\bar{m},\bar{n}}$ | - | Fourier series coefficients of $\rho$ | $[kg/m^3]$ |
| $\rho_{\bar{m}-m,\bar{n}-n}$ | - | Fourier series coefficients of $\rho$ | $[kg/m^3]$ |
| $\rho_{\tilde{m}-m,\tilde{n}-n}$ | - | Fourier series coefficients of $\rho$ | $[kg/m^3]$ |
| $\sigma_1$ | - | component of vector $\boldsymbol{\sigma}$ on $x$ direction | [1] |
| $\sigma_2$ | - | component of vector $\boldsymbol{\sigma}$ on $y$ direction | [1] |
| $\omega$ | - | angular frequency | $[rad/s]$ |
| $\omega_i$ | - | natural frequency of the *i*th resonator | $[rad/s]$ |

***Acronyms***

| | | |
|---|---|---|
| BE | - | Boundary Element |
| BESO | - | Bi-Directional Evolutionary Structure Optimization |
| DOI | - | Digital Object Identifier |
| EM | - | Elastic Metamaterial |
| EPWE | - | Extended Plane Wave Expansion |
| FBZ | - | First Brillouin Zone |
| FIBZ | - | First Irreducible Brillouin Zone |
| FDTD | - | Finite-Difference Time-Domain |
| FE | - | Finite Element |
| IPWE | - | Improved Plane Wave Expansion |
| MAC | - | Model Assurance Criterion |
| MM | - | Mechanical Metamaterial |
| MST | - | Multi-Scattering Theory |
| P | - | Pressure Modes |
| PnC | - | Phononic Crystal |
| PWE | - | Plane Wave Expansion |
| SE | - | Spectral Element |
| SEM | - | Scanning Electron Microscope |
| SH | - | Horizontally Polarised Shear Modes |
| SnC | - | Sonic Crystal |
| SV | - | Vertically Polarised Shear Modes |
| TM | - | Transfer Matrix |
| WFE | - | Wave Finite Element |
| WSE | - | Wave Spectral Element |
| WSFE | - | Wave Spectral Finite Element |

***Other Notations***

| | | |
|---|---|---|
| 1D | - | one-dimensional |
| 2D | - | two-dimensional |
| 3D | - | three-dimensional |
| $\Re(\ )$ | - | real part of a number |
| $\Im(\ )$ | - | imaginary part of a number |
| $\|\|\ \|\|$ | - | euclidean norm of a vector |
| $\|\|\ \|\|_H$ | - | hermitian norm of a vector |
| $[\ ]$ | - | Toeplitz matrix of a function |
| capital letter and bold font-weight | - | matrix |
| minuscule letter and bold font-weight | - | vector |

# Table of Contents

# 1 INTRODUCTION

## 1.1 Motivation

In the early 30's, the band theory of conduction had been established by Alan Herries Wilson (Wilson, 1931) and the concept of band gaps had been developed. He formulated a theory explaining how energy bands of electrons can make a material as conductor, semiconductor or insulator. Similarly to the electronic band gaps for semiconductors and insulators, in the late 80's, Yablonovitch (1987) and John (1987) simultaneously started to study photonic band gaps in photonic crystals. Photonic crystals can be defined as artificial composites consisting of periodic distribution of dielectric scatterers embedded in a host medium with different dielectric properties. Yablonovitch (1987) and John (1987) triggered the primary emphasis in periodic systems due to the propagation properties of electromagnetic waves inside of photonic crystals. They observed that photonic crystals exhibit ranges of frequencies related to the structure periodicity where there are no electromagnetic propagating waves, *i.e.*, photonic band gaps. There are only electromagnetic evanescent waves in these ranges of frequencies.

After the advent of photonic crystals, phononic crystals (PnCs) were proposed (Sigalas and Economou, 1992; Sigalas and Economou, 1993). For a brief review of phononic band structures, see the study of Kushwaha *et al.* (1994). PnCs are artificial periodic composites designed to exhibit phononic band gaps. Similar to photonic crystals, there are no mechanical (elastic or acoustic) propagating waves in phononic band gaps, only evanescent waves. These band gaps are opened up by the periodically mismatch between the constituent materials. This mismatch can be considered to arise either from difference of material properties or geometry (continuum-scale theory), or from interatomic force constants and masses (atomic-scale theory). The acoustic version of a PnC is known as a sonic crystal (SnC). An important study about SnCs was performed by Martínez-Sala and co-workers in 1995 (Martínez-Sala *et al.*, 1995) and since then the enthusiasm related to these periodic structures appears because of their applications in several branches of science and technology (Liu *et al.*, 2000a; Ho *et al.*, 2003).

The physical origin of phononic and photonic band gaps can be understood at micro-scale using the classical wave theory to describe the Bragg and Mie resonances based on the scattering of mechanical and electromagnetic waves propagating within the crystal. In addition, for modelling acousto-optical interactions at microscale and nanoscale, much effort has been devoted in order to open simultaneous phononic and photonic band gaps. The materials which provide simultaneous phononic and photonic band gaps are known as phoxonic crystals (Maldovan and Thomas, 2006).

PnCs have many applications, such as vibration isolation technology (Jensen, 2003; Casadei *et al.*, 2012a), acoustic barriers/filters (Ho *et al.*, 2003), noise suppression devices (Casadei *et al.*, 2012b), sound shields (Gorishnyy *et al.*, 2005), surface acoustic devices (Benchabane *et al.*, 2006), acoustic diodes (Cheng *et al.*, 2007), architectural design (Comerio, 2006), piezoelectric PnCs (Qian *et al.*, 2008), piezomagnetic PnCs (Robillard *et al.*, 2009), magnetoelec-

troelastic PnCs (Wang *et al.*, 2008), PnCs with defects for waveguides or to constitute resonators or filters (Feng *et al.*, 2015), among others. Figure 1.1 illustrates some examples of PnCs. In this thesis, different applications of PnCs for passive vibration control are explored, *i.e.*, flexural wave band gaps in one-dimensional (1D) PnC Euler-Bernoulli beams with steel and polyethylene (Appendix A), flexural wave band gaps in $Al_2O_3$/epoxy thick plates (Appendix B), carbon nanostructure and nano-piezoelectric PnCs for vibration management in GHz (Appendices C and D), and full band gaps in magnetoelectroelastic PnCs (Appendix E).

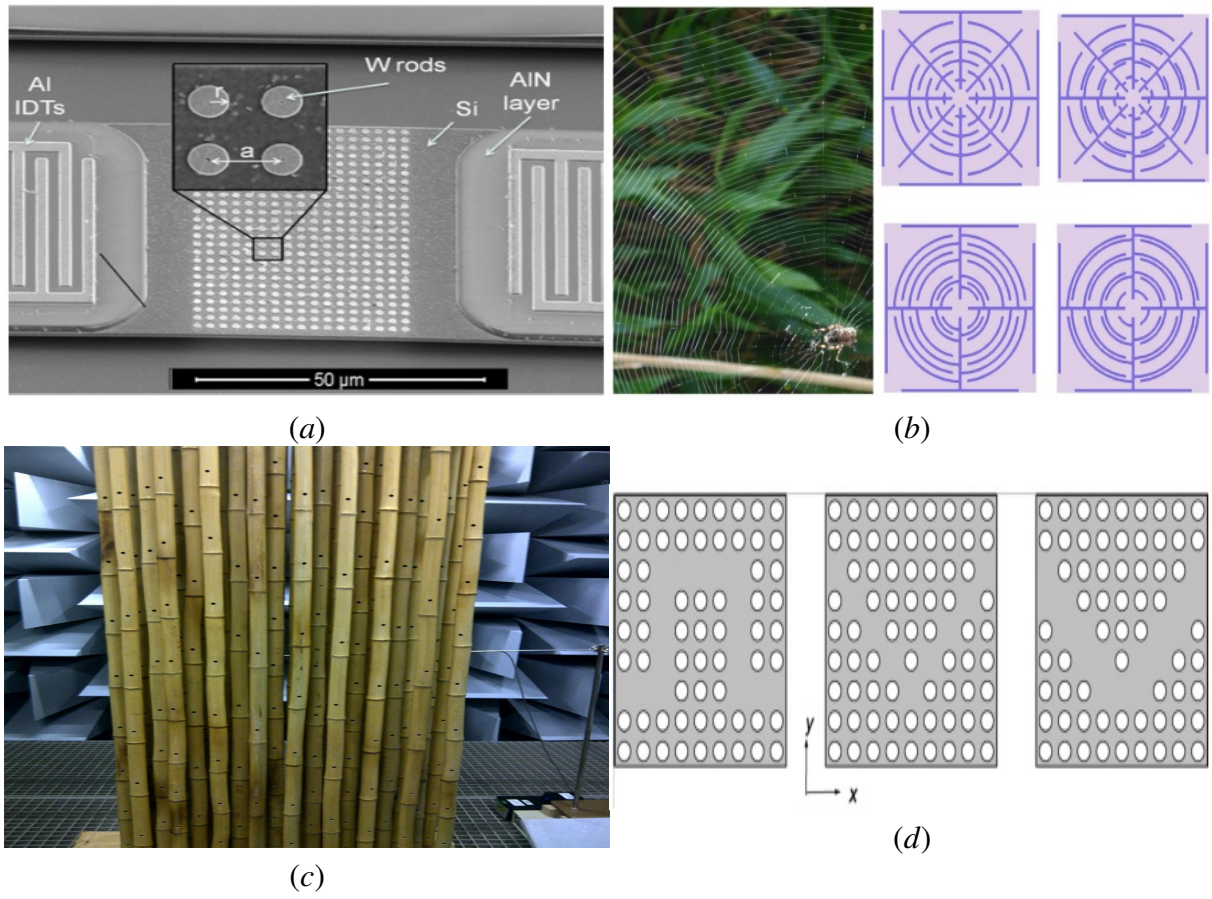


(*a*) (*b*) (*c*) (*d*)

Figure 1.1: Examples of PnC applications: an scanning electron microscope (SEM) image showing the PnC and aluminum nitride (AlN) transducers (Soliman *et al.*, 2010) $(a)$, a spider web woven by a garden spider Araneus diadematus and unit cells of a spider webstructured labyrinthine acoustic metamaterials (Krushynska *et al.*, 2017a) $(b)$, a sustainable SnC made of resonating bamboo rods (array of Helmholtz resonators) (Lagarrigue *et al.*, 2013) $(c)$, and cross sections of three supercells of PnCs with linear defects (Li and Liu, 2017) $(d)$.

Besides the concepts of photonic, phononic and phoxonic crystals, another important class of materials are the metamaterials. Metamaterials are engineered materials which exhibit unique properties that are not commonly observed or physically inconceivable in nature. The first efforts in order to develop these unusual materials had been mostly focussed on new electromagnetic materials to control electromagnetic waves. The concept of metamaterial was proposed from the study of Veselago (1968). He demonstrated theoretically that materials with simultaneous negative permittivity and permeability possess a negative refractive index under certain

frequencies. Due to the technology limitation in synthesis and fabrication, this novel concept remained to be an academic curiosity at that time (Li and Wang, 2016a). Recently, with the possibility of designing this type of metamaterials (known as left-handed electromagnetic materials or electromagnetic metamaterials or locally resonant photonic crystals), for instance using three-dimensional (3D) printing, they were successfully developed to achieve effectively negative permittivity and permeability (Smith *et al.*, 2000; Shelby *et al.*, 2001; Pendry, 2006).

Similar to the electromagnetic metamaterials, in recent years, mechanical (acoustic or elastic) metamaterials (MMs), also known as locally resonant PnCs, were designed. MMs exhibit negative effective mass and/or negative modulus. The main difference between PnCs and MMs is associated with the band gap formation. In PnC investigation, band gap formation is based on the Bragg scattering mechanism, whose frequency location is governed by Bragg's law, *i.e.*, $a \sin\theta = \tilde{n}(\lambda/2), (\tilde{n} \in \mathbb{N}_{>0})$, where $\theta$ is the incident angle, $a$ is the lattice parameter of periodic system and $\lambda$ is the wave length in host material. Bragg's law implies that is difficult to achieve a low-frequency Bragg-type band gap for small size PnCs. Difficulties to design PnCs with low frequency band gaps for small sizes instigated researchers to explore other dissipative mechanisms together with periodicity effect, such as local mechanical resonance in MMs. A brief discussion about locally resonant and Bragg-type band gaps is provided in Annexe A.3.

The first design of such materials was developed by Liu *et al.* (2000a). They considered embedding heavy spheres coated with soft silicon rubber in epoxy to obtain, experimentally, negative mass at certain loading frequencies. The underlying mechanism related to these metamaterials is the local mechanical resonance. These resonance-type band gaps were obtained by Liu *et al.* (2000a) in a frequency range two orders of magnitude lower than that given by the Bragg's limit. Locally resonant band gaps arise on the vicinity of resonator natural frequency and they do not depend on periodicity, while Bragg-type band gaps typically occur at wave lengths of the order of unit cell size. Even though PnCs and MMs have different concepts, as explained, some authors consider the MMs as an application of PnCs. Hence, MMs are also known as locally resonant PnCs, as already mentioned.

MMs have been extensively applied in the last years, for instance, as harnessed shape morphing (Cheng *et al.*, 2014a), topological protection (Chen *et al.*, 2014), instabilities and non-linear response (Bertoldi *et al.*, 2010), resonant circuit shunts (Zhou *et al.*, 2015), sustainable metamaterials (Lagarrigue *et al.*, 2013), piezoelectric metastructures (Sugino *et al.*, 2017), bio-inspired metamaterials (Krushynska *et al.*, 2017a), metamaterials supporting edge waves (Pal and Ruzzene, 2017), metamaterials-based enhanced energy harvesting (Chen *et al.*, 2014), thermal metamaterials (Davis and Hussein, 2014), granular crystals (nonlinear metamaterials) (Chong *et al.*, 2017), among others. Figure 1.2 shows some MM applications. In this thesis, elastic metamaterial (EM) beams (Appendix F) and plates (Appendix G) with multiple periodic arrays of multiple degrees of freedom (M-DOF) resonators are investigated for passive vibration control.

In order to handle PnCs and EMs, many methods have been applied, such as finite element

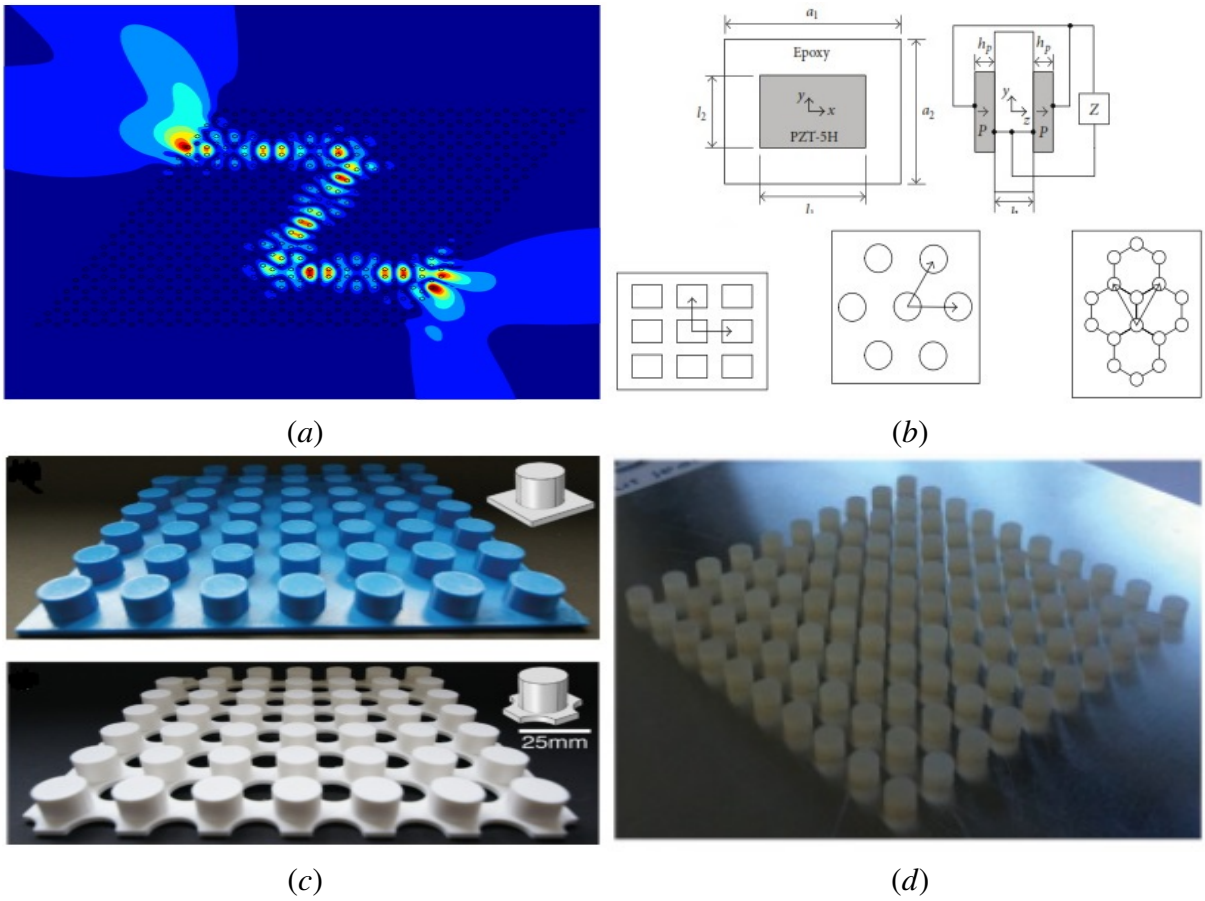


(*a*) (*b*)

(*c*) (*d*)

Figure 1.2: Examples of MM applications: edge waves in elastic metamaterial plates (Pal and Ruzzene, 2017) $(a)$, a unit cell of a two-dimensional PnC with circuits of orthogonal lattice and Wigner-Seitz unit cells for orthogonal, triangular and hexagonal lattices (Lian *et al.*, 2016) $(b)$, a metamaterial plate with pillars and a trampoline metamaterial composed of pillars and holes (Bilal *et al.*, 2017) $(c)$ and an EM plate with a periodic stubbed surface consisting of 10 x 10 silicone rubber stubs deposited on a thin aluminum plate (Oudich *et al.*, 2011) $(d)$.

(FE) (Wen *et al.*, 2009), spectral element (SE) (Wu *et al.*, 2009), wave finite element (WFE) (Nobrega *et al.*, 2016), wave spectral element (WSE) (Nobrega *et al.*, 2016), wave spectral finite element (WSFE) (Nascimento, 2009), boundary element (BE) (Henríquez *et al.*, 2017), plane wave expansion (PWE) (Kushwaha *et al.*, 1994), improved plane wave expansion (IPWE) (Xie *et al.*, 2017), extended plane wave expansion (EPWE) (Laude *et al.*, 2009), hybrid finite element-plane wave expansion (FE-PWE) (Mazzotti *et al.*, 2017), finite-difference time-domain method (FDTD) (Cao *et al.*, 2004), wavelet-based (Yan *et al.*, 2008), transfer matrix (TM) (Ni *et al.*, 2014), multi-scattering theory (MST) (Liu *et al.*, 2000b) methods, among others.

All the methods mentioned have advantages and drawbacks (Li *et al.*, 2016b). In this thesis, the methods most used to calculate the band structure, also know as dispersion relation or dispersion diagram, of PnCs and EMs are the PWE, IPWE and EPWE methods. However, FE, SE, TM, WFE and WSE methods are also used for some cases (Appendices A and F), in order to compare and to calculate the harmonic forced response of PnCs and EMs.

Since PnCs and MMs exhibit properties and functionalities that cannot be realized by

conventional materials and with the advances of additive manufacturing and nanofabrication, the design of new PnCs and MMs for passive vibration control is a current research topic and its application seems to constitute an open research topic. Bertoldi *et al.* (2017) outlined future challenges for the design, creation and conceptualization of advanced MMs.

## 1.2 Literature review

Wave propagation in periodic structures (Yablonovitch, 1987; Kushwaha *et al.*, 1994; Martínez-Sala *et al.*, 1995) has received increasing attention in the last years. In this subsection, some studies about PnCs, SnCs and MMs are addressed.

### 1.2.1 Phononic crystals

The first study about PnCs was carried out by Sigalas and Economou (1992). They regarded a PnC composed by periodic spheres embedded in a matrix, *i.e.*, 3D periodicity. Bulk wave propagation in an isotropic PnC solid was addressed and a phononic band gap was observed theoretically for the first time using the PWE approach. Other initial investigations (Sigalas and Economou, 1993; Kushwaha *et al.*, 1993; Kushwaha *et al.*, 1994) were also very important in order to stablish basic concepts related to PnCs. One of first reviews about PnCs was reported by Kushwaha (1996a). He focused on a briefly systematic survey of the historical development of the principles, tools and applications of band theory for electrons, photons, phonons and vibrations giving some background for basic concepts of photonic and phononic crystals.

After the PnC emergence in nineties, many researches have been developed. Djafari-Rouhani *et al.* (2008) investigated the existence of absolute band gaps and localized modes related to a guide in thin films of PnCs. Two different structures based on two-dimensional (2D) PnCs were considered, namely a free standing plate and a plate deposited on a silicon substrate. The 2D PnC was constituted by a square array of cylindrical holes drilled in an active piezoelectric PZT5A matrix. They demonstrated the existence of an absolute band gap in the band structure of the PnC plate and the possibility of guided modes inside a linear defect created by removing one row of air holes.

Based on Mindlin's piezoelectric plate theory and on the PWE, Hsu and Wu (2008) proposed a formulation to study the frequency band gaps and dispersion relations of the lower-order Lamb waves in 2D piezoelectric PnC plates. The method was applied to analyse PnC plates composed by solid-solid and air-solid constituents with square and triangular lattices, respectively. For solid/solid PnC plates, it was suggested that the filling material can be chosen with larger mass density, proper stiffness, and weak anisotropic factor embedded in a soft matrix in order to obtain wider complete band gaps of the lower-order Lamb waves. On the other hand, for air/solid PnC plates, a background material itself with proper anisotropy and a high filling

fraction of air may favour the opening of the complete Lamb wave gaps.

Wang *et al.* (2009) explored the elastic wave propagation in periodic cylinder magnetoelectroelastic PnCs with Kagomé lattice. The band structure characteristics of magnetoelectroelastic rods embedded in polymer matrix and the reverse case were investigated taking the electric, magnetic and mechanical coupling effects into account. The generalised eigenvalue equation was derived to analyse the in-plane and out-of-plane modes, respectively. They observed that the rule that high-density rods in low-density matrix is more easily to generate wave band gaps for pure elastic solid/solid periodic structures is also valid for the magnetoelectroelastic composites. Furthermore, the band gap properties and widths can be affected by the magnetoelectric effects.

Zhou *et al.* (2011) analysed theoretically the modulation of band gaps of in-plane elastic waves by the out-of-plane wave number that is parallel to the piezoelectric material rod axis in piezoelectric PnCs. The dependence of band gaps of in-plane elastic waves on the out-of-plane wave number and the filling fraction was calculated with and without the piezoelectricity. The in-plane band gaps can be opened (or closed) and the in-plane wave modes can be tuned by controlling the propagation of out-of-plane elastic waves. The in-plane band gap in the low-frequency range can be easily obtained by introducing an out-of-plane wave number, and was almost independent of the piezoelectricity. However, the widths and starting frequencies of in-plane band gaps in a relatively high-frequency range can be modulated by the filling fraction and piezoelectricity. The authors highlighted that the piezoelectric PnC is very useful in the design of ultrasonic transducers to avoid the invalid modes of in-plane elastic waves without affecting the working modes corresponding to the out-of-plane wave number.

Feng and Liu (2012) studied experimentally and theoretically the mechanism for the shift of the band gap in two kinds of finite PnCs, *i.e.*, steel/epoxy and aluminium/epoxy with different initial stresses. The experimental results and theoretical analysis simultaneously indicated that the initial stress efficiently tune the location and width of band gap.

Escalante *et al.* (2013) investigated the dispersion of PnC waveguides formed by evanescent coupling of a chain of defect cavities and supporting slow-wave propagation. It was considered a 2D PnC with square lattice of tungsten inclusions in a silicon matrix. The coupled-resonator acoustic waveguide dispersion can be controlled by increasing the distance between cavities, with the result of decreasing their coupling, and hence flattening the dispersion relation.

Huang *et al.* (2014) studied the band structures of shear horizontal waves in a periodically corrugated piezoelectric plate by using the supercell plane wave expansion method. The periodically corrugated piezoelectric plates with different types of symmetry gave rise to different kinds of band gaps and the associated defect states. The increase of defect size lowers the frequency of defect bands, and it can be used to tune the narrow-passband frequencies in band gaps. Symmetry breaking was also introduced by reducing the lower corrugation depth of the periodically corrugated piezoelectric plate. Results showed that symmetry breaking leads to both the appearance and disappearance of new kinds of band gaps and the corresponding defect

bands in these band gaps.

Feng *et al.* (2015) proposed a methodology for continuous tuning of confined line defect modes in 2D PnCs with hexagonal lattice. Different from the general method, where line defects are formed by removing several rows of cells from a perfect PnC, the line defect was considered as a free vibrating plate, and separated from the surrounding phononic structure. Thus, width of the line defect was adjusted. Resonant frequency of the confined defect mode could be continuously modified, and precisely determined to keep it locating at the central part of the phononic band gaps. It was also illustrated that different resonant modes (*i.e.*, flexural and extensional modes) have different relationships with the width of the line defect, and the unwanted resonant mode could be excluded from the phononic band gaps by carefully selecting the defect width. The simulation results indicated that each defect mode has an optimal width, in which case quality factor of the defect mode is maximum.

Bayat and Gordaninejad (2015) presented the wave propagation in a tunable PnC with square lattice consisting of a porous hyperelastic magnetorheological elastomer subjected to an external magnetic field. They observed that finite deformations and magnetic induction influence PnC characteristics through altering the geometry and material properties of the unit cell. They demonstrated that large deformations and magnetic induction could change the location and width of band gaps.

Guo *et al.* (2016) studied the effects of functionally graded interlayers on dispersion relations of elastic waves in a 1D piezoelectric/piezomagnetic PnC. Based on the transfer matrices of the piezoelectric slab, piezomagnetic slab and functionally graded interlayers, the total transfer matrix of a single cell was obtained. Further, from Floquet-Bloch's theorem, resultant dispersion equations of in-plane and anti-plane Bloch waves were obtained. Five kinds of profiles of functionally graded interlayers between a piezoelectric slab and a piezomagnetic slab were considered. It was shown that the functionally graded interlayers have evident influence on the band structures and band gaps.

Sadat and Wang (2016) investigated colloidal nanocrystal superlattices as PnCs with 3D periodicity. The nanoscale periodicity and acoustic contrast between the hard nanocrystal cores and soft ligand matrix led to phononic band gaps with centre frequencies on the order of $\sim 10^2$ GHz and band gap widths on the order of $\sim$10 GHz. Moreover, these characteristics can be tuned by changing the nanocrystal core diameter, nanocrystal core elastic modulus, interparticle distance, and ligand modulus. They underlined that colloidal nanocrystal superlattices are promising candidates for use in high frequency PnC applications that exert control over sound and heat.

Schneider *et al.* (2016) reported an indirect hypersonic phononic band gap and an anomalous dispersion of the acoustic-like branch from inelastic (Brillouin) light scattering experiments under varying applied elastic strains. They showed the mechanical nonlinearity of the silk structure generates a unique region of negative group velocity, that together with the global (mechanical) anisotropy provides novel symmetry conditions for band gap formation.

Chen *et al.* (2017) extended the bi-directional evolutionary structure optimization (BESO) method to design PnCs for maximizing spatial decay of evanescent waves. The optimization objective was to enlarge the minimum imaginary part of wave vectors at a specified frequency. They considered bulk wave propagation (out-of-plane and in-plane waves) in isotropic PnCs with 2D periodicity and square lattice. Numerical examples demonstrated that the optimization algorithm proposed was effective for designing PnCs with maximum spatial decay of evanescent waves. Various topological patterns of optimized PnCs were obtained.

Qian and Shi (2017) coupled the PWE and FE methods to calculate the band structures of semi-infinite beam-like PnCs with infinite periodicity in $z$ direction and finiteness in $xy$ plane. Explicit matrix formulations were developed for the calculation of band structures. First, PWE/FE method was applied to calculate the band structures of the Pb/rubber beam-like PnCs with circular and rectangular cross sections, respectively. Then, it was used to obtain the band structures of steel/epoxy and steel/aluminium beam-like PnCs with the same geometric parameters. Last, the band structure of the three-component beam-like PnC was calculated by the proposed method. Furthermore, all the results from the PWE/FE method were compared with those calculated by FE, and the corresponding results were in good agreement.

For some brief reviews about PnCs, see for instance the studies of Pennec *et al.* (2010), Li and Wang (2012) and Kushwaha (2016).

### 1.2.2 Sonic crystals

As mentioned before, SnCs are the acoustic version of PnCs. Laude (2015) defines SnCs as artificial crystals for acoustic or pressure waves in fluids. In the literature, the terms PnC and SnC are often used indifferently for all cases of artificial crystals, considering mechanical waves. However, in this thesis, SnCs are associated with acoustic waves, whereas PnCs are related to elastic waves. Some common examples of SnCs are fluid inclusions in a fluid matrix and solid inclusions in a fluid matrix. For the last case, it is not regarded the coupling among elastic and acoustic waves, and some associated effects. It must be underlined that fluid inclusions in a solid matrix is considered as a PnC. In Annexe A.2, it is discussed the equations that describe acoustic and elastic waves in SnCs and PnCs, respectively.

Kushwaha *et al.* (1998) calculated extensive the band structures for cubic arrays of rigid spheres and cubes in air. Full band gaps were obtained for the face-centred-cubic structure. However, there was no band gap for the body-centered-cubic and simple-cubic structures. They also proposed a tandem structure that allows the achievement of an ultrawideband filter for environmental or industrial noise in the desired frequency range. The authors mentioned that their study was motivated by the experimental measurement of sound attenuation on the sculpture, by Eusebio Sempere, exhibited at the Juan March Foundation in Madrid (Martínez-Sala *et al.*, 1995).

Zhang *et al.* (2004) investigated defect modes created by introducing a bend-shaped linear defect in a 2D SnC consisting of water cylinders in mercury background. They used the supercell plane wave approach. The bend-shaped linear defect was made up of water cylinders with different size, and the size of the defect cylinders was shown to strongly influence the defect modes existing in the frequency regime of the band gap. By analysing the pressure field of defect modes, they found the waves are localized in the bend-shaped linear defect. It provided a foundation in theory to design a bent waveguide in engineering application.

Martínez-Sala *et al.* (2006) demonstrated that it is possible to improve the sound attenuation obtained from a mass of trees by arranging them in a periodic lattice. The outdoor experimental results showed that the largest sound attenuation, within a certain range of frequencies, was obtained for a range of frequencies associated with the array periodicity. These arrays of trees worked like SnCs. Therefore, the authors suggested that these periodic arrays could be used as green acoustic screens.

Qiu and Liu (2006) investigated numerically the radiation of a line acoustic source placed inside a SnC of square lattice composed by steel inclusions in water. Their results showed that it is possible to obtain a highly directional acoustic source with a large radiation enhancement, operating at the band-edge frequency of the SnC. The angular distributions of the radiation power and the radiation enhancement factor are strongly dependent on the position of the acoustic source relative to the unit cell in which it is placed.

Romero-García *et al.* (2007) presented an interferometric method of characterizing directly the refraction index of SnCs. They focused their research on SnCs constructed with a periodic distribution of rigid cylinders in air. The interferometric method used was based on the acoustical analog of an optical device called Fresnel's biprism. Their numerical results were in good agreement with the experimental results and allowed to estimate the refraction index for very low frequencies. They concluded that this method offers certain advantages with respect to the classical method used to obtain the refraction index in SnCs with airborne propagation, that is the phase delay method.

Sánchez-Dehesa *et al.* (2011) studied noise barriers based on SnCs made of cylinders that used recycled materials like absorbing component. The barriers consisted of only three rows of perforated metal shells filled with rubber crumb. Measurements of reflectance and transmittance by these barriers were reported. The attenuation properties resulted from a combination of sound absorption by the rubber crumb and reflection by the periodic distribution of scatterers. They concluded that the porous cylinders can be used as building blocks in order to design barriers adapted to different noisy environments.

Romero-García *et al.* (2012) reported theoretically and experimentally inverse-designed scattering acoustical elements, called quasi-ordered structures, showing their possibilities as attenuation devices. Multiobjective evolutionary algorithms together with MST were used to design a distribution of vacancies in a SnC in order to create a quasi-ordered structure with predetermined properties. The authors highlighted that moulding the acoustic attenuation is one

of the most important properties for the design of effective filters.

Castiñeira-Ibáñez *et al.* (2012) presented the design and the manufacturing processes, as well as the acoustics standardization tests, of an acoustic barrier formed by a set of multi-phenomena cylindrical scatterers. The multiple scattering of waves inside SnCs led to attenuation bands related to the periodicity of the structure by means of Bragg scattering. In order to design the acoustic barrier, they proposed two strategies, *i.e.*, the arrangement of scatterers was based on fractal geometries to maximize the Bragg scattering and multi-phenomena scatterers with several noise control mechanisms, as resonances or absorption, were designed and used to construct the periodic array. They asserted that the acoustic barrier designed provides a high technological solution in the field of noise control.

Martins *et al.* (2013) used 2D SnCs as noise barriers to mitigate road traffic noise by means of an approach based on a numerical technique called the method of fundamental solutions. The method of fundamental solutions was used to evaluate the performance of SnCs composed by circular inclusions, studying the effect of varying dimensions and spacing of the crystal elements as well as their acoustic absorption in the sound attenuation provided by the global structure. When comparing the effect of using a triangular or square lattice, the results showed a trend for better performance, in terms of the calculated insertion loss, when structures with a triangular lattice were used.

Morandi *et al.* (2016) carried out sound insulation and sound reflection measurements conducted over SnC noise barriers according to the European standards EN 1793-2, EN 1793-5 and EN 1793-6. They performed free-field measurements over a real-sized sample in order to window out all diffraction components and to verify the points of strength and weakness of the application of standardised measurements to SnCs. Since the target frequency range for traffic noise spectrum is centred at around 1000 Hz, as mentioned by them, a FE based parametric investigation was performed to design unit cells capable of generating band gaps in the one-third octave bands ranging from 800 Hz to 1250 Hz. Then, $3 \times 3$ m SnC noise barriers were installed in the Laboratory of the University of Bologna and sound insulation and sound reflection measurements were performed for normal incidence. The standardised measurements allowed a direct comparison between the performance of SnCs and common noise barriers.

### 1.2.3 Mechanical metamaterials

Lagarrigue *et al.* (2013) investigated experimentally and theoretically the acoustic transmission coefficient of a MM made of hollow bamboo rods. The hollow bamboo rods were drilled between each node to create an array of Helmholtz resonators. It was shown that the presence of Helmholtz resonators leads to locally resonant band gaps in the low-frequency part of the transmission coefficient.

Cheng and Shi (2014b) studied the attenuation zones of 2D periodic rubber concrete panels. Both the Bragg-scattering periodic panels (PnCs) and the local-resonant periodic panels

(EMs) were addressed. They found that complete attenuation zones in the low frequency region can be obtained in the considered panels by proper design. Furthermore, the study of parameters showed that non-symmetric periodic panels with directional attenuation zones are much suitable for engineering applications. This investigation also showed that vibration can be reduced significantly by using a periodic structure with only three units.

Zhu *et al.* (2015) studied analytically and numerically plane wave propagation and reflection in semi-infinite EMs with doubly or triply negative material properties. The unique negative refractions for the longitudinal and transverse waves were captured by the proposed generalized Snell's law. The effects of different angles of incidence were also investigated for both double-negative and triple-negative transmitted media and some unusual wave propagation phenomena, such as complete wave mode conversion was numerically demonstrated. They mentioned that this study can serve as the theoretical foundation for engineering and designing general metamaterial-based elastic wave devices.

Xiao *et al.* (2014) reported theoretical examination and experimental demonstration of EM plates consisting of a periodic array of beam-like resonators attached to a thin homogeneous plate. They demonstrated that a low-frequency complete band gap for flexural plate waves can be created in the proposed structure owing to the interaction between the localized resonant modes of the beam-like resonators and the flexural wave modes of the host plate. They showed that the location and width of the complete band gap can be dramatically tuned by changing the properties of the beam-like resonators. They also performed experimental measurements of a specimen fabricated by an array of double-stacked aluminium beam-like resonators attached to a thin aluminium plate with 5 cm structure periodicity. The experimental results evidenced a complete band gap extending from 465 Hz to 860 Hz, matching well with their theoretical prediction.

Assouar *et al.* (2016) provided theoretical and numerical analyses of the behaviour of an acoustic metamaterial plate considered in an air-borne sound environment in view of sound mitigation application. They regarded two plate configurations, that is a spring-mass one and a pillar system-based one. They observed that a high sound transmission loss up to 82 dB was reached with a metamaterial plate with a thickness of 0.5 mm. Comparison between sound transmission loss, band structure, displacement fields and effective mass density of the metamaterial plate was performed in order to understand the different mechanisms involved.

Achaoui *et al.* (2016) investigated stop band properties of a theoretical cubic array of iron spheres connected to a bulk of concrete via iron or rubber ligaments. Each sphere moved freely within a surrounding air cavity, however, ligaments coupled it to the bulk and facilitated bending and rotational motions. They found complete band gaps in the range [16, 21] Hz ([6, 11] Hz) for 7.4 m (0.74 m) diameter iron spheres with a 10 m (1 m) centre-to-centre spacing, when they were connected to concrete via steel (rubber) ligaments. They observed that only bending modes were responsible for damping and rotational modes were totally overwritten by bending modes. The authors highlighted that their results represented a preliminary step in the design of

seismic shields placed around, or underneath, foundations of large civil infrastructures.

Claeys *et al.* (2016) performed the numerical design and experimental validation of acoustic insulation based on the concept of metamaterials: a hollow core periodic sandwich structure with added local resonant structures. They studied a set of variations on the nominal design in order to investigate the sensitivity to specific parameters in the metamaterial design and the design robustness. The stop bands were numerically predicted through unit cell modelling after which a full vibro-acoustic FE model was applied to predict the insertion loss of the demonstrator. They concluded that the results of these analyses and the measurements indicate that this metamaterial concept can be applied to combine light weight, compact volume and good acoustic behaviour.

Yi *et al.* (2016) designed and analysed a piezo-lens to focus flexural waves in thin plates. The piezoelectric patches were shunted with negative capacitance circuits. The effective refractive indexes inside the piezo-lens were designed to fit a hyperbolic secant distribution by tuning the negative capacitance values. Numerical results showed that the piezo-lens can focus flexural waves by bending their trajectories, and was effective in a large frequency band. The piezo-lens had the ability to focus flexural waves at different locations by tuning the shunting negative capacitance values. They underlined that piezo-lens showed to be effective for flexural waves generated by different types of sources.

Ai and Gao (2017) designed four metallic metamaterials with tailorable mechanical properties using bi-material star-shaped re-entrant planar lattice structures, which did not involve pins, adhesive, welding or pressure-fit joints and can be fabricated through laser-based additive manufacturing. Three length parameters, one angle parameter and three material combinations were used in order to explore structure-property relations. It was found that the bi-material lattice structures can be tailored to obtain 3D printable metallic metamaterials with positive, near-zero or negative Poisson's ratio and coefficient of thermal expansion together with an uncompromised Young's modulus. They also showed that one of the four metamaterials can exhibit both a negative Poisson's ratio and a non-positive coefficient of thermal expansion simultaneously. They mentioned that these metallic metamaterials can find applications in structures or devices such as antennas and precision instruments to reduce thermomechanical stresses and extend service lives.

Two-dimensional metamaterials consisting of plates with resonant cylinders have been shown to attenuate waves much larger than their characteristic unit cell size by opening sub-wavelength band gaps. However the bandwidth of the band gap correlates strongly with the resonator mass, which limits metamaterials functionality in mass sensitive applications (Bilal *et al.*, 2017). To overcome this limitation, Bilal *et al.* (2017) showed theoretically that trampoline phenomena broaden the width of the first partial band gap by up to a factor 4 of the linear resonant band gap. They provided an experimental demonstration of the trampoline phenomena in 3D-printed plates, consisting of pillars and holes, composed of a single material. They showed numerically and experimentally that trampoline plates increase both partial and full

band gaps widths, while reducing the base-plate's mass by $\approx 30\%$ in the studied configurations.

Pal and Ruzzene (2017) investigated EMs characterized by topologically non-trivial band gaps supporting backscattering suppressed edge waves. These edge waves are topologically protected and are obtained by breaking inversion symmetry within the unit cell. This concept was implemented on an EM plate featuring an array of resonators arranged according to a hexagonal topology. The resulting continuous structures showed non-trivial band gaps supporting edge waves at the interface between two media with different topological invariants.

Krushynska *et al.* (2017b) compared the wave dispersion for 2D and 3D metamaterials with multilayered inclusions. Numerical study revealed that dual-resonant structures with cylindrical inclusions possess only a single (compared to two in the 2D case) band gap for certain height-to-width ratios. In contrast, they observed that the wave dispersion in metamaterials with multiple spherical resonators can be accurately evaluated using a 2D approximation, enabling a significant simplification of resource-consuming 3D models.

Li *et al.* (2017) numerically and experimentally demonstrated the low-frequency broadband elastic wave attenuation and vibration suppression by using an EM plate, which is constituted of periodic double-sides stepped resonators deposited on a 2D phononic plate with steel matrix. In contrast to the typical phononic plates consisting of periodic stepped resonators deposited on a homogeneous steel plate, the proposed EM can yield large band gap in the low-frequency range, resulting in the low-frequency broadband elastic wave attenuation. They observed that the formation mechanism of opening the low-frequency band gap is attributed to the coupling between the local resonant Lamb modes of 2D phononic plate and the resonant modes of the stepped resonators. The band gap can be significantly modulated by the material and geometrical parameters.

Chang *et al.* (2018) discussed the wave propagation behaviour and attenuation mechanism of the EM with locally resonant sub-structure. The dynamically equivalent properties, *i.e.*, mass and elastic property, of the single resonance system were derived and found to be frequency dependent. Negative effective properties were found in the vicinity of the local resonance. They examined whether the band gap always coincides with the frequency range of negative effective properties. From this analysis, they observed that when the stop frequency, which is the highest propagating frequency of the main structure, was lower than the local resonance of the sub-structure, the band gap would not totally overlap with the frequency range of negative effective properties. They also reported that the coupled Bragg-resonance band gap is much wider than the narrow-banded local resonance and the corresponding effective material properties at band gap could be either positive or negative.

## 1.3 Objectives

The main objective of this thesis is to study 1D and 2D PnCs and EMs for passive vibration control in different applications by means of PWE, IPWE and EPWE approaches. The specific objectives of this thesis are listed in the following.

- Present the band structure of 1D PnC rods, 2D SnCs and 1D EM Euler-Bernoulli beams by means of PWE, IPWE and EPWE.
- Analyse the Bragg-type band gap formation, band structure, harmonic forced response and attenuation constant of a 1D PnC beam using the FE, SE, WFE, WSE, PWE and IPWE methods.
- Study the flexural wave band gaps in a 2D PnC plate with different lattices and inclusions considering Mindlin-Reissner theory.
- Evaluate the elastic band structure of a carbon nanostructure PnC and a nano-piezoelectric PnC with different lattices and inclusions, considering wave propagation in the *xy* plane and 2D periodicity.
- Compare the band structure of a nano-piezoelectric PnC, considering Z modes with and without piezoelectricity.
- Investigate the band structure of a 2D magnetoelectroelastic PnC composed by $BaTiO_3$-$CoFe_2O_4$ inclusions in a polymeric matrix, considering wave propagation in the *xy* plane in an inhomogeneous transversely isotropic elastic solid.
- Investigate the band structure of flexural waves propagating in an EM beam and its harmonic forced response, considering periodic arrays of single degree of freedom (S-DOF) and M-DOF resonators.
- Compare the elastic band structure obtained by means of PWE, EPWE, WFE and WSE methods, considering an EM beam with periodic arrays of S-DOF and M-DOF resonators.
- Analyse the elastic band structure of flexural waves propagating in an EM thin plate with multiple periodic arrays of attached M-DOF resonators, considering square and triangular lattices.

## 1.4 Outline of the thesis

This thesis is organized as follows.

In Chapter 2, PWE, IPWE and EPWE approaches are formulated for simple cases, *i.e.*, 1D PnC rods, 2D SnCs and 1D EM Euler-Bernoulli beams. Some advantages and drawbacks are also underlined.

In Chapter 3, simulated examples of mechanical wave propagation in 1D PnC rods, 2D SnCs and 1D EM Euler-Bernoulli beams are carried out using PWE, IPWE and EPWE methods.

In Chapter 4, general conclusions regarding this thesis are drawn. Then, original contributions of this study are highlighted in a list of the publications that resulted during the thesis

progress.

In Annexe A, some basic concepts of 2D periodic systems, such as geometric properties, wave propagation and band gaps are reported.

In Appendices A–G, attached papers are provided and some applications of PnCs and EMs for passive vibration control are investigated.

In Appendix A, the band structure and the harmonic forced response of a 1D PnC Euler-Bernoulli beam are investigated.

In Appendix B, it is studied flexural wave band gaps in a 2D PnC thick plate, composed by an epoxy matrix reinforced by $Al_2O_3$ inclusions.

In Appendices C and D, it is discussed the influence of different inclusion cross sections and different lattices on the band structures of 2D carbon nanostructure PnCs and 2D nano-piezoelectric PnCs.

In Appendix E, the piezoelectricity and piezomagnetism are considered on the band structure of a 2D magnetoelectroelastic PnC.

In Appendix F, the harmonic forced response and the band structure of a 1D EM Euler-Bernoulli beam with periodically attached spring-mass resonators are calculated.

In Appendix G, it is analysed the complex band structure of flexural waves propagating in an 2D EM thin plate with multiple periodic arrays of M-DOF resonators in square and triangular lattices.

In Appendix H, some implemented codes in MATLAB® are available.

# 2 THEORETICAL MODELS

In this section, PWE, IPWE and EPWE approaches are presented for simple cases. First, it is considered a 1D PnC rod composed by two materials. Next, it is regarded a 2D SnC with square lattice, consisting of periodic circular solid inclusions in a fluid matrix. Finally, a 1D EM Euler-Bernoulli beam with periodic array of resonators is addressed.

## 2.1 Plane wave expansion method

PWE is the most used method to calculate the band structure of periodic systems, such as photonic crystals (El-Naggar, 2012), PnCs (Kushwaha *et al.*, 1994; Sigalas and Economou, 1992; Laude *et al.*, 2009), SnCs (Kushwaha and Halevi, 1994) and MMs (Xiao *et al.*, 2012a; Xiao *et al.*, 2012b). PWE has also been applied to calculate the band structure of smart PnCs, for instance, piezoelectric (Qian *et al.*, 2008), piezomagnetic (Vasseur *et al.*, 2011) and magnetoelectroelastic (Wang *et al.*, 2008) PnCs.

PWE uses the system periodicity and Floquet-Bloch's theorem (Floquet, 1883; Bloch, 1928) to solve the wave equation, obtaining an eigenvalue problem $\omega(\mathbf{k})$. This eigenvalue problem must be solved for each Bloch wave vector value into the first irreducible Brillouin zone (FIBZ) (Brillouin, 1946). One of the main advantages of using PWE method is its facility of being implemented. PWE is regarded as a semi-analytical method, because Fourier series expansion in reciprocal space must be truncated. This method has also some drawbacks, for instance, when there is high geometry or material mismatch PWE presents slow convergence and IPWE method must be used.

PWE formulation is presented in detail for 1D PnC Euler-Bernoulli beams (Appendix A), 2D PnC thick plates (Appendix B), 2D PnC solids (Appendix C), 2D piezoelectric PnC solids (Appendix D) and 2D magnetoelectroelastic PnC solids (Appendix E). In this subsection, it is considered just 1D PnC rods, 2D SnCs and 1D EM Euler-Bernoulli beams.

### 2.1.1 PWE formulation for 1D phononic crystal rods

From simple rod theory, the governing equation for longitudinal vibrations in a infinite uniform rod system can be written as (Lee, 2009):

$$\frac{\partial}{\partial x}\left[ES\frac{\partial \hat{u}_1(x,t)}{\partial x}\right] = \rho S\frac{\partial^2 \hat{u}_1(x,t)}{\partial t^2}, \tag{2.1}$$

where $E$ is the Young's modulus, $S$ is the cross section area, $\hat{u}_1$ is the longitudinal displacement in time domain, $x$ is the spatial position and $t$ is the time.

Applying the temporal Fourier transform on Eq. (2.1), results:

$$\frac{\partial}{\partial x}\left[ES\frac{\partial u_1(x,\omega)}{\partial x}\right] + \omega^2 \rho S u_1(x,\omega) = 0, \tag{2.2}$$

where $\omega$ is the angular frequency and $u_1(x,\omega)$ is the longitudinal displacement in frequency domain. Considering a 1D PnC rod consisting of periodic unit cells with different materials, one may write $E = E(x)$ and $\rho = \rho(x)$. Note that $E(x) = E(x+a)$ and $\rho(x) = \rho(x+a)$, where $a$ is the lattice parameter, *i.e.*, unit cell length. From now on, it is regarded $u_1(x,\omega) = u_1(x)$ for simplification.

Hereafter, basic concepts of Solid State Physics are necessary, see Annexes A.1 and A.2. Applying the Floquet-Bloch's theorem and considering wave propagation on the $x$ axis ($k_2$,$k_3 = 0$), gives:

$$u_1(x) = e^{jkx} u_{1_k}(x), \tag{2.3}$$

where $k = k_1$, $k \in \mathbb{R}$, is the Bloch wave vector, also known as wave number and has its value within the FIBZ in reciprocal space, $\left[0, \frac{\pi}{a}\right]$, or within the FBZ, $\left[-\frac{\pi}{a}, \frac{\pi}{a}\right]$, $j = \sqrt{-1}$ and $u_{1_k}(x)$ is the Bloch wave amplitude. Note that $u_{1_k}(x) = u_{1_k}(x+a)$, $u_1(x+a) = u_1(x)e^{jka}$, where $e^{jka}$ is the Floquet-Bloch periodic boundary condition. Expanding Bloch wave amplitude as Fourier series in reciprocal space, yields:

$$u_1(x) = e^{jkx} \sum_{m=-\infty}^{+\infty} u_{1_m} e^{jg_m x} = \sum_{m=-\infty}^{+\infty} u_{1_m} e^{j(k+g_m)x}, \tag{2.4}$$

where $u_{1_m} = u_{1_{k_m}}$, $g_m = \frac{2\pi m}{a}$ is the reciprocal lattice vector and $m \in \mathbb{Z}$. Note that $g_m$ is a constant, since it is considered 1D periodicity. Furthermore, material properties can also be expanded as Fourier series in the reciprocal space as:

$$\bar{P}(x) = \sum_{\bar{m}=-\infty}^{+\infty} \bar{P}_{\bar{m}} e^{jg_{\bar{m}}x}, \tag{2.5}$$

where $\bar{P}(x)$ is one of $\alpha(x) = \rho(x)S$, $\gamma(x) = E(x)S$ and $g_{\bar{m}} = \frac{2\pi\bar{m}}{a}$, $\bar{m} \in \mathbb{Z}$. It is used $g_{\bar{m}}$ and $\bar{m}$ to highlight the difference between the expansions of material properties and displacement. Fourier series coefficients $\bar{P}_{\bar{m}}$ in Eq. (2.5) can be calculated by:

$$\bar{P}_{\bar{m}} = \frac{1}{a}\int_{-a/2}^{a/2} \bar{P}(x) e^{-jg_{\bar{m}}x} dx. \tag{2.6}$$

Substituting Eqs. (2.4) and (2.5) in Eq. (2.2), gives:

$$\sum_{m=-\infty}^{+\infty} \sum_{\bar{m}=-\infty}^{+\infty} \left[\gamma_{\bar{m}} u_{1_m}(k+g_m)(k+g_m+g_{\bar{m}}) - \omega^2 \alpha_{\bar{m}} u_{1_m}\right] e^{j(k+g_m+g_{\bar{m}})x} = 0. \tag{2.7}$$

Making a variable change $g_{\tilde{m}} = g_{\bar{m}} + g_m$, results:

$$\sum_{m=-\infty}^{+\infty} \sum_{\tilde{m}=-\infty}^{+\infty} \left[\gamma_{\tilde{m}-m} u_{1_m}(k+g_m)(k+g_{\tilde{m}}) - \omega^2 \alpha_{\tilde{m}-m} u_{1_m}\right] e^{j(k+g_{\tilde{m}})x} = 0. \tag{2.8}$$

Multiplying Eq. (2.8) by $e^{-jg_{\bar{m}}x}$, integrating over the unit cell, one can write for all $x$:

$$\sum_{m=-\infty}^{+\infty} \sum_{\tilde{m}=-\infty}^{+\infty} \left[\gamma_{\tilde{m}-m} u_{1_m}(k+g_m)(k+g_{\tilde{m}}) - \omega^2 \alpha_{\tilde{m}-m} u_{1_m}\right] \frac{1}{a} \int_{-a/2}^{a/2} e^{j(g_{\tilde{m}}-g_{\bar{m}})x} dx = 0. \tag{2.9}$$

Remembering the definition of $\delta_{\tilde{m}\bar{m}}$:

$$\delta_{\tilde{m}\bar{m}} = \frac{1}{a} \int_{-a/2}^{a/2} e^{j(g_{\tilde{m}}-g_{\bar{m}})x} dx, \tag{2.10}$$

Eq. (2.9) can be rewritten as:

$$\sum_{m=-\infty}^{+\infty} \left[\gamma_{\bar{m}-m} u_{1_m}(k+g_m)(k+g_{\bar{m}}) - \omega^2 \alpha_{\bar{m}-m} u_{1_m}\right] = 0. \tag{2.11}$$

Equation (2.11) is an infinite system of equations, thus Fourier series must be truncated, *i.e.*, $m, \bar{m} = [-M, \ldots, M]$, $M \in \mathbb{Z}$, and the total number of plane waves is $2M+1$. Then, Eq. (2.11) can be rewritten as:

$$\mathbf{A}\bar{\mathbf{u}}_1 = \omega^2 \mathbf{B}\bar{\mathbf{u}}_1, \tag{2.12}$$

where the coefficients of vector $\bar{\mathbf{u}}_1$ are $u_{1_m}$ and the coefficients of matrices $\mathbf{A}$ and $\mathbf{B}$ are given by:

$$A_{m\bar{m}} = \gamma_{\bar{m}-m}(k+g_m)(k+g_{\bar{m}}),\ B_{m\bar{m}} = \alpha_{\bar{m}-m}. \tag{2.13}$$

Equation (2.12) represents a generalized eigenvalue problem of $\omega^2(k)$ and should be solved for each $k$ into the FIBZ or FBZ.

### 2.1.2 PWE formulation for 2D sonic crystals

The wave equation for an isotropic medium of infinite extension in absence of an external force, regarding acoustic case (see Annexe A.2) and 2D problem ($\partial/\partial x_3 = 0$), can be written as (Kushwaha and Halevi, 1996b):

$$c_{11}^{-1} \frac{\partial^2 \hat{p}(\mathbf{r},t)}{\partial t^2} = \nabla \cdot [\rho^{-1} \nabla \hat{p}(\mathbf{r},t)], \tag{2.14}$$

where $c_{11}$ is the elastic constant, $\hat{p}$ is the pressure in time domain and $\mathbf{r} = x\mathbf{e}_1 + y\mathbf{e}_2$ is the 2D spatial vector. Note that $c_{11}(\mathbf{r}) = c_{11}(\mathbf{r}+\bar{\mathbf{r}})$ and $\rho(\mathbf{r}) = \rho(\mathbf{r}+\bar{\mathbf{r}})$, where $\bar{\mathbf{r}}$ is the lattice vector (see Annexe A.1).

Applying the temporal Fourier transform on Eq. (2.14), gives:

$$\nabla \cdot [\rho^{-1} \nabla p(\mathbf{r},\omega)] + \omega^2 c_{11}^{-1} p(\mathbf{r},\omega) = 0, \tag{2.15}$$

where $p$ is the pressure in frequency domain.

Considering a SnC with periodic solid inclusions embedded in a fluid matrix, one can write $c_{11} = \rho c_l^2 = c_{11}(\mathbf{r})$ and $\rho = \rho(\mathbf{r})$, where $c_l$ is the longitudinal speed of sound. It must be highlighted that the Eq. (2.14) is valid only whether waves propagating through the SnC can be regarded as purely longitudinal as long as coupling of shear elastic waves inside the solid inclusions to acoustic waves in the fluid matrix can be completely ignored (Laude, 2015). Equation (2.14) is more suitable neglecting inclusion shear rigidity, *e.g.*, for a latex wall ($c_t \ll c_l$) (Kushwaha and Halevi, 1997), where $c_t$ is the transverse speed of sound in the inclusion, or supposing infinite density in the case of metallic inclusions (Kushwaha *et al.*, 1998). This implies that sound does not penetrate the inclusion and acoustic wave propagation is confined in the air (Kushwaha *et al.*, 1998). We regard this assumption for the solid inclusions.

Applying the Floquet-Bloch's theorem and considering wave propagation on the $xy$ plane ($k_3 = 0$), results in:

$$p(\mathbf{r}) = e^{j\mathbf{k}\cdot\mathbf{r}} p_{\mathbf{k}}(\mathbf{r}), \tag{2.16}$$

where $p(\mathbf{r},\omega) = p(\mathbf{r})$ for brevity, $\mathbf{k} = \bar{u}\mathbf{b}_1 + \bar{v}\mathbf{b}_2$, $\bar{u},\bar{v} \in \mathbb{Q}$ are symmetry points within the FIBZ in reciprocal space, or $\mathbf{k} = k_1\mathbf{e}_1 + k_2\mathbf{e}_2$, $k_1,k_2 \in \mathbb{R}$ are the point coordinates within FIBZ in Figure A.3 (f-j) for the reciprocal space. The basis vectors in reciprocal and real spaces, $\mathbf{b}_i (i = 1,2)$ and $\mathbf{a}_i (i = 1,2)$, are defined in Annexe A.1. Hereafter, it is considered a SnC with square lattice. Furthermore, note that $p_{\mathbf{k}}(\mathbf{r}) = p_{\mathbf{k}}(\mathbf{r} + \bar{\mathbf{r}})$ and $p(\mathbf{r} + \bar{\mathbf{r}}) = p(\mathbf{r}) e^{j\mathbf{k}\cdot\bar{\mathbf{r}}}$, where $e^{j\mathbf{k}\cdot\bar{\mathbf{r}}}$ is the Floquet-Bloch periodic boundary condition.

Expanding Bloch wave amplitude $p_{\mathbf{k}}(\mathbf{r})$ as Fourier series in reciprocal space, yields:

$$p(\mathbf{r}) = e^{j\mathbf{k}\cdot\mathbf{r}} \sum_{m=-\infty}^{+\infty} \sum_{n=-\infty}^{+\infty} p_{m,n} e^{j\mathbf{g}_{m,n}\cdot\mathbf{r}} = \sum_{m=-\infty}^{+\infty} \sum_{n=-\infty}^{+\infty} p_{m,n} e^{j(\mathbf{k}+\mathbf{g}_{m,n})\cdot\mathbf{r}}, \tag{2.17}$$

where $p_{m,n} = p_{\mathbf{k}_{m,n}}$, $\mathbf{g}_{m,n} = \frac{2\pi}{a}(m\mathbf{e}_1 + n\mathbf{e}_2)$ is the reciprocal lattice vector for square lattice (see Annexe A.1) and $m, n \in \mathbb{Z}$. Furthermore, material properties can also be expanded as Fourier series in the reciprocal space as:

$$P(\mathbf{r}) = \sum_{\bar{m}=-\infty}^{+\infty} \sum_{\bar{n}=-\infty}^{+\infty} P_{\bar{m},\bar{n}} e^{j\mathbf{g}_{\bar{m},\bar{n}}\cdot\mathbf{r}}, \tag{2.18}$$

where $P(\mathbf{r})$ is one of $\rho^{-1}(\mathbf{r})$, $c_{11}^{-1}(\mathbf{r})$ and $\mathbf{g}_{\bar{m},\bar{n}} = \frac{2\pi}{a}(\bar{m}\mathbf{e}_1 + \bar{n}\mathbf{e}_2)$, $\bar{m}, \bar{n} \in \mathbb{Z}$. It is used $\mathbf{g}_{\bar{m},\bar{n}}$ and $\bar{m},\bar{n}$ to highlight the difference between the expansions of material properties and pressure. The Fourier series coefficients $P_{\bar{m},\bar{n}}$ in Eq. (2.18) can be calculated by:

$$P_{\bar{m},\bar{n}} = \frac{1}{S_C}\int\int P(\mathbf{r})e^{-j\mathbf{g}_{\bar{m},\bar{n}}\cdot\mathbf{r}}d^2r, \tag{2.19}$$

where the integral is evaluated over the unit cell and $S_C = ||\mathbf{a}_1 \times \mathbf{a}_2||$ is the cross section area of the unit cell. Substituting Eqs. (2.17) and (2.18) in Eq. (2.15), gives:

$$\sum_{m=-\infty}^{+\infty}\sum_{n=-\infty}^{+\infty}\sum_{\bar{m}=-\infty}^{+\infty}\sum_{\bar{n}=-\infty}^{+\infty}\{\rho^{-1}_{\bar{m},\bar{n}}p_{m,n}[(k_1+g_{1_m})(k_1+g_{1_m}+g_{1_{\bar{m}}})+(k_2+g_{2_n})(k_2+g_{2_n} +g_{2_{\bar{n}}})] - \omega^2 c^{-1}_{11_{\bar{m},\bar{n}}}p_{m,n}\}e^{j(\mathbf{k}+\mathbf{g}_{m,n}+\mathbf{g}_{\bar{m},\bar{n}})\cdot\mathbf{r}} = 0. \tag{2.20}$$

Making a variable change $\mathbf{g}_{\tilde{m},\tilde{n}} = \mathbf{g}_{\bar{m},\bar{n}} + \mathbf{g}_{m,n}$, results:

$$\sum_{m=-\infty}^{+\infty}\sum_{n=-\infty}^{+\infty}\sum_{\tilde{m}=-\infty}^{+\infty}\sum_{\tilde{n}=-\infty}^{+\infty}\{\rho^{-1}_{\tilde{m}-m,\tilde{n}-n}p_{m,n}[(k_1+g_{1_m})(k_1+g_{1_{\tilde{m}}})+(k_2+g_{2_n})(k_2+g_{2_{\tilde{n}}})] -\omega^2 c^{-1}_{11_{\tilde{m}-m,\tilde{n}-n}}p_{m,n}\}e^{j(\mathbf{k}+\mathbf{g}_{\tilde{m},\tilde{n}})\cdot\mathbf{r}} = 0. \tag{2.21}$$

Multiplying Eq. (2.21) by $e^{-j\mathbf{g}_{\bar{m},\bar{n}}\cdot\mathbf{r}}$, integrating over the unit cell, one can write for all $\mathbf{r}$:

$$\sum_{m=-\infty}^{+\infty}\sum_{n=-\infty}^{+\infty}\sum_{\tilde{m}=-\infty}^{+\infty}\sum_{\tilde{n}=-\infty}^{+\infty}\{\rho^{-1}_{\tilde{m}-m,\tilde{n}-n}p_{m,n}[(k_1+g_{1_m})(k_1+g_{1_{\tilde{m}}})+(k_2+g_{2_n})(k_2+g_{2_{\tilde{n}}})] -\omega^2 c^{-1}_{11_{\tilde{m}-m,\tilde{n}-n}}p_{m,n}\}\frac{1}{S_C}\int\int e^{j(\mathbf{g}_{\tilde{m},\tilde{n}}-\mathbf{g}_{\bar{m},\bar{n}})\cdot\mathbf{r}}d^2r = 0. \tag{2.22}$$

Remembering the definition of $\delta_{\mathbf{g}_{\tilde{m},\tilde{n}}\mathbf{g}_{\bar{m},\bar{n}}}$:

$$\delta_{\mathbf{g}_{\tilde{m},\tilde{n}}\mathbf{g}_{\bar{m},\bar{n}}} = \frac{1}{S_C}\int\int e^{j(\mathbf{g}_{\tilde{m},\tilde{n}}-\mathbf{g}_{\bar{m},\bar{n}})\cdot\mathbf{r}}d^2r, \tag{2.23}$$

where the integral is evaluated over the unit cell, Eq. (2.22) can be rewritten as:

$$\sum_{m=-\infty}^{+\infty}\sum_{n=-\infty}^{+\infty}\{\rho^{-1}_{\bar{m}-m,\bar{n}-n}p_{m,n}[(k_1+g_{1_m})(k_1+g_{1_{\bar{m}}})+(k_2+g_{2_n})(k_2+g_{2_{\bar{n}}})] - \omega^2 c^{-1}_{11_{\bar{m}-m,\bar{n}-n}}p_{m,n}\} = 0. \tag{2.24}$$

Equation (2.24) is an infinite system of equations, thus Fourier series must be truncated, *i.e.*, $m,n,\bar{m},\bar{n} = [-M,\ldots,M]$, $M \in \mathbb{Z}$, and the total number of plane waves is $(2M+1)^2$. Then, Eq. (2.24) can be rewritten as:

$$\mathbf{C}\mathbf{p} = \omega^2\mathbf{D}\mathbf{p}, \tag{2.25}$$

where the coefficients of vector $\mathbf{p}$ are $p_{m,n}$ and the coefficients of matrices $\mathbf{C}$ and $\mathbf{D}$ are given

by:

$$C_{m,\bar{m},n,\bar{n}} = \rho^{-1}_{\bar{m}-m,\bar{n}-n}[(k_1+g_{1_m})(k_1+g_{1_{\bar{m}}})+(k_2+g_{2_n})(k_2+g_{2_{\bar{n}}})],\ D_{m,\bar{m},n,\bar{n}} = c^{-1}_{11_{\bar{m}-m,\bar{n}-n}}. \tag{2.26}$$

Equation (2.25) represents a generalized eigenvalue problem of $\omega^2(\mathbf{k})$ and should be solved for each $\mathbf{k}$ into the FIBZ or FBZ.

### 2.1.3 PWE formulation for 1D elastic metamaterial Euler-Bernoulli beams

From Euler-Bernoulli beam theory, the governing equation for flexural vibrations of a uniform beam system of an infinite extension can be written as:

$$EI\frac{\partial^4 \hat{u}_3(x,t)}{\partial x^4} + \rho S\frac{\partial^2 \hat{u}_3(x,t)}{\partial t^2} = 0, \tag{2.27}$$

where $I$ is the second moment of area and $\hat{u}_3$ is the beam transverse displacement in time domain. Applying the temporal Fourier transform to Eq. 2.27, and omitting frequency dependence it produces:

$$EI\frac{\partial^4 u_3(x)}{\partial x^4} - \omega^2\rho S u_3(x) = 0, \tag{2.28}$$

where $u_3$ is the beam transverse displacement in frequency domain.

Now, considering an infinite 1D EM Euler-Bernoulli beam with S-DOF resonators attached in each unit cell (see Figure 1 in Appendix F), Eq. (2.28) can be rewritten as (Xiao *et al.*, 2012a):

$$EI\frac{\partial^4 u_3(x)}{\partial x^4} - \omega^2\rho S u_3(x) = \sum_{i=1}^{N}\sum_{n=-\infty}^{+\infty} q_i(x_i+na)\delta[x-(x_i+na)], \tag{2.29}$$

$$q_i(x_i+na) = -\tilde{k}_i[u_3(x_i+na) - w_i(x_i+na)], \tag{2.30}$$

$$-\omega^2 m_i w_i(x_i+na) = -q_i(x_i+na), \tag{2.31}$$

where $N$ is the number of resonators in each unit cell, $q_i(x_i+na)$ refers to the force applied to the beam by the resonator spring located at $x_i+na$, $\delta$ is Dirac delta function, $\tilde{k}_i$ is the stiffness of the *i*th resonator, $m_i$ is the mass of the *i*th resonator, and $w_i(x_i+na)$ and $u_3(x_i+na)$ are the *i*th resonator and beam flexural displacements at $x_i+na$.

Applying the Floquet-Bloch's theorem and considering wave propagation on the $x$ axis ($k_2$,$k_3=0$), gives:

$$u_3(x) = e^{jkx}u_{3_k}(x). \tag{2.32}$$

Expanding Bloch wave amplitude $u_{3_k}(x)$ as Fourier series in reciprocal space, yields:

$$u_3(x) = e^{jkx} \sum_{\bar{m}=-\infty}^{+\infty} u_{3_{\bar{m}}} e^{jg_{\bar{m}}x} = \sum_{\bar{m}=-\infty}^{+\infty} u_{3_{\bar{m}}} e^{j(k+g_{\bar{m}})x}, \tag{2.33}$$

where $u_{3_{\bar{m}}} = u_{3_{k_{\bar{m}}}}$.

Similarly, applying Floquet-Bloch's theorem and expanding in Fourier series in reciprocal space the variable $u_3(x_i)$, results:

$$u_3(x_i) = e^{jkx_i} \sum_{\tilde{m}=-\infty}^{+\infty} u_{3_{\tilde{m}}} e^{jg_{\tilde{m}}x_i} = \sum_{\tilde{m}=-\infty}^{+\infty} u_{3_{\tilde{m}}} e^{j(k+g_{\tilde{m}})x_i}. \tag{2.34}$$

Likewise, applying Floquet-Bloch's theorem to $u_3(x_i + na)$, gives:

$$\begin{aligned} u_3(x_i + na) = e^{jk(x_i+na)} u_{3_k}(x_i + na) = e^{jkna} e^{jkx_i} u_{3_k}(x_i + na) = e^{jkna} e^{jkx_i} u_{3_k}(x_i) \\ = e^{jkna} u_3(x_i). \end{aligned} \tag{2.35}$$

Equation 2.35 can be obtained directly from Floquet-Bloch periodic boundary condition. Similarly, for $w_i(x_i + na)$, yields:

$$w_i(x_i + na) = e^{jkna} w_i(x_i). \tag{2.36}$$

Then, substituting Eq. (2.30) in Eq. (2.29), produces:

$$EI \frac{\partial^4 u_3(x)}{\partial x^4} - \omega^2 \rho S u_3(x) = -\sum_{i=1}^{N} \sum_{n=-\infty}^{+\infty} \tilde{k}_i [u_3(x_i + na) - w_i(x_i + na)] \delta[x - (x_i + na)]. \tag{2.37}$$

Next, substituting Eqs. (2.35) and (2.36) in Eq. (2.37), one can obtain:

$$EI \frac{\partial^4 u_3(x)}{\partial x^4} - \omega^2 \rho S u_3(x) = -\sum_{i=1}^{N} \tilde{k}_i [u_3(x_i) - w_i(x_i)] \sum_{n=-\infty}^{+\infty} e^{ikna} \delta[x - (x_i + na)]. \tag{2.38}$$

The infinite sum in Eq. (2.38) $\sum_{n=-\infty}^{+\infty} e^{ikna} \delta[x - (x_i + na)]$ is a periodic function, which can be expanded as Fourier series in reciprocal space as:

$$\sum_{n=-\infty}^{+\infty} e^{jkna} \delta[x - (x_i + na)] = \sum_{\bar{m}=-\infty}^{+\infty} \delta_{\bar{m}} e^{jg_{\bar{m}}x} = \frac{1}{a} e^{jk(x-x_i)} \sum_{\bar{m}=-\infty}^{+\infty} e^{-jg_{\bar{m}}x_i} e^{jg_{\bar{m}}x}, \tag{2.39}$$

where $\frac{1}{a} e^{-jg_{\bar{m}}x_i} e^{jk(x-x_i)}$ are the Fourier series coefficients.

Inserting Eq. (2.39) and Eqs. (2.33)-(2.34) in Eq. (2.38), multiplying by $a$ and hereafter

$w_i(x_i) = w_i$ for brevity, one can obtain:

$$\sum_{\bar{m}=-\infty}^{+\infty} [EIa(k+g_{\bar{m}})^4 - \omega^2\rho Sa]e^{j(k+g_{\bar{m}})x}u_{3_{\bar{m}}} = -\sum_{i=1}^{N}\sum_{\bar{m}=-\infty}^{+\infty} \tilde{k}_i e^{j(k+g_{\bar{m}})x}e^{-j(k+g_{\bar{m}})x_i}$$
$$\sum_{\tilde{m}=-\infty}^{+\infty} u_{3_{\tilde{m}}}e^{j(k+g_{\tilde{m}})x_i} + \sum_{i=1}^{N}\sum_{\bar{m}=-\infty}^{+\infty} \tilde{k}_i e^{j(k+g_{\bar{m}})x}e^{-j(k+g_{\bar{m}})x_i}w_i. \tag{2.40}$$

Multiplying Eq. (2.40) by $e^{-jg_m x}$ and integrating over the unit cell, results for all $x$:

$$\sum_{\bar{m}=-\infty}^{+\infty} [EIa(k+g_{\bar{m}})^4 - \omega^2\rho Sa]u_{3_{\bar{m}}}\frac{1}{a}\int_{-a/2}^{a/2} e^{j(g_{\bar{m}}-g_m)x}dx = -\sum_{i=1}^{N}\sum_{\bar{m}=-\infty}^{+\infty} \tilde{k}_i e^{-j(k+g_{\bar{m}})x_i}$$
$$\sum_{\tilde{m}=-\infty}^{+\infty} u_{3_{\tilde{m}}}e^{j(k+g_{\tilde{m}})x_i}\frac{1}{a}\int_{-a/2}^{a/2} e^{j(g_{\tilde{m}}-g_m)x}dx + \sum_{i=1}^{N}\sum_{\bar{m}=-\infty}^{+\infty} \tilde{k}_i e^{-j(k+g_{\bar{m}})x_i}w_i\frac{1}{a}\int_{-a/2}^{a/2} e^{j(g_{\bar{m}}-g_m)x}dx, \tag{2.41}$$

and remembering the definition of $\delta_{\bar{m}m}$ in Eq. (2.10), Eq. (2.41) can be simplified:

$$EIa(k+g_m)^4 u_{3_m} + \sum_{i=1}^{N}\tilde{k}_i e^{-j(k+g_m)x_i}\sum_{\tilde{m}=-\infty}^{+\infty} u_{3_{\tilde{m}}}e^{j(k+g_{\tilde{m}})x_i} - \sum_{i=1}^{N}\tilde{k}_i e^{-j(k+g_m)x_i}w_i$$
$$-\omega^2\rho Sa u_{3_m} = 0. \tag{2.42}$$

An observation is that the terms $e^{-j(k+g_m)x_i}$ and $e^{j(k+g_{\tilde{m}})x_i}$ in Eq. 2.42 can be written just as $e^{-jg_m x_i}$ and $e^{jg_{\tilde{m}}x_i}$. In addition, substituting Eq. (2.31) in Eq. (2.30), gives:

$$\omega^2 m_i w_i(x_i + na) = -\tilde{k}_i[u_3(x_i+na) - w_i(x_i+na)], \tag{2.43}$$

and inserting Eqs. (2.35),(2.36) and (2.34) in Eq. (2.43), provides:

$$-\tilde{k}_i\sum_{\tilde{m}=-\infty}^{+\infty} u_{3_{\tilde{m}}}e^{j(k+g_{\tilde{m}})x_i} + \tilde{k}_i w_i - \omega^2 m_i w_i = 0. \tag{2.44}$$

Equations (2.42) and (2.44) are an infinite system of equations, thus Fourier series must be truncated, *i.e.*, $m, \tilde{m} = [-M, \ldots, M]$. Then, Eqs. (2.42) and (2.44) can be rewritten as:

$$\mathbf{K}\tilde{\mathbf{u}} = \omega^2\mathbf{M}\tilde{\mathbf{u}}, \tag{2.45}$$

where the vector $\tilde{\mathbf{u}}$ is $[\bar{\mathbf{u}}_3\ \mathbf{w}]^{\mathrm{T}}$, and coefficients of vectors $\bar{\mathbf{u}}_3$ and $\mathbf{w}$ are $u_{3_m}$ and $w_i$, respectively.

Moreover, the coefficients of matrices $\mathbf{K}$ and $\mathbf{M}$ are given by:

$$K_{m,\tilde{m},i} = EIa(k+g_m)^4 + \sum_{i=1}^{N} \tilde{k}_i e^{-j(k+g_m)x_i} \sum_{\tilde{m}=-\infty}^{+\infty} e^{j(k+g_{\tilde{m}})x_i} - \tilde{k}_i \sum_{\tilde{m}=-\infty}^{+\infty} e^{j(k+g_{\tilde{m}})x_i} - \sum_{i=1}^{N} \tilde{k}_i e^{-j(k+g_m)x_i} + \tilde{k}_i, \tag{2.46}$$

$$M_{m,\tilde{m},i} = \rho Sa + m_i. \tag{2.47}$$

Similar to Eq. (2.12), Eq. (2.45) represents a generalized eigenvalue problem of $\omega^2(k)$ and should be solved for each $k$ into the FIBZ or FBZ.

## 2.2 Improved plane wave expansion method

IPWE approach has the advantage of presenting higher Fourier series convergence than the traditional PWE and it is useful when there is high geometry or material mismatch (Cao *et al.*, 2004b). Thus, IPWE approach is very important when locally resonant PnCs or MMs are considered. Li (1996) proposed the first study of IPWE method for photonic crystals. After that, Cao *et al.* (2004b) extended IPWE in order to handle PnCs. In this subsection it is just highlighted the main differences between PWE and IPWE formulations.

For instance considering the 1D PnC of Subsection 2.1.1, Eq. (2.11) truncated is rewritten as:

$$\sum_{m=-M}^{M} \left[\gamma_{\bar{m}-m} u_{1_m}(k+g_m)(k+g_{\bar{m}}) - \omega^2 \alpha_{\bar{m}-m} u_{1_m}\right] = 0. \tag{2.48}$$

In Eq. 2.48, it is explicit the Laurent's rule (Cao *et al.*, 2004b) in the product of $\gamma_{\bar{m}-m}u_{1_m}$ and $\alpha_{\bar{m}-m}u_{1_m}$. However, in order to regard IPWE approach, instead of Laurent's rule, an inverse rule must be applied, and Eq. (2.48) must rewritten as:

$$\sum_{m=-M}^{M} \left\{ \left[\frac{1}{\gamma}\right]^{-1}_{\bar{m}-m} u_{1_m}(k+g_m)(k+g_{\bar{m}}) - \omega^2 \alpha_{\bar{m}-m} u_{1_m} \right\} = 0, \tag{2.49}$$

where $[1/\gamma]$ denotes the Toeplitz matrix of a function $1/\gamma$ with $(\bar{m},m)$th element being $1/\gamma_{\bar{m}-m}$, and -1 denotes the inverse matrix. The detailed mathematical contents of the above theory are not given in this investigation, and for mathematical demonstrations, one can see Li (1996) and Cao *et al.* (2004b) studies. Another interesting investigation using IPWE approach was addressed by Yao *et al.* (2009). They studied flexural wave propagation in a 2D PnC thin plate with a point defect.

Then, Eq. (2.49) can be written as:

$$\bar{\mathbf{A}}\bar{\mathbf{u}}_1 = \omega^2 \mathbf{B}\bar{\mathbf{u}}_1, \tag{2.50}$$

where the coefficients of matrix $\bar{\mathbf{A}}$ are given by:

$$\bar{A}_{m\bar{m}} = \left[\frac{1}{\gamma}\right]^{-1}_{\bar{m}-m} (k+g_m)(k+g_{\bar{m}}). \tag{2.51}$$

In Appendix A, a comparison between PWE and IPWE is provided for a 1D PnC Euler-Bernoulli beam.

## 2.3 Extended plane wave expansion method

Propagating waves inside a periodic system are a set of solutions of wave equations satisfying the translational symmetry. They are characterized by the transmission bands in PWE and IPWE methods. However, finite periodic structures or periodic structures with defects, where the translational symmetry is broken, can support the evanescent modes characterized by a complex Bloch wave vector (García, 2010). Evanescent waves can propagate within the periodic structure, however with an attenuation distance determined by the value of Bloch wave vector imaginary part. Hence, the energy of these waves are spatially concentrated in the vicinity of the structure excitation source.

From EPWE, also known as $\mathbf{k}(\omega)$ method, it is possible to obtain the complex values of Bloch wave vector. This is the striking issue of using EPWE method, *i.e.*, evanescent modes are obtained naturally and they are not ignored as well as on PWE and IPWE. PWE and IPWE methods consider only the propagating modes, that is to say when Bloch wave vector is only real. Furthermore, Bloch wave vector is not restricted to the FIBZ considering EPWE method (Laude *et al.*, 2009). Hsue and Freeman (2005) proved that the evanescent modes obtained by EPWE obey Floquet-Bloch's theorem.

In this subsection, it is presented the EPWE formulation for the 2D SnC and 1D EM Euler-Bernoulli beam reported in Subsections 2.1.2 and 2.1.3.

### 2.3.1 EPWE formulation for 2D sonic crystals

The starting point is rewrite Eq. (2.25) as (Romero-García *et al.*, 2011; Laude *et al.*, 2009):

$$\bar{\mathbf{C}}\mathbf{p} = \omega^2 \mathbf{D}\mathbf{p}, \tag{2.52}$$

where the coefficients of matrix $\bar{\mathbf{C}}$ are given by:

$$\bar{C}_{m,\bar{m},n,\bar{n}} = \Gamma_{1_{mn}} \rho^{-1}_{\bar{m}-m,\bar{n}-n} \Gamma_{1_{mn}} + \Gamma_{2_{mn}} \rho^{-1}_{\bar{m}-m,\bar{n}-n} \Gamma_{2_{mn}}, \tag{2.53}$$

with

$$\Gamma_{1_{mn}} = \delta_{mn}(k_1 + g_{1_m}),\ \Gamma_{2_{mn}} = \delta_{mn}(k_2 + g_{2_n}). \tag{2.54}$$

Next, the following vector must be defined:

$$\boldsymbol{\phi}_i = \mathbf{P}\boldsymbol{\Gamma}_i\mathbf{p}, \tag{2.55}$$

where $i = 1,2$, the coefficients of matrix $\boldsymbol{\Gamma}_i$ are described in Eq. (2.54) and the coefficients of $\mathbf{P}$ are $\rho^{-1}_{\bar{m}-m,\bar{n}-n}$. Thus, Eq. (2.52) can be rewritten as an equation system:

$$\boldsymbol{\phi}_i = \mathbf{P}\boldsymbol{\Gamma}_i\mathbf{p}, \tag{2.56}$$

$$\sum_{i=1}^{2}\boldsymbol{\Gamma}_i\boldsymbol{\phi}_i = \omega^2\mathbf{D}\mathbf{p}. \tag{2.57}$$

In order to obtain an eigenvalue problem of $\mathbf{k}(\omega)$, one can write $\mathbf{k} = k\boldsymbol{\sigma}$, where $\boldsymbol{\sigma}$ is a unit vector which indicates the incidence direction and $k = \|\mathbf{k}\|$. Then, matrices $\boldsymbol{\Gamma}_1, \boldsymbol{\Gamma}_2$ are rewritten as:

$$\boldsymbol{\Gamma}_1 = \mathbf{G}_1 + k\sigma_1\mathbf{I},\ \boldsymbol{\Gamma}_2 = \mathbf{G}_2 + k\sigma_2\mathbf{I}, \tag{2.58}$$

where $\sigma_i$ $(i = 1,2)$ are the components of $\boldsymbol{\sigma}$ on $x$ and $y$ directions, $\mathbf{I}$ is the identity matrix and the coefficients of matrices $\mathbf{G}_1$ and $\mathbf{G}_2$ are given by $\delta_{mn}g_{1_m}$ and $\delta_{mn}g_{2_n}$. Finally, after some mathematical manipulations (Romero-García *et al.*, 2011), Eq. (2.52) can be rewritten as:

$$\begin{bmatrix} \omega^2\mathbf{D} - \sum_{i=1}^{2}\mathbf{G}_i\mathbf{P}\mathbf{G}_i & \mathbf{0} \\ -\sum_{i=1}^{2}\mathbf{P}\mathbf{G}_i & \mathbf{I} \end{bmatrix} \begin{Bmatrix} \mathbf{p} \\ \bar{\boldsymbol{\phi}} \end{Bmatrix} = k \begin{bmatrix} \sum_{i=1}^{2}\mathbf{G}_i\mathbf{P}\sigma_i\mathbf{I} & \mathbf{I} \\ \sum_{i=1}^{2}\mathbf{P}\sigma_i\mathbf{I} & \mathbf{0} \end{bmatrix} \begin{Bmatrix} \mathbf{p} \\ \bar{\boldsymbol{\phi}} \end{Bmatrix}, \tag{2.59}$$

where $\bar{\boldsymbol{\phi}} = \sum_{i=1}^{2}\sigma_i\mathbf{I}\boldsymbol{\phi}_i$.

Eq. (2.59) represents a generalized eigenvalue problem of $\mathbf{k}(\omega)$. It is must be highlighted, even though it is usually not mentioned in studies which use EPWE approach, that is necessary to apply a criterion for tracking the frequency evolution of wave modes when EPWE method is used, since wave modes are computed at several discrete frequencies. Then, it is necessary to associate, among all modes defined at a given frequency $(\omega + \Delta\omega)$, the one which matches a given mode defined at the previous frequency $(\omega)$.

In this thesis, the modal assurance criterion (MAC) is used to estimate the correlation among wave shapes. This criterion is based on the hermitian scalar product and it is useful for very low frequencies (Mencik, 2010). Given a wave mode $l$ defined at an specific frequency $\omega$ and for a sufficiently small $\Delta\omega$, the wave mode $l$ defined at frequency $\omega + \Delta\omega$ results in:

$$\left|\left| \frac{\boldsymbol{\psi}_l^{\mathrm{H}}(\omega)}{||\boldsymbol{\psi}_l(\omega)||_{\mathrm{H}}} \frac{\boldsymbol{\psi}_l(\omega+\Delta\omega)}{||\boldsymbol{\psi}_l(\omega+\Delta\omega)||_{\mathrm{H}}} \right|\right| = max_s \left\{ \left|\left| \frac{\boldsymbol{\psi}_l^{\mathrm{H}}(\omega)}{||\boldsymbol{\psi}_l(\omega)||_{\mathrm{H}}} \frac{\boldsymbol{\psi}_s(\omega+\Delta\omega)}{||\boldsymbol{\psi}_s(\omega+\Delta\omega)||_{\mathrm{H}}} \right|\right| \right\}, \tag{2.60}$$

where $\|\boldsymbol{\psi}_l\|_{\mathrm{H}} = \sqrt{\boldsymbol{\psi}_l^{\mathrm{H}}\boldsymbol{\psi}_l}$ denotes the hermitian norm of the eigenvectors $\boldsymbol{\psi}_l$ of the eigenvalue problem $\mathbf{k}(\omega)$. The indexes $l,s \in \mathbb{N}_{>0}$ are associated with the size of the eigenvector and $(\cdot)^{\mathrm{H}}$ indicates the conjugate transpose.

### 2.3.2 EPWE formulation for 1D elastic metamaterial Euler-Bernoulli beams

Since there are no external forces acting on the resonator masses, one can write:

$$q_i(x_i + na) = -D_i u_3(x_i + na), \tag{2.61}$$

where $D_i$ is the dynamic stiffness of the $i$th resonator given by:

$$D_i = \frac{-\omega^2 m_i}{1 - \omega^2/\omega_i^2}, \tag{2.62}$$

and $\omega_i = 2\pi f_i = \sqrt{\tilde{k}_i/m_i}$ is the natural angular frequency of the $i$th resonator. Then, Equation (2.29) can be rewritten as:

$$EI\frac{\partial^4 u_3(x)}{\partial x^4} - \omega^2 \rho S u_3(x) + \sum_{i=1}^{N}\sum_{n=-\infty}^{+\infty} D_i u_3(x_i + na)\delta[x - (x_i + na)] = 0. \tag{2.63}$$

Inserting Eqs. (2.33)-(2.35) in Eq. (2.63), gives:

$$\sum_{\bar{m}=-\infty}^{+\infty} [EI(k + g_{\bar{m}})^4 - \omega^2 \rho S] e^{j(k+g_{\bar{m}})x} u_{3_{\bar{m}}} + \sum_{i=1}^{N}\sum_{\tilde{m}=-\infty}^{+\infty} D_i e^{j(k+g_{\tilde{m}})x_i} u_{3_{\tilde{m}}} \sum_{n=-\infty}^{+\infty} e^{kna}\delta[x - (x_i + na)] = 0. \tag{2.64}$$

Substituting Eq. (2.39) in Eq. (2.64) and multiplying by $a$, one can obtain:

$$\sum_{\bar{m}=-\infty}^{+\infty} [EIa(k + g_{\bar{m}})^4 - \omega^2 \rho S a] e^{j(k+g_{\bar{m}})x} u_{3_{\bar{m}}} + \sum_{i=1}^{N}\sum_{\tilde{m}=-\infty}^{+\infty}\sum_{\bar{m}=-\infty}^{+\infty} D_i e^{-j(k+g_{\bar{m}})x_i} e^{j(k+g_{\tilde{m}})x_i} e^{j(k+g_{\bar{m}})x} u_{3_{\tilde{m}}} = 0. \tag{2.65}$$

Multiplying Eq. (2.65) by $e^{-g_m x}$ and integrating over the unit cell, it can be rewritten for all $x$ (*i.e.*, including $x_i$):

$$\sum_{\bar{m}=-\infty}^{+\infty} [EIa(k + g_{\bar{m}})^4 - \omega^2 \rho S a] u_{3_{\bar{m}}} \frac{1}{a}\int_{-a/2}^{a/2} e^{j(g_{\bar{m}} - g_m)x} dx + \sum_{i=1}^{N}\sum_{\tilde{m}=-\infty}^{+\infty}\sum_{\bar{m}=-\infty}^{+\infty} D_i e^{-jg_{\bar{m}}x_i} e^{jg_{\tilde{m}}x_i} u_{3_{\tilde{m}}} \frac{1}{a}\int_{-a/2}^{a/2} e^{j(g_{\bar{m}} - g_m)x} dx = 0, \tag{2.66}$$

and using the definition of Eq. (2.10) for $\delta_{\bar{m}m}$, Eq. (2.66) can be rewritten as:

$$[EIa(k + g_m)^4 - \omega^2 \rho S a] u_{3_m} + \sum_{i=1}^{N}\sum_{\tilde{m}=-\infty}^{+\infty} D_i e^{-jg_m x_i} e^{jg_{\tilde{m}}x_i} u_{3_{\tilde{m}}} = 0. \tag{2.67}$$

The terms $(k+g_m)^4$ can be expanded as:

$$\left(k+\frac{2\pi m}{a}\right)^4 = \frac{1}{a^4}[(ka)^4+8m\pi(ka)^3+24(m\pi)^2(ka)^2+32(m\pi)^3(ka)+16(m\pi)^4]. \quad (2.68)$$

Inserting Eq. (2.68) in Eq. (2.67), multiplying by $a^3/EI$, results:

$$\left[\hat{k}^4+8m\pi\hat{k}^3+24(m\pi)^2\hat{k}^2+32(m\pi)^3\hat{k}+16(m\pi)^4-\frac{\omega^2\rho Sa^4}{EI}\right]u_{3_m}+\sum_{i=1}^{N}\sum_{\tilde{m}=-\infty}^{+\infty}\frac{D_i a^3}{EI} e^{-jg_m x_i}e^{jg_{\tilde{m}}x_i}u_{3_{\tilde{m}}}=0, \quad (2.69)$$

where $\hat{k}=ka$.

After truncating Eq. (2.69), *i.e.*, $m,\tilde{m}=[-M,\ldots,M]$, it can be rewritten as:

$$\left[\hat{k}^4\mathbf{I}+\hat{k}^3\mathbf{X}_3+\hat{k}^2\mathbf{X}_2+\hat{k}\mathbf{X}_1+\mathbf{X}_0\right]\mathbf{u}_3=\mathbf{0}, \quad (2.70)$$

where the coefficients of vector $\mathbf{u}_3$ are $u_{3_m}$ and coefficients of matrices $\mathbf{X}_i$ $(i=0,\ldots,3)$ are given by:

$$X_{3_{m\tilde{m}}}=\delta_{m\tilde{m}}8m\pi,\ X_{2_{m\tilde{m}}}=\delta_{m\tilde{m}}24(m\pi)^2,\ X_{1_{m\tilde{m}}}=\delta_{m\tilde{m}}32(m\pi)^3, \quad (2.71)$$

$$X_{0_{m\tilde{m}}}=\delta_{m\tilde{m}}\left[16(m\pi)^4-\frac{\omega^2\rho Sa^4}{EI}\right]+\sum_{i=1}^{N}\sum_{\tilde{m}=-\infty}^{+\infty}\frac{D_i a^3}{EI}e^{-jg_m x_i}e^{jg_{\tilde{m}}x_i}. \quad (2.72)$$

Finally, Eq. (2.70) can be rewritten as:

$$\begin{bmatrix} -\mathbf{X}_3 & -\mathbf{X}_2 & -\mathbf{X}_1 & -\mathbf{X}_0 \\ \mathbf{I} & \mathbf{0} & \mathbf{0} & \mathbf{0} \\ \mathbf{0} & \mathbf{I} & \mathbf{0} & \mathbf{0} \\ \mathbf{0} & \mathbf{0} & \mathbf{I} & \mathbf{0} \end{bmatrix}\begin{Bmatrix} \hat{k}^3\mathbf{u}_3 \\ \hat{k}^2\mathbf{u}_3 \\ \hat{k}\mathbf{u}_3 \\ \mathbf{u}_3 \end{Bmatrix}=\hat{k}\begin{Bmatrix} \hat{k}^3\mathbf{u}_3 \\ \hat{k}^2\mathbf{u}_3 \\ \hat{k}\mathbf{u}_3 \\ \mathbf{u}_3 \end{Bmatrix}. \quad (2.73)$$

Equation (2.73) represents a generalized eigenvalue problem of $\hat{k}(\omega)$. MAC is also used to estimate the correlation among wave shapes, as discussed in Subsection 2.3.1.

# 3 ELASTIC WAVE PROPAGATION IN PHONONIC CRYSTALS, SONIC CRYSTALS AND ELASTIC METAMATERIALS

In this chapter, simulated examples of band structures of PnCs, SnCs and EMs are reported. This chapter is divided into three parts. In first part, Subsection 3.0.1, it is investigated the band structure of longitudinal waves propagating in a 1D PnC rod. PWE and IPWE comparison are performed. In second part, Subsection 3.0.2, it is analysed the complex band structure of bulk waves propagating in a 2D SnC with circular inclusions and square lattice. PWE and IPWE comparison is also carried out. In Subsection 3.0.3, it is studied the band structure of flexural waves propagating in a 1D EM Euler-Bernoulli beam with a periodic array of resonators. PWE and EPWE approaches are used in order to obtain the complex band structure.

Furthermore, detailed studies of elastic wave propagation in PnCs and EMs are discussed in Appendices A-G. In these appendices, the following cases are considered: flexural wave propagation in 1D PnC Euler-Bernoulli beams (A), flexural wave band gaps in 2D PnC thick plates (B), bulk wave propagation in 2D PnC solids (C), bulk wave propagation in 2D PnC solids with piezoelectricity (D), bulk wave propagation in 2D PnC solids with piezoelectricity and piezomagnetism (E), flexural waves in 1D EM Euler-Bernoulli beams (F) and flexural waves in 2D EM thin plates (G).

### 3.0.1 1D Phononic crystal rod

An infinite 1D PnC rod composed by two materials, *i.e.*, aluminium and epoxy, is considered. This PnC is illustrated in Figure 3.1, where blue and white colours represent epoxy and aluminium, respectively.

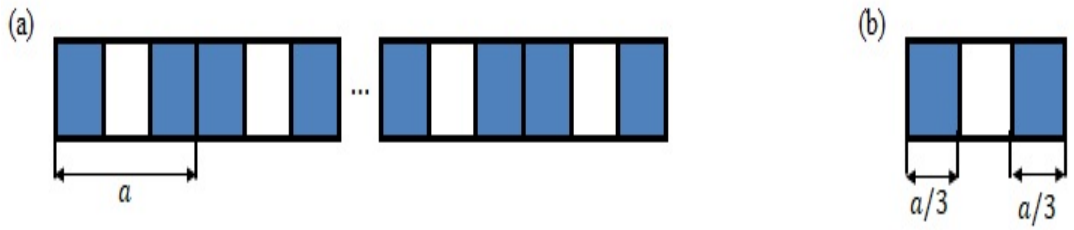


Figure 3.1: Schematic representation of the 1D PnC rod with unit cells of aluminium (white) and epoxy (blue) (a). PnC rod unit cell is illustrated in (b).

The length of aluminium in the middle of unit cell is $a_A = 0.05$ m and the length of epoxy parts are $a_B = 0.01$ m, where subscripts $A$ and $B$ are associated with aluminium and epoxy, thus unit cell length $a = a_A + 2a_B = 0.07$ m. PnC rod geometry and material properties are shown in Table 3.1.

Figure 3.2 illustrates the band structure, *i.e.*, real part of reduced Bloch wave vector versus frequency, calculated following the formulation in Subsection 2.1.1 (see also Fourier series

Table 3.1: PnC rod geometry and material properties.

| Geometry/Property | Value |
|---|---|
| Unit-cell length ($a$) | 0.07 m |
| Square cross section area ($S = b \times h$) | 0.01 $\times$ 0.01 m$^2$ |
| Young's modulus ($E_A$,$E_B$) | 77.6 $\times$ 10$^9$ N/m$^2$, 4.35 $\times$ 10$^9$ N/m$^2$ |
| Mass density ($\rho_A$,$\rho_B$) | 2730 kg/m$^3$, 1180 kg/m$^3$ |

coefficients in Appendix A), using $M = 10$ harmonic terms in Fourier series expansion. By choosing $M = 10$ implies that $m = \bar{m} = [-10, \ldots, 10]$, which means $2M + 1 = 21$ plane waves. The first bands and first Bragg-type band gaps are illustrated in Figure 3.2 $(b)$ by blue shaded regions.

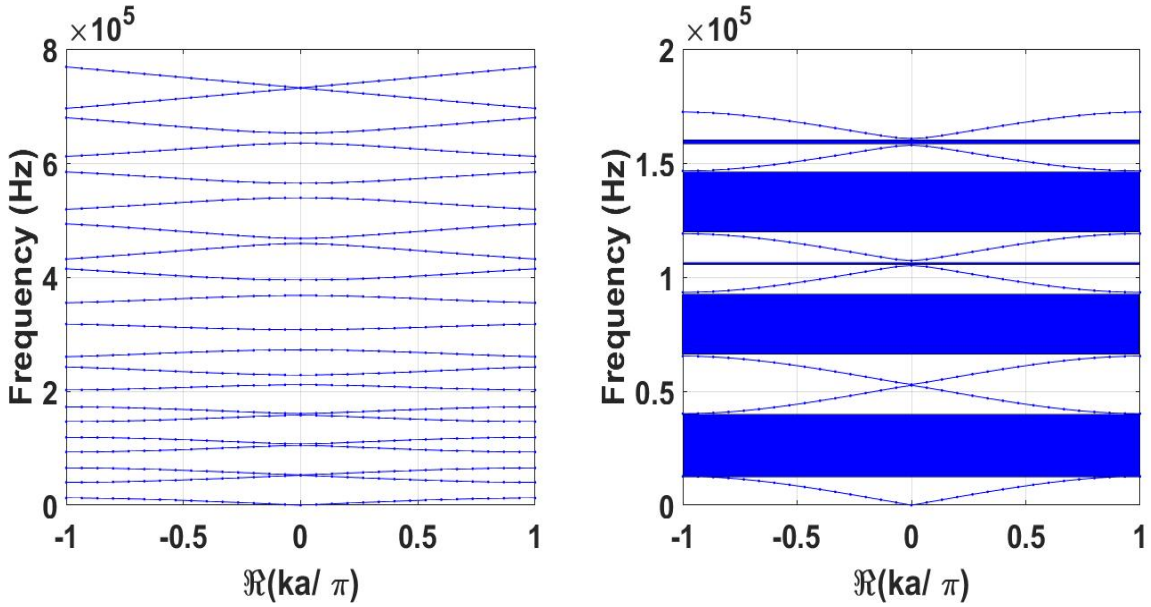


$(a)$ $(b)$

Figure 3.2: Band structure of the 1D PnC rod calculated by PWE approach, considering 21 plane waves $(a)$. The first branches of the band structure and Bragg-type band gaps in blue shaded regions $(b)$.

Whether the PnC rod is composed only by aluminium or by epoxy, *i.e.*, a homogeneous rod, thus there is no Bragg scattering and band gaps are not opened up, as shown in Figure 3.3. In this figure, 21 plane waves are considered for Fourier series expansion. In Figures 3.2 and 3.3, it must be highlighted that the reduced Bloch wave vector does not have values higher than -1 and 1, since in PWE approach Bloch wave vector has only values within FBZ.

Figure 3.4 compares the band structure of the PnC rod considering PWE and IPWE approaches for 21 plane waves. It can be observed that PWE does not match with IPWE only for higher bands. IPWE results were obtained from the formulation reported in Subsection 2.2.

In order to analyse $\gamma(x)$ (see Eq. 2.5) convergence, Figure 3.5 $(a)$ shows $\gamma(x)$ calculated by PWE for 3 $(M = 1)$, 21 $(M = 10)$ and 201 $(M = 100)$ plane waves. In Figure 3.5, it can be seen that $\gamma(x)$ converges to a square wave when the number of plane waves is increased.

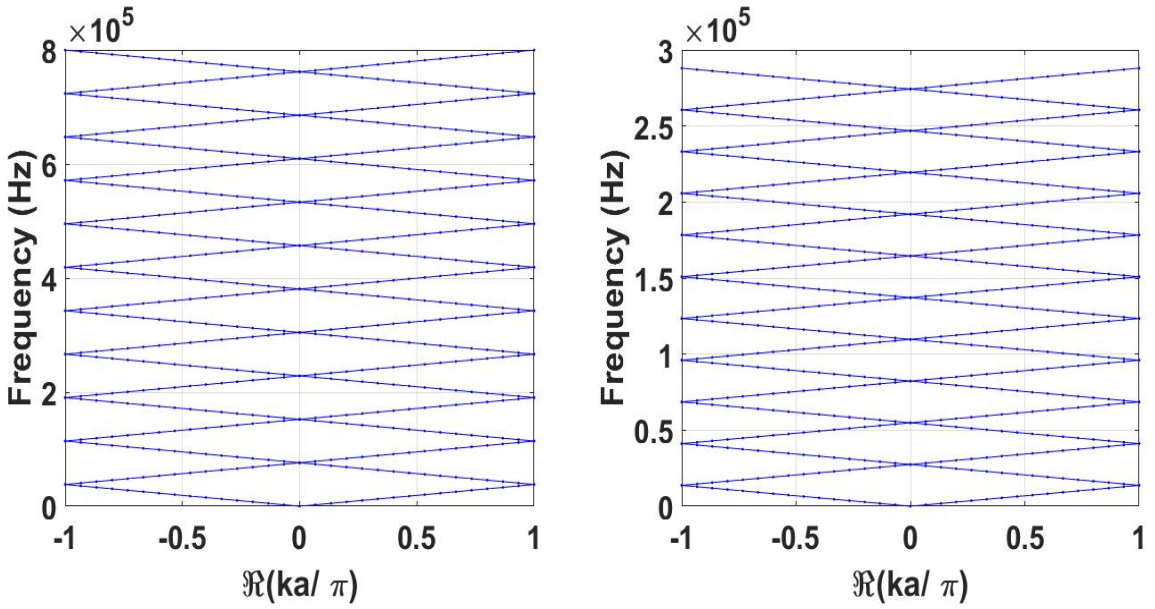


Figure 3.3: Band structure of a homogeneous rod composed by aluminium $(a)$ and epoxy $(b)$.

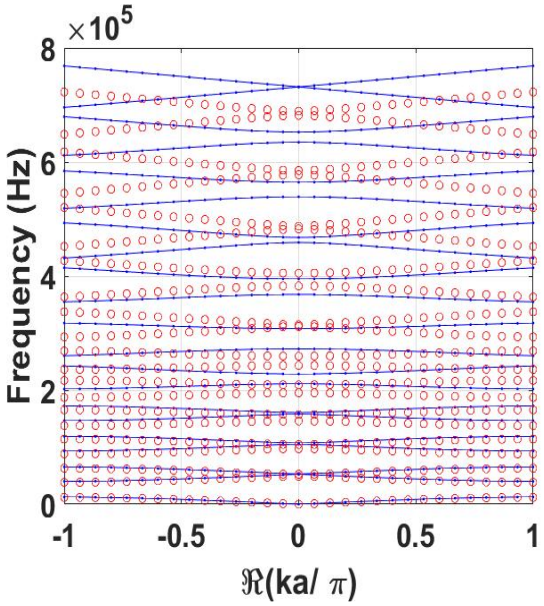


Figure 3.4: Band structure comparison of the PnC rod using PWE (blue points) and IPWE (red circles) approaches.

However, Gibbs phenomenon does not disappear even though more plane waves are added to the sum, as expected. In order to have some information about Fourier coefficients, it is shown in Figure 3.6 the Fourier series coefficients ($\gamma_m$) for 3 $(a)$, 21 $(b)$ and 201 $(c)$ plane waves.

In addition, in Appendix A, it is investigated other effects, such as the influence of steel percentage variation within the unit cell of a 1D PnC Euler-Bernoulli beam, the influence of unit cell length and an experiment is proposed.

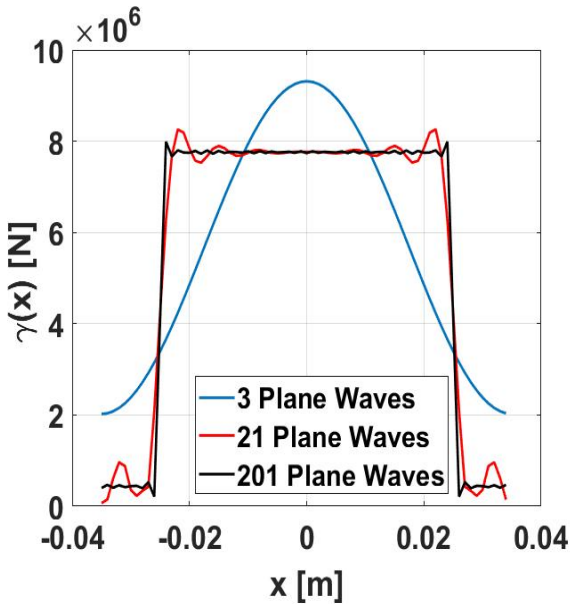


Figure 3.5: Convergence comparison of $\gamma(x)$ for the 1D PnC rod regarding 3, 21 and 201 plane waves.

### 3.0.2 2D Sonic crystal

A 2D SnC with square lattice (see for instance Figure 1 (a) and (c) in Appendix B) composed by steel circular inclusions in air is addressed. The 2D SnC geometry and material properties are described in Table 3.2.

Table 3.2: 2D SnC geometry and material properties.

| Geometry/Property | Value |
|---|---|
| Unit-cell length ($a$) | 0.022 m |
| Filling fraction ($\bar{f}$) | 0.274 |
| Mass density ($\rho_A$,$\rho_B$) | 7800 kg/m$^3$, 1.2 kg/m$^3$ |
| Elastic constant ($c_{11_A}$,$c_{11_B}$) | 290.4 $\times$ 10$^9$ N/m$^2$, 1.41 $\times$ 10$^5$ N/m$^2$ |

The filling fraction (see Annexe A.1) in Table 3.2 is defined as the cross section area ratio of inclusion and unit cell, *i.e.*, $\bar{f} = \pi r^2/a^2$, where $r$ is inclusion radius. Initially, for PWE and IPWE approaches, the integers $m$,$\bar{m}$,$n$,$\bar{n}$ are limited to the interval $[-10,10]$, *i.e.*, 441 plane waves.

Figure 3.7 illustrates the band structure of the 2D SnC calculated by PWE approach (see the formulation in Subsection 2.1.2). Partial Bragg-type band gaps are opened up and they can be identified by blue shaded region along $\Gamma X$ direction. The types of band gaps are discussed in Annexe A.3.

Whether the SnC is composed just by steel, thus band gaps are not opened up, as presented in Figure 3.8.

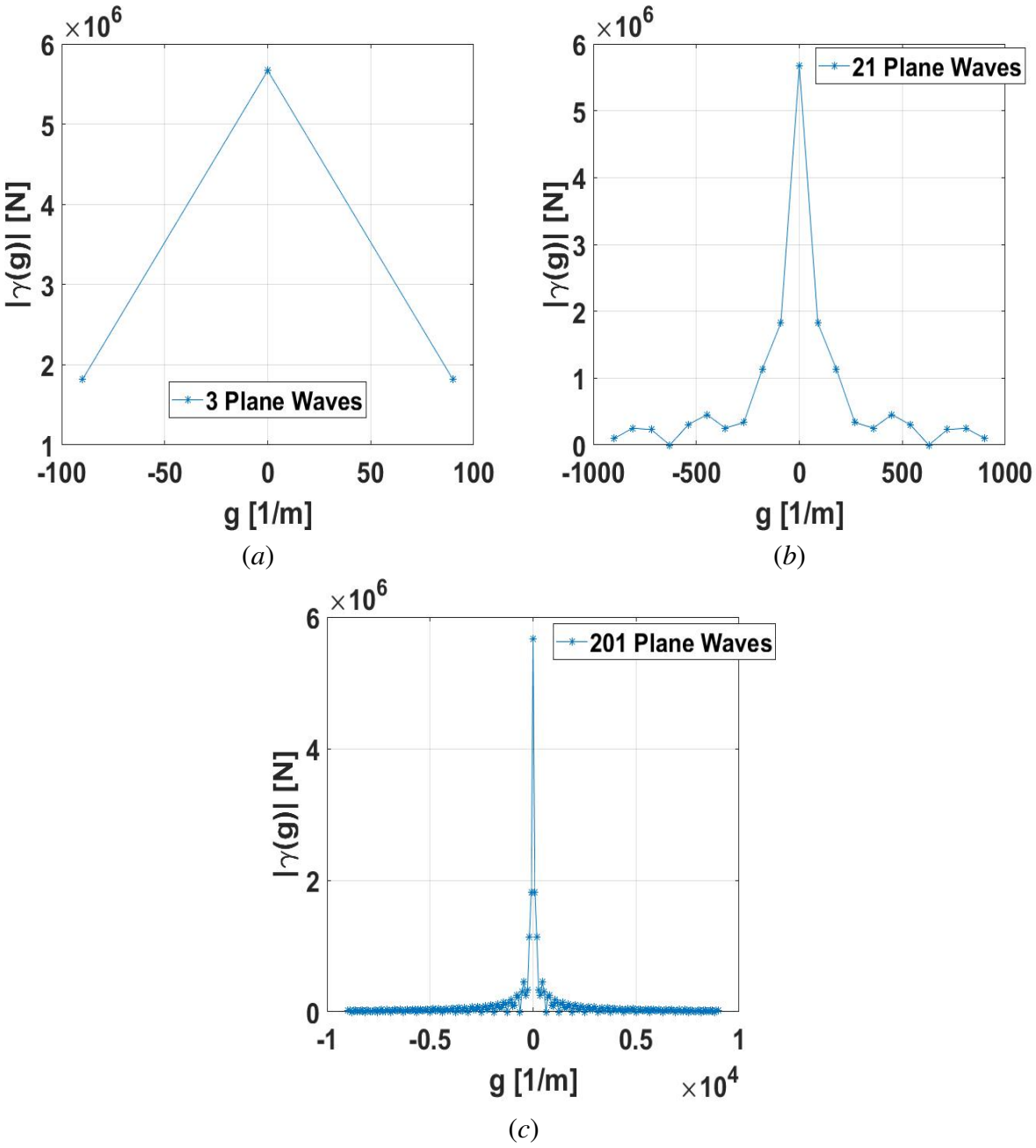


Figure 3.6: Fourier series coefficients for the 1D PnC rod regarding 3 $(a)$, 21 $(b)$ and 201 $(c)$ plane waves.

A comparison between PWE and IPWE approaches, considering 441 plane waves, is shown in Figure 3.9. From Figure 3.9, it can be seen that there is a mismatch between PWE and IPWE approaches even though for lower branches.

In order to calculate the SnC complex band structure, EPWE (see formulation in Subsection 2.3.1) is used. To reduce computational time, the integers $m$,$\bar{m}$,$n$,$\bar{n}$ are limited to the interval $[-1,1]$, *i.e.*, 9 plane waves and $a = 22$ m, since the main purpose is to compare PWE and EPWE results and to validate EPWE approach.

Figure 3.10 shows the complex band structure of the 2D SnC calculated using both $(a)$

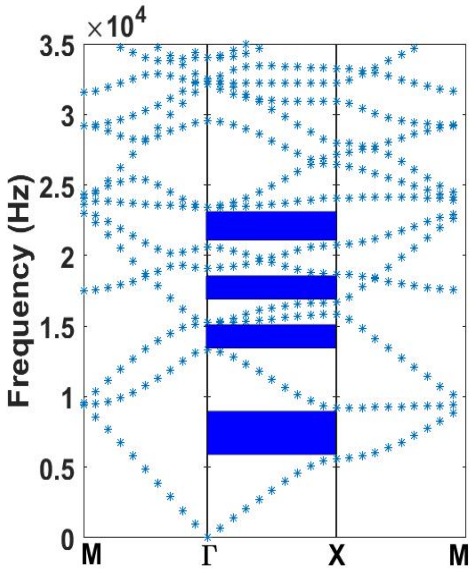


Figure 3.7: Band structure of the 2D SnC with steel circular inclusions in a square lattice.

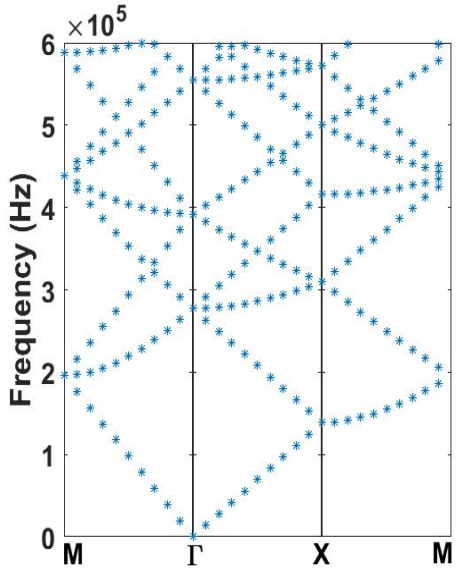


Figure 3.8: Band structure of a SnC with a square lattice composed just by steel.

PWE (red asterisks) and $(a - b)$ EPWE (black points) approaches.

From Figure 3.10, it can be seen that Bragg-type band gaps are opened up in low frequencies, since a high unit cell length, $a = 22$ m, is regarded. Furthermore, the real reduced Bloch wave vectors calculated by these approaches match well. However, PWE can only identify propagating modes ($\Im\{\mathbf{k}\} = 0$). Unlike PWE, EPWE method also identifies other complex modes in Figure 3.10, which are evanescent modes ($\Im\{\mathbf{k}\} \neq 0$) with $\Re\{\mathbf{k}\} \neq 0$. The evanescent modes can propagate within the SnC, however, with an attenuation distance determined by the value of Bloch wave vector imaginary part, as already mentioned. In addition, real part of Bloch wave vector calculated by PWE is restricted to the FIBZ. Imaginary part of Bloch wave

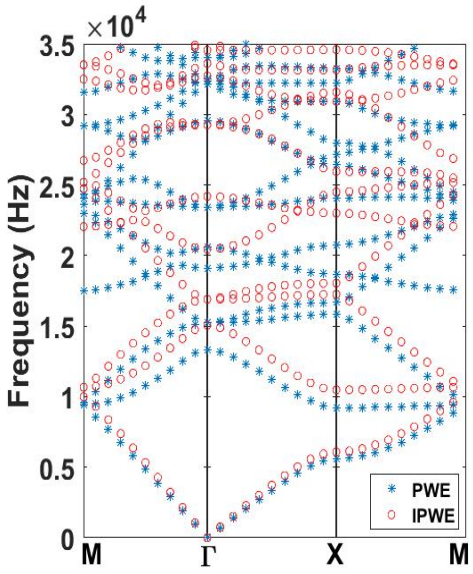


Figure 3.9: Band structure comparison of the 2D SnC with circular steel inclusions in a square lattice performed by PWE (blue asterisks) and IPWE (red circles) approaches.

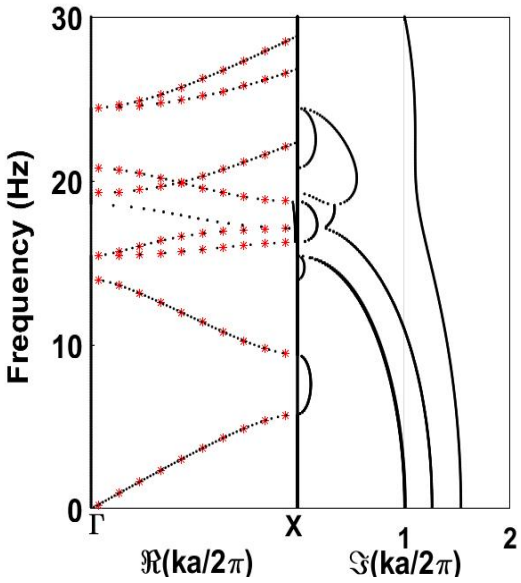


Figure 3.10: Complex band structure of the 2D SnC with steel circular inclusions in a square lattice performed by $(a)$ PWE (red asterisks) and $(a-b)$ EPWE (black points) approaches.

vector is displayed up to 2 (larger values exist). In Figure 3.10, for a specific frequency, the difference between evanescent modes higher to 1 ($\Im\{\mathbf{k}a/2\pi\} \geq 1$) lies in their symmetry with respect to the unit cell centre (Laude *et al.*, 2009).

It can also be observed in Figure 3.10 that each frequency inside the band gap (for instance $f = 10$ Hz) is characterized by some values of $\Im\{\mathbf{k}a/2\pi\}$, which correspond to the harmonics of the multi-exponential decay of the evanescent modes (Romero-García *et al.*, 2010). Romero-García *et al.* (2010) showed that only the first value of the $\Im\{\mathbf{k}a/2\pi\}$ contributes to the decay

of the mode, thus higher harmonics can be neglected and it can be approximated in the same way as an exponential-like decay. The spatial decay inside the band gap is multi-exponential and dominated by the minimum imaginary part of wave vectors (Chen *et al.*, 2017).

In Appendices B and C, other effects that influence Bragg-type band gap formation on 2D PnCs are investigated, *e.g.*, the influence of filling fraction, inclusion geometry, type of lattice and piezoelectricity.

### 3.0.3 1D Elastic metamaterial Euler-Bernoulli beam

An infinite 1D EM Euler-Bernoulli beam with an attached single periodic array of S-DOF resonator is regarded (Figure 3.11).

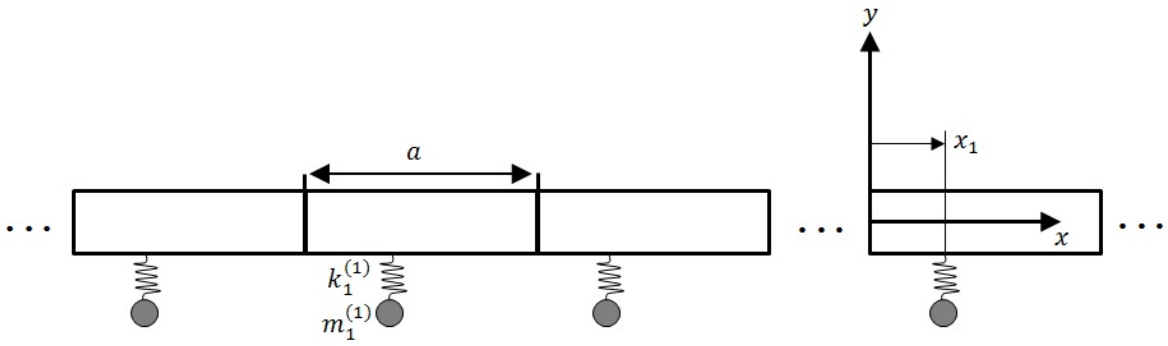


Figure 3.11: Infinite EM beam with an attached single periodic array of S-DOF resonator.

EM beam geometry and material properties are shown in Table 3.3.

Table 3.3: EM beam geometry and material properties.

| Geometry/Property | Value |
|---|---|
| Unit-cell length ($a$) | 0.1 m |
| Cross section area ($S = b \times h$) | $0.02 \times 0.002$ m$^2$ |
| Young's modulus ($E$) | $70 \times 10^9$ Pa |
| Mass density ($\rho$) | 2700 kg/m$^3$ |
| Structural damping ($\eta$) | 0.01 |
| Second moment of area ($I$) | $1.3333 \times 10^{-11}$ m$^4$ |

S-DOF resonator parameters are: $\eta_1 = 0.05$, $x_1 = 0.05$ m, $f_1 = 200$ Hz and $m_1 = \bar{\gamma}_1 \rho S a = 0.0054$ kg, where $\bar{\gamma}_1 = 0.5$ is the ratio of resonator mass to the beam unit cell mass. Resonator stiffness is obtained by $\tilde{k}_1 = m_1(2\pi f_1)^2(1+j\eta_1)$. Parameters and material properties are chosen the same as Xiao *et al.* (2012a).

Figure 3.12 illustrates the elastic band structure calculated by PWE-Euler-Bernoulli formulation (see Subsection 2.1.3) using $M = 1$ harmonic terms in Fourier series expansion (3 plane waves).

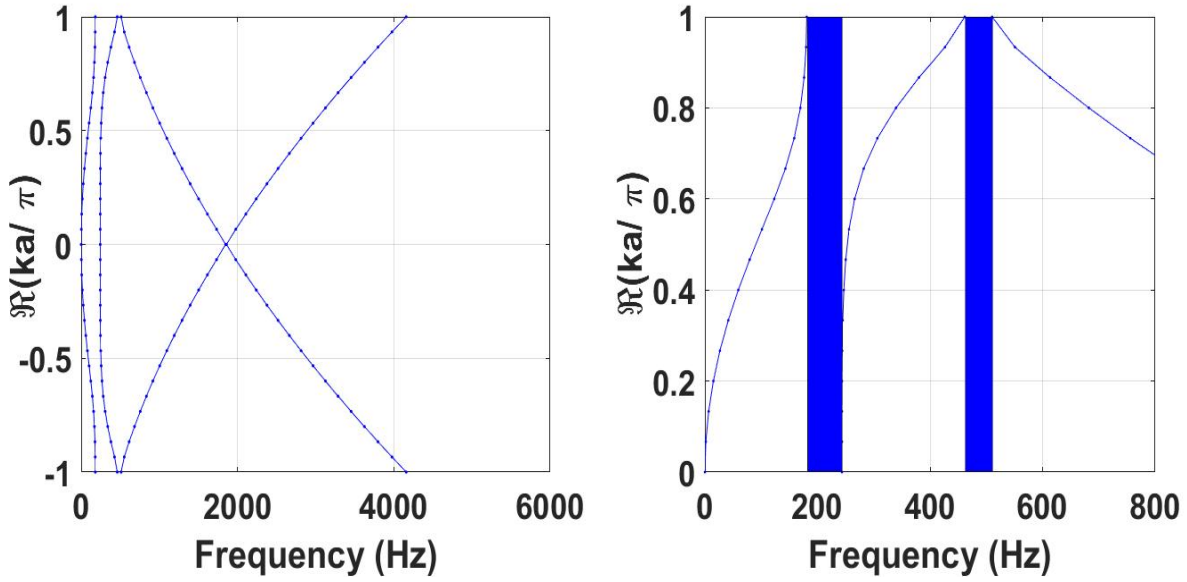


Figure 3.12: Elastic band structure of the EM Euler-Bernoulli beam using 3 plane waves $(a)$. The first bands of the EM beam band structure, showing the locally resonant and Bragg-type band gaps in blue shaded regions $(b)$.

From Figure 3.12, it can be identified both the locally resonant band gap around the resonator natural frequency (200 Hz), and the Bragg-type band gap around 460 Hz. From Bragg's law, $a = n(\lambda/2) \therefore ka = n\pi$, $n \in \mathbb{Z}$, and considering low frequency bands, where Euler-Bernoulli beam theory is valid, Bloch wave vector can be assumed as $k = \sqrt{2\pi f}\sqrt[4]{\rho S/EI}$ (Lee, 2009). Thus the first Bragg frequency can be obtained as:

$$f_{B_1} = \frac{1}{2\pi}(\frac{n\pi}{a})^2\sqrt{\frac{EI}{\rho S}} \approx 461.8 \text{ Hz}. \tag{3.1}$$

Figure 3.13 shows the complex band structure of the EM beam calculated by EPWE using 3 plane waves. All Bloch wave vector solutions are presented in Figure 3.13. The black lines in Figure 3.13 $(a)$ indicate the limits of FBZ normalized.

All the curves in Figure 3.13 $(b)$ are the imaginary values of Bloch wave vector, however, only some components are the most accurate. The most accurate imaginary components are that associated with the real components (Fig. 3.13 $(a)$) that intersect one of the FBZ limits. These components are shown in Figure 3.14. From Figure 3.14, it can be seen that the most accurate components of the Bloch wave vector arise on pairs of negative and positive Bloch wave vector values.

In order to compare PWE and EPWE results, it is presented the real components of Bloch wave vector calculated by PWE (blue points) and EPWE (red circles) approaches in Figure 3.15 for 3 plane waves.

Moreover, in Appendices F and G, it is investigated the elastic band structure of flex-

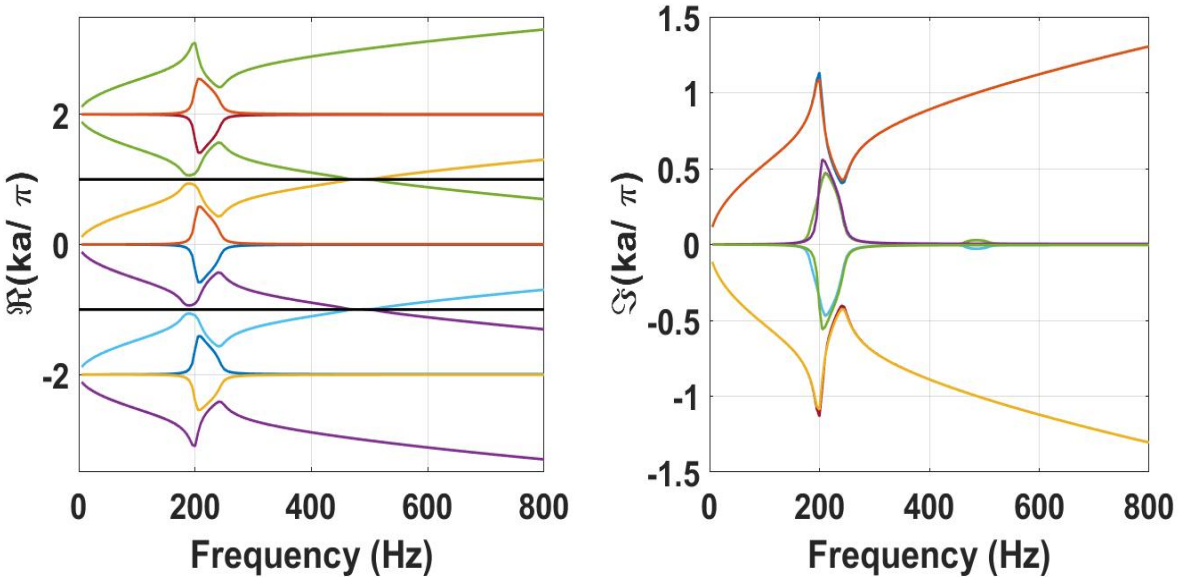


(*a*) (*b*)

Figure 3.13: Complex band structure of the EM Euler-Bernoulli beam using 3 plane waves calculated by EPWE: $(a)$ real and $(b)$ imaginary parts of Bloch wave vector.

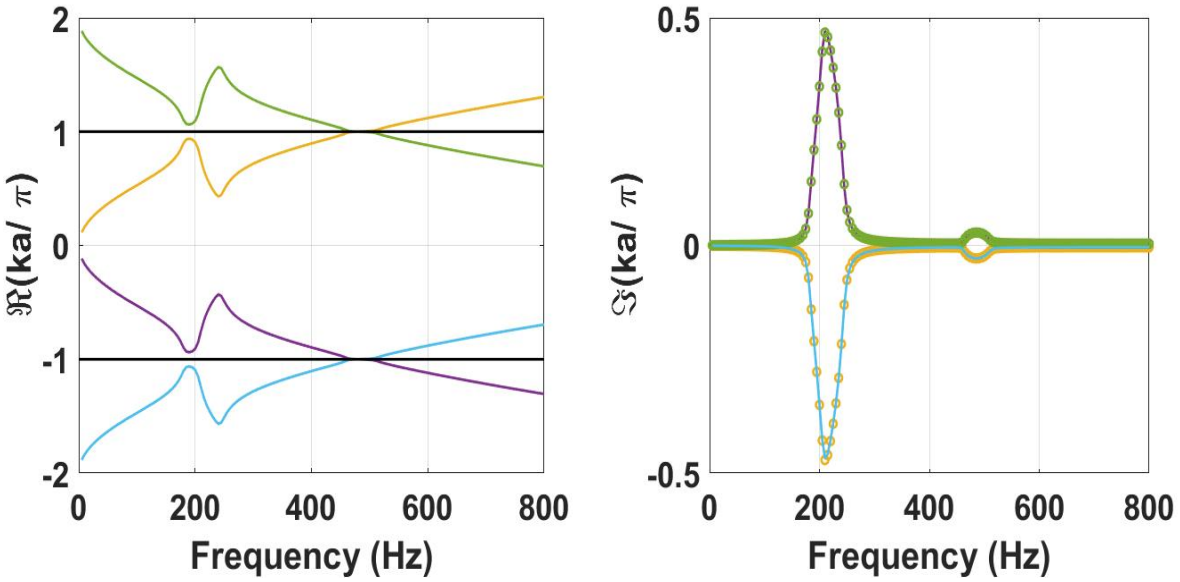


(*a*) (*b*)

Figure 3.14: The most accurate components of the Bloch wave vector calculated by EPWE with $M = 1$: $(a)$ real and $(b)$ imaginary parts.

ural waves in 1D EM Euler-Bernoulli beams and 2D EM thin plates considering other effects that influence band gap formation, such as band gap coupling between Bragg-type and locally resonant band gaps, type of lattice, among others.

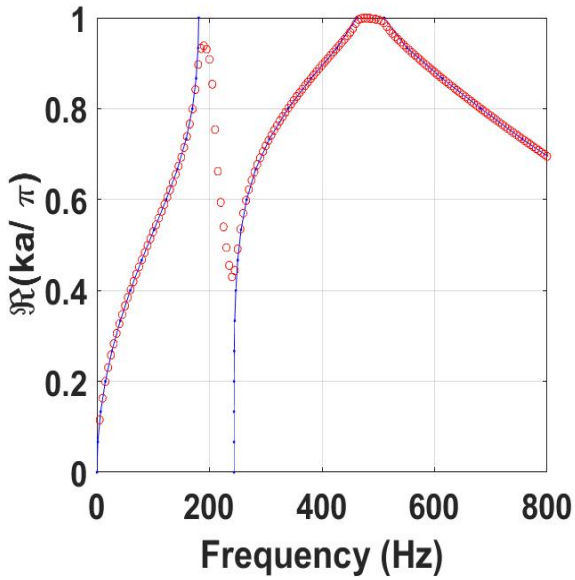


(*a*)

Figure 3.15: Comparison of Bloch wave vector real part calculated by PWE (blue points) and EPWE (red circles) approaches with $M = 1$.

# 4 GENERAL CONCLUSIONS

PnCs and EMs have been extensively applied in the last years for passive vibration control. They can open up ranges of frequency where there are only evanescent waves, *i.e.*, band gaps. These band gaps can be classified into locally resonant and Bragg-type. In this thesis, it is investigated different applications of PnCs and EMs for passive vibration control.

The semi-analytical approaches proposed are based on PWE, IPWE and EPWE. Some advantages and drawbacks of these approaches are highlighted. Simulated examples are carried out in order to obtain the band structure of 1D PnC rods, 2D SnCs and 1D EM Euler-Bernoulli beams using these methods.

Next, in the attached articles, it was considered first a simple 1D PnC Euler-Bernoulli beam composed of steel and epoxy. The polyethylene and steel percentages into the unit cell is an important variable and its influence in the unit cell attenuation constant is complex and depends on the unit cell length. It was shown some ranges of frequency, regarding fixed unit cell lengths, with no unit cell attenuation, independently of the polyethylene and steel quantities. It is also shown regions that presented higher attenuation. The analytical and numerical results presented a good agreement with the experimental ones and they localized the band gap position and width close to the experimental.

After that, flexural wave band gaps in an epoxy PnC plate reinforced by $Al_2O_3$ inclusions were investigated regarding Mindlin-Reissner theory. Complete band gaps were observed for all types of inclusion and the best performance was found for rotated square and circular inclusions, considering square and triangular lattices, respectively.

The band structure of elastic waves propagating in carbon nanostructure PnCs with square, rectangular, triangular, honeycomb and Kagomé lattices was also studied. Full band gaps between XY and Z modes were observed for all types of carbon nanostructures. The best performance was for circular carbon nanostructures in a triangular lattice with high band gap width in a broad range of filling fraction. This result suggests that carbon nanostructure PnCs may be feasible for elastic vibration management in GHz.

Afterwards, nano-piezoelectric and magnetoelectroelastic PnCs were analysed. Broad full band gaps were obtained for the piezoelectric PnC and triangular lattice with circular inclusion presented the broadest full band gap, considering a fixed filling fraction of 0.335. Piezoelectric effect is significant on band gaps for all lattices and inclusions. For the magnetoelectroelastic PnC, the broadest full band gap was found for hollow inclusion in a triangular lattice, regarding the filling fraction of 0.45.

It was also studied the elastic wave propagation in 1D and 2D EMs. A 1D EM Euler-Bernoulli beam and a 2D EM thin plate, both with multiple periodic attached M-DOF resonators, are regarded. Different resonator configurations are discussed. The 1D EM Euler-Bernoulli beam with five arrays of S-DOF resonators presented a broad band gap created by the coupling between locally resonant and Bragg-type band gaps. For the 1D EM Euler-Bernoulli beam

with five arrays of 2-DOF resonators, two broad band gaps were opened up from the coupling between locally resonant band gaps. It was also observed that 2D EM thin plates with S-DOF resonators provide higher attenuation for the last locally resonant and for Bragg-type band gaps than 2D EM thin plates with M-DOF resonators. Furthermore, the attenuation related to the Bragg-type band gaps was higher for square lattice than triangular lattice.

Finally, the different applications of the periodic systems considered in this thesis, *i.e.*, smart PnCs, nano-PnCs, 1D PnC beam and EMs with periodic attached resonators, provide interesting results for passive vibration control in different ranges of frequency.

## 4.1 Future work

In the following, topics which appear as future prospects for continuation of the research developed in this thesis are listed.

- Improve the performance of the semi-analytical approaches proposed in this thesis by means of using parallel programming and code optimization.
- Consider the quantum effects for the band structure calculation of nanophononic crystals.
- Fabricate nanophononic crystals with advance techniques, for instance, electron beam lithography.
- Study the variability related to the physical parameters of PnCs and EMs manufactured in a 3D printer.
- Formulate new PWE and EPWE approaches associated with optimization techniques in order to identify the best inclusion geometry that opens up broader band gaps.
- Propose new PWE and EPWE formulations for PnCs and MMs including other effects, such as temperature and viscoelasticity.
- Extend the formulation of PWE and EPWE for EMs with shunting circuits.
- Investigate other complex materials, for instance, photonic crystals, phoxonic crystals, thermal metamaterials, quasi-periodic structures, nonlinear metamaterials, granular crystals, bio-inspired PnCs, magnonic crystals, magnetostrictive PnCs, plasmonic metamaterials, among others.
- Use PWE and EPWE methods associated with the supercell technique to include line defects in PnCs for waveguides and by confining standing waves in the defects. It could also be used to constitute resonators and filters. These could be interesting for local sound enhancement and energy harvesting.
- Explore new recent concepts originally from electronics which have inspired some applications in photonics and phononics, such as interface modes, also known as edge modes, on periodic acoustic systems.

## 4.2 List of publications

• Articles in indexed journals:

- MIRANDA, E.J.P., Jr.; DOS SANTOS, J.M.C. Elastic wave band gaps in a two-dimensional magnetoelectroelastic phononic crystal. **Revista Interdisciplinar de Pesquisa em Engenharia**, v. 2, 13-26, 2016.
- MIRANDA, E.J.P., Jr.; DOS SANTOS, J.M.C. Evanescent Bloch waves and complex band structure in magnetoelectroelastic phononic crystals. **Mechanical Systems and Signal Processing** (accepted), 2017.
- MIRANDA, E.J.P., Jr.; NOBREGA, E.D.; FERREIRA, A.H.R.; DOS SANTOS, J.M.C. Flexural wave band gaps in a multi-resonator elastic metamaterial plate using Kirchhoff-Love theory. **Mechanical Systems and Signal Processing** (under review), 2017.
- MIRANDA, E.J.P., Jr.; DOS SANTOS, J.M.C. Flexural wave band gaps in a multi-resonator elastic metamaterial Timoshenko beam. **Wave Motion** (under review), 2017.
- MIRANDA, E.J.P., Jr.; RODRIGUES, S.F.; DOS SANTOS, J.M.C. Band structure in a sustainable sonic crystal. **Materials Science Forum** (under review), 2017.
- MIRANDA, E.J.P., Jr.; ANGELIN, A.F.; RODRIGUES, S.F.; GACHET-BARBOSA, L.A.; DOS SANTOS, J.M.C. Influence of spheroid and fiber-like waste-tire rubbers on the sound absorption coefficient of rubberized mortars. **Materials Science Forum** (under review), 2017.
- MIRANDA, E.J.P., Jr.; DOS SANTOS, J.M.C. Flexural wave band gaps in phononic crystal Euler-Bernoulli beams. **Materials Research Ibero-American Journal of Materials** (in press), 2017. http://dx.doi.org/10.1590/1980-5373-mr-2016-0877.
- MIRANDA, E.J.P., Jr.; DOS SANTOS, J.M.C. Complete band gaps in nano-piezoelectric phononic crystals. **Materials Research Ibero-American Journal of Materials**, v. 20(suppl. 1), 15-38, 2017.
- MIRANDA, E.J.P., Jr.; DOS SANTOS, J.M.C. Band structure in carbon nanostructure phononic crystals. **Materials Research Ibero-American Journal of Materials** (in press), 2017. http://dx.doi.org/10.1590/1980-5373-mr-2016-0898.
- MIRANDA, E.J.P., Jr.; DOS SANTOS, J.M.C. Phononic band gaps in $Al_2O_3$/epoxy composite. **Materials Science Forum**, v. 912, 112-117, 2018.

• Book Chapters:

- MIRANDA, E.J.P., Jr.; DOS SANTOS, J.M.C. Flexural wave band gaps in a 1D phononic crystal beam. **ABCM Series on Mechanical Sciences and Engineering: Selected Papers of the XVII International Symposium on Dynamic Problems of Mechanics** (accepted), 2017.
- MIRANDA, E.J.P., Jr.; DOS SANTOS, J.M.C. Elastic wave band gaps in a steel-concrete elastic metamaterial. **Trends in Engineering Mechanics Special Publications**

**(TEMSP)** (under review), 2017.

- Full Papers and Abstracts in Conference Proceedings:
  - MIRANDA, E.J.P., Jr.; DOS SANTOS, J.M.C. Flexural wave band gaps in metamaterial elastic beam. In **Proceedings of the 23rd ABCM International Congress of Mechanical Engineering (COBEM)**, pp. 1-8. Rio de Janeiro, Brazil, December 6-11 2015.
  - MIRANDA, E.J.P., Jr.; DOS SANTOS, J.M.C. Flexural wave band gaps in $Al_2O_3$/epoxy composite rectangular plate using Mindlin theory. In **Proceedings of the Brazilian Conference on Composite Materials (BCCM-3)**, pp. 138. Gramado, Brazil, August 28-31 2016.
  - MIRANDA, E.J.P., Jr.; DOS SANTOS, J.M.C. Flexural wave band gaps in elastic metamaterial thin plate. In **Proceedings of the IX Congresso Nacional de Engenharia Mecânica (CONEM)**, pp. 1-10. Fortaleza, Brazil, August 21-25 2016.
  - MIRANDA, E.J.P., Jr.; DOS SANTOS, J.M.C. Flexural wave band gaps in an elastic metamaterial beam with periodically attached spring-mass resonators. In **Proceedings of the International Conference Noise and Vibration Engineering (ISMA)**, pp. 2099-2113. Leuven, Belgium, September 19-21 2016.
  - MIRANDA, E.J.P., Jr.; DOS SANTOS, J.M.C. Phononic band gaps in $Al_2O_3$/epoxy composite. In **Proceedings of the 60° Congresso Brasileiro de Cerâmica (CBC)**, pp. 1507. Águas de Lindóia, Brazil, May 15-18 2016.
  - MIRANDA, E.J.P., Jr.; DOS SANTOS, J.M.C. Band structures in carbon nanostructure phononic crystals. In **Proceedings of the 22° Congresso Brasileiro de Engenharia e Ciência dos Materiais (CBECiMat)**, pp. 4520. Natal, Brazil, November 06-10 2016.
  - MIRANDA, E.J.P., Jr.; DOS SANTOS, J.M.C. Flexural wave band gaps in phononic crystal Euler-Bernoulli beam using wave spectral element method. In **Proceedings of the 22° Congresso Brasileiro de Engenharia e Ciência dos Materiais (CBECiMat)**, pp. 4413. Natal, Brazil, November 06-10 2016.
  - MIRANDA, E.J.P., Jr.; DOS SANTOS, J.M.C. Flexural wave band gaps in a 1D phononic crystal beam. In **Proceedings of the XVII International Symposium on Dynamic Problems of Mechanics (DINAME)**, pp. 1-10. São Sebastião, Brazil, March 5-10 2017.
  - MIRANDA, E.J.P., Jr.; DOS SANTOS, J.M.C. Bandas proibidas de ondas elásticas em cristais fonôninos sustentáveis. In **Proceedings of the XXVII Encontro da Sociedade Brasileira de Acústica (SOBRAC)**, pp. 1238-1247. Brasília, Brazil, May 28-31 2017.
  - MIRANDA, E.J.P., Jr.; DOS SANTOS, J.M.C.; RODRIGUES, S.F. Band structure in a sustainable sonic crystal. In **Proceedings of the 61° Congresso Brasileiro de Cerâmica (CBC)**, pp. 1826. Gramado, Brazil, June 04-07 2017.
  - MIRANDA, E.J.P., Jr.; ANGELIN, A.F.; RODRIGUES, S.F.; GACHET-BARBOSA, L.A.; DOS SANTOS, J.M.C. Influence of spheroid and fiber-like waste-tire rubbers on the sound absorption coefficient of rubberized mortars. In **Proceedings of the 61° Con-**

**gresso Brasileiro de Cerâmica (CBC)**, pp. 1659. Gramado, Brazil, June 04-07 2017.

- MIRANDA, E.J.P., Jr.; DOS SANTOS, J.M.C. Complete band gaps in two-dimensional magnetoelectroelastic phononic crystals. In **International Conference on Structural Engineering Dynamics (ICEDyn)**, pp. 1-17. Ericeira, Portugal, July 3-5 2017.
- MIRANDA, E.J.P., Jr.; Ferreira, A.H.R.; DOS SANTOS, J.M.C. Flexural wave band gaps in a multi-resonator elastic metamaterial thin plate. In **International Conference on Structural Engineering Dynamics (ICEDyn)**, pp. 1-13. Ericeira, Portugal, July 3-5 2017.
- FERREIRA, A.H.R.; DOS SANTOS, J.M.C.; MIRANDA, E.J.P., Jr.; Ramos, R. Semi-analytical formulation for sound transmission loss analysis through a thick plate with periodically attached spring-mass resonators. In **International Conference on Structural Engineering Dynamics (ICEDyn)**, pp. 1-13. Ericeira, Portugal, July 3-5 2017.

# References

ACHAOUI, Y.; LAUDE, V.; BENCHABANE, S. and KHELIF, A. Local resonances in phononic crystals and in random arrangements of pillars on a surface. **Journal of Applied Physics**, v. 114, 104503–104506, 2013.

ACHAOUI, Y.; UNGUREANU, B.; ENOCH, S. and BRÛLÉ, S. Seismic waves damping with arrays of inertial resonators. **Extreme Mechanics Letters**, v. 8, 30–37, 2016.

AI, L. and GAO, X.L. Metamaterials with negative Poisson's ratio and non-positive thermal expansion. **Composite Structures**, v. 162, 70–84, 2017.

ARMENISE, M.; CAMPANELLA, C.; CIMINELLI, C.; DELL'OLIO, F. and PASSARO, V. Phononic and photonic band gap structures: modelling and applications. **Physics Procedia**, v. 3, 357–364, 2010.

ASSOUAR, B.; OUDICH, M. and ZHOU, X. Acoustic metamaterials for sound mitigation. **Comptes Rendus Physique**, v. 17, 524–532, 2016.

BARNELL, E.G. **One and two-dimensional propagation of waves in periodic heterogeneous media: Transient effects and band-gap tuning**. 2014. PhD (Thesis). University of Manchester, School of Mathematics.

BAYAT, A. and GORDANINEJAD, F. Band-gap of a soft magnetorheological phononic crystal. **Journal of Vibration and Acoustics**, v. 137, 011011–011018, 2015.

BENCHABANE, S.; KHELIF, A.; ROBERT, L.; RAUCH, J.; PASTUREAUD, T. and LAUDE, V. Elastic band gaps for surface modes in an ultrasonic lithium niobate phononic crystal. **Proceedings of SPIE Photonics Europe**, v. 133, 618216–618228, 2006.

BERTOLDI, K.; REIS, P.; WILLSHAW, S. and MULLIN, T. Negative Poisson's ratio behavior induced by an elastic instability. **Advanced Materials**, v. 22, 361–366, 2010.

BERTOLDI, K.; VITELLI, V.; CHRISTENSEN, J. and VAN HECKE, M. Flexible mechanical metamaterials. **Nature Reviews**, v. 2, 17066–17076, 2017.

BILAL, O.; FOEHR, A. and DARAIO, C. Observation of trampoline phenomena in 3D-printed metamaterial plates. **Extreme Mechanics Letters**, v. 15, 103–107, 2017.

BLOCH, F. Über die quantenmechanik der elektronen in kristallgittern. **Zeitschrift für Physik**, v. 52, 555–600, 1928.

BRILLOUIN, L. **Wave propagation in periodic structures**. Dover Publications, 1946.

CAO, Y.; HOU, Z. and LIU, Y. Finite difference time domain method for band-structure calculations of two-dimensional phononic crystals. **Solid State Communications**, v. 132, 539–543, 2004a.

CAO, Y.; HOU, Z. and LIU, Y. Convergence problem of plane-wave expansion method for phononic crystals. **Physics Letters A**, v. 327, 247–253, 2004b.

CASADEI, F.; BECK, B.; CUNEFARE, K. and RUZZENE, M. Vibration control of plates through hybrid configurations of periodic piezoeletric shunts. **Journal of Intelligent Material Systems and Structures**, v. 23, 1169–1177, 2012a.

CASADEI, F.; DOZIO, L.; RUZZENE, M. and CUNEFARE, K. Periodic shunts arrays for the control of noise radiation in an enclosure. **Journal of Sound and Vibration**, v. 329, 3632–3646, 2012b.

CASTIÑEIRA-IBÁÑEZ, S.; RUBIO, C.; ROMERO-GARCÍA, V.; SÁNCHEZ-PÉREZ, J. and GARCÍA-RAFFI, L. Design, manufacture and characterization of an acoustic barrier made of multi-phenomena cylindrical scatterers arranged in a fractal-based geometry. **Archives of Acoustics**, v. 37, 455–462, 2012.

CHANG, I.L.; LIANG, Z.X.; KAO, H.W.; CHANG, S.H. and YANG, C.H. The wave attenuation mechanism of the periodic local resonant metamaterial. **Journal of Sound and Vibration**, v. 412, 349–359, 2018.

CHEN, B.; LIU, B.; EVANS, A.; PAULOSE, J.; COHEN, I.; VITELLI, V. and SANTANGELO, C. Topological mechanics of origami and kirigami. **Physical Review Letters**, v. 116, 135501–135505, 2016.

CHEN, Y.; HUANG, X.; SUN, G.; YAN, X. and LI, G. Maximizing spatial decay of evanescent waves in phononic crystals by topology optimization. **Computers and Structures**, v. 182, 430–447, 2017.

CHEN, Z.; GUO, B.; YANG, Y. and CHENG, C. Metamaterials-based enhanced energy harvesting: A review. **Physica B**, v. 438, 1–8, 2014.

CHENG, L.; DEEPAKSHYAM, K.; GORAN, K.; HONGYU, Y. and HANQING, J. Origami based mechanical metamaterials. **Scientific Reports**, v. 4, 5979–5985, 2014a.

CHENG, W.; SAINIDOU, R.; BURGARDT, P.; STEFANOU, N.; KIYANOVA, A.; EFREMOV, M.; FYTAS, G. and NEALEY, P. Elastic properties and glass transition of supported polymer thin films. **Macromolecules**, v. 40, 7283–7290, 2007.

CHENG, Z. and SHI, Z. Vibration attenuation properties of periodic rubber concrete panels. **Construction and Building Materials**, v. 50, 257–265, 2014b.

CHONG, C.; PORTER, M.; KEVREKIDIS, P. and DARAIO, C. Nonlinear coherent structures in granular crystals. **Journal of Physics: Condensed Matter**, v. 29, 413002–413025, 2017.

CLAEYS, C.; DECKERS, E.; PLUYMERS, B. and DESMET, W. A lightweight vibro-acoustic metamaterial demonstrator: Numerical and experimental investigation. **Mechanical Systems and Signal Processing**, v. 70-71, 853–880, 2016.

COMERIO, M. Can buildings be made earthquake-safe? **Science**, v. 312, 204–206, 2006.

DAVIS, B. and HUSSEIN, M. Nanophononic metamaterial: Thermal conductivity reduction by local resonance. **Physical Review Letters**, v. 112, 055505–055509, 2014.

DJAFARI-ROUHANI, B.; VASSEUR, J.; HLADKY-HENNION, A.; DEYMIER, P.; DUVAL, F.; DUBUS, B. and PENNEC, Y. Absolute band gaps and waveguiding in free standing and supported phononic crystal slabs. **Photonics and Nanostructures - Fundamentals and Applications**, v. 6, 32–37, 2008.

EL-NAGGAR, S. Dependency of the photonic band gaps in two-dimensional metallic photonic crystals on the shapes and orientations of rods. **Optical Engineering**, v. 51, 068001–068008,

2012.

ESCALANTE, J.; MARTÍNEZ, A. and LAUDE, V. Dispersion relation of coupled-resonator acoustic waveguides formed by defect cavities in a phononic crystal. **Journal of Physics D: Applied Physics**, v. 46, 475301–475307, 2013.

FENG, D.; XU, D.; XIONG, B. and WANG, Y. Continuous tuning of line defect modes in silicon two-dimensional phononic crystal. **Journal of Physics D: Applied Physics**, v. 48, 225102–225108, 2015.

FENG, R. and LIU, K. Tuning the band-gap of phononic crystals with an initial stress. **Physica B**, v. 407, 2032–2036, 2012.

FLOQUET, G. Sur les équations différentielles linéaires à coefficients périodiques. **Annales de l'École Normale Supérieure**, v. 12, 47–88, 1883.

GARCÍA, V.R. **On the control of propagating acoustic waves in sonic crystals: analytical, numerical and optimization techniques**. 2010. PhD (Thesis). Universidad Politécnica de Valencia.

GORISHNYY, T.; ULLAL, C.; MALDOVAN, M.; FYTAS, G. and THOMAS, E. Hypersonic phononic crystals. **Physical Review Letters**, v. 94, 115501–115504, 2005.

GRAFF, K. **Wave motion in elastic solids**. Dover, 1975.

GUO, X.; WEI, P. and LI, L. Dispersion relations of elastic waves in one-dimensional piezoelectric/piezomagnetic phononic crystal with functionally graded interlayers. **Ultrasonics**, v. 70, 158–171, 2016.

HENRÍQUEZ, V.; ANDERSEN, P. and JENSEN, J. A numerical model of an acoustic metamaterial using the boundary element method including viscous and thermal losses. **Journal of Computational Acoustics**, v. 25, 1750006–1750016, 2017.

HO, K.; CHENG, C.; YANG, Z.; ZHANG, X. and SHENG, P. Broadband locally resonant sonic shields. **Applied Physics Letters**, v. 83, 5566–5568, 2003.

HSU, J.C. and WU, T.T. Calculations of Lamb wave band gaps and dispersions for piezoelectric phononic plates using Mindlin's theory-based plane wave expansion method. **IEEE Transactions on Ultrasonics, Ferroelectrics, and Frequency Control**, v. 55, 431–441, 2008.

HSUE, Y. and FREEMAN, A. Extended plane-wave expansion method in three-dimensional anisotropic photonic crystals. **Physical Review B**, v. 72, 195118–195127, 2005.

HUANG, Y.; ZHANG, C. and CHEN, W. Elastic wave band structures and defect states in a periodically corrugated piezoelectric plate. **Journal of Applied Mechanics**, v. 81, 081005–081010, 2014.

JENSEN, J. Phononic band gaps and vibrations in one- and two-dimensional mass-spring structures. **Journal of Sound and Vibration**, v. 266, 1053–1078, 2003.

JOHN, S. Strong localization of photons in certain disordered dielectric superlattices. **Physical Review Letters**, v. 58, 2486–2489, 1987.

KITTEL, C. **Introduction to solid state physics**. Wiley, 2004.

KRUSHYNSKA, A.; BOSIA, F.; MINIACI, M. and PUGNO, N. Theory of acoustic band structure of periodic elastic composites. **New Journal of Physics**, v. 19, 105001–105012, 2017a.

KRUSHYNSKA, A.; MINIACI, M.; KOUZNETSOVA, V. and GEERS, M. Multilayered inclusions in locally resonant metamaterials: two-dimensional versus three-dimensional modeling. **Journal of Vibration and Acoustics**, v. 139, 024501–024504, 2017b.

KUSHWAHA, M. Classical band structure of periodic elastic composites. **International Journal of Modern Physics B**, v. 10, 977–1094, 1996a.

KUSHWAHA, M. The phononic crystals: An unending quest for tailoring acoustics. **Modern Physics Letters B**, v. 30, 1630004–1630025, 2016.

KUSHWAHA, M.; DJAFARI-ROUHANI, B.; DOBRZYNSKI, L. and VASSEUR, J. Sonic stop-bands for cubic arrays of rigid inclusions in air. **The European Physical Journal B**, v. 3, 155–161, 1998.

KUSHWAHA, M. and HALEVI, P. Giant acoustic stop bands in two-dimensional periodic arrays of liquid cylinders. **Applied Physics Letters**, v. 69, 31–33, 1996b.

KUSHWAHA, M. and HALEVI, P. Stop bands for cubic arrays of spherical balloons. **Journal of the Acoustical Society of America**, v. 101, 619–622, 1997.

KUSHWAHA, M.; HALEVI, P.; DOBRZYNSKI, L. and DJAFARI-ROUHANI, B. Acoustic band structure of periodic elastic composites. **Physical Review Letters**, v. 71, 2022–2025, 1993.

KUSHWAHA, M.; HALEVI, P. and MARTÍNEZ, G. Theory of acoustic band structure of periodic elastic composites. **Physical Review B**, v. 49, 2313–2322, 1994.

LAGARRIGUE, C.; GROBY, J. and TOURNAT, V. Sustainable sonic crystal made of resonating bamboo rods. **Journal of the Acoustical Society of America**, v. 133, 247–254, 2013.

LAUDE, V. **Phononic crystals: Artificial crystals for sonic, acoustic, and elastic waves.** De Gruyter, 2015.

LAUDE, V.; ACHAOUI, Y.; BENCHABANE, S. and KHELIF, A. Evanescent Bloch waves and the complex band structure of phononic crystals. **Physical Review B**, v. 80, 092301–092304, 2009.

LEE, U. **Spectral element method in structural dynamics.** Wiley, 2009.

LI, F. and WANG, Y. Elastic wave propagation and localization in band gap materials: A review. **Science China Physics, Mechanics & Astronomy**, v. 55, 1734–1746, 2012.

LI, F.; WANG, Y. and ZHANG, C. Boundary element method for calculation of elastic wave transmission in two-dimensional phononic crystals. **Science China Physics, Mechanics & Astronomy**, v. 59, 664602–664611, 2016b.

LI, L. Use of Fourier series in the analysis of discontinuous periodic structures. **Journal of the Optical Society of America A**, v. 13, 1870–1876, 1996.

LI, X. and LIU, Z. Bending and branching of acoustic waves in two-dimensional phononic crystals with linear defects. **Physics Letters A**, v. 338, 413–419, 2005.

LI, Y.; ZHU, L. and CHEN, T. Plate-type elastic metamaterials for low-frequency broadband elastic wave attenuation. **Ultrasonics**, v. 73, 34–42, 2017.

LI, Z. and WANG, X. On the dynamic behaviour of a two-dimensional elastic metamaterial system. **International Journal of Solids and Structures**, v. 78-79, 174–181, 2016a.

LIAN, Z.; JIANG, S.; HU, H.; DAI, L.; CHEN, X. and JIANG, W. An enhanced plane wave expansion method to solve piezoelectric phononic crystal with resonant shunting circuits. **Shock and Vibration**, v. 2016, 4015363–4015374, 2016.

LIU, Z.; CHAN, C.; SHENG, P.; GOERTZEN, A. and PAGE, J. Elastic wave scattering by periodic structures of spherical objects: Theory and experiment. **Physical Review B**, v. 62, 2446–2457, 2000b.

LIU, Z.; ZHANG, X.; MAO, Y.; ZHU, Y.; YANG, Z.; CHAN, C. and SHENG, P. Locally resonant sonic materials. **Science**, v. 289, 1734–1736, 2000a.

MALDOVAN, M. and THOMAS, E. Simultaneous localization of photons and phonons in two-dimensional periodic structures. **Applied Physics Letters**, v. 88, 250917–250919, 2006.

MARTINS, M.; GODINHO, L. and PICADO-SANTOS, L. Numerical evaluation of sound attenuation provided by periodic structures. **Archives of Acoustics**, v. 38, 503–516, 2013.

MARTÍNEZ-SALA, R.; RUBIO, C.; GARCÍA-RAFFI, L.; SÁNCHEZ-PÉREZ, J.; SÁNCHEZ-PÉREZ, E. and LLINARES, J. Control of noise by trees arranged like sonic crystals. **Journal of Sound and Vibration**, v. 291, 100–106, 2006.

MARTÍNEZ-SALA, R.; SANCHO, J.; SÁNCHEZ, J.; GÓMEZ, V. and LLINARES, J. Sound attenuation by sculpture. **Nature**, v. 378, 241, 1995.

MAZZOTTI, M.; MINIACI, M. and BARTOLI, I. Band structure analysis of leaky Bloch waves in 2D phononic crystal plates. **Ultrasonics**, v. 74, 140–143, 2017.

MENCIK, J.M. On the low- and mid-frequency forced response of elastic structures using wave finite elements with one-dimensional propagation. **Computers and Structures**, v. 88, 674–689, 2010.

MORANDI, F.; MINIACI, M.; MARZANI, A.; BARBARESI, L. and GARAI, M. Standardised acoustic characterisation of sonic crystals noise barriers: Sound insulation and reflection properties. **Applied Acoustics**, v. 114, 294–306, 2016.

NASCIMENTO, R.F. **Propagação de ondas utilizando modelos de elementos finitos em guias de onda estruturais**. 2009. PhD (Thesis). Universidade Estadual de Campinas, Faculdade de Engenharia Mecânica.

NI, Z.Q.; ZHANG, Y.; JIANG, L.H. and HAN, L. Bending vibration band structure of phononic crystal beam by modified transfer matrix method. **International Journal of Modern Physics B**, v. 28, 1450093–1450106, 2014.

NOBREGA, E.; GAUTIER, F.; PELAT, A. and DOS SANTOS, J.M.C. Vibration band gaps for elastic metamaterial rods using wave finite element method. **Mechanical Systems and Signal Processing**, v. 79, 192–202, 2016.

OUDICH, M.; SENESI, M.; ASSOUAR, M.; RUZZENE, M.; SUN, J.H.; VICENT, B.; HOU, Z. and WU, T.T. Experimental evidence of locally resonant sonic band gap in two-dimensional phononic stubbed plates. **Physical Review B**, v. 84, 165136–165141, 2011.

PAL, R. and RUZZENE, M. Edge waves in plates with resonators: an elastic analogue of the quantum valley Hall effect. **New Journal of Physics**, v. 19, 025001–025017, 2017.

PENDRY, J. Negative refraction makes a perfect lens. **Physical Review Letters**, v. 85, 3966–3969, 2000.

PENNEC, Y.; VASSEUR, J.; DJAFARI-ROUHANI, B.; DOBRZYńSKI, L. and DEYMIER, P. Two-dimensional phononic crystals: Examples and applications. **Surface Science Reports**, v. 65, 229–291, 2010.

QIAN, D. and SHI, Z. Using PWE/FE method to calculate the band structures of the semi-infinite beam-like PCs: Periodic in z-direction and finite in x-y plane. **Physics Letters A**, v.

381, 1516–1524, 2017.

QIAN, Z.; JIN, F.; LI, F. and KISHIMOTO, K. Complete band gaps in two-dimensional piezoelectric phononic crystals with {1-3} connectivity family. **International Journal of Solids and Structures**, v. 45, 4748–4755, 2008.

QIU, C. and LIU, Z. Acoustic directional radiation and enhancement caused by band-edge states of two-dimensional phononic crystals. **Applied Physics Letters**, v. 89, 063106–063108, 2006.

ROBILLARD, J.F.; BOU MATAR, O.; VASSEUR, J.; DEYMIER, P.; STIPPINGER, M.; HLADKY-HENNION, A.C.; PENNEC, Y. and DJAFARI-ROUHANI, B. Tunable magnetoelastic phononic crystals. **Applied Physics Letters**, v. 95, 124104–124106, 2009.

ROMERO-GARCÍA, V.; FUSTER-GARCIA, E.; GARCÍA-RAFFI, L.; SÁNCHEZ-PÉREZ, J. and URIS, A. Interferometric method of determining the refraction index of two-dimensional sonic crystals. **Physical Review B**, v. 75, 224305–224312, 2007.

ROMERO-GARCÍA, V.; GARCIA-RAFFI, L. and SÁNCHEZ-PÉREZ, J. Evanescent waves and deaf bands in sonic crystals. **AIP Advances**, v. 1, 041601–041609, 2011.

ROMERO-GARCÍA, V.; SÁNCHEZ-PÉREZ, J. and GARCÍA-RAFFI, L. Molding the acoustic attenuation in quasi-ordered structures: Experimental realization. **Applied Physics Express**, v. 5, 087301–087303, 2012.

ROMERO-GARCÍA, V.; SÁNCHEZ-PÉREZ, J. and GARCIA-RAFFI, L. Evanescent modes in sonic crystals: Complex dispersion relation and supercell approximation. **Journal of Applied Physics**, v. 108, 044907–044912, 2010.

SADAT, S. and WANG, R. Colloidal nanocrystal superlattices as phononic crystals: plane wave expansion modeling of phonon band structure. **RSC Advances**, v. 6, 44578–44587, 2016.

SCHNEIDER, D.; GOMOPOULOS, M.; KOH, C.; PAPADOPOULOS, P.; KREMER, F.; THOMAS, E. and FYTAS, G. Nonlinear control of high-frequency phonons in spider silk. **Nature Materials**, v. 15, 1079–1084, 2016.

SHELBY, R.; SMITH, D. and SCHULTZ, S. Experimental verification of a negative index of refraction. **Science**, v. 292, 77–79, 2001.

SIGALAS, M. and ECONOMOU, E. Elastic and acoustic wave band structure. **Journal of Sound and Vibration**, v. 158, 377–382, 1992.

SIGALAS, M. and ECONOMOU, E. Band structure of elastic waves in two dimensional systems. **Solid State Communications**, v. 86, 141–143, 1993.

SILVA, P.B. **Dynamic analysis of periodic structures via wave-based numerical approaches and substructuring techniques**. 2015. PhD (Thesis). Universidade Estadual de Campinas, Faculdade de Engenharia Mecânica.

SMITH, D.; PADILLA, W.; VIER, D.; NEMAT-NASSER, S. and SCHULTZ, S. Composite medium with simultaneously negative permeability and permittivity. **Physical Review Letters**, v. 84, 4184–4187, 2000.

SÁNCHEZ-DEHESA, J.; GARCIA-CHOCANO, V.; TORRENT, D.; CERVERA, F.; CABRERA, S. and SIMON, F. Noise control by sonic crystal barriers made of recycled materials. **The Journal of the Acoustical Society of America**, v. 129, 1173–1183, 2011.

SOLIMAN, Y.; SU, M.; LESEMAN, Z.; REINKE, C.; EL-KADY, I. and OLSSON III, R. Phononic crystals operating in the gigahertz range with extremely wide band gaps. **Applied Physics Letters**, v. 97, 193502–193504, 2010.

SUGINO, C.; LEADENHAM, S.; RUZZENE, M. and ERTURK, A. An investigation of electroelastic bandgap formation in locally resonant piezoelectric metastructures. **Smart Materials and Structures**, v. 26, 55029–55038, 2017.

VASSEUR, J.; BOU MATAR, O.; ROBILLARD, J.; HLADKY-HENNION, A.C. and DEYMIER, P. Band structures tunability of bulk 2D phononic crystals made of magneto-elastic materials. **AIP Advances**, v. 1, 041904–041915, 2011.

VESELAGO, V. The electrodynamics of substances with simultaneously negative values of $\epsilon$ and $\mu$. **Soviet Physics Uspekhi**, v. 10, 509–514, 1968.

WANG, Y.; LI, F.; HUANG, W.; JIANG, X.; WANG, Y. and KISHIMOTO, K. Wave band gaps in two-dimensional piezoelectric/piezomagnetic phononic crystals. **International Journal of Solids and Structures**, v. 48, 4203–4210, 2008.

WANG, Y.Z.; LI, F.M.; ; KISHIMOTO, K.; WANG, Y.S. and HUANG, W.H. Band gap behaviours of periodic magnetoelectroelastic composite structures with kagome lattices. **Waves in Random and Complex Media**, v. 19, 509–520, 2009.

WEN, J.H.; YU, D.L.; LIU, J.W.; XIAO, Y. and WEN, X.S. Theoretical and experimental investigations of flexural wave propagation in periodic grid structures designed with the idea of phononic crystals. **Chinese Physics B**, v. 18, 2404–2411, 2009.

WILSON, A. The theory of electronic semi-conductors. **Proceedings of the Royal Society A**, v. 133, 448–491, 1931.

WU, M.L.; WU, L.Y.; YANG, W.P. and CHEN, L.W. Elastic wave band gaps of one-dimensional phononic crystals with functionally graded materials. **Smart Materials and Structures**, v. 18, 115013–115020, 2009.

XIAO, Y.; WEN, J.; HUANG, L. and WEN, X. Analysis and experimental realization of locally resonant phononic plates carrying a periodic array of beam-like resonators. **Journal of Physics D: Applied Physics**, v. 47, 045307–045318, 2014.

XIAO, Y.; WEN, J. and WEN, X. Broadband locally resonant beams containing multiple periodic arrays of attached resonators. **Physics Letters A**, v. 376, 1384–1390, 2012a.

XIAO, Y.; WEN, J. and WEN, X. Flexural wave band gaps in locally resonant thin plates with periodically attached spring-mass resonators. **Journal of Physics D: Applied Physics**, v. 45, 195401–195412, 2012b.

XIE, L.; XIA, B.; LIU, J.; HUANG, G. and LEI, J. An improved fast plane wave expansion method for topology optimization of phononic crystals. **International Journal of Mechanical Sciences**, v. 120, 171–181, 2017.

YABLONOVITCH, E. Inhibited spontaneous emission in solid-state physics and electronics. **Physical Review Letters**, v. 58, 2059–2062, 1987.

YAN, Z.; WANG, Y. and ZHANG, C. Wavelet method for calculating the defect states of two-dimensional phononic crystals. **Acta Mechanica Solida Sinica**, v. 21, 104–109, 2008.

YAO, Z.J.; YU, G.L.; WANG, Y.S. and SHI, Z.F. Propagation of bending waves in phononic crystal thin plates with a point defect. **International Journal of Solids and Structures**, v. 46, 2571–2576, 2009.

YI, K.; COLLET, M.; ICHCHOU, M. and LI, L. Flexural waves focusing through shunted piezoelectric patches. **Smart Materials and Structures**, v. 25, 075007–075025, 2016.

ZHANG, X.; LIU, Z.; LIU, Y. and WU, F. Defect states in 2D acoustic band-gap materials with bend-shaped linear defects. **Solid State Communications**, v. 130, 67–71, 2004.

ZHOU, W.; WU, Y. and ZUO, L. Vibration and wave propagation attenuation for metamaterials by periodic piezoelectric arrays with high-order resonant circuit shunts. **Smart Materials and Structures**, v. 24, 65021–65030, 2015.

ZHOU, X.Y.; XU, S.Z.; LIANG, B. and CHENG, J.C. Modulation of the bandgaps of in-plane elastic waves by out-of-plane wavenumber in the piezoelectric composite structures. **Smart Materials and Structures**, v. 20, 035009–035016, 2011.

ZHU, R.; LIU, X. and HUANG, G. Study of anomalous wave propagation and reflection in semi-infinite elastic metamaterials. **Wave Motion**, v. 55, 73–83, 2015.

# APPENDIX A – Article in Indexed Journal

*Materials Research*.
DOI: http://dx.doi.org/10.1590/1980-5373-MR-2016-0877


## Flexural Wave Band Gaps in Phononic Crystal Euler-Bernoulli Beams Using Wave Finite Element and Plane Wave Expansion Methods

***Edson Jansen Pedrosa de Miranda Jr.[a,b]*, José Maria Campos Dos Santos[a]***

*[a]Departamento de Mecânica Computacional - DMC, Universidade Estadual de Campinas - UNICAMP, Rua Mendeleyev, 200, CEP 13083-970, Campinas, SP, Brazil*
*[b]Departamento de Educação Profissional - DEP, Instituto Federal de Educação, Ciência e Tecnologia do Maranhão - IFMA, Rua Afonso Pena, 174, CEP 65010-030, São Luís, MA, Brazil*

Received: November 24, 2016; Revised: October 13, 2017; Accepted: November 27, 2017

We investigate theoretically and experimentally the forced response of flexural waves propagating in a 1D phononic crystal (PC) Euler-Bernoulli beam, composed by steel and polyethylene, and its band structure. The finite element, spectral element, wave finite element, wave spectral element, conventional and improved plane wave expansion methods are applied. We demonstrate that the vibration attenuation of the unit cell can be improved choosing correctly the polyethylene and steel quantities and we suggest the best percentages of these materials, considering different unit cell lengths. An experiment with a 1D PC beam is proposed and the numerical results can localize the band gap position and width close to the experimental results. A small Bragg-type band gap with low attenuation is observed between 405 Hz - 720 Hz. The 1D PC beam with unit cells of steel and polyethylene presents potential application for vibration control.

**Keywords:** *1D phononic crystal, Euler-Bernoulli beam, flexural vibration, band gaps, vibration control.*

## 1. Introduction

Artificial periodic composites known as phononic crystals (PCs), consisting of a periodic array of scatterers embedded in a host medium, have been quite studied[1-14]. They have received renewed attention because they exhibit band gaps where there are only mechanical (elastic or acoustic) evanescent waves. There are no mechanical propagating waves in the band gaps. This ability of creating phononic band gaps is similar to the electronic and photonic band gaps in semiconductors and photonic crystals, respectively.

The physical origin of phononic and photonic band gaps can be understood at micro-scale using the classical wave theory to describe the Bragg and Mie resonances based on the scattering of mechanical and electromagnetic waves propagating within the crystal[15].

PCs have many applications, such as vibration isolation technology[16-20], acoustic barriers/filters[21-23], noise suppression devices[24,25], surface acoustic devices[26], architectural design[27], sound shields[28], acoustic diodes[29] and elastic/acoustic metamaterials[19,20,23,25,30-32] (EM/AM), also known as locally resonant phononic crystals (LRPC).

LRPCs, differently from the traditional PCs which create the Bragg-type band gaps, present the locally resonant (LR) band gaps. These LR band gaps can be obtained in a frequency range of orders of magnitude lower than that given by the Bragg limit. LR band gaps arise in the vicinity of the natural frequency of the local resonators while Bragg-type band gaps typically occur at wavelengths of the order of the unit cell size. The concept of an EM or LRPC generally involves the inclusion of local resonators, and the periodicity is advantageous (creates the Bragg-type band gaps), but it is not necessary in an EM[31,32].

Most of the studies concerning PCs focused on investigation of bulk mechanical waves[1,2,7-10,12] and its results have shown that the band gaps may appear because of the contrast between the physical properties, for instance elastic modulus and density of the inclusions and matrix. Other important properties that influence the band gap width are the inclusion geometry, filling fraction and PC lattice. The band gaps may also be affected by the physical nature of PC, which can be: solid/solid[9,10,12], fluid/fluid[33] and mixed solid/fluid[34] PCs.

Some studies have concentrated on 1D PCs[11,35-48] and all of them considered solid/solid PC. Among them, some researches focused on flexural vibration in beams[11,35,36,40,41,43,45-47], longitudinal vibration in rods[39,48] and wave propagation in one direction in a 1D solid (considering one-dimensional periodicity)[37,38,42,44]. Almost all of them used the traditional analytical (spectral element - SE[49]), semi-analytical (plane wave expansion - PWE[1,2]) and/or numerical (finite element - FE[50], transfer matrix - TM[51]) methods to obtain the forced response and/or the band structure.

Only few researchers used methods developed recently[46,48]. Junyi *et al.*[46] developed an inverse method to calculate the band structure of one dimensional periodic structures based on Bloch wave boundary conditions and wave superposition,

*e-mail: edson.jansen@ifma.edu.br

# APPENDIX B – Full Paper in Conference Proceedings

BCCM-3 – Brazilian Conference on Composite Materials
Gramado, RS - Brazil, August 28-31, 2016

# FLEXURAL WAVE BAND GAPS IN $AL_2O_3$/EPOXY COMPOSITE RECTANGULAR PLATE USING MINDLIN THEORY

**Edson J.P. Miranda Jr.[1],*, José M.C. Dos Santos[1]**

[1]Department of Computational Mechanics, University of Campinas, Campinas, São Paulo, Brazil

*Corresponding author: edson.jansen@ifma.edu.br

**Abstract:** In this investigation, we study the formation of flexural wave band gaps in an epoxy composite rectangular plate reinforced by $Al_2O_3$ inclusions using Mindlin theory. We consider four types of inclusion cross sections: circular, hollow circular, square and rotated square with a 45° angle of rotation with respect to the *x*, *y* axes. The influence of the inclusion geometry and the type of lattice – square and hexagonal, of the phononic crystal plate on the band structure are analyzed. The study is performed by using the plane wave expansion (PWE) method to predict the band structure. The complete band gaps are observed for all types of cross section inclusion and the best performance is found for rotated square cross section inclusion, considering square lattice, and for circular cross section inclusion, considering hexagonal lattice. We suggest that the $Al_2O_3$/epoxy composite rectangular plate could be feasible for vibration control.

**Keywords**: Composite rectangular plate, flexural wave band gaps, Mindlin theory, plane wave expansion method, vibration control.

## 1. INTRODUCTION

Artificial periodic composites known as phononic crystals (PCs), consisting of a periodic array of scatterers embedded in a host medium, have been quite studied in the last decades [1–2]. They have received renewed attention because PCs exhibit complete band gaps where mechanical (elastic or acoustic) wave propagation is forbidden. The physical origins of phononic and photonic band gaps can be understood at micro-scale using the classical wave theory to describe the Bragg and Mie resonances, respectively, based on the scattering of mechanical and electromagnetic waves propagating within the crystal [3].

Most of the studies concerning PCs focused on investigation of bulk mechanical waves [4–7]. However, recently, some researchers are interested in elastic wave propagating in a finite thickness plate. Most of studies focused on thin plate considering the classical plate theory [8–12], *i.e.* Kirchhoff-Love plate theory [13–14]. There are only a few studies tacking into account higher theories [15–17], such as Mindlin plate theory [18]. PCs can be applied in many engineering applications, such as vibrationless environment for high-precision mechanical systems, acoustic barriers, noise suppression devices, design of transducers and other devices, perfect acoustic mirrors, filters, and high efficiency waveguides.

Theoretical models of two-dimensional PCs [7,19–20] based on the plane wave expansion (PWE) method have shown that the width and the localization of the elastic or acoustic band gaps depends on the composition, the filling fraction, the geometry of the inclusion and the PC lattice. However, only few studies investigated these variables in a PC plate [9–10]. The $Al_2O_3$/Epoxy PC have already been

studied [10–11]. However, this system was investigated considering transverse vibration in a thin plate. Here we considered the transverse vibration in an inhomogeneous isotropic elastic thick plate. The main purpose of this study is to investigate the elastic band structure of $Al_2O_3$/Epoxy composite rectangular plate using Mindlin theory, considering transverse vibration in a square and hexagonal lattices and different types of inclusion geometry cross section: circular, hollow circular, square and rotated square with a 45° angle of rotation with respect to the *x*, *y* axes.

## 2. THE MODEL

Figure 1 (a) and (b) sketch the cross section of the $Al_2O_3$/epoxy composite rectangular plate taking in to account square and hexagonal lattices (most widely used for PCs), respectively, with arbitrary inclusion geometry. Note that the type of lattice influences on the band structure of the composite rectangular plate. Figure 1 (c) and (d) represent the irreducible Brillouin zone (IBZ) (1/8 of the first Brillouin zone, in shaded region) for square and hexagonal lattices, respectively. In this study, we consider four types of inclusion as mentioned before: circular, hollow circular, square and rotated square with a 45° angle of rotation with respect to the *x*, *y* axes.

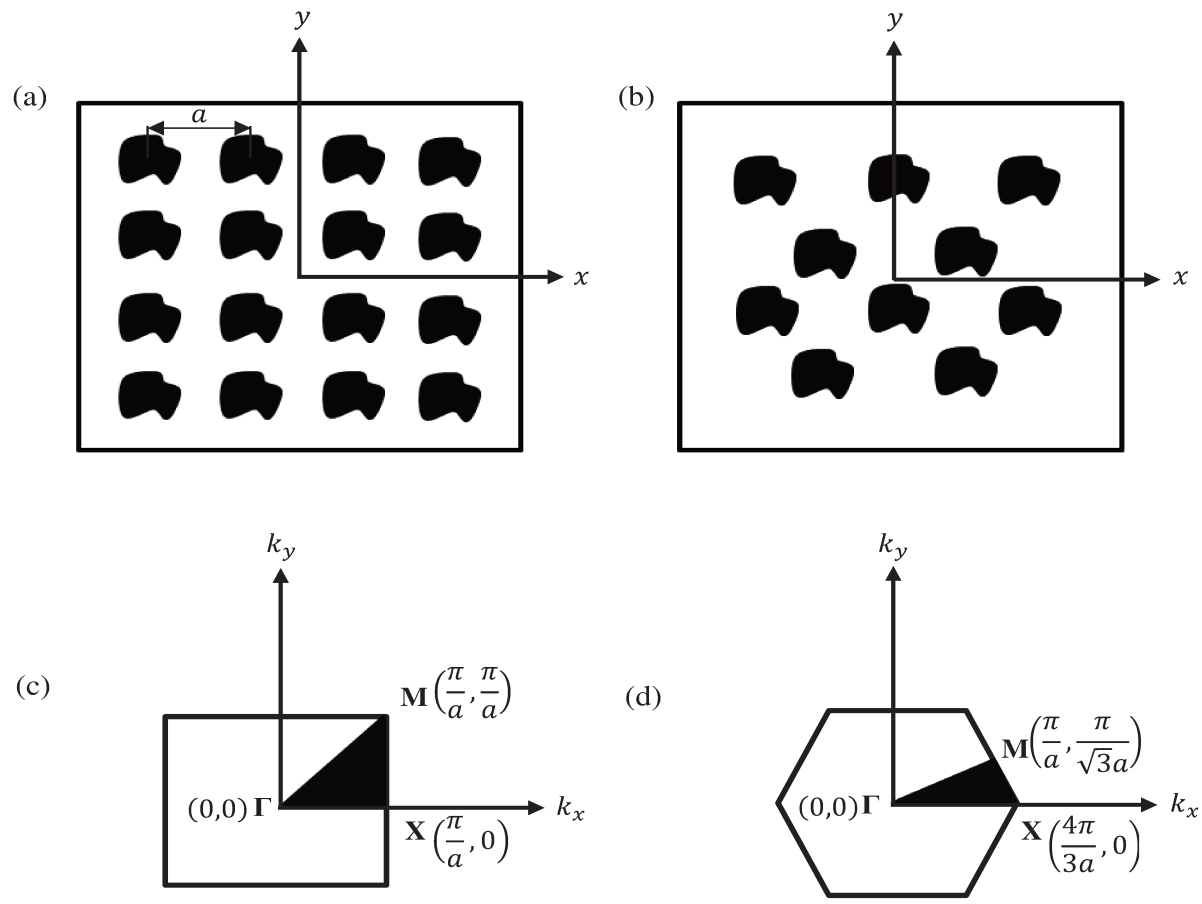


Figure 1: A transverse cross section of the binary composite system: an array of inclusions ($Al_2O_3$) periodically distributed in a matrix (epoxy) for square (a) and hexagonal (b) lattices. The IBZ (in shaded region) for square (c) and hexagonal (d) lattices.

From Mindlin theory [18], considering the isotropic case, the plate equations of motion are:

$$-\alpha\left(\Psi_x+\frac{\partial w}{\partial x}\right)+\frac{\partial}{\partial x}\left(D\frac{\partial \Psi_x}{\partial x}+\beta\frac{\partial \Psi_y}{\partial y}\right)+\frac{\partial}{\partial y}\left(\gamma\frac{\partial \Psi_y}{\partial x}+\gamma\frac{\partial \Psi_x}{\partial y}\right)=\delta\frac{\partial^2\Psi_x}{\partial t^2}, \tag{1a}$$

$$-\alpha\left(\Psi_y+\frac{\partial w}{\partial y}\right)+\frac{\partial}{\partial x}\left(\gamma\frac{\partial \Psi_y}{\partial x}+\gamma\frac{\partial \Psi_x}{\partial y}\right)+\frac{\partial}{\partial y}\left(D\frac{\partial \Psi_y}{\partial y}+\beta\frac{\partial \Psi_x}{\partial x}\right)=\delta\frac{\partial^2\Psi_y}{\partial t^2}, \tag{1b}$$

$$\frac{\partial}{\partial x}\left[\alpha\left(\Psi_x+\frac{\partial w}{\partial x}\right)\right]+\frac{\partial}{\partial y}\left[\alpha\left(\Psi_y+\frac{\partial w}{\partial y}\right)\right]=\tau\frac{\partial^2 w}{\partial t^2}, \tag{1c}$$

where $\alpha=\alpha(\mathbf{r})=\kappa^2\mu h$, $\mathbf{r}=x\mathbf{e}_1+y\mathbf{e}_2$ is the two-dimensional spatial vector, $\mathbf{e}_i$ $(i=1,2)$ are the basis vectors in the real space, $\kappa^2=\frac{\pi^2}{12}$ is a constant, $\mu$ is the shear modulus, $h$ is the plate thickness, $\Psi_x$=$\Psi_x(\mathbf{r},t)$ is the local rotation on the $x$ direction, $D=D(\mathbf{r})=\frac{Eh^3}{12(1-\nu^2)}$, $E$ is the Young's modulus, $\nu$ is the Poisson's ratio, $\beta=\beta(\mathbf{r})=D\nu$, $\Psi_y$=$\Psi_y(\mathbf{r},t)$ is the local rotation on the $y$ direction, $\gamma=\frac{D(1-\nu)}{2}$, $\delta=\delta(\mathbf{r})=\frac{\rho h^3}{12}$, $\rho$ is the density, $\tau=\tau(\mathbf{r})=\rho h$ and $w$=$w(\mathbf{r},t)$ is the displacement on $z$ direction.

In order to eliminate the factor time in Eq. (1), we imposed a harmonic time dependence on the displacement and rotations, thus $w(\mathbf{r},t)=w(\mathbf{r})e^{i\omega t}$, $\Psi_x(\mathbf{r},t)=\Psi_x(\mathbf{r})e^{i\omega t}$ and $\Psi_y(\mathbf{r},t)=\Psi_y(\mathbf{r})e^{i\omega t}$, where $\omega$ is the angular frequency. Applying the Floquet-Bloch's theorem [21–22] and expanding $w$, $\Psi_x$ and $\Psi_y$ as a Fourier series, one may write:

$$T(\mathbf{r})=e^{i\mathbf{K}.\mathbf{x}}\sum_{\mathbf{G}=-\infty}^{+\infty}T(\mathbf{G})\,e^{i\mathbf{G}.\mathbf{x}}=\sum_{\mathbf{G}=-\infty}^{+\infty}T(\mathbf{G})\,e^{i(\mathbf{K}+\mathbf{G}).\mathbf{x}}, \tag{2}$$

where $\mathbf{K}=u\mathbf{b}_1+v\mathbf{b}_2$ is the Bloch wave vector, $u,v\in\mathbb{Q}$ are the symmetry points within the IBZ in reciprocal space, or one may write $\mathbf{K}=k_x\mathbf{e}_1+k_y\mathbf{e}_2$, $k_x,k_y\in\mathbb{R}$ are the point coordinates within the IBZ in Figure 1 (c) and (d) for the real space, $\mathbf{b}_i$ $(i=1,2)$ are the basis vectors in the reciprocal space defined as $\mathbf{a}_i\cdot\mathbf{b}_i=2\pi\delta_{ij}$, $\mathbf{b}_1=2\pi\frac{\mathbf{a}_2\times\mathbf{a}_3}{\mathbf{a}_1\cdot(\mathbf{a}_2\times\mathbf{a}_3)}$, $\mathbf{b}_2=2\pi\frac{\mathbf{a}_3\times\mathbf{a}_1}{\mathbf{a}_2\cdot(\mathbf{a}_3\times\mathbf{a}_1)}$, $\mathbf{a}_i$ $(i=1,2)$ are the components of the lattice vector $\mathbf{R}=(\bar{m}\mathbf{a}_1+\bar{n}\mathbf{a}_2)$, $\bar{m},\bar{n}\in\mathbb{Z}$. For a square lattice $\mathbf{a}_i=a\mathbf{e}_i$ $(i=1,2)$, for hexagonal lattice $\mathbf{a}_1=a\mathbf{e}_1$, $\mathbf{a}_2=\frac{a}{2}\mathbf{e}_1+\frac{a\sqrt{3}}{2}\mathbf{e}_2$, $a$ is the lattice parameter, $T(\mathbf{r})$ can be $w(\mathbf{r})$, $\Psi_x(\mathbf{r})$ or $\Psi_y(\mathbf{r})$. For square lattice, the reciprocal lattice vector is defined as $\mathbf{G}=\frac{2\pi}{a}(m\mathbf{e}_1+n\mathbf{e}_2)$ and for hexagonal lattice $\mathbf{G}=\frac{2\pi}{a}\left[m\mathbf{e}_1+\frac{(-m+2n)}{\sqrt{3}}\mathbf{e}_2\right]$, $m,n\in\mathbb{Z}$.

Furthermore, one may write:

$$H(\mathbf{r})=\sum_{\mathbf{G}''=-\infty}^{+\infty}H(\mathbf{G}'')\,e^{i\mathbf{G}''.\mathbf{x}}, \tag{3}$$

where $H$ is one of the $\alpha,D,\beta,\gamma,\delta,\tau$, and $\mathbf{G}''$ has the same expressions of $\mathbf{G}$ with $m''$, $n''\in\mathbb{Z}$. Substituting Eqs. (2) and (3) in Eq. (1), one may write for all $\mathbf{r}$ and for each $\mathbf{G}'$:

$$\sum_{\mathbf{G}}\left(\begin{bmatrix}Q_{11}&Q_{12}&Q_{13}\\Q_{21}&Q_{22}&Q_{23}\\Q_{31}&Q_{32}&Q_{33}\end{bmatrix}-\omega^2\begin{bmatrix}\delta(\mathbf{G}'-\mathbf{G})&0&0\\0&\delta(\mathbf{G}'-\mathbf{G})&0\\0&0&\tau(\mathbf{G}'-\mathbf{G})\end{bmatrix}\right)\begin{Bmatrix}\Psi_x(\mathbf{G})\\\Psi_y(\mathbf{G})\\w(\mathbf{G})\end{Bmatrix}=\mathbf{0}, \tag{4}$$

where

$$Q_{11}=\alpha(\mathbf{G}'-\mathbf{G})+D(\mathbf{G}'-\mathbf{G})(\mathbf{K}_x+\mathbf{G}_x)(\mathbf{K}_x+\mathbf{G}'_x)+\gamma(\mathbf{G}'-\mathbf{G})(\mathbf{K}_y+\mathbf{G}_y)(\mathbf{K}_y+\mathbf{G}'_y),$$

$$Q_{12} = \beta(\mathbf{G}' - \mathbf{G})\big(\mathbf{K}_y + \mathbf{G}_y\big)(\mathbf{K}_x + \mathbf{G}'_x) + \gamma(\mathbf{G}' - \mathbf{G})(\mathbf{K}_x + \mathbf{G}_x)\big(\mathbf{K}_y + \mathbf{G}'_y\big),$$
$$Q_{13} = i\alpha(\mathbf{G}' - \mathbf{G})(\mathbf{K}_x + \mathbf{G}_x),$$
$$Q_{21} = \gamma(\mathbf{G}' - \mathbf{G})\big(\mathbf{K}_y + \mathbf{G}_y\big)(\mathbf{K}_x + \mathbf{G}'_x) + \beta(\mathbf{G}' - \mathbf{G})(\mathbf{K}_x + \mathbf{G}_x)\big(\mathbf{K}_y + \mathbf{G}'_y\big),$$
$$Q_{22} = \alpha(\mathbf{G}' - \mathbf{G}) + \gamma(\mathbf{G}' - \mathbf{G})(\mathbf{K}_x + \mathbf{G}_x)(\mathbf{K}_x + \mathbf{G}'_x) + D(\mathbf{G}' - \mathbf{G})\big(\mathbf{K}_y + \mathbf{G}_y\big)\big(\mathbf{K}_y + \mathbf{G}'_y\big),$$
$$Q_{23} = i\alpha(\mathbf{G}' - \mathbf{G})\big(\mathbf{K}_y + \mathbf{G}_y\big),$$
$$Q_{31} = -i\alpha(\mathbf{G}' - \mathbf{G})(\mathbf{K}_x + \mathbf{G}'_x),$$
$$Q_{32} = -i\alpha(\mathbf{G}' - \mathbf{G})\big(\mathbf{K}_y + \mathbf{G}'_y\big),$$
$$Q_{33} = \alpha(\mathbf{G}' - \mathbf{G})(\mathbf{K}_x + \mathbf{G}_x)(\mathbf{K}_x + \mathbf{G}'_x) + \alpha(\mathbf{G}' - \mathbf{G})\big(\mathbf{K}_y + \mathbf{G}_y\big)\big(\mathbf{K}_y + \mathbf{G}'_y\big), \quad (5)$$

with $\mathbf{G}' = \mathbf{G}'' + \mathbf{G}$, and $\mathbf{G}'$ has the same expressions of $\mathbf{G}$ with $m'$, $n' \in \mathbb{Z}$. The Fourier coefficients are:

$$H(\mathbf{G}) = \begin{cases} fH_{\mathrm{A}} + (1-f)H_{\mathrm{B}} \text{ for } \mathbf{G} = \mathbf{0} \\ (H_{\mathrm{A}} - H_{\mathrm{B}})F(\mathbf{G}) \text{ for } \mathbf{G} \neq \mathbf{0} \end{cases}. \quad (6)$$

The indexes A and B are related to the inclusion ($Al_2O_3$) and matrix (epoxy), respectively, and $f$ is the filling fraction of each type of inclusion, *i.e.* circular section of radius $r$, square section of width $2l$, rotated square section of width $2l$ with a 45° angle of rotation with respect to $x$ and $y$ axes and a hollow circular section with external radius $R$ and internal radius $r$, $R > r$. The hollow cylinder has an internal radius $r$ of epoxy and a thickness $R - r$ of $Al_2O_3$. The filling fraction $f$ for square lattice is:

$$f = \begin{cases} \pi r^2/a^2 \text{ for circular section}, & 0 \le f \le \pi/4 \\ 4l^2/a^2 \text{ for square section}, & 0 \le f \le 1 \\ 4l^2/a^2 \text{ for square rotated section}, & 0 \le f \le 1/2 \\ \pi(R^2 - r^2)/a^2 \text{ for hollow section}, & 0 \le f \le \pi/4 \end{cases}, \quad (7)$$

and for hexagonal lattice:

$$f = \begin{cases} 2\pi r^2/\sqrt{3}a^2 \text{ for circular section}, & 0 \le f \le \pi/2\sqrt{3} \\ 8l^2/\sqrt{3}a^2 \text{ for square section}, & 0 \le f \le 2/\sqrt{3} \\ 8l^2/\sqrt{3}a^2 \text{ for square rotated section}, & 0 \le f \le 1/\sqrt{3} \\ 2\pi(R^2 - r^2)/\sqrt{3}a^2 \text{ for hollow section}, & 0 \le f \le \pi/2\sqrt{3} \end{cases}. \quad (8)$$

The structure function $F(\mathbf{G})$ is defined as:

$$F(\mathbf{G}) = \frac{1}{S}\iint e^{-i\mathbf{G}\cdot\mathbf{r}}\, dr^2, \quad (9)$$

with $S$ denoting the area of the unit cell and the integral being performed over the cross section of the $Al_2O_3$ inclusion. The structure functions of the inclusions cited above are:

$$F(\mathbf{G}) = \begin{cases} 2fJ_1(Gr)/Gr \text{ for circular section} \\ f(\sin(G_x r)/G_x r)\big(\sin(G_y r)/G_y r\big) \text{ for square section} \\ f\left(\dfrac{\sin\big[(l/\sqrt{2})(G_x + G_y)\big]}{(l/\sqrt{2})(G_x + G_y)}\right)\left(\dfrac{\sin\big[(l/\sqrt{2})(-G_x + G_y)\big]}{(l/\sqrt{2})(-G_x + G_y)}\right) \text{ for square rotated section} \\ 2f[J_1(GR) - (r/R)J_1(GR)]/(GR) \text{ for hollow section} \end{cases}. \quad (10)$$

Equation 4 represents a generalized eigenvalue problem of $\omega^2(\mathbf{K})$ and should be solved for each $\mathbf{K}$ into the IBZ for square, Fig. 1 (c), and hexagonal lattices, Fig. 1 (d).



## 3. RESULTS AND DISCUSSION

Epoxy and $Al_2O_3$ are polycrystalline materials, and may be treated as isotropic on macroscopic scale. The physical parameters of $Al_2O_3$ (material A) and epoxy (material B) were obtained from Yao *et al.* [10], $\rho_A = 3970\ \mathrm{kg/m^3}$, $E_A = 402.7\ \mathrm{GPa}$, $\nu_A = 0.23$, $\rho_B = 1142\ \mathrm{kg/m^3}$, $E_B = 4.35\ \mathrm{GPa}$ and $\nu_B = 0.378$.

We calculated the band structure (the first ten bands) considering a fixed filling fraction (0.283), thickness ($h = a$) and lattice parameter (0.022 m) for the four inclusions considering square and hexagonal lattices. It should be noted that the classical plate theory applicable only for thin plate and long wavelengths is restricted for $kh \ll 1, h/a \ll 1$ [10]. In the course of the numerical calculations, the integers $m,\ n,\ m',\ n'$ were limited to the interval $[-8, 8]$ for all results, *i.e.* 289 plane waves. This resulted in a very good convergence.

The Fig. 2 (a-d) compares the band structures of a square lattice illustrated in Fig. 1 (a) and (c) considering flexural vibration and Mindlin plate theory, *i.e.* Eq. 4, for the four types of inclusions. We plot the band structure in the three principal symmetry directions of the IBZ (Figure 1 (c)). The plots are given in terms of frequency in Hz versus the reduced Bloch wave vector $\mathbf{k} = \mathbf{K}a/2\pi$.

In Fig. 2 (a), one complete band gap was found around 130 kHz for circular cross section. The relation between the parameters $R$ and $r$ for hollow circular cross section was fixed in $r = 0.2R$ and we do not investigate the influence of the thickness $R - r$ of $Al_2O_3$ in the band structure. Figure 2 (b) does not present any complete band gap. One can observe that the bands in Fig. 2 (b) occur in higher frequencies compared to circular cross section in Fig. 2 (a). Figure 2 (c) shows two narrow complete band gaps for square cross section inclusion, however, when these inclusions are rotated 45° with respect to $x$ and $y$ axes, two broader gaps are created in higher frequencies as illustrated in Figure 2 (d). The square rotated cross section inclusion presented the best performance (broader band gaps) compared to the other inclusions for square lattice.

Figure 3 shows the band structure for the hexagonal lattice. Considering circular cross section inclusion, Fig. 3 (a), the complete band gap is broader than the band gap of the same inclusion in a square lattice, Fig. 2 (a). For the hollow circular cross section inclusion, Fig. 3 (b) presents a complete band gap narrower than the band gap in circular cross section, Fig. 3 (a), in higher frequencies. The behavior of the band structure in a hexagonal lattice for rotated square cross section inclusions have not been improved comparing to square cross section inclusion. In Fig. 3 (c), only one broad complete band gap was observed. While for a square lattice two narrow forbidden bands were achieved, as illustrated in Fig. 2 (c). Furthermore, for a hexagonal lattice, the band structures of the circular, square and rotated square cross section inclusion present a similar behavior, just one complete band gap near 130 kHz. In a general way, considering the conditions specified above, the hexagonal lattice presents broader complete band gaps than square lattice. The circular cross section inclusion presents the best performance compared to the other inclusions for hexagonal lattice.

## 4. CONCLUSIONS

We obtain relatively broad complete band gaps where the propagation of elastic waves is forbidden. In the case of hexagonal array of $Al_2O_3$ inclusions embedded in an epoxy background, the band structures of circular, square and rotated square with a 45° angle of rotation with respect to the $x$, $y$ axes present approximately a similar behavior and the complete band gap arise in almost the same ranges of frequency. The hollow circular cross section inclusion does not present a complete band gap for $r = 0.2R$, considering a square lattice. Unlike hexagonal lattice, for the square lattice, different behaviors of the band structure have been obtained for all inclusions. The best performance is found for rotated square cross section inclusion in a square lattice and circular cross section inclusion in a

hexagonal lattice. We consider square and hexagonal arrays of inclusions perfectly embedded in an elastic background. This means that we neglected the effects due to decohesion of the fibres from the epoxy matrix and to roughness at the interface between the $Al_2O_3$ inclusions and the matrix. These defects could modify the elastic wave propagation in composite materials, altering the band structure of them. The phononic band gaps in $Al_2O_3$/epoxy composite plate enlarge the potential applications for vibration management.

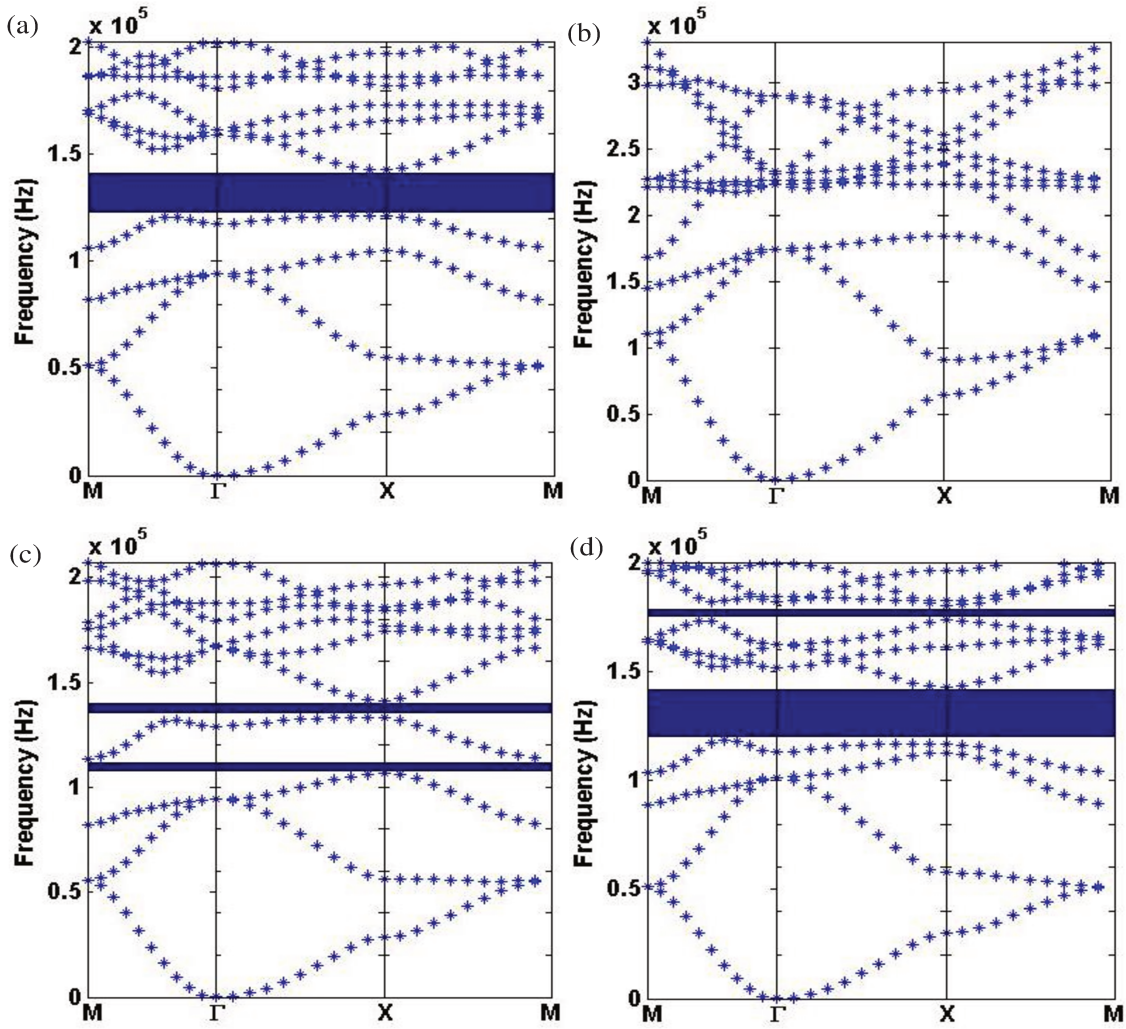


Figure 2: Elastic band structure of $Al_2O_3$ inclusions in an epoxy matrix for a square lattice. The following types of inclusions are considered: (a) circular, (b) hollow circular, (c) square and (d) rotated square with a 45° angle of rotation with respect to the *x*, *y* axes.

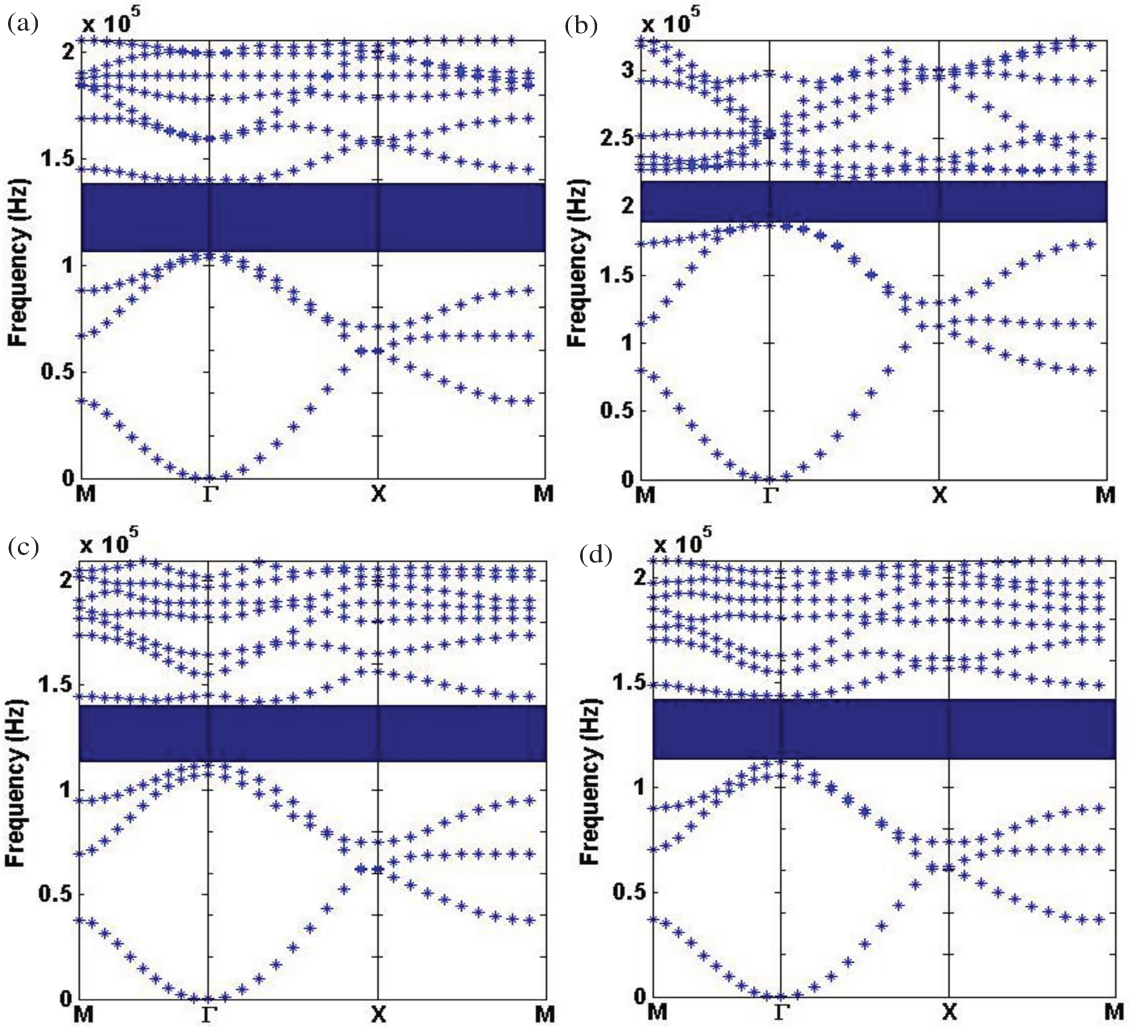


Figure 3: Elastic band structure of $Al_2O_3$ inclusions in an epoxy matrix for a hexagonal lattice. The following types of inclusions are considered: (a) circular, (b) hollow circular, (c) square and (d) rotated square with a 45° angle of rotation with respect to the *x*, *y* axes.

## ACKNOWLEDGEMENTS

The authors gratefully acknowledge the Brazilian research funding agency FAPEMA and IFMA for their financial support of this investigation.

## REFERENCES

[1] M.M. Sigalas, E.N. Economou, Elastic and acoustic wave band structure, *Journal of Sound and Vibration*, **158**, pp. 377–382, 1992.

[2] M.S. Kushwaha, P. Halevi, G. Martínez, Theory of acoustic band structure of periodic elastic composites, *Physical Review B*, **49**, pp. 2313–2322, 1994.

[3] R.H. Olsson III, I. El-Kady, Microfabricated phononic crystal devices and applications, *Measurement Science and Technology*, **20**, 012002, pp. 1–13, 2009.

[4] Y. Pennec, J.O. Vasseur, B. Djafari-Rouhani, L. Dobrzyński, P.A. Deymier, Two-dimensional phononic crystals: Examples and applications, *Surface Science Reports*, **65**, pp. 229–291, 2010.

[5] J. Huang, Z. Shi, Attenuation zones of periodic pile barriers and its application in vibration reduction for plane waves, *Journal of Sound and Vibration*, **332**, pp. 4423–4439, 2013.

[6] K. Yu, T. Chen, X. Wang, Band gaps in the low-frequency range based on the two-dimensional phononic crystals plates composed of rubber matrix with periodic steel stubs, *Physica B*, **416**, pp. 12-16, 2013.

[7] V. Anjos, A. Arantes, Phononic band structure in carbon microtube composites, *RSC Advances*, **5** pp. 11248–11253, 2015.

[8] M.M. Sigalas, E.N. Economou, Elastic waves in plates with periodically placed inclusions, Journal of Applied Physics, **75**, pp. 2845–2850, 1994.

[9] J. Wen, D. Yu, Y. Liu, Directional propagation characteristics of flexural wave in two-dimensional periodic grid-like plate structures, *Proceedings of the 14th International Congress on Sound & Vibration – ICSV14,* Cairns, pp. 1–6, 2007.

[10] Z.J. Yao, G.L. Yu, Y.S. Wang, Z.F. Shi, Propagation of bending waves in phononic crystal thin plates with a point defect, *International Journal of Solids and Structures*, **46**, pp. 2571–2576, 2009.

[11] Z.J. Yao, G.L. Yu, Y.S. Wang, W.J. Hu, Linear defect states of phononic crystal thin plates – an application of finite element method, *Advanced Materials Research*, **652–654**, pp. 48–51, 2013.

[12] Y. Zhang, Z.-Q. Ni, L. Han, Z.-M. Zhang, H.-Y. Chen, Study of improved plane wave expansion method on phononic crystal, *Optoelectronics and Advanced Materials – Rapid Communications*, **5**, pp. 870–873, 2011.

[13] A.E.H. Love, The small free vibrations and deformation of a thin elastic shell, *Philosophical Transactions of the Royal Society A*, **179**, pp. 491–546, 1888.

[14] G. Kirchhoff, Über das Gleichgewicht und die Bewegung einer elastischen Scheibe, *Journal für die reine und angewandte Mathematik*, **40**, pp. 51–88, 1850.

[15] J.-C. Hsu, T.-T. Wu, Efficient formulation for band-structure calculations of two-dimensional phononic-crystal plates, *Physical Review B*, **74**, 144303, pp. 1–7, 2006.

[16] J.-C. Hsu, T.-T. Wu, Lamb waves in binary locally resonant phononic plates with two-dimensional lattices, *Applied Physics Letters*, **90**, 201904, pp. 1–3.

[17] T.-T. Wu, J.-C. Hsu, J.-H. Sun, Phononic Plate Waves, *IEEE Transactions on Ultrasonics, Ferroelectrics, and Frequency Control*, **58**, pp. 2146–2161, 2011.

[18] R.D. Mindlin, Thickness-shear and flexural vibrations of crystal plates, *Journal of Applied Physics*, **22**, pp. 316–323, 1951.

[19] Y.F. Wang, Y.S. Wang, X.X. Su, Large bandgaps of two-dimensional phononic crystals with cross-like holes, *Journal of Applied Physics*, **110**, 113520, pp. 1–13, 2011.

[20] J.O. Vasseur, B. Djafari-Rouhani, L. Dobrzynski, M.S. Kushwaha, P. Halevi, Complete acoustic band gaps in periodic fibre reinforced composite materials: the carbon/epoxy composite and some metallic systems, *Journal of Physics: Condensed Matter*, **6**, pp. 8759–8770, 1994.

[21] G. Floquet, Sur les équations différentielles linéaires à coefficients périodiques, *Annales scientifiques de l'École Normale Supérieure*, **12**, pp. 47–88, 1883.

[22] F. Bloch, Über die Quantenmechanik der Electron in Kristallgittern, *Zeitschrift für Physik*, **52**, pp. 550–600, 1928.

# APPENDIX C – Article in Indexed Journal

*Materials Research*.
DOI: http://dx.doi.org/10.1590/1980-5373-MR-2016-0898



## Band Structure in Carbon Nanostructure Phononic Crystals

***Edson Jansen Pedrosa de Miranda Júnior[a,b]*, José Maria Campos Dos Santos[a]***

*[a]Departamento de Mecânica Computacional - DMC, Universidade Estadual de Campinas - UNICAMP, Rua Mendeleyev, 200, CEP 13083-970, Campinas, SP, Brasil.*
*[b]Departamento de Educação Profissional - DEP, Instituto Federal de Educação, Ciência e Tecnologia do Maranhão - IFMA, Rua Afonso Pena, 174, CEP 65010-030, São Luís, MA, Brasil.*

Received: November 30, 2016; Revised: August 28, 2017; Accepted: October 05, 2017

We investigate the band structure of elastic waves propagating in carbon nanostructure phononic crystals with square, rectangular, triangular, honeycomb and Kagomé lattices. We also study the influence of carbon nanostructure cross section geometry - circular, hollow circular, square and rotated square with a 45° angle of rotation with respect to the *x* and *y* axes. Plane wave expansion method is used to solve the governing equations of motion of a isotropic solid based on classical elasticity theory, ignoring nanoscopic size effects, considering two-dimensional periodicity and wave propagation in the *xy* plane. Complete band gaps between XY and Z modes are observed for all types of nanostructures. The best performance is for nanophononic crystal with circular carbon nanostructures in a triangular lattice with high band gap width in a broad range of filling fraction. We suggest that carbon nanostructure phononic crystals are feasible for elastic vibration management in GHz.

**Keywords:** *carbon nanostructure phononic crystal, band structure, plane wave expansion method, complete band gaps, vibration control*

## 1. Introduction

Recently, artificial periodic composites known as phononic crystals (PCs) have been quite studied[1-14]. They are created by arranging periodically two or more materials with different vibrational properties. Elastic/acoustic mismatch between the constituent materials can be considered to arise either from difference of material properties/geometric parameters (*e.g.*, density, elastic modulus, cross-sectional area) - continuum-scale theory, or from interatomic force constants and masses - atomic-scale theory.

PCs have received renewed attention because they exhibit band gaps where there are only mechanical (elastic or acoustic) evanescent waves and no mechanical propagating waves. Novel physical properties of PCs arise from the possibility of creating phononic band gaps and negative refraction (phonon branches with negative group velocity)[4]. Phononic band gaps are similar to electronic and photonic band gaps in semiconductors and photonic crystals[15,16], respectively.

The physical origin of phononic and photonic band gaps can be understood at micro-scale using the classical wave theory to describe Bragg and Mie resonances, respectively, based on the scattering of mechanical and electromagnetic waves propagating within the crystal[17]. PCs have many applications, such as vibration isolation technology[18-22], acoustic barriers/filters[23-25], noise suppression devices[26,27], surface acoustic devices[28], architectural design[29], sound shields[30], acoustic diodes[31], elastic/acoustic metamaterials[21,22,25,27,32] (EM/AM), also known as locally resonant phononic crystals (LRPC), and thermal metamaterials[33-39] (TM), also known as phononic thermocrystals or locally resonant phononic thermocrystals.

Phononic thermocrystals can reduce the thermal conductivity in a nanostructured semiconducting material without affecting other important factors, especially electrical conductivity.

LRPCs, differently from traditional PCs which create Bragg-type band gaps, present locally resonant (LR) band gaps. LR band gaps can be obtained in a frequency range of orders of magnitude lower than that given by Bragg limit. LR band gaps arise in the vicinity of the local resonator natural frequency while Bragg-type band gaps typically occur at wavelengths of the order of unit cell size. The concept of EM or LRPC generally involves local resonators, and the periodicity is advantageous (creates Bragg-type band gaps), but it is not necessary in an EM[33,34].

Researchers have been studied PCs on μm[10,17,40,41] - mm scales, with frequency band gaps ranging from GHz and kHz to MHz, respectively. However, they present poor electronic and optical applications. More recently, with the advance of nanomaterial fabrication, nanophononic crystals have been studied and it is possible to control wave propagation in a frequency range from hypersonic[3-6,42-51] to thermal[33-39]. Only few studies have focused on carbon microstructure[10] and carbon nanostructure PCs in a hypersonic frequency range for elastic wave propagation control. Anjos & Arantes[10] studied the influence of carbon microtubes in an epoxy matrix achieving band gaps ranging from GHz scale. These researchers[10] only studied hollow circular cross section geometry in a square lattice.

*e-mail: edson.jansen@ifma.edu.br

# APPENDIX D – Article in Indexed Journal

*Materials Research.* 2017; 20(Suppl. 1): 15-38
DOI: http://dx.doi.org/10.1590/1980-5373-MR-2017-0298


## Complete Band Gaps in Nano-Piezoelectric Phononic Crystals

***Edson Jansen Pedrosa de Miranda Jr.*[a,b]*, *José Maria Campos Dos Santos*[a]**

[a]*Departamento de Mecânica Computacional - DMC, Universidade Estadual de Campinas - UNICAMP, Rua Mendeleyev, 200, CEP 13083-970, Campinas, SP, Brasil.*
[b]*Departamento de Educação Profissional - DEP, Instituto Federal de Educação, Ciência e Tecnologia do Maranhão - IFMA, Rua Afonso Pena, 174, CEP 65010-030, São Luís, MA, Brasil.*

Received: March 17, 2017; Revised: August 16, 2017; Accepted: September 17, 2017

We study the band structure of elastic waves propagating in a nano-piezoelectric phononic crystal consisting of a polymeric matrix reinforced by $BaTiO_3$ inclusions in square, rectangular, triangular, honeycomb and Kagomé lattices. We also investigate the influence of inclusion cross section geometry - circular, hollow circular, square and rotated square with a 45º angle of rotation with respect to *x* and *y* axes. Plane wave expansion method is used to solve the governing equations of motion of a piezoelectric solid based on classical elasticity theory, ignoring nanoscopic size effects, considering two-dimensional periodicity and wave propagation in the *xy* plane. Complete band gaps between XY and Z modes are observed for all inclusions and the best performance is for circular inclusion in a triangular lattice. Piezoelectricity influences significantly the band gaps for hollow circular inclusion in lower frequencies. We suggest that nano-piezoelectric phononic crystals are feasible for elastic vibration management in GHz.

**Keywords:** *nano-piezoelectric phononic crystal, band structure, plane wave expansion method, complete band gaps, vibration control.*

## 1. Introduction

Phononic crystals (PCs) are artificial periodic composites designed to exhibit phononic band gaps and they have been quite studied[1-14]. There are no mechanical (elastic or acoustic) propagating waves in phononic band gaps, only evanescent waves. These band gaps are created by the periodically mismatch between the constituent materials. This mismatch can be considered to arise either from difference of material properties or geometry (continuum-scale theory), or from interatomic force constants and masses (atomic-scale theory).

The ability of creating phononic band gaps is similar to the electronic and photonic band gaps in semiconductors and photonic crystals[15-16], respectively. The physical origin of phononic and photonic band gaps can be understood at micro-scale using the classical wave theory to describe the Bragg and Mie resonances, respectively, based on the scattering of mechanical and electromagnetic waves propagating within the crystal[17].

PCs have many applications, such as vibration isolation technology[18-22], acoustic barriers/filters[23-25], noise suppression devices[26-27], surface acoustic devices[28], architectural design[29], sound shields[30], acoustic diodes[31], elastic metamaterials[21-22,25,27,32] and thermal metamaterials[33-39].

There are also smart PCs that have been studied, such as piezoelectric[40-54], piezomagnetic[55-58] and magnetoelectroelastic[14,59-63] PCs. Among these intelligent PCs, piezoelectric PCs are sensitive to elastic and electric field. Even though the band structure behavior of piezoelectric PCs have been already investigated, to our knowledge only few studies[46-49,51] focused on the influence of inclusion geometry and lattice on band gap formation. Wang and co-workers[46] considered a piezoelectric PC with square lattice and different inclusion geometries (regular triangle, square, hexagon, circle and oval). They found that the largest complete band gap is obtained by selecting the inclusion with the same symmetry of lattice for the first band gap. Hsu *et al.*[47] studied the band structure of a piezoelectric PC with square and triangular lattices using Mindlin-Reissner plate theory and considering only circular inclusion. Qian and co-workers[48] studied the band structure of piezoelectric PCs with square lattice and circular and square inclusions. They revealed the existence of several very large complete band gaps in PZT rods reinforced polythene composite. Zhou *et al.*[49] investigated the band structure of piezoelectric PCs consisting of rectangular inclusion in an epoxy substrate. They considered a PC with square and triangular lattices. Wang and co-workers[51] considered a piezoelectric PC with circular inclusions and square and rectangular lattices. They verified that the largest band gap width is not always obtained for a square lattice. In some cases, rectangular lattice can produce broader gaps. In this context, we extend the studies about piezoelectric PCs[40-54] considering the influence of different inclusion geometries - circular, hollow circular, square and rotated square with 45º angle of rotation with respect to the *x* and *y* axes, and different lattices - square, rectangular, triangular, honeycomb and Kagomé on the band structure.

*e-mail: edson.jansen@ifma.edu.br

# APPENDIX E – Full Paper in Conference Proceedings

# COMPLETE BAND GAPS IN TWO-DIMENSIONAL MAGNETOELECTROELASTIC PHONONIC CRYSTALS

Miranda Júnior, E.J.P.[a,b] and Dos Santos, J.M.C.[a]

[a] *University of Campinas, UNICAMP-FEM-DMC-LVA, Mendeleyev Street, 200, 13083970, Campinas, SP, Brazil.*
[b] *Federal Institute of Education, Science and Technology of Maranhão, IFMA-CCH-NIB-DEP, Afonso Pena Street, 174, 65010030, São Luís, MA, Brazil.*
*E-mail of the corresponding author: edson.jansen@ifma.edu.br*

**ABSTRACT**
During the last decades many researches have been interested in the field of wave propagation in periodic composite systems known as phononic crystals. Phononic crystals are designed to have exotic behaviour and this concept has been first conceived for photonic crystals. They consist of a periodic array of scatterers embedded in a host medium. Due to its periodicity, mechanical waves are forbidden to propagate (band gaps) in some frequency ranges. We investigate the band structure of elastic waves propagating in a magnetoelectroelastic phononic crystal, consisting of a polymeric matrix reinforced by $BaTiO_3$-$CoFe_2O_4$ inclusions in a square, rectangular, triangular, honeycomb and Kagomé lattices. We also study the influence of inclusion geometry - circular, hollow circular, square and rotated square. The plane wave expansion method is used to solve the constitutive equations of a magnetoelectroelastic material considering wave propagation on the xy plane. The complete band gaps between the XY and Z modes are observed to all types of inclusion in all lattices. The best performance for square and rectangular lattices is found for rotated square inclusion. For triangular lattice, the circular, square and rotated square inclusios present, approximately, the same behaviour and the best performance for honeycomb and Kagomé lattices is found for circular and hollow circular inclusions, respectively. The best performance for the magnetoelectroelastic phononic crystal studied is for hollow circular inclusion in a triangular lattice with a band gap width of 20.55 kHz.

**KEYWORDS:** magnetoelectroelastic phononic crystal, complete band gaps, vibration control, plane wave expansion method.

## 1. INTRODUCTION

Recently, artificial periodic composites known as phononic crystals (PCs) have been quite studied [1, 2, 3, 4, 5, 6, 7, 8, 9]. They are composed by a periodic arrangement of two or more materials with different properties. The mismatch between the constituent materials may arise either from difference of material properties and/or geometry (density, elastic modulus, cross-sectional area) - continuum-scale theory, or of interatomic force constants and masses - atomic-scale theory.
PCs have received renewed attention because they exhibit band gaps where mechanical (elastic or acoustic) wave propagation is forbidden. The novel physical properties of the PCs arise from the possibility of creating band gaps and negative refraction (phonon branches with negative group velocity) [10]. The ability of creating phononic band gaps is similar to the creation of electronic and photonic band gaps in semiconductors and photonic crystals [11, 12], respectively.
The physical origin of phononic and photonic band gaps can be understood at micro-scale from the classical wave theory to describe the Bragg and Mie resonances, respectively, based on the scattering of mechanical and electromagnetic waves propagating within the crystal [13]. PCs have many applications, such as vibration isolation technology [14, 15, 16, 17, 18], acoustic barriers/filters [19, 20, 21], noise suppression devices [22, 23], surface acoustic devices [24], architectural design [25], sound shields [26], acoustic diodes [27], elastic/acoustic metamaterials [17, 18, 21, 23, 28], also known as locally resonant phononic crystals, and thermal metamaterials [29, 30], also known as phononic thermocrystals or locally resonant phononic thermocrystals.

There are also smart PCs that have been studied, for instance, piezoelectric [31, 32, 33, 34, 35, 36, 37, 38, 39, 40, 51, 52, 43, 44, 45] and piezomagnetic [46, 47, 48, 49]. However, few studies focused on magnetoelectroelastic phononic crystals (MPCs) [50, 51, 52, 53, 54].

The main purpose of this study is to investigate the elastic band structure, also known as dispersion diagram, of a MPC composed by $BaTiO_3$-$CoFe_2O_4$ inclusions in a polymeric matrix. It is considered wave propagation on the xy plane (longitudinal-transverse vibration, XY mode, and transverse vibration, Z mode) in an inhomogeneous transversely isotropic elastic solid. The MPC has two-dimensional periodicity and different inclusion geometries - circular, hollow circular, square and rotated square with a 45° angle of rotation with respect to the *x* and *y* axes in a square, rectangular, triangular, honeycomb and Kagomé lattices. The semi-analytical plane wave expansion [1, 2] (PWE) method is used to obtain the elastic band structure. Complete band gaps between XY and Z modes are observed to all types of inclusions in all lattices.

## 2. MAGNETOELECTROELASTIC PHONONIC CRYSTAL MODELLING

This section presents the PWE formulation for a MPC. PWE, also known as $\omega(\mathbf{k})$, is one of the most used methods to calculate the elastic band structure of PCs and it has been applied in MPCs [50, 51, 52]. In structural dynamics, PWE method can be comparable to the space-harmonics approach, when uniform beams and plates with periodic supports or stiffeners are usually considered [55, 56, 57].

We also consider a two-dimensional periodicity, *i.e.* 2D MPC, transversely isotropic elastic solid and wave propagation in the xy plane. Figure 1 (a-j) sketches the cross section of the $BaTiO_3$-$CoFe_2O_4$/polymer MPC taking into account square, rectangular, triangular, honeycomb and Kagomé lattices, respectively, with an arbitrary inclusion geometry. Figure 1 (f-j) represents the irreducible Brillouin zone [58] (IBZ), in shaded region, for the square, rectangular, triangular, honeycomb and Kagomé lattices, respectively.

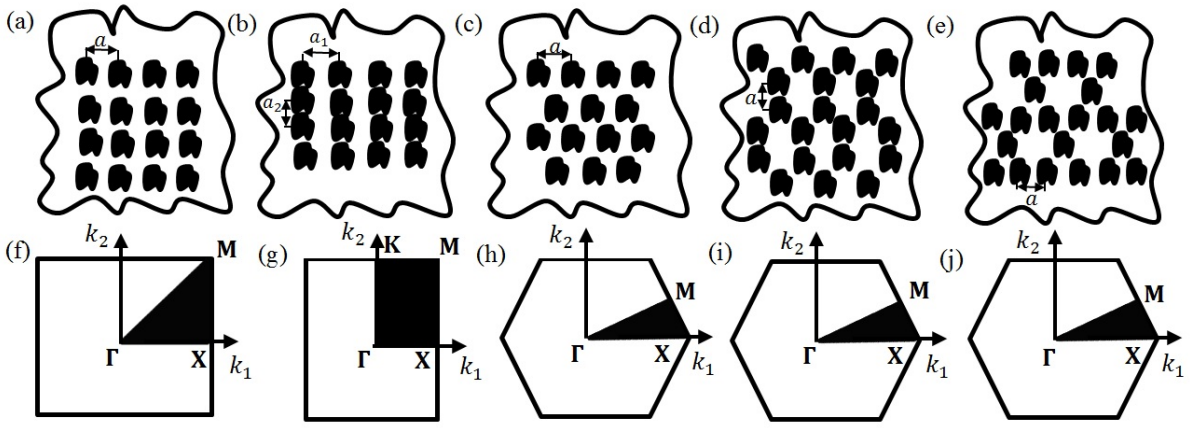


Figure 1 – Transverse cross section of the MPC: an array of $BaTiO_3$-$CoFe_2O_4$ inclusions periodically distributed in a polymeric matrix for (a) square, (b) rectangular, (c) triangular, (d) honeycomb and (e) Kagomé lattices. The irreducible Brillouin zone (IBZ), shaded region, for (f) square, (g) rectangular, (h) triangular, (i) honeycomb and (j) Kagomé lattices.

There are three variations of hexagonal lattice: triangular, honeycomb (or graphite) and Kagomé lattices [59]. We consider four types of inclusion: circular, hollow circular, square and rotated square with a 45° angle of rotation with respect to the *x*, *y* axes.

The IBZ points in Figure 1 (f-j) are $\mathbf{\Gamma}\ (0,0)$, $\mathbf{X}\ (\pi/a,0)$ and $\mathbf{M}\ (\pi/a,\pi/a)$ for square lattice, $\mathbf{\Gamma}\ (0,0)$, $\mathbf{X}\ (\pi/a_1,0)$, $\mathbf{M}\ (\pi/a_1,\pi/a_2)$ and $\mathbf{K}\ (0,\pi/a_2)$, with $a_1 > a_2$, for rectangular lattice, $\mathbf{\Gamma}\ (0,0)$, $\mathbf{X}\ (4\pi/3a,0)$ and $\mathbf{M}\ (\pi/a,\pi/\sqrt{3}a)$ for triangular lattice, $\mathbf{\Gamma}\ (0,0)$, $\mathbf{X}\ (4\pi/3\sqrt{3}a,0)$ and $\mathbf{M}\ (\pi/\sqrt{3}a,\pi/3a)$ for honeycomb lattice, and $\mathbf{\Gamma}\ (0,0)$, $\mathbf{X}\ (2\pi/3a,0)$ and $\mathbf{M}\ (\pi/2a,\pi/2\sqrt{3}a)$ for Kagomé lattice.

### 2.1. PWE Formulation

The constitutive equations of a magnetoelectroelastic material are [60]:

$$\sigma_{ij} = c_{ijkl}u_{k,l} - e_{lij}E_l - q_{lij}H_l, \tag{1}$$

$$D_i = e_{ikl}u_{k,l} + \varepsilon_{il}E_l + \lambda_{il}H_l, \tag{2}$$

$$B_i = q_{ikl}u_{k,l} + \lambda_{il}E_l + \Gamma_{il}H_l, \tag{3}$$

where $i,j,k,l = 1,2,3$, $\sigma_{ij}$ is the elastic stress tensor, $D_i$ is the electric displacement vector, $B_i$ is the magnetic induction vector, $u_i$ is the elastic displacement vector, $\phi$ is the electric potential, $\varphi$ is the magnetic potential, $e_{lij}$ is the piezoelectric tensor, $q_{lij}$ is the piezomagnetic tensor, $\varepsilon_{il}$ is the dielectric tensor, $\Gamma_{il}$ is the magnetic permeability tensor, $\lambda_{il}$ is the electromagnetic tensor and $c_{ijkl}$ is the elastic stiffness tensor. The standard tensor notation is used with Latin indices running from 1 to 3. They obey Einstein's summation convention when repeated.
We restrict the treatment to linear media, thus the elastic strain tensor $\varepsilon_{kl}$ is simplified:

$$\varepsilon_{kl} = \frac{1}{2}(u_{k,l} + u_{l,k}). \tag{4}$$

Besides, based on the quasi-static approximation, there are no electromagnetic sources and the curls are zero, thus the electric and magnetic fields are taken as gradients of scalar potentials and one can write Eqs. (5) and (6):

$$E_l = -\phi_{,l}, \tag{5}$$
$$H_l = -\varphi_{,l}, \tag{6}$$

where $E_l$ and $H_l$ are the electric and magnetic field vectors, respectively.
The differential equations of motion in the absence of body forces are given by:

$$\sigma_{ij,i} = \rho\ddot{u}_j, \tag{7}$$
$$D_{i,i} = 0, \tag{8}$$
$$B_{i,i} = 0, \tag{9}$$

where $\rho$ is the mass density and dot denotes differentiation with respect to time. Substituting Eqs. (1-3) in Eqs. (7-9), applying the simplifications of Eqs. (4-6), considering a transversely isotropic elastic solid, with a $z$ axis normal to the plane of isotropy, and a two-dimensional problem, $\partial/\partial x_3 = 0$, results:

$$\rho\ddot{u}_1 = (c_{11}u_{1,1} + c_{12}u_{2,2})_{,1} + [c_{66}(u_{1,2} + u_{2,1})]_{,2}, \tag{10}$$
$$\rho\ddot{u}_2 = (c_{12}u_{1,1} + c_{11}u_{2,2})_{,2} + [c_{66}(u_{1,2} + u_{2,1})]_{,1}, \tag{11}$$
$$\rho\ddot{u}_3 = (c_{44}u_{3,1} + e_{15}\phi_{,1} + q_{15}\varphi_{,1})_{,1} + (c_{44}u_{3,2} + e_{15}\phi_{,2} + q_{15}\varphi_{,2})_{,2}, \tag{12}$$
$$0\ddot{\phi} = (e_{15}u_{3,1} - \varepsilon_{11}\phi_{,1} - \lambda_{11}\varphi_{,1})_{,1} + (e_{15}u_{3,2} - \varepsilon_{11}\phi_{,2} - \lambda_{11}\varphi_{,2})_{,2}, \tag{13}$$
$$0\ddot{\varphi} = (q_{15}u_{3,1} - \lambda_{11}\phi_{,1} - \Gamma_{11}\varphi_{,1})_{,1} + (q_{15}u_{3,2} - \lambda_{11}\phi_{,2} - \Gamma_{11}\varphi_{,2})_{,2}, \tag{14}$$

where $c_{66} = \frac{1}{2}(c_{11} - c_{12})$.
We apply the temporal Fourier transform to Eqs. (10-14) and omitting frequency dependence, gives:

$$-\omega^2\rho u_1 = (c_{11}u_{1,1} + c_{12}u_{2,2})_{,1} + [c_{66}(u_{1,2} + u_{2,1})]_{,2}, \tag{15}$$
$$-\omega^2\rho u_2 = (c_{12}u_{1,1} + c_{11}u_{2,2})_{,2} + [c_{66}(u_{1,2} + u_{2,1})]_{,1}, \tag{16}$$
$$-\omega^2\rho u_3 = (c_{44}u_{3,1} + e_{15}\phi_{,1} + q_{15}\varphi_{,1})_{,1} + (c_{44}u_{3,2} + e_{15}\phi_{,2} + q_{15}\varphi_{,2})_{,2}, \tag{17}$$
$$-\omega^2 0\phi = (e_{15}u_{3,1} - \varepsilon_{11}\phi_{,1} - \lambda_{11}\varphi_{,1})_{,1} + (e_{15}u_{3,2} - \varepsilon_{11}\phi_{,2} - \lambda_{11}\varphi_{,2})_{,2}, \tag{18}$$
$$-\omega^2 0\varphi = (q_{15}u_{3,1} - \lambda_{11}\phi_{,1} - \Gamma_{11}\varphi_{,1})_{,1} + (q_{15}u_{3,2} - \lambda_{11}\phi_{,2} - \Gamma_{11}\varphi_{,2})_{,2}, \tag{19}$$

where $\omega$ is the angular frequency.
In order to consider a MPC, one can note that $c_{11} = c_{11}(\mathbf{r})$, $c_{12} = c_{12}(\mathbf{r})$, $c_{66} = c_{66}(\mathbf{r})$, $c_{44} = c_{44}(\mathbf{r})$, $e_{15} = e_{15}(\mathbf{r})$, $q_{15} = q_{15}(\mathbf{r})$, $\varepsilon_{11} = \varepsilon_{11}(\mathbf{r})$, $\lambda_{11} = \lambda_{11}(\mathbf{r})$, $\Gamma_{11} = \Gamma_{11}(\mathbf{r})$, $\rho = \rho(\mathbf{r})$, $u_i = u_i(\mathbf{r},t)$, $\phi = \phi(\mathbf{r},t)$ and $\varphi = \varphi(\mathbf{r},t)$, because we consider two different materials - $BaTiO_3$-$CoFe_2O_4$ (inclusion) and a polymer (matrix). For two-dimensional periodicity (the system has translational symmetry in $z$ direction and the material parameters depend only on the $x$ and $y$ coordinates), thus $\mathbf{r} = x\mathbf{e}_1 + y\mathbf{e}_2$ $(x,y \in \mathbb{R})$ is the two-dimensional spatial vector and $\mathbf{e}_i$ $(i = 1,2)$ are the basis vectors in the real space. Besides, each one of the parameters $c_{11}(\mathbf{r})$, $c_{12}(\mathbf{r})$, $c_{66}(\mathbf{r})$, $c_{44}(\mathbf{r})$, $e_{15}(\mathbf{r})$, $q_{15}(\mathbf{r})$, $\varepsilon_{11}(\mathbf{r})$, $\lambda_{11}(\mathbf{r})$, $\Gamma_{11}(\mathbf{r})$, $\rho(\mathbf{r})$ is represented in Eq. (20) by $P(\mathbf{r})$ and has a position dependence expressed by [63]:

$$P(\mathbf{r}) = P_B + \sum_{j=1}^{N_C}\sum_{\bar{\mathbf{r}}=-\infty}^{+\infty}(P_A - P_B)H(\alpha_j - ||\mathbf{r} - \bar{\mathbf{u}}_j - \bar{\mathbf{r}}||), \tag{20}$$

where $\bar{\mathbf{r}} = p\mathbf{a}_1 + q\mathbf{a}_2$ $(p,q \in \mathbb{Z})$ is the lattice vector, $\mathbf{a}_i$ $(i = 1,2)$ are its vectorial components (also known as primitive vectors), $\bar{\mathbf{u}}_j$ is the position vector of the $j$-th inclusion, the indexes $A$ and $B$ are related to the inclusion ($BaTiO_3$-$CoFe_2O_4$) and matrix (polymer), respectively, $N_C$ is the number of inclusions into the unit cell, $H(x)$ is the Heaviside function defined as $H(x) = 1$, if $x \geq 0$ and $H(x) = 0$, if $x < 0$ and $\alpha_j$ is a parameter associated with

the $j$-th inclusion. This parameter can be the inclusion radius, $\tilde{r}$ (for circular cross section), the inclusion width, $2l$ (for square and rotated square cross sections) and the inclusion radius thickness, $\tilde{R}-\tilde{r}$ (for hollow circular cross section), with $\tilde{R}>\tilde{r}$. Note that the hollow circular inclusion has a internal radius, $\tilde{r}$, of polymer and a thickness, $\tilde{R}-\tilde{r}$, of $BaTiO_3$-$CoFe_2O_4$.

The primitive vectors are given by square lattice $\mathbf{a}_i = a\mathbf{e}_i$ $(i=1,2)$, rectangular, $\mathbf{a}_1 = a_1\mathbf{e}_1$, $\mathbf{a}_2 = a_2\mathbf{e}_2$, triangular lattice, $\mathbf{a}_1 = a\mathbf{e}_1$, $\mathbf{a}_2 = \frac{a}{2}\mathbf{e}_1 + \frac{a\sqrt{3}}{2}\mathbf{e}_2$, honeycomb lattice, $\mathbf{a}_1 = \frac{a\sqrt{3}}{2}\mathbf{e}_1 + \frac{3a}{2}\mathbf{e}_2$, $\mathbf{a}_2 = -\frac{a\sqrt{3}}{2}\mathbf{e}_1 + \frac{3a}{2}\mathbf{e}_2$ and Kagomé lattice, $\mathbf{a}_1 = a\mathbf{e}_1 + a\sqrt{3}\mathbf{e}_2$, $\mathbf{a}_2 = -a\mathbf{e}_1 + a\sqrt{3}\mathbf{e}_2$. The lattice parameter for square, triangular, honeycomb and Kagomé lattices is denoted by $a$ whereas $a_1$ and $a_2$ are the lattice parameters for rectangular lattice. It is important to highlight that the square, rectangular and triangular lattices have one inclusion into the unit cell $(N_C = 1)$, whereas honeycomb and Kagomé have two $(N_C = 2)$ and three $(N_C = 3)$ inclusions, respectively.

Due to the system periodicity, one can invoke the Floquet-Bloch's theorem [61, 62]:

$$T(\mathbf{r}) = e^{i\mathbf{k}\cdot\mathbf{r}} T_{\mathbf{k}}(\mathbf{r}), \tag{21}$$

where $T(\mathbf{r})$ can be $u_i(\mathbf{r})$, $\phi(\mathbf{r})$ or $\varphi(\mathbf{r})$, $T_{\mathbf{k}}(\mathbf{r})$ is the Bloch wave amplitude, it can be $u_{i_{\mathbf{k}}}(\mathbf{r})$, $\phi_{\mathbf{k}}(\mathbf{r})$ or $\varphi_{\mathbf{k}}(\mathbf{r})$, and $\mathbf{k} = k_1\mathbf{e}_1 + k_2\mathbf{e}_2$ is the Bloch wave vector, also known as wavenumber, and it is restricted to the IBZ, where $(k_1, k_2 \in \mathbb{R})$ are the points coordinates within the IBZ in Figure 1 (f-j) for the reciprocal space. Note that $T_{\mathbf{k}}(\mathbf{r}) = T_{\mathbf{k}}(\mathbf{r}+\bar{\mathbf{r}})$, $T(\mathbf{r}+\bar{\mathbf{r}}) = T(\mathbf{r})e^{i\mathbf{k}\cdot\bar{\mathbf{r}}}$, where the exponential $e^{i\mathbf{k}\cdot\bar{\mathbf{r}}}$ is called Bloch periodic boundary condition.

Expanding $u_{i_{\mathbf{k}}}(\mathbf{r})$, $\phi_{\mathbf{k}}(\mathbf{r})$ or $\varphi_{\mathbf{k}}(\mathbf{r})$ as Fourier series on the reciprocal space and considering wave propagation in the $xy$ plane $(k_3 = 0)$, we can rewrite Eq. (21):

$$T(\mathbf{r}) = e^{i\mathbf{k}\cdot\mathbf{r}} \sum_{\mathbf{g}=-\infty}^{+\infty} T_{\mathbf{k}}(\mathbf{g}) e^{i\mathbf{g}\cdot\mathbf{r}} = \sum_{\mathbf{g}=-\infty}^{+\infty} T_{\mathbf{k}}(\mathbf{g}) e^{i(\mathbf{k}+\mathbf{g})\cdot\mathbf{r}}, \tag{22}$$

where $\mathbf{g}$ is the reciprocal lattice vector and it is calculated for square lattice, $\mathbf{g} = \frac{2\pi}{a}(m\mathbf{e}_1 + n\mathbf{e}_2)$, for rectangular lattice, $\mathbf{g} = 2\pi(\frac{m}{a_1}\mathbf{e}_1 + \frac{n}{a_2}\mathbf{e}_2)$, for triangular lattice, $\mathbf{g} = \frac{2\pi}{a}[m\mathbf{e}_1 + \frac{(-m+2n)}{\sqrt{3}}\mathbf{e}_2]$, for honeycomb lattice, $\mathbf{g} = \frac{2\pi}{a\sqrt{3}}[(m-n)\mathbf{e}_1 + \frac{(m+n)}{\sqrt{3}}\mathbf{e}_2]$, and for Kagomé lattice, $\mathbf{g} = \frac{\pi}{a}[(m-n)\mathbf{e}_1 + \frac{(m+n)}{\sqrt{3}}\mathbf{e}_2]$, with $m, n \in \mathbb{Z}$.

We can also expand the materials properties in Fourier series in the reciprocal space as:

$$P(\mathbf{r}) = \sum_{\bar{\mathbf{g}}=-\infty}^{+\infty} P(\bar{\mathbf{g}}) e^{i\bar{\mathbf{g}}\cdot\mathbf{r}}, \tag{23}$$

where $\bar{\mathbf{g}}$ has the same expressions of $\mathbf{g}$ for each lattice, with $\bar{m}, \bar{n} \in \mathbb{Z}$. We use $\bar{\mathbf{g}}$ instead of using $\mathbf{g}$ to highlight the difference between the Fourier series expansions of material properties and the displacements and potentials.

The Fourier series coefficients, $P(\bar{\mathbf{g}})$, are defined as:

$$P(\bar{\mathbf{g}}) = \frac{1}{S_C} \int\int P(\mathbf{r}) e^{-i\bar{\mathbf{g}}\cdot\mathbf{r}} d^2r, \tag{24}$$

where $S_C = ||\mathbf{a}_1 \times \mathbf{a}_2||$ is the cross section area of the unit cell.

Substituting Eq. (20) in Eq. (24) and calculating the integral, we can rewrite Eq. (24) as:

$$P(\bar{\mathbf{g}}) = \bar{P}\delta_{\bar{\mathbf{g}}\mathbf{0}} + (P_A - P_B)(1 - \delta_{\bar{\mathbf{g}}\mathbf{0}}) \sum_{j=1}^{N_C} F(\bar{\mathbf{g}}) e^{-i\bar{\mathbf{g}}\cdot\bar{\mathbf{u}}_j}, \tag{25}$$

where $\delta_{\bar{\mathbf{g}}\mathbf{0}}$ is the Kronecker delta, it is defined as $\delta_{\bar{\mathbf{g}}\mathbf{0}} = 1$ if $\bar{\mathbf{g}} = \mathbf{0}$ and $\delta_{\bar{\mathbf{g}}\mathbf{0}} = 0$ if $\bar{\mathbf{g}} \neq \mathbf{0}$, $\bar{P} = \bar{f}P_A + (1-\bar{f})P_B$, $\bar{f} = \frac{S_A}{S_C}$ is the filling fraction, $S_A$ is the cross section area of the inclusion and $F(\bar{\mathbf{g}})$ is the structure function associated with each geometry (circular, hollow circular, square and rotated square), and it is defined as:

$$F(\bar{\mathbf{g}}) = \frac{1}{S_C} \int\int e^{-i\bar{\mathbf{g}}\cdot\mathbf{r}} d^2r. \tag{26}$$

The structure function, $F(\bar{\mathbf{g}})$, calculated by Eq. (26) for circular, hollow circular, square and square circular inclu-

sions are:

$$F(\bar{\mathbf{g}}) = 2\bar{f}\,\frac{J_1(\bar{g}\tilde{r})}{\bar{g}\tilde{r}}, \tag{27a}$$

$$F(\bar{\mathbf{g}}) = \bar{f}\,\frac{\sin(\bar{g}_1\tilde{r})}{\bar{g}_1\tilde{r}}\frac{\sin(\bar{g}_2\tilde{r})}{\bar{g}_2\tilde{r}}, \tag{27b}$$

$$F(\bar{\mathbf{g}}) = \bar{f}\,\frac{\sin[(l/\sqrt{2})(\bar{g}_1+\bar{g}_2)]}{(l/\sqrt{2})(\bar{g}_1+\bar{g}_2)}\frac{\sin[(l/\sqrt{2})(-\bar{g}_1+\bar{g}_2)]}{(l/\sqrt{2})(-\bar{g}_1+\bar{g}_2)}, \tag{27c}$$

$$F(\bar{\mathbf{g}}) = 2\bar{f}\,\frac{[J_1(\bar{g}\tilde{R}) - (\tilde{r}/\tilde{R})J_1(\bar{g}\tilde{R})]}{\bar{g}\tilde{R}}, \tag{27d}$$

respectively, where $\bar{g} = ||\bar{\mathbf{g}}||$, $\bar{g}_{1,2} = ||\bar{\mathbf{g}}_{1,2}||$.
The Fourier series coefficients, Eq. (25), can be rewritten for a square, rectangular and triangular lattices ($N_C = 1$) with the inclusion localized at $\bar{\mathbf{u}}_1 = \mathbf{0}$:

$$P(\bar{\mathbf{g}}) = \bar{P}\delta_{\bar{\mathbf{g}}\mathbf{0}} + (P_A - P_B)(1 - \delta_{\bar{\mathbf{g}}\mathbf{0}})F(\bar{\mathbf{g}}). \tag{28}$$

For honeycomb lattice ($N_C = 2$), we can rewrite Eq. (25) as:

$$P(\bar{\mathbf{g}}) = \bar{P}\delta_{\bar{\mathbf{g}}\mathbf{0}} + (P_A - P_B)(1 - \delta_{\bar{\mathbf{g}}\mathbf{0}})2\cos(\bar{\mathbf{g}}\cdot\bar{\mathbf{u}}_1)F(\bar{\mathbf{g}}), \tag{29}$$

where $\bar{\mathbf{u}}_1 = -\bar{\mathbf{u}}_2 = \frac{a}{2}\mathbf{e}_2$. We chose these vectors similar to Gao *et al.* [64].
For Kagomé lattice ($N_C = 3$), we can rewrite Eq. (25) as:

$$P(\bar{\mathbf{g}}) = \bar{P}\delta_{\bar{\mathbf{g}}\mathbf{0}} + (P_A - P_B)(1 - \delta_{\bar{\mathbf{g}}\mathbf{0}})\sum_{j=1}^{3} F(\bar{\mathbf{g}})e^{-i\bar{\mathbf{g}}\cdot\bar{\mathbf{u}}_j}, \tag{30}$$

where $\bar{\mathbf{u}}_1 = -\frac{a}{2}\mathbf{e}_1 - \frac{\sqrt{3}a}{6}\mathbf{e}_2$, $\bar{\mathbf{u}}_2 = \frac{a}{2}\mathbf{e}_1 - \frac{\sqrt{3}a}{6}\mathbf{e}_2$ and $\bar{\mathbf{u}}_3 = \frac{\sqrt{3}a}{3}\mathbf{e}_1$.
The expression $\sum_{j=1}^{3} F(\bar{\mathbf{g}})e^{-i\bar{\mathbf{g}}\cdot\bar{\mathbf{u}}_j}$ can be split in its real and imaginary components as:

$$\sum_{j=1}^{3} F(\bar{\mathbf{g}})e^{-i\bar{\mathbf{g}}\cdot\bar{\mathbf{u}}_j} = \Re[\sum_{j=1}^{3} F(\bar{\mathbf{g}})e^{-i\bar{\mathbf{g}}\cdot\bar{\mathbf{u}}_j}] + i\Im[\sum_{j=1}^{3} F(\bar{\mathbf{g}})e^{-i\bar{\mathbf{g}}\cdot\bar{\mathbf{u}}_j}], \tag{31}$$

where the real and imaginary components are:

$$\Re[\sum_{j=1}^{3} F(\bar{\mathbf{g}})e^{-i\bar{\mathbf{g}}\cdot\bar{\mathbf{u}}_j}] = [2\cos(\bar{g}_1\bar{u}_{1_1})\cos(\bar{g}_2\bar{u}_{1_2}) + \cos(2\bar{g}_2\bar{u}_{1_2})]F(\bar{\mathbf{g}}), \tag{32}$$

$$\Im[\sum_{j=1}^{3} F(\bar{\mathbf{g}})e^{-i\bar{\mathbf{g}}\cdot\bar{\mathbf{u}}_j}] = [-2\cos(\bar{g}_1\bar{u}_{1_1})\sin(\bar{g}_2\bar{u}_{1_2}) + \sin(2\bar{g}_2\bar{u}_{1_2})]F(\bar{\mathbf{g}}). \tag{33}$$

where $\bar{u}_{j_{1,2}} = ||\bar{\mathbf{u}}_{j_{1,2}}||$, with $j = 1, 2$.
Substituting Eqs. (22-23) in Eqs. (15-19), with $\tilde{\mathbf{g}} = \bar{\mathbf{g}} + \mathbf{g}$, we may write:

$$\sum_{\mathbf{g}=-\infty}^{+\infty}\sum_{\tilde{\mathbf{g}}=-\infty}^{+\infty}\{-\omega^2\rho(\tilde{\mathbf{g}}-\mathbf{g})u_{1_\mathbf{k}}(\mathbf{g}) + c_{11}(\tilde{\mathbf{g}}-\mathbf{g})u_{1_\mathbf{k}}(\mathbf{g})(k+g)_1(k+\tilde{g})_1 + c_{12}(\tilde{\mathbf{g}}-\mathbf{g})u_{2_\mathbf{k}}(\mathbf{g})(k+g)_2(k+\tilde{g})_1$$
$$+c_{66}(\tilde{\mathbf{g}}-\mathbf{g})[u_{1_\mathbf{k}}(\mathbf{g})(k+g)_2 + u_{2_\mathbf{k}}(\mathbf{g})(k+g)_1](k+\tilde{g})_2\}e^{i(\mathbf{k}+\tilde{\mathbf{g}})\cdot\mathbf{r}} = 0, \tag{34}$$

$$\sum_{\mathbf{g}=-\infty}^{+\infty}\sum_{\tilde{\mathbf{g}}=-\infty}^{+\infty}\{-\omega^2\rho(\tilde{\mathbf{g}}-\mathbf{g})u_{2_\mathbf{k}}(\mathbf{g}) + c_{12}(\tilde{\mathbf{g}}-\mathbf{g})u_{1_\mathbf{k}}(\mathbf{g})(k+g)_1(k+\tilde{g})_2 + c_{11}(\tilde{\mathbf{g}}-\mathbf{g})u_{2_\mathbf{k}}(\mathbf{g})(k+g)_2(k+\tilde{g})_2$$
$$+c_{66}(\tilde{\mathbf{g}}-\mathbf{g})[u_{1_\mathbf{k}}(\mathbf{g})(k+g)_2 + u_{2_\mathbf{k}}(\mathbf{g})(k+g)_1](k+\tilde{g})_1\}e^{i(\mathbf{k}+\tilde{\mathbf{g}})\cdot\mathbf{r}} = 0, \tag{35}$$

$$\sum_{\mathbf{g}=-\infty}^{+\infty}\sum_{\tilde{\mathbf{g}}=-\infty}^{+\infty}\{-\omega^2\rho(\tilde{\mathbf{g}}-\mathbf{g})u_{3_\mathbf{k}}(\mathbf{g}) + c_{44}(\tilde{\mathbf{g}}-\mathbf{g})u_{3_\mathbf{k}}(\mathbf{g})(k+g)_1(k+\tilde{g})_1 + e_{15}(\tilde{\mathbf{g}}-\mathbf{g})\phi_\mathbf{k}(\mathbf{g})(k+g)_1(k+\tilde{g})_1$$
$$+q_{15}(\tilde{\mathbf{g}}-\mathbf{g})\varphi_\mathbf{k}(\mathbf{g})(k+g)_1(k+\tilde{g})_1 + c_{44}(\tilde{\mathbf{g}}-\mathbf{g})u_{3_\mathbf{k}}(\mathbf{g})(k+g)_2(k+\tilde{g})_2 + e_{15}(\tilde{\mathbf{g}}-\mathbf{g})\phi_\mathbf{k}(\mathbf{g})(k+g)_2(k+\tilde{g})_2$$
$$+q_{15}(\tilde{\mathbf{g}}-\mathbf{g})\varphi_\mathbf{k}(\mathbf{g})(k+g)_2(k+\tilde{g})_2\}e^{i(\mathbf{k}+\tilde{\mathbf{g}})\cdot\mathbf{r}} = 0, \tag{36}$$

$$\sum_{\mathbf{g}=-\infty}^{+\infty}\sum_{\tilde{\mathbf{g}}=-\infty}^{+\infty}\{-\omega^2 0\phi_{\mathbf{k}}(\mathbf{g})+e_{15}(\tilde{\mathbf{g}}-\mathbf{g})u_{3_{\mathbf{k}}}(\mathbf{g})(k+g)_1(k+\tilde{g})_1-\varepsilon_{11}(\tilde{\mathbf{g}}-\mathbf{g})\phi_{\mathbf{k}}(\mathbf{g})(k+g)_1(k+\tilde{g})_1$$
$$-\lambda_{11}(\tilde{\mathbf{g}}-\mathbf{g})\varphi_{\mathbf{k}}(\mathbf{g})(k+g)_1(k+\tilde{g})_1+e_{15}(\tilde{\mathbf{g}}-\mathbf{g})u_{3_{\mathbf{k}}}(\mathbf{g})(k+g)_2(k+\tilde{g})_2-\varepsilon_{11}(\tilde{\mathbf{g}}-\mathbf{g})\phi_{\mathbf{k}}(\mathbf{g})(k+g)_2(k+\tilde{g})_2$$
$$-\lambda_{11}(\tilde{\mathbf{g}}-\mathbf{g})\varphi_{\mathbf{k}}(\mathbf{g})(k+g)_2(k+\tilde{g})_2\}e^{i(\mathbf{k}+\tilde{\mathbf{g}})\cdot\mathbf{r}}=0, \tag{37}$$

$$\sum_{\mathbf{g}=-\infty}^{+\infty}\sum_{\tilde{\mathbf{g}}=-\infty}^{+\infty}\{-\omega^2 0\varphi_{\mathbf{k}}(\mathbf{g})+q_{15}(\tilde{\mathbf{g}}-\mathbf{g})u_{3_{\mathbf{k}}}(\mathbf{g})(k+g)_1(k+\tilde{g})_1-\lambda_{11}(\tilde{\mathbf{g}}-\mathbf{g})\phi_{\mathbf{k}}(\mathbf{g})(k+g)_1(k+\tilde{g})_1$$
$$-\Gamma_{11}(\tilde{\mathbf{g}}-\mathbf{g})\varphi_{\mathbf{k}}(\mathbf{g})(k+g)_1(k+\tilde{g})_1+q_{15}(\tilde{\mathbf{g}}-\mathbf{g})u_{3_{\mathbf{k}}}(\mathbf{g})(k+g)_2(k+\tilde{g})_2-\lambda_{11}(\tilde{\mathbf{g}}-\mathbf{g})\phi_{\mathbf{k}}(\mathbf{g})(k+g)_2(k+\tilde{g})_2$$
$$-\Gamma_{11}(\tilde{\mathbf{g}}-\mathbf{g})\varphi_{\mathbf{k}}(\mathbf{g})(k+g)_2(k+\tilde{g})_2\}e^{i(\mathbf{k}+\tilde{\mathbf{g}})\cdot\mathbf{r}}=0. \tag{38}$$

Multiplying Eqs. (34-38) by $e^{-i\bar{\mathbf{g}}\cdot\mathbf{r}}$ and integrating over the unit cell, gives:

$$\sum_{\mathbf{g}=-\infty}^{+\infty}\{-\omega^2\rho(\bar{\mathbf{g}}-\mathbf{g})u_{1_{\mathbf{k}}}(\mathbf{g})+c_{11}(\bar{\mathbf{g}}-\mathbf{g})u_{1_{\mathbf{k}}}(\mathbf{g})(k+g)_1(k+\bar{g})_1+c_{12}(\bar{\mathbf{g}}-\mathbf{g})u_{2_{\mathbf{k}}}(\mathbf{g})(k+g)_2(k+\bar{g})_1$$
$$+c_{66}(\bar{\mathbf{g}}-\mathbf{g})[u_{1_{\mathbf{k}}}(\mathbf{g})(k+g)_2+u_{2_{\mathbf{k}}}(\mathbf{g})(k+g)_1](k+\bar{g})_2\}=0, \tag{39}$$

$$\sum_{\mathbf{g}=-\infty}^{+\infty}\{-\omega^2\rho(\bar{\mathbf{g}}-\mathbf{g})u_{2_{\mathbf{k}}}(\mathbf{g})+c_{12}(\bar{\mathbf{g}}-\mathbf{g})u_{1_{\mathbf{k}}}(\mathbf{g})(k+g)_1(k+\bar{g})_2+c_{11}(\bar{\mathbf{g}}-\mathbf{g})u_{2_{\mathbf{k}}}(\mathbf{g})(k+g)_2(k+\bar{g})_2$$
$$+c_{66}(\bar{\mathbf{g}}-\mathbf{g})[u_{1_{\mathbf{k}}}(\mathbf{g})(k+g)_2+u_{2_{\mathbf{k}}}(\mathbf{g})(k+g)_1](k+\bar{g})_1\}=0, \tag{40}$$

$$\sum_{\mathbf{g}=-\infty}^{+\infty}\{-\omega^2\rho(\bar{\mathbf{g}}-\mathbf{g})u_{3_{\mathbf{k}}}(\mathbf{g})+c_{44}(\bar{\mathbf{g}}-\mathbf{g})u_{3_{\mathbf{k}}}(\mathbf{g})(k+g)_1(k+\bar{g})_1+e_{15}(\bar{\mathbf{g}}-\mathbf{g})\phi_{\mathbf{k}}(\mathbf{g})(k+g)_1(k+\bar{g})_1$$
$$+q_{15}(\bar{\mathbf{g}}-\mathbf{g})\varphi_{\mathbf{k}}(\mathbf{g})(k+g)_1(k+\bar{g})_1+c_{44}(\bar{\mathbf{g}}-\mathbf{g})u_{3_{\mathbf{k}}}(\mathbf{g})(k+g)_2(k+\bar{g})_2+e_{15}(\bar{\mathbf{g}}-\mathbf{g})\phi_{\mathbf{k}}(\mathbf{g})(k+g)_2(k+\bar{g})_2$$
$$+q_{15}(\bar{\mathbf{g}}-\mathbf{g})\varphi_{\mathbf{k}}(\mathbf{g})(k+g)_2(k+\bar{g})_2\}=0, \tag{41}$$

$$\sum_{\mathbf{g}=-\infty}^{+\infty}\{-\omega^2 0\phi_{\mathbf{k}}(\mathbf{g})+e_{15}(\bar{\mathbf{g}}-\mathbf{g})u_{3_{\mathbf{k}}}(\mathbf{g})(k+g)_1(k+\bar{g})_1-\varepsilon_{11}(\bar{\mathbf{g}}-\mathbf{g})\phi_{\mathbf{k}}(\mathbf{g})(k+g)_1(k+\bar{g})_1$$
$$-\lambda_{11}(\bar{\mathbf{g}}-\mathbf{g})\varphi_{\mathbf{k}}(\mathbf{g})(k+g)_1(k+\bar{g})_1+e_{15}(\bar{\mathbf{g}}-\mathbf{g})u_{3_{\mathbf{k}}}(\mathbf{g})(k+g)_2(k+\bar{g})_2-\varepsilon_{11}(\bar{\mathbf{g}}-\mathbf{g})\phi_{\mathbf{k}}(\mathbf{g})(k+g)_2(k+\bar{g})_2$$
$$-\lambda_{11}(\bar{\mathbf{g}}-\mathbf{g})\varphi_{\mathbf{k}}(\mathbf{g})(k+g)_2(k+\bar{g})_2\}=0, \tag{42}$$

$$\sum_{\mathbf{g}=-\infty}^{+\infty}\{-\omega^2 0\varphi_{\mathbf{k}}(\mathbf{g})+q_{15}(\bar{\mathbf{g}}-\mathbf{g})u_{3_{\mathbf{k}}}(\mathbf{g})(k+g)_1(k+\bar{g})_1-\lambda_{11}(\bar{\mathbf{g}}-\mathbf{g})\phi_{\mathbf{k}}(\mathbf{g})(k+g)_1(k+\bar{g})_1$$
$$-\Gamma_{11}(\bar{\mathbf{g}}-\mathbf{g})\varphi_{\mathbf{k}}(\mathbf{g})(k+g)_1(k+\bar{g})_1+q_{15}(\bar{\mathbf{g}}-\mathbf{g})u_{3_{\mathbf{k}}}(\mathbf{g})(k+g)_2(k+\bar{g})_2-\lambda_{11}(\bar{\mathbf{g}}-\mathbf{g})\phi_{\mathbf{k}}(\mathbf{g})(k+g)_2(k+\bar{g})_2$$
$$-\Gamma_{11}(\bar{\mathbf{g}}-\mathbf{g})\varphi_{\mathbf{k}}(\mathbf{g})(k+g)_2(k+\bar{g})_2\}=0. \tag{43}$$

Eqs. (39-43) are an infinite system of equations, thus the Fourier series needs to be truncated. Choosing $m=\bar{m}=n=\bar{n}=[-M,\ldots,M]$, the total number of plane waves is $(2M+1)^2$. Therefore, Eqs. (39-43) can be expressed in a matrix form as:

$$(\mathbf{K}-\omega^2\mathbf{M})\mathbf{q}=\mathbf{0}, \tag{44}$$

where

$$\mathbf{K}=\begin{bmatrix}\mathbf{K}_{11} & \mathbf{K}_{12} & \mathbf{0} & \mathbf{0} & \mathbf{0}\\ \mathbf{K}_{21} & \mathbf{K}_{22} & \mathbf{0} & \mathbf{0} & \mathbf{0}\\ \mathbf{0} & \mathbf{0} & \mathbf{K}_{33} & \mathbf{K}_{34} & \mathbf{K}_{35}\\ \mathbf{0} & \mathbf{0} & \mathbf{K}_{43} & \mathbf{K}_{44} & \mathbf{K}_{45}\\ \mathbf{0} & \mathbf{0} & \mathbf{K}_{53} & \mathbf{K}_{54} & \mathbf{K}_{55}\end{bmatrix}. \tag{45}$$

The sub-matrices in Eq. (45) are given by:

$$\mathbf{K}_{11} = \mathbf{C}_{11}(\bar{\mathbf{g}}-\mathbf{g}) \circ (\bar{\mathbf{K}}+\mathbf{G})_1 \circ (\bar{\mathbf{K}}+\bar{\mathbf{G}})_1 + \mathbf{C}_{66}(\bar{\mathbf{g}}-\mathbf{g}) \circ (\bar{\mathbf{K}}+\mathbf{G})_2 \circ (\bar{\mathbf{K}}+\bar{\mathbf{G}})_2, \tag{46}$$

$$\mathbf{K}_{12} = \mathbf{C}_{12}(\bar{\mathbf{g}}-\mathbf{g}) \circ (\bar{\mathbf{K}}+\mathbf{G})_2 \circ (\bar{\mathbf{K}}+\bar{\mathbf{G}})_1 + \mathbf{C}_{66}(\bar{\mathbf{g}}-\mathbf{g}) \circ (\bar{\mathbf{K}}+\mathbf{G})_1 \circ (\bar{\mathbf{K}}+\bar{\mathbf{G}})_2, \tag{47}$$

$$\mathbf{K}_{21} = \mathbf{C}_{12}(\bar{\mathbf{g}}-\mathbf{g}) \circ (\bar{\mathbf{K}}+\mathbf{G})_1 \circ (\bar{\mathbf{K}}+\bar{\mathbf{G}})_2 + \mathbf{C}_{66}(\bar{\mathbf{g}}-\mathbf{g}) \circ (\bar{\mathbf{K}}+\mathbf{G})_2 \circ (\bar{\mathbf{K}}+\bar{\mathbf{G}})_1, \tag{48}$$

$$\mathbf{K}_{22} = \mathbf{C}_{11}(\bar{\mathbf{g}}-\mathbf{g}) \circ (\bar{\mathbf{K}}+\mathbf{G})_2 \circ (\bar{\mathbf{K}}+\bar{\mathbf{G}})_2 + \mathbf{C}_{66}(\bar{\mathbf{g}}-\mathbf{g}) \circ (\bar{\mathbf{K}}+\mathbf{G})_1 \circ (\bar{\mathbf{K}}+\bar{\mathbf{G}})_1, \tag{49}$$

$$\mathbf{K}_{33} = \mathbf{C}_{44}(\bar{\mathbf{g}}-\mathbf{g}) \circ (\bar{\mathbf{K}}+\mathbf{G})_1 \circ (\bar{\mathbf{K}}+\bar{\mathbf{G}})_1 + \mathbf{C}_{44}(\bar{\mathbf{g}}-\mathbf{g}) \circ (\bar{\mathbf{K}}+\mathbf{G})_2 \circ (\bar{\mathbf{K}}+\bar{\mathbf{G}})_2, \tag{50}$$

$$\mathbf{K}_{34} = \mathbf{E}_{15}(\bar{\mathbf{g}}-\mathbf{g}) \circ (\bar{\mathbf{K}}+\mathbf{G})_1 \circ (\bar{\mathbf{K}}+\bar{\mathbf{G}})_1 + \mathbf{E}_{15}(\bar{\mathbf{g}}-\mathbf{g}) \circ (\bar{\mathbf{K}}+\mathbf{G})_2 \circ (\bar{\mathbf{K}}+\bar{\mathbf{G}})_2, \tag{51}$$

$$\mathbf{K}_{35} = \mathbf{Q}_{15}(\bar{\mathbf{g}}-\mathbf{g}) \circ (\bar{\mathbf{K}}+\mathbf{G})_1 \circ (\bar{\mathbf{K}}+\bar{\mathbf{G}})_1 + \mathbf{Q}_{15}(\bar{\mathbf{g}}-\mathbf{g}) \circ (\bar{\mathbf{K}}+\mathbf{G})_2 \circ (\bar{\mathbf{K}}+\bar{\mathbf{G}})_2, \tag{52}$$

$$\mathbf{K}_{44} = -\mathbf{F}_{11}(\bar{\mathbf{g}}-\mathbf{g}) \circ (\bar{\mathbf{K}}+\mathbf{G})_1 \circ (\bar{\mathbf{K}}+\bar{\mathbf{G}})_1 - \mathbf{F}_{11}(\bar{\mathbf{g}}-\mathbf{g}) \circ (\bar{\mathbf{K}}+\mathbf{G})_2 \circ (\bar{\mathbf{K}}+\bar{\mathbf{G}})_2, \tag{53}$$

$$\mathbf{K}_{45} = -\mathbf{\Lambda}_{11}(\bar{\mathbf{g}}-\mathbf{g}) \circ (\bar{\mathbf{K}}+\mathbf{G})_1 \circ (\bar{\mathbf{K}}+\bar{\mathbf{G}})_1 - \mathbf{\Lambda}_{11}(\bar{\mathbf{g}}-\mathbf{g}) \circ (\bar{\mathbf{K}}+\mathbf{G})_2 \circ (\bar{\mathbf{K}}+\bar{\mathbf{G}})_2, \tag{54}$$

$$\mathbf{K}_{55} = -\mathbf{\Gamma}_{11}(\bar{\mathbf{g}}-\mathbf{g}) \circ (\bar{\mathbf{K}}+\mathbf{G})_1 \circ (\bar{\mathbf{K}}+\bar{\mathbf{G}})_1 - \mathbf{\Gamma}_{11}(\bar{\mathbf{g}}-\mathbf{g}) \circ (\bar{\mathbf{K}}+\mathbf{G})_2 \circ (\bar{\mathbf{K}}+\bar{\mathbf{G}})_2, \tag{55}$$

where $\circ$ represents the Hadamard product, and for $i, j = 3,4,5$,

$$\mathbf{K}_{ij} = \mathbf{K}_{ji}. \tag{56}$$

The matrices $\mathbf{C}_{11}(\bar{\mathbf{g}}-\mathbf{g}), \mathbf{C}_{12}(\bar{\mathbf{g}}-\mathbf{g}), \mathbf{C}_{44}(\bar{\mathbf{g}}-\mathbf{g}), \mathbf{C}_{66}(\bar{\mathbf{g}}-\mathbf{g}), \mathbf{E}_{15}(\bar{\mathbf{g}}-\mathbf{g}), \mathbf{Q}_{15}(\bar{\mathbf{g}}-\mathbf{g}), \mathbf{F}_{11}(\bar{\mathbf{g}}-\mathbf{g}), \mathbf{\Lambda}_{11}(\bar{\mathbf{g}}-\mathbf{g}), \mathbf{\Gamma}_{11}(\bar{\mathbf{g}}-\mathbf{g})$ are the matrix form of the Fourier series coefficients, $c_{11}(\bar{\mathbf{g}}-\mathbf{g})$, $c_{12}(\bar{\mathbf{g}}-\mathbf{g})$, $c_{44}(\bar{\mathbf{g}}-\mathbf{g})$, $c_{66}(\bar{\mathbf{g}}-\mathbf{g})$, $e_{15}(\bar{\mathbf{g}}-\mathbf{g})$, $q_{15}(\bar{\mathbf{g}}-\mathbf{g})$, $\varepsilon_{11}(\bar{\mathbf{g}}-\mathbf{g})$, $\lambda_{11}(\bar{\mathbf{g}}-\mathbf{g})$, $\Gamma_{11}(\bar{\mathbf{g}}-\mathbf{g})$, respectively, and can be defined by Eq. (25) in a matrix form:

$$\mathbf{P}(\bar{\mathbf{g}}-\mathbf{g}) = \bar{P}\mathbf{I} + (P_A + P_B)(\mathbf{J}-\mathbf{I}) \circ \sum_{j=1}^{N_C} \mathbf{F}(\bar{\mathbf{g}}-\mathbf{g}) e^{-i(\bar{\mathbf{g}}-\mathbf{g})\cdot\bar{\mathbf{u}}_j}, \tag{57}$$

where $\mathbf{I}$ is the identity matrix, $\mathbf{J}$ is the unit matrix (all elements consisting of 1), and the matrix form of the structure function, $\mathbf{F}(\bar{\mathbf{g}}-\mathbf{g})$, is given by:

$$\mathbf{F}(\bar{\mathbf{g}}-\mathbf{g}) = \begin{bmatrix} F[\bar{\mathbf{g}}(-M)-\mathbf{g}(-M)] & F[\bar{\mathbf{g}}(-M+1)-\mathbf{g}(-M)] & \dots & F[\bar{\mathbf{g}}(M)-\mathbf{g}(M)] \\ F[\bar{\mathbf{g}}(-M)-\mathbf{g}(-M+1)] & F[\bar{\mathbf{g}}(-M+1)-\mathbf{g}(-M+1)] & \dots & F[\bar{\mathbf{g}}(M)-\mathbf{g}(M+1)] \\ \vdots & \vdots & \ddots & \vdots \\ F[\bar{\mathbf{g}}(-M)-\mathbf{g}(M)] & F[\bar{\mathbf{g}}(-M+1)-\mathbf{g}(M)] & \dots & F[\bar{\mathbf{g}}(M)-\mathbf{g}(M)] \end{bmatrix}, \tag{58}$$

where $F(\bar{\mathbf{g}}-\mathbf{g})$ is defined in Eqs. (27a-27d) for each inclusion geometry.
The matrices $\bar{\mathbf{K}}$, $\mathbf{G}$ and $\bar{\mathbf{G}}$ in Eqs. (46-55) are given by:

$$\bar{\mathbf{K}}_i = k_i \mathbf{J}, \tag{59}$$

and

$$\bar{\mathbf{G}}_i = \begin{Bmatrix} 1 \\ 1 \\ \vdots \\ 1 \end{Bmatrix} \otimes \begin{Bmatrix} \bar{g}_i(-M) \\ \bar{g}_i(-M+1) \\ \vdots \\ \bar{g}_i(M) \end{Bmatrix} = \begin{bmatrix} \bar{g}_i(-M) & \bar{g}_i(-M+1) & \dots & \bar{g}_i(M) \\ \bar{g}_i(-M) & \bar{g}_i(-M+1) & \dots & \bar{g}_i(M) \\ \vdots & \vdots & \ddots & \vdots \\ \bar{g}_i(-M) & \bar{g}_i(-M+1) & \dots & \bar{g}_i(M)] \end{bmatrix}, \tag{60}$$

with $i = 1,2$, $\otimes$ is tensor product, also known as dyadic or outer product, and $\mathbf{G}_i = \bar{\mathbf{G}}_i^{\mathrm{T}}$.
The matrix $\mathbf{M}$ is expressed by:

$$\mathbf{K} = \begin{bmatrix} \boldsymbol{\rho}(\bar{\mathbf{g}}-\mathbf{g}) & \mathbf{0} & \mathbf{0} & \mathbf{0} & \mathbf{0} \\ \mathbf{0} & \boldsymbol{\rho}(\bar{\mathbf{g}}-\mathbf{g}) & \mathbf{0} & \mathbf{0} & \mathbf{0} \\ \mathbf{0} & \mathbf{0} & \boldsymbol{\rho}(\bar{\mathbf{g}}-\mathbf{g}) & \mathbf{0} & \mathbf{0} \\ \mathbf{0} & \mathbf{0} & \mathbf{0} & \mathbf{0} & \mathbf{0} \\ \mathbf{0} & \mathbf{0} & \mathbf{0} & \mathbf{0} & \mathbf{0} \end{bmatrix}. \tag{61}$$

where $\boldsymbol{\rho}(\bar{\mathbf{g}}-\mathbf{g})$ is defined by Eq. (57).
The vector $\mathbf{q}$ in Eq. (44) is given by:

$$\mathbf{q} = \begin{Bmatrix} \mathbf{u}_{1_\mathbf{k}}(\mathbf{g}) \\ \mathbf{u}_{2_\mathbf{k}}(\mathbf{g}) \\ \mathbf{u}_{3_\mathbf{k}}(\mathbf{g}) \\ \boldsymbol{\phi}_\mathbf{k}(\mathbf{g}) \\ \boldsymbol{\varphi}_\mathbf{k}(\mathbf{g}) \end{Bmatrix}, \tag{62}$$

where the vectors $\mathbf{u}_{i_\mathbf{k}}(\mathbf{g})$, $\boldsymbol{\phi}_\mathbf{k}(\mathbf{g})$, $\boldsymbol{\varphi}_\mathbf{k}(\mathbf{g})$ can be represented by $\mathbf{T}_\mathbf{k}(\mathbf{g})$ as:

$$\mathbf{T}_\mathbf{k}(\mathbf{g}) = \left\{ \begin{array}{cccc} T_\mathbf{k}[\mathbf{g}(-M)] & T_\mathbf{k}[\mathbf{g}(-M+1)] & \ldots & T_\mathbf{k}[\mathbf{g}(M)] \end{array} \right\}. \tag{63}$$

The Eq. (44) represents a generalized eigenvalue problem of $\omega(\mathbf{k})$. This equation must be solved for each Bloch wave vector into the IBZ (Fig. 1 (f-j)). For each value of the Bloch wave vector, $5(2M+1)^2$ eigenvalues are obtained.

## 3. SIMULATED EXAMPLES

The physical parameters of $BaTiO_3$-$CoFe_2O_4$ (A) and the polymer (B) are listened in Table 1.

Table 1 – Physical parameters of $BaTiO_3$-$CoFe_2O_4$ (A) and polymer (B) [51].

| Geometry/Property | Value |
|---|---|
| Unit-cell length ($a$) | 0.022 m |
| Filling fraction ($\bar{f}$) | 0.45 |
| Mass density ($\rho_A$, $\rho_B$) | 5.73 kg/m$^3$, 1.15 kg/m$^3$ |
| Elastic constant ($c_{11_A}$, $c_{11_B}$) | $166 \times 10^9$ N/m$^2$, $7.8 \times 10^9$ N/m$^2$ |
| Elastic constant ($c_{12_A}$, $c_{12_B}$) | $77 \times 10^9$ N/m$^2$, $4.7 \times 10^9$ N/m$^2$ |
| Elastic constant ($c_{44_A}$, $c_{44_B}$) | $43 \times 10^9$ N/m$^2$, $4.6 \times 10^9$ N/m$^2$ |
| Elastic constant ($c_{66_A}$, $c_{66_B}$) | $44.5 \times 10^9$ N/m$^2$, $1.55 \times 10^9$ N/m$^2$ |
| Piezoelectric coefficient ($e_{15_A}$, $e_{15_B}$) | 11.6 C/m$^2$, 0 C/m$^2$ |
| Dielectric coefficient ($\varepsilon_{11_A}$, $\varepsilon_{11_B}$) | $11.2 \times 10^{-9}$ C$^2$/Nm$^2$, $0.0398 \times 10^{-9}$ C$^2$/Nm$^2$ |
| Piezomagnetic coefficient ($q_{15_A}$, $q_{15_B}$) | 550 N/Am, 0 N/Am |
| Magnetic permeability ($\Gamma_{11_A}$, $\Gamma_{11_B}$) | 5 Ns$^2$/C$^2$, 5 Ns$^2$/C$^2$ |
| Electromagnetic constant ($\lambda_{11_A}$, $\lambda_{11_B}$) | $0.005 \times 10^{-9}$ Ns/VC, 0 Ns/VC |

We calculate the elastic band structure considering a fixed filling fraction, 0.45, for the four inclusion cross section geometries (circular, hollow circular, square and rotated square with a 45° angle of rotation with respect to the $x$, $y$ axes) in a square, rectangular, triangular, honeycomb and Kagomé lattices. In the course of numerical calculations, we choose 441 plane waves for the Fourier series expansion ($M = 10$), which resulted in a good convergence.

We restrict the band structure plots until a maximum frequency of 150 kHz and to the IBZ illustrated in Fig. 1 ($f$-$j$). The plots are given in terms of frequency in Hz versus the reduced Bloch wave vector $\bar{\mathbf{k}} = \mathbf{k}a/2\pi$. The reduced Bloch wave vector for rectangular lattice is calculated by $a = \sqrt{(a_1^2 + a_2^2)}$. Furthermore, the relation between the parameters $\tilde{R}$ and $\tilde{r}$ for hollow inclusion is fixed in $\tilde{r} = 0.2\tilde{R}$ and we do not investigate the influence of the $BaTiO_3$-$CoFe_2O_4$ thickness, $\tilde{R} - \tilde{r}$, on the band structure.

Fig. 2 ($a$-$d$) illustrates the band structure of a MPC with square lattice for the four types of inclusion, considering the XY (red) and Z (blue) modes. Note from Eqs. (10-14) that only the Z mode contains the piezoelectric and piezomagnetic effects. There are two complete band gaps for circular inclusion, Fig. 2 ($a$). For hollow circular inclusion, Fig. 2 ($b$), only one complete band gap is observed and the first bands occur in higher frequencies compared to the other inclusions.

Figure 2 ($c$) shows two complete band gaps for square inclusion. When these square inclusions are rotated 45° with respect to $x$ and $y$ axes, three complete band gaps are created, instead of two, as illustrated in Figure 2 ($d$). The band structure for rotated square inclusion presents more complete band gaps than the other inclusions and the broadest band gap with a 16.15 kHz of bandwidth.

The band structure for a rectangular lattice is illustrated in Fig. 3. The band structure behaviour for circular and hollow circular inclusions in a rectangular lattice is similar to square lattice. For all inclusions, the complete band gaps for rectangular lattice are narrower than square lattice. Besides, the number of band gaps for square and rotated square inclusions, Figs. 3 ($c$-$d$), respectively, in a rectangular lattice is lower than in a square lattice, Figs. 2 $a$, $c$ and $d$. The broadest complete band gap in a rectangular lattice is for rotated square inclusion, similar to square lattice, and the bandwidth is 11.360 kHz.

Figure 4 shows the band structures for triangular lattice. For square and rotated square inclusions, Figure 4 ($c$-$d$), respectively, we observe a complete wide band gap in, approximately, the same range of frequency, *i.e.* 61.04 kHz - 42.98 kHz. The broadest band gap is observed for the hollow circular inclusion with a complete band gap width of 20.55 kHz. Comparing the band structures of triangular lattice to the square and rectangular lattices, we observe that the triangular lattice present broader complete band gaps for all inclusions.

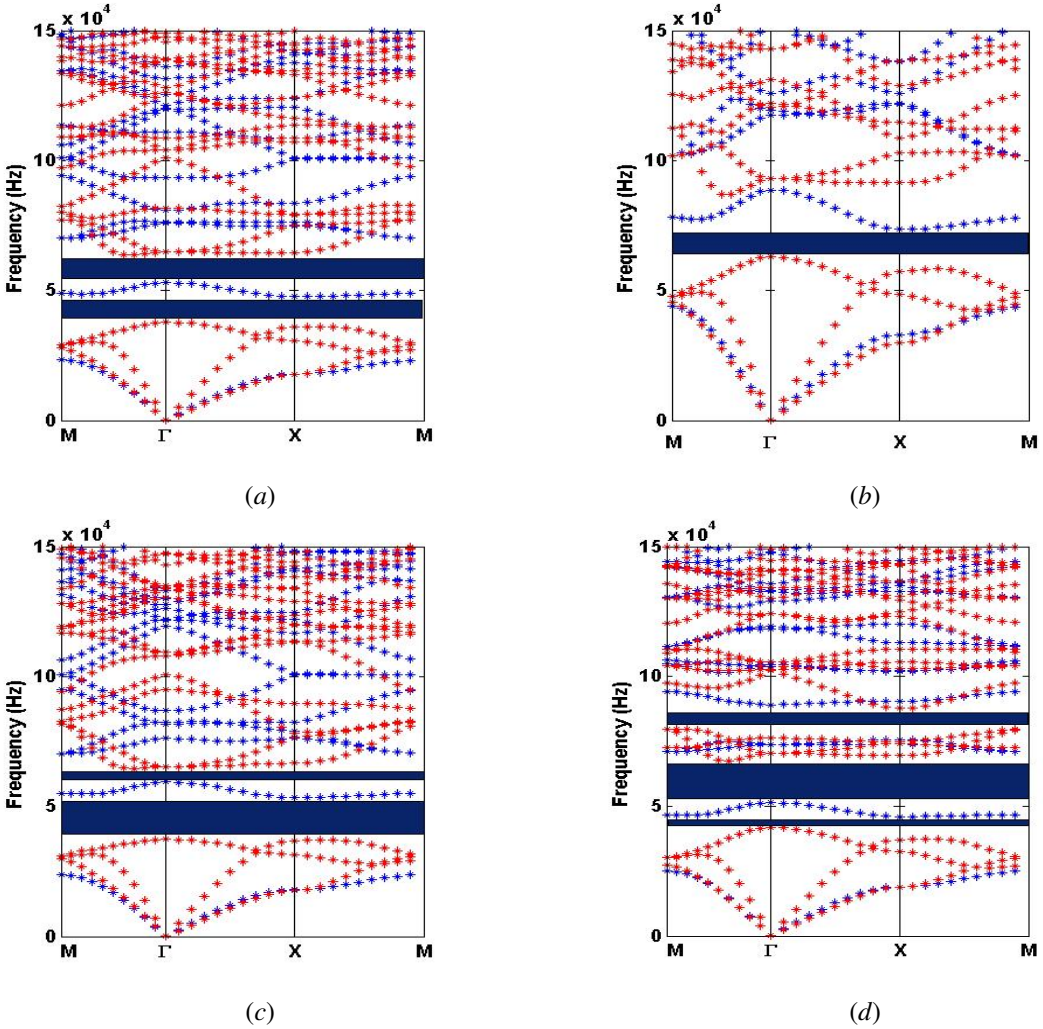


Figure 2 – Elastic band structures of XY (red) and Z (blue) modes of the magnetoelectroelastic phononic crystal for square lattice, considering $(a)$ circular, $(b)$ hollow circular, $(c)$ square and $(d)$ rotated square inclusions.

Figure 5 illustrates the band structures for honeycomb lattice. Two complete band gaps are opened up for all inclusions. The broadest band gap is observed for the circular inclusion with a bandwidth of 13.320 kHz.
In Fig. 6, it can be observed the band structures for Kagomé lattice. The square and rotated square inclusions, Figure 6 $(c$-$d)$, respectively, present a complete band gap at the same frequency range and the hollow inclusion presents the broadest band gap with 11.97 kHz of bandwidth, similar to triangular lattice.
The best performance of the MPC depends on the number of complete band gaps and its bandwidth. The triangular lattice presents the broadest complete band gaps for all inclusions and the hollow circular inclusion band gap is broader than the others. Furthermore, the square and Kagomé lattices have more complete band gaps than other lattices.

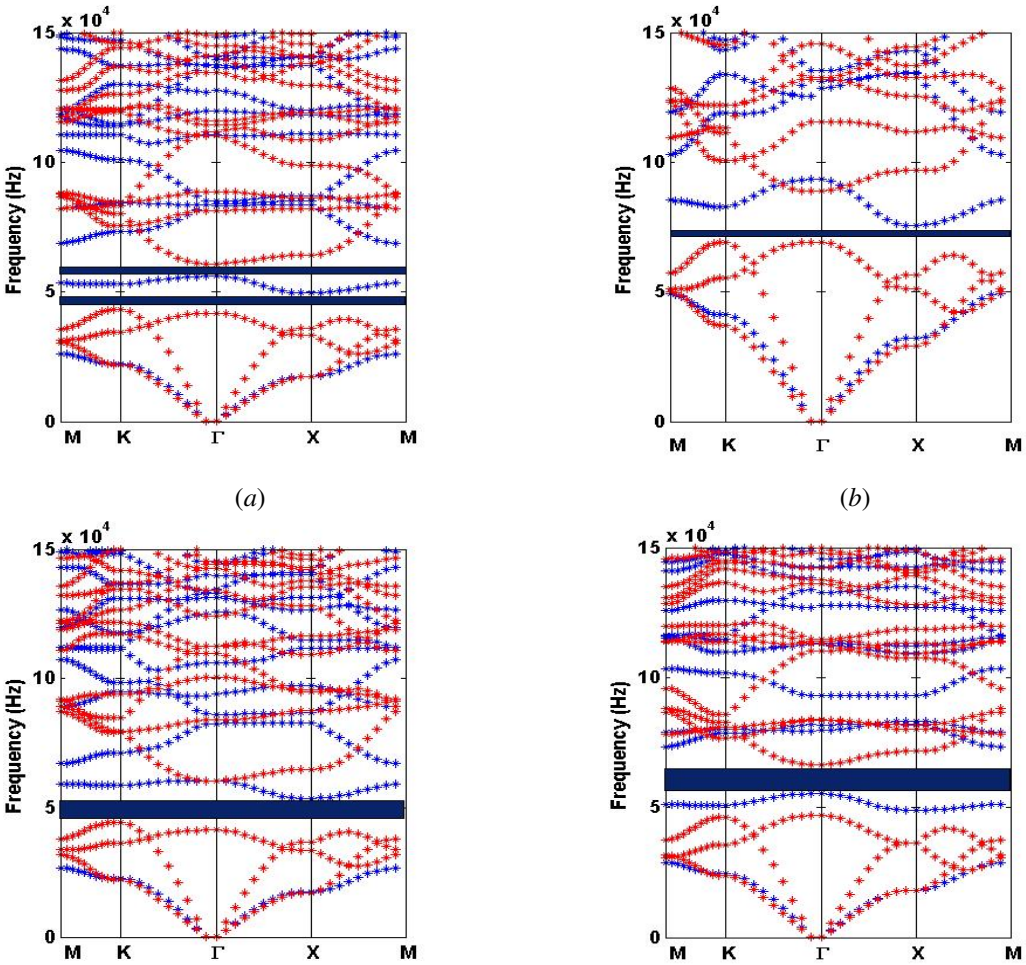


(*a*) (*b*)

(*c*) (*d*)

Figure 3 – Elastic band structures of XY (red) and Z (blue) modes of the magnetoelectroelastic phononic crystal for rectangular lattice, considering (*a*) circular, (*b*) hollow circular, (*c*) square and (*d*) rotated square inclusions.

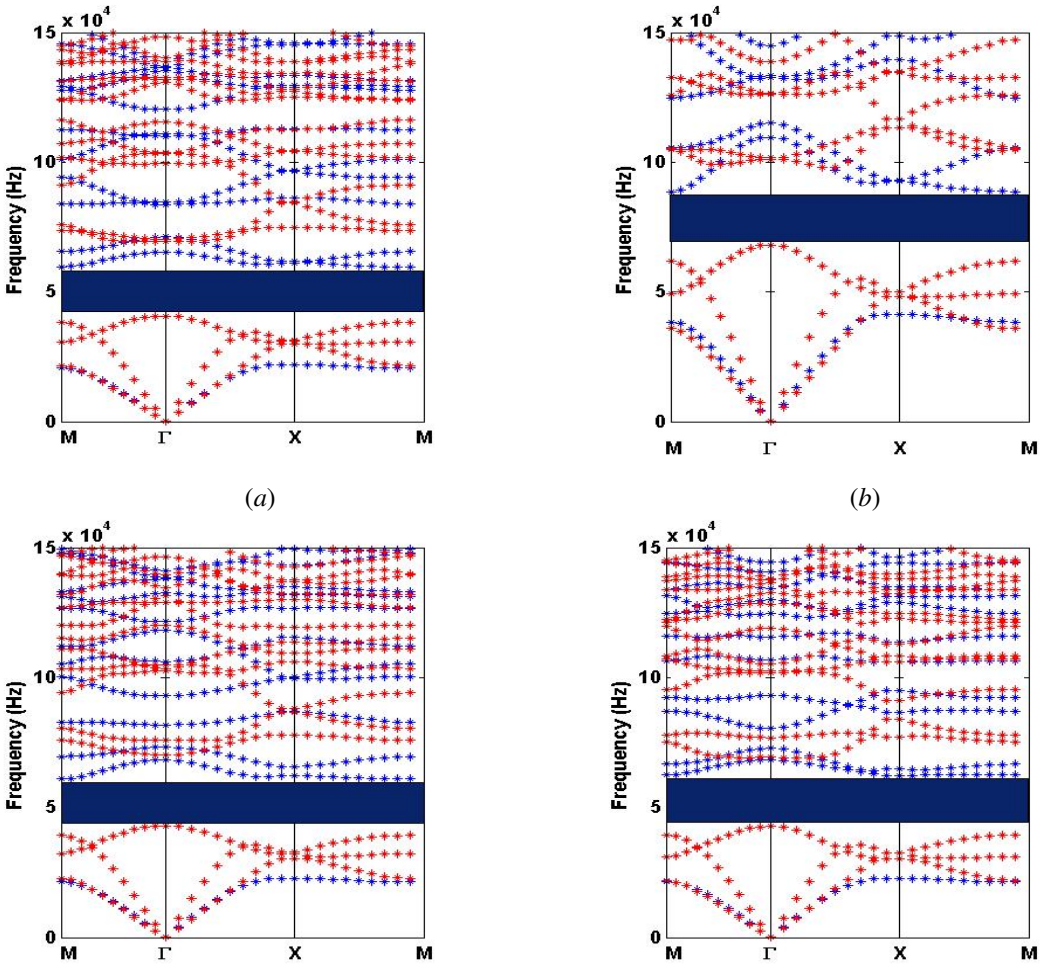


Figure 4 – Elastic band structures of XY (red) and Z (blue) modes of the magnetoelectroelastic phononic crystal for triangular lattice, considering $(a)$ circular, $(b)$ hollow circular, $(c)$ square and $(d)$ rotated square inclusions.

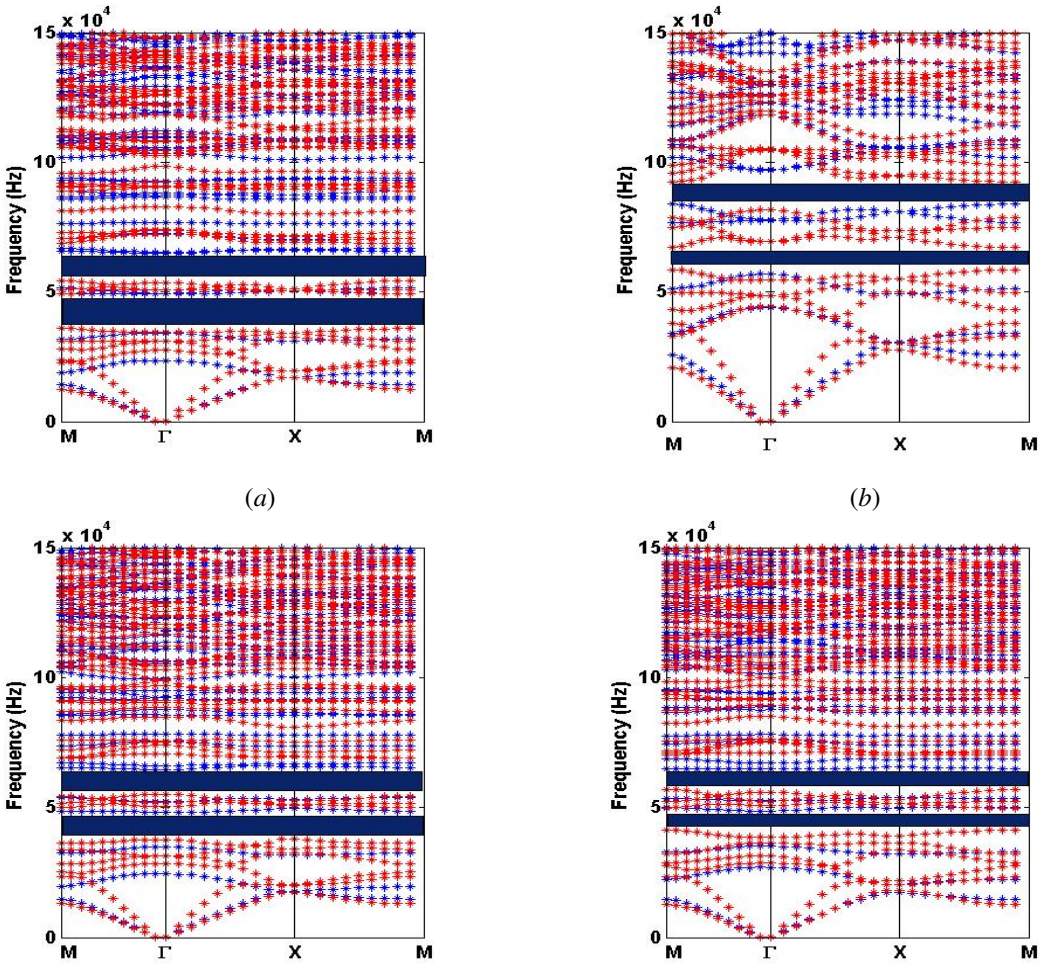


Figure 5 – Elastic band structures of XY (red) and Z (blue) modes of the magnetoelectroelastic phononic crystal for honeycomb lattice, considering $(a)$ circular, $(b)$ hollow circular, $(c)$ square and $(d)$ rotated square inclusions.

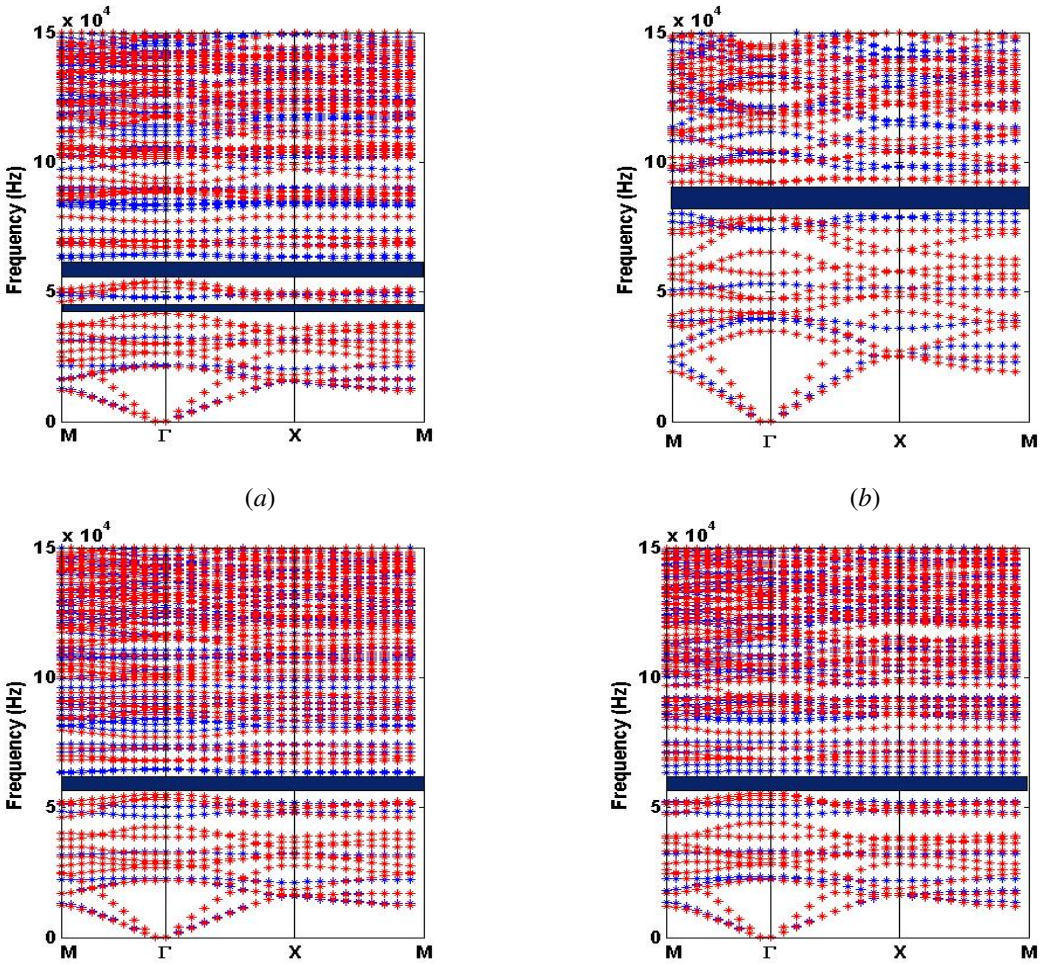


Figure 6 – Elastic band structures of XY (red) and Z (blue) modes of the magnetoelectroelastic phononic crystal for Kagomé lattice, considering $(a)$ circular, $(b)$ hollow circular, $(c)$ square and $(d)$ rotated square inclusions.

## 4. CONCLUSION

We obtain broad complete band gaps between XY and Z modes, where the elastic wave propagation is forbidden, for a MPC. The elastic band structure is investigated for $BaTiO_3$-$CoFe_2O_4$ inclusions embedded in an polymeric matrix for a fixed filling fraction, 0.45.
The broadest complete band gap for square lattice is found to the rotated square inclusion with 16.15 kHz of bandwidth. This inclusion geometry is also the best one for rectangular lattice. The broadest band gap for triangular and Kagomé lattices is observed for hollow circular inclusion with a complete band gap width of 20.55 kHz and 11.97 kHz, respectively. The best performance for honeycomb lattice is found for circular inclusion with 13.320 Hz of band gap width. The triangular lattice presents broader complete band gaps than other lattices for all inclusions and the square and Kagomé lattices have more complete band gaps.
In a general way, the best performance observed for the MPC studied is found for hollow inclusions in a triangular lattice. Finally, we consider square, rectangular, triangular, honeycomb and Kagomé arrays of $BaTiO_3$-$CoFe_2O_4$ perfectly embedded in an elastic background. This means that we neglect the effects due to decohesion of the $BaTiO_3$-$CoFe_2O_4BaTiO_3$-$CoFe_2O_4$ from the polymer matrix and to roughness at the interface between the inclusions and matrix. These defects can modify the elastic wave propagation in composite materials, altering the band structure of them. The complete elastic band gaps in a MPC enlarge the potential applications for vibration management with smart structures.

## ACKNOWLEDGEMENTS

The authors gratefully acknowledge the Brazilian research funding agency FAPEMA and IFMA for their financial support of this investigation.

## REFERENCES

[1] Sigalas, M.M., Economou, E.N., “Elastic Waves in Plates with Periodically Placed Inclusions”, Journal of Applied Physics, 75, 1994, pp. 2845-2850.

[2] Kushwaha, M.S., Halevi, P., Martínez, G., “Theory of Acoustic Band Structure of Periodic Elastic Composites”, Physical Review B, 49, 1994, pp. 2313-2322.

[3] Pennec, Y., Vasseur, J.O., Djafari-Rouhani, B., Dobrzyński, L., Deymier, P.A., “Two-Dimensional Phononic Crystals: Examples and Applications”, Surface Science Reports, 65, 2010, pp. 229-291.

[4] Huang, J., Shi, Z., “Attenuation Zones of Periodic Pile Barriers and its Application in Vibration Reduction for Plane Waves”, Journal of Sound and Vibration, 332, 2013, pp. 4423-4439.

[5] Yu, K., Chen, T., Wang, X., “Band Gaps in the Low-Frequency Range Based on the Two-Dimensional Phononic Crystals Plates Composed of Rubber Matrix with Periodic Steel Stubs”, Physica B, 416, 2013, pp. 12-16.

[6] Anjos, V., Arantes, A., “Phononic Band Structure in Carbon Microtube Composites”, RSC Advances, 5, 2015, pp. 11248-11253.

[7] Miranda Júnior, E.J.P., Dos Santos, J.M.C., “Flexural Wave Band Gaps in Metamaterial Elastic Beam”, Proceedings of the 23rd ABCM International Congress of Mechanical Engineering (COBEM2015), Rio de Janeiro, Brazil, December 2015, pp. 1-8.

[8] Miranda Júnior, E.J.P., Dos Santos, J.M.C., “Flexural Wave Band Gaps in $Al_2O_3$/Epoxy Composite Rectangular Plate Using Mindlin Theory”, Proceedings of the 3rd Brazilian Conference on Composite Materials (BCCM-3), Gramado, Brazil, August 2016, pp. 1-8.

[9] Miranda Júnior, E.J.P., Dos Santos, J.M.C., “Elastic Wave Band Gaps in a Two-Dimensional Magnetoelectroelastic Phononic Crystal”, Revista Interdisciplinar de Pesquisa em Engenharia, 2(13), 2016, pp. 13-26.

[10] Hepplestone, S.P., Srivastava, G.P., “Hypersonic Modes in Nanophononic Semiconductors”, Physical Review Letters, 101(105502), 2008, pp. 1-4.

[11] Yablonovitch, E., “Inhibited Spontaneous Emission in Solid-State Physics and Electronics”, Physical Review Letters, 50(20), 1987, pp. 2059-2062.

[12] John, S., “Strong Localization of Photons in Certain Disordered Dielectric Superlattices”, Physical Review Letters, 58(23), 1987, pp. 2486-2489.

[13] Olsson III, R.H., El-Kady, I., “Microfabricated Phononic Crystal Devices and Applications”, Measurement Science and Technology, 20(012002), 2009, pp. 1-13.

[14] Jensen, J.S., “Phononic Band Gaps and Vibrations in One- and Two-Dimensional Mass-Spring Structures”, Journal of Sound and Vibration, 266, 2003, pp. 1053-1078.

[15] Wang, G., Wen, J.H., Wen, X.S., “Quasi-One-Dimensional Phononic Crystals Studied Using the Improved Lumped-Mass Method: Application to Locally Resonant Beams with Flexural Wave Band Gap”, Physical Review B, 71(104302), 2005, pp. 1-5.

[16] Casadei, F., Beck, B.S., Cunefare, K.A., Ruzzene, M., “Vibration Control of Plates through Hybrid Configurations of Periodic Piezoeletric Shunts”, Journal of Intelligent Material Systems and Structures, 23(10), 2012, pp. 1169-1177.

[17] Miranda Júnior, E.J.P., Dos Santos, J.M.C., “Flexural Wave Band Gaps in Elastic Metamaterial Thin Plate”, Proceedings of the IX Mechanical Engineering Brazilian Congress (CONEM 2016), Fortaleza, Brazil, August 2016, pp. 1-10.

[18] Miranda Júnior, E.J.P., Dos Santos, J.M.C., “Flexural Wave Band Gaps in Elastic Metamaterial Beam”, Proceedings of the International Conference on Noise and Vibration Engineering (ISMA2016), Leuven, Belgium, September 2016, pp. 2099-2113.

[19] Ho, K.M., Cheng, C.K., Yang, Z., Zhang, X.X., Sheng, P., “Broadband Locally Resonant Sonic Shields”, Applied Physics Letters, 83(26), 2003, pp. 5566-5568.

[20] Qiu, C.Y., Liu, Z.Y., Mei, J., Shi, J., “Mode-Selecting Acoustic Filter by Using Resonant Tunneling of Two-Dimensional Double Phononic Crystals”, Applied Physics Letters, 87(104101), 2005, pp. 1-3.

[21] Yang, Z., Dai, H.M., Chan, N.H., Ma, G.C., “Acoustic Metamaterial Panels for Sound Attenuation in the 50-1000 Hz Regime”, Applied Physics Letters, 96(0411906), 2010, pp. 1-3.

[22] Casadei, F., Dozio, L., Ruzzene, M., Cunefare, K.A., “Periodic Shunts Arrays for the Control of Noise Radiation in an Enclosure”, Journal of Sound and Vibration, 329, 2010, pp. 3632-3646.

[23] Xiao, Y., Wen, J., Wen, X., “Sound Transmission Loss of Metamaterial-Based Thin Plates with Multiple Subwavelength Arrays of Attached Resonators”, Journal of Sound and Vibration, 331, 2012, pp. 5408-5423.

[24] Benchabane, S., Khelif, A., Robert, L., Rauch, J.Y., “Elastic Band Gaps for Surface Modes in an Ultrasonic Lithium Niobate Phononic Crystal”, Proceedings SPIE, Strasbourg, France, April 2006, 6182, pp. 1-13.

[25] Comerio, M.C., “Can Buildings be made Earthquake-Safe?”, Science, 312, 2006, pp. 204-206.

[26] Gorishnyy, T., Ullal, C.K., Maldovan, M., Fytas, G., Thomas, E.L., “Hypersonic Phononic Crystals”, Physical Review Letters, 94(115501), 2005, pp. 1-4.

[27] Cheng, W., Sainidou, R., Burgardt, P., Stefanou, N., Kiyanova, A., Efremov, M., Fytas, G., Nealey, P.F., “Elastic Properties and Glass Transition of Supported Polymer Thin Films”, Macromolecules, 40, 2007, pp. 7283-7290.

[28] Liu, Z., Zhang, X., Mao, Y., Zhu, Y.Y., Yang, Z., Chan, C.T., Sheng, P., “Locally Resonant Sonic Materials”, Science, 289(5485), 2000, pp. 1734-1736.

[29] Davis, B.L., Hussein, M., “Nanophononic Metamaterial: Thermal Conductivity Reduction by Local Resonance”, Physical Review Letters, 112(055505), 2014, pp. 1-5.

[30] Wagner, M.R., Graczykowski, B., Reparaz, J.S., Sachat, A.E., Sledzinska, M., Alzina, F., Torres, C.M.S., “Two-Dimensional Phononic Crystals: Disorder Matters”, Nano Letters, 16, 2016, pp. 5661-5668.

[31] Wilm, M., Ballandras, S., Laude, V., Pastureaud, T., “A Plane-Wave-Expansion Approach for Modelling Acoustic Propagation in 2D and 3D Piezoelectric Periodic Structures”, IEEE Ultrasonics Symposium, Atlanta, USA, October 2001, 2, pp. 977-980.

[32] Wilm, M., Ballandras, S., Laude, V., Pastureaud, T., " A Full 3D Plane-Wave-Expansion Model for 1-3 Piezoelectric Composite Structures", Journal of the Acoustical Society of America, 112(3), 2002, pp. 943-952.

[33] Wilm, M., Khelif, A., Ballandras, S., Laude, V., " Out-of-Plane Propagation of Elastic Waves in Two-Dimensional Phononic Band-Gap Materials", Physical Review E, 67(065602), 2003, pp. 1-4.

[34] Hou, Z., Wu, F., Liu, Y., "Phononic Crystals Containing Piezoelectric Material", Solid State Communications, 130, 2004, pp. 745-749.

[35] Wu, T.-T., Hsu, Z.-C., Huang, Z.-G., "Band Gaps and the Electromechanical Coupling Coefficient of a Surface Acoustic Wave in a Two-Dimensional Piezoelectric Phononic Crystal", Physical Review B, 71(064303), 2005, pp. 1-5.

[36] Hsu, J.-C., Wu, T.-T., "Bleustein-Gulyaev-Shimizu Surface Acoustic Waves in Two-Dimensional Piezoelectric Phononic Crystals", IEEE Transactions on Ultrasonics, Ferroelectrics, and Frequency Control, June 2006, 53(6), pp. 1169-1176.

[37] Wang, Y.-Z., Li, F.-M., Huang, W.-H., Wang, Y.-S., "Effects of Inclusion Shapes on the Band Gaps in Two-Dimensional Piezoelectric Phononic Crystals", Journal of Physics: Condensed Matter, 19(496204), pp. 1-9.

[38] Hsu, J.-C., Wu, T.-T., "Calculations of Lamb Wave Band Gaps and Dispersions for Piezoelectric Phononic Plates Using Mindlin's Theory-Based Plane Wave Expansion Method", IEEE Transactions on Ultrasonics, Ferroelectrics, and Frequency Control, February 2008, 55(2), pp. 431-441.

[39] Qian, Z.-H., Jin, F., Li, F.-M., Kishimoto, K., "Complete Band Gaps in Two-Dimensional Piezoelectric Phononic Crystals with {1-3} Connectivity Family", International Journal of Solids and Structures, 45, 2008, pp. 4748-4755.

[40] Zou, X.-Y., Chen, Q., Liang, B., Cheng, J.-C., "Control of the Elastic Wave Bandgaps in Two-Dimensional Piezoelectric Periodic Structures", Smart Materials and Structures, 17(015008), 2008, pp. 1-5.

[41] Wang, Y.-Z., Li, F.-M., Kishimoto, K., Wang, Y.-W., Huang, W.-H., "Wave Band Gaps in Three-Dimensional Periodic Piezoelectric Structures", Mechanics Research Communications, 36, 2009, pp. 461-468.

[42] Wang, Y., Li, F., Wang, Y., Kishimoto, K., Huang, W., "Tuning of Band Gaps for a Two-Dimensional Piezoelectric Phononic Crystal with a Rectangular Lattice", Acta Mechanica Sinica, 25, 2009, pp. 65-71.

[43] Huang, Y., Zhang, C.L., Chen, W.Q., "Elastic Wave Band Structures and Defect States in a Periodically Corrugated Piezoelectric Plate", Journal of Applied Mechanics, 81(081005), 2014, pp. 1-6.

[44] Lian, Z., Jiang, S., Hu, H., Dai, L., Chen, X., Jiang, W., "An Enhanced Plane Wave Expansion Method to Solve Piezoelectric Phononic Crystal with Resonant Shunting Circuits", Shock and Vibration, 2016(4015363), 2016, pp. 1-13.

[45] Li, L., Guo, Y., "Analysis of Longitudinal Waves in Rod-Type Piezoelectric Phononic Crystals", Crystals, 6(45), 2016, pp. 1-28.

[46] Robillard, J.-F., Bou Matar, O., J.F., Vasseur, J.O., Deymier P.A., Stippinger, M., Hladky-Hennion, A.-C, Pennec, Y., Djafari-Rouhani, B., "Tunable Magnetoelastic Phononic Crystals", Applied Physics Letters, 95(124104), 2016, pp. 1-4.

[47] Vasseur, J.O., Bou Matar, O., J.F., Robillard, J.-F., Hladky-Hennion, A.-C, Deymier P.A., "Band Structures Tunability of Bulk 2D Phononic Crystals Made of Magneto-Elastic Materials", AIP Advances, 1(041904), 2011, pp. 1-13.

[48] Bou Matar, O., Robillard, J.F., Vasseur, J.O., Hladky-Hennion, A.-C., Deymier P.A., "Band Gap Tunability of Magneto-Elastic Phononic Crystal", Journal of Applied Physics, 111(054901), 2012, pp. 1-15.

[49] Zhou, C., Sai, Y., Chen, J., "Tunable Lamb Wave Band Gaps in Two-Dimensional Magnetoelastic Phononic Crystal Slabs by an Applied External Magnetostatic Feld", Ultrasonics, 71, 2016, pp. 69-74.

[50] Wang, Y.-Z., Li, F.-M., Huang, W.-H., Jiang, X., Wang, Y.-S., Kishimoto, K., "Wave Band Gaps in Two-Dimensional Piezoelectric/Piezomagnetic Phononic Crystals", International Journal of Solids and Structures, 48, 2008, pp. 4203-4210.

[51] Wang, Y.-Z., Li, F.-M., Kishimoto, K., Wang, Y.-S., Huang, W.-H., "Elastic Wave Band Gaps in Magneto-electroelastic Phononic Crystals", Wave Motion, 46, 2009, pp. 47-56.

[52] Wang, Y.-Z., Li, F.-M., Kishimoto, K., Wang, Y.-S., Huang, W.-H., "Band Gap Behaviours of Periodic Magnetoelectroelastic Composite Structures with Kagome Lattices", Waves in Random an Complex Media, 19(3), 2009, pp. 509-520.

[53] Lan, M., Wei, P., "Band Gap of Piezoelectric/Piezomagnetic Phononic Crystal with Graded Interlayer", Acta Mechanica, 225, 2014, pp. 1779-1794.

[54] Guo, X., Wei, P., Lan, M., Li, L., "Dispersion Relations of Elastic Waves in One-Dimensional Piezoelectric/Piezomagnetic Phononic Crystal with Functionally Graded Interlayers", Ultrasonics, 70, 2016, pp. 158-171.

[55] Mead, D.J., Pujara, K.K., "Space-Harmonic Analysis of Periodically Supported Beams: Response to Convected Random Loading", Journal of Sound and Vibration, 14(4), 1971, pp. 525-541.

[56] Mace, B.R., "Periodically Stiffened Fluid-Loaded Plates, I: Response to Convected Harmonic Pressure and Free Wave Propagation", Journal of Sound and Vibration, 73(4), 1980, pp. 473-486.

[57] Mead, D.J., "Wave Propagation in Continuous Periodic Structures: Research Contributions from Southampton, 1994-1995", Journal of Sound and Vibration, 190(3), 1996, pp. 495-524.

[58] Brillouin, L., "Wave Propagation in Periodic Structures", New York/USA, Dover Publications, 1946.

[59] Dyogtyev, A.V., Sukhoivanov, I.A., De La Rue, R.M., "Photonic Band-Gaps Maps for Different Two Dimensionally Periodic Photonic Crystal Structures", Journal of Applied Physics, 107(013108), 2010, pp. 1-7.

[60] Wang, X.-M., Shen, Y.-P., "The conservations Laws and Path-Independent Integrals with an Application for Linear Electro-Magneto-Elastic Media", International Journal of Solids and Structures, 33(6), 1996, pp. 865-878.

[61] Floquet, G., "Sur les Équations Différentielles Linéaires à Coefficients Périodiques", Annales Scientifiques de L'École Normale Supérieure, France, 12, 1883, pp. 47-88.

[62] Bloch, F., "Über die Quantenmechanik der Electron in Kristallgittern", Zeitschrift für Physik, 52, 1928, pp. 555-600.

[63] Cassagne, D., Jouanin, C., Bertho, D., "Hexagonal Photonic-Band-Gap Structures", Physical Review B, 53(11), 1996, pp. 7134-7142.

[64] Gao, Z., Fang, J., Zhang, Y., Jiang, L., "Band Structure Research of a 2D Honeycomb Lattice Phononic Crystal", International Journal of Electrochemical Science, 8, 2013, pp. 7918-7925.

## APPENDIX F – Full Paper in Conference Proceedings

# Flexural Wave Band Gaps in an Elastic Metamaterial Beam with Periodically Attached Spring-Mass Resonators

**E.J.P. Miranda Jr.[1], J.M.C. Dos Santos[1]**
[1] University of Campinas, Computational Mechanics Department
Mendeleyev Street, 200, Cidade Universitária "Zeferino Vaz", Barão Geraldo, 13083860, Campinas, SP, Brazil
e-mail: **edson.jansen@ifma.edu.br**

## Abstract
In this study, we investigate theoretically the band structure of elastic waves propagating in an elastic metamaterial (EM) beam and its forced response. The influence of periodic arrays of single degree of freedom (SDOF) and multiple degrees of freedom (MDOF) force-only resonators attached in the unit cell of the EM beam was studied. The study is performed by using seven approaches, the transfer-matrix (TM) method, the finite element (FE) method, the spectral element (SE) method, the wave finite element (WFE) method, the wave spectral element (WSE) method, the plane wave expansion (PWE) method and the extended plane wave expansion (EPWE) method. Taking into account five arrays of SDOF force-only resonators, it is observed the coupling between locally resonant (LR) and Bragg-type gaps at frequencies around the first Bragg frequency. Furthermore, the configuration of multiple arrays of MDOF attached force-only resonators enlarges the application potentials of EMs for vibration management.

## 1 Introduction

In recent years, artificial periodic composite materials known as phononic crystals (PCs), consisting of a periodic array of scatterers embedded in a host medium, have been quite studied [1–8]. They have been investigated because PCs exhibit complete band gaps within which mechanical (elastic or acoustic) wave propagation is forbidden. The physical origins of phononic band gaps can be understood at micro-scale using the classical wave theory to describe the Bragg and Mie resonance based scattering of mechanical waves propagating within the crystal [9]. Most of the studies concerning PCs focused on investigation of bulk mechanical waves [1–2,7–9], *i.e.* mechanical wave propagation in solids, such as inhomogeneous isotropic elastic medium.

The band gaps created by the Bragg scattering mechanism, also called Bragg reflection mechanism, are known as Bragg-type gaps, whose frequency location is governed by the Bragg condition $a = n''(\lambda/2)$, $(n'' = 1,2,3,\dots)$, where $a$ is the lattice constant of the periodic system and $\lambda$ is the wavelength of waves in the host material. The Bragg condition implies that it is difficult to achieve a low frequency Bragg-type gap in PCs with small size.

Recently, in contrast, Liu et al. [10] proposed a type of locally resonant (LR) PC, also known as elastic metamaterial (EM), containing an array of localized resonant structures. This resonance-type band gaps were obtained in a frequency range two orders of magnitude lower than that given by the Bragg limit. LR gaps arise in the vicinity of the natural frequency of the local resonators while Bragg-type gaps typically occur at wavelengths of the order of the unit cell size.

PCs and EMs can be applied in many situations. One can consider engineering applications, such as vibrationless environment for high-precision mechanical systems, acoustic barriers, noise suppression devices, design of transducers and other devices. There are various types of elastic structures being investigated containing an array of local resonators, such as rods [11], beams [12–17] and plates [18].

The main purpose of this paper is to investigate the band structure of elastic waves propagating in an EM beam and its forced response, considering periodic arrays of single degree of freedom (SDOF) and multiple degrees of freedom (MDOF) force-only resonators. Another important purpose is to compare the elastic band structure obtained by the plane wave expansion (PWE), extended plane wave expansion (EPWE), wave finite element (WFE) and wave spectral element (WSE) methods, and the forced response obtained by the transfer-matrix (TM), finite element (FE), spectral element (SE), WFE and WSE methods.

## 2 Model and Methods

Figure 1 sketches an EM beam with multiple periodic arrays of attached local force-only resonators considering MDOF. In Fig. 1, there are $N$ MDOF force-only resonators attached in each unit cell with a lattice constant of $a$. Each resonator has a spring constant $k_j^{(i)}$ and a mass $m_j^{(i)}$ into the unit cell, where $j = 1,2,3,\ldots,N$ is the index related to the $j$th resonator and $i = 1,2,3,\ldots,N'$ is the index related to the DOFs of the $j$th resonator.

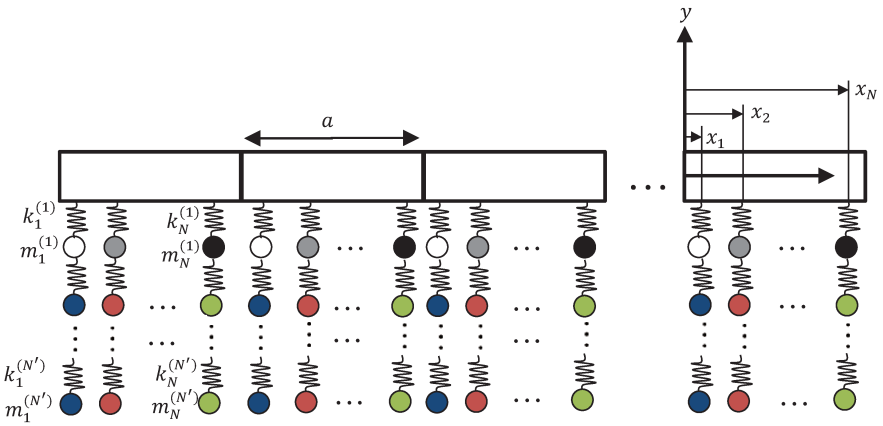


Figure 1: EM beam with multiple arrays of attached MDOF force-only resonators.

Here we expanded the analysis of Xiao *et al.* [11] for $N$ MDOF force-only resonators. The equation of motion of the $j$th resonator can be written as:

$$\left(\begin{bmatrix} k_j^{(1)} & \mathbf{k}_{j_{lr}} \\ \mathbf{k}_{j_{rl}} & \mathbf{k}_{j_{rr}} \end{bmatrix} - \omega^2 \begin{bmatrix} m_j^{(0)} & \mathbf{0} \\ \mathbf{0} & \mathbf{m}_{j_{rr}} \end{bmatrix}\right) \begin{Bmatrix} u_j^{(0)} \\ \mathbf{u}_{j_r} \end{Bmatrix} = \begin{Bmatrix} F_j^{(0)} \\ \mathbf{F}_{j_r} \end{Bmatrix} \text{ or } \left(\mathbf{K}_j - \omega^2 \mathbf{M}_j\right)\mathbf{u}_j = \mathbf{F}_j, \tag{1}$$

where $\mathbf{D}_j = \mathbf{K}_j - \omega^2 \mathbf{M}_j$, the indexes $l$ and $r$ represent left and right sides of the $j$th resonator, $m_j^{(0)}$, $u_j^{(0)}$ and $F_j^{(0)}$ are the mass, the displacement and the force, respectively, at the attachment point between the $j$th resonator and the beam unit cell. The stiffness and the mass matrices and the vectors of displacements and forces are:

$$\mathbf{k}_{j_{rl}} = \mathbf{k}_{j\,lr}^T = \begin{bmatrix} -k_j^{(1)} \\ 0 \\ 0 \\ \vdots \\ 0 \end{bmatrix}, \mathbf{k}_{j_{rr}} = \begin{bmatrix} k_j^{(1)} + k_j^{(2)} & -k_j^{(2)} & 0 & \ldots & 0 \\ -k_j^{(2)} & k_j^{(2)} + k_j^{(3)} & -k_j^{(3)} & \ldots & \vdots \\ 0 & -k_j^{(3)} & \ddots & \vdots & 0 \\ \vdots & \vdots & \ldots & k_j^{(N'-1)} + k_j^{(N')} & -k_j^{(N')} \\ 0 & 0 & \ldots & -k_j^{(N')} & k_j^{(N')} \end{bmatrix},$$

$$\mathbf{m}_{j_{rr}} = \begin{bmatrix} m_j^{(1)} & 0 & 0 & \dots & 0 \\ 0 & m_j^{(2)} & 0 & \dots & 0 \\ 0 & 0 & \ddots & \vdots & \vdots \\ \vdots & \vdots & \dots & m_j^{(N'-1)} & 0 \\ 0 & 0 & \dots & 0 & m_j^{(N')} \end{bmatrix}, \mathbf{u}_{j_r} = \begin{Bmatrix} u_j^{(1)} \\ u_j^{(2)} \\ \vdots \\ u_j^{(N'-1)} \\ u_j^{(N')} \end{Bmatrix}, \mathbf{F}_{j_r} = \begin{Bmatrix} F_j^{(1)} \\ F_j^{(2)} \\ \vdots \\ F_j^{(N'-1)} \\ F_j^{(N')} \end{Bmatrix}, \quad (2)$$

By considering that there are no external forces acting on the masses of the *j*th resonator so that $\mathbf{F}_{j_r} = \mathbf{0}$ and the resonator displacement vector $\mathbf{u}_{j_r}$ can be condensed. Therefore, Eq. (1) can be rewritten as $F_j^{(0)} = D_j^{(0)} u_j^{(0)}$, where $D_j^{(0)}$ is the dynamic stiffness of the *j*th resonator at the attachment point, which can be expressed as:

$$D_j^{(0)} = \left(k_j^{(1)} - \omega^2 m_j^{(0)}\right) - \mathbf{k}_{j_{lr}} \left(\mathbf{k}_{j_{rr}} - \omega^2 \mathbf{m}_{j_{rr}}\right) \mathbf{k}_{j_{rl}}. \quad (3)$$

## 2.1 SE and FE methods

The global dynamic stiffness matrix for a finite Euler-Bernoulli (EB) beam is given by $\mathbf{D}_{beamfe} = \mathbf{K}_{beamfe} - \omega^2 \mathbf{M}_{beamfe}$, where $\mathbf{K}_{beamfe}$ and $\mathbf{M}_{beamfe}$ are obtained from FE EB beam model. In this investigation, we calculated the dynamic stiffness matrix from using two methods, that is, one analytical, SE method and the other numerical, FE method. The dynamic stiffness matrix of the EB beam element modeled by SE method [19] is:

$$\mathbf{D}_{beamse}^e = \frac{EI}{L_{se}^3} \begin{bmatrix} k_{11} & k_{12} & k_{13} & k_{14} \\ k_{21} & k_{22} & k_{23} & k_{24} \\ k_{31} & k_{32} & k_{33} & k_{34} \\ k_{41} & k_{42} & k_{43} & k_{44} \end{bmatrix}, \quad (4)$$

where

$$k_{11} = \frac{(KL_{se})^3}{\Delta}(z_{11}z_{22} - iz_{12}z_{21}),$$

$$k_{12} = \frac{(KL_{se})^2 L_{se}}{2\Delta}(1+i)({z_{12}}^2 - {z_{11}}^2), k_{13} = \frac{(KL_{se})^3}{\Delta}(iz_{12}z_{22} - z_{11}z_{21}),$$

$$k_{14} = \frac{(KL_{se})^2 L_{se}}{\Delta}(i-1)z_{11}z_{12}, k_{22} = \frac{KL_{se}^3}{\Delta}(iz_{11}z_{22} - z_{12}z_{21}), k_{24} = \frac{KL_{se}^3}{\Delta}(z_{12}z_{22} - iz_{11}z_{21}),$$

$$k_{ij} = k_{ji},\ k_{23} = -k_{14},\ k_{33} = k_{11},\ k_{34} = -k_{12},\ k_{44} = k_{22},$$

$$z_{11} = \left(1 - e^{-iKL_{se}} e^{KL_{se}}\right), z_{12} = e^{-iKL_{se}} - e^{KL_{se}}, z_{21} = e^{-iKL_{se}} + e^{KL_{se}}, z_{22} = \left(1 + e^{-iKL_{se}} e^{KL_{se}}\right),$$

$$\Delta = \frac{z_{11}^2 + z_{12}^2}{1+i}, k = \left(\frac{\omega^2 \rho S}{EI}\right)^{\frac{1}{4}}, \quad (5)$$

where $K$ is the Bloch wave vector, also known as wavenumber, $E$ is the Young's modulus, $\rho$ is the density, $I$ is the second moment of area, $L_{se}$ is the length of the spectral element, $i = \sqrt{-1}$ and $S$ is the cross-sectional area of the beam. If the geometry of the beam is uniform, the global dynamic stiffness matrix of the EB beam element modeled by SE method is $\mathbf{D}_{beamse} = \mathbf{D}_{beamse}^e$. However, we discretized each unit cell in $j+1$ spectral elements, because we need $j$ nodes in each unit cell for the $j$ resonators. Thus, the global dynamic stiffness matrix can be obtained by the assembly of the dynamic stiffness matrices of the EB beam elements modeled by SE method.

The dynamic stiffness matrix can also be obtained by the FE method, $\mathbf{D}_{beamfe}^e = \mathbf{K}_{beamfe}^e - \omega^2 \mathbf{M}_{beamfe}^e$, where [19]:

$$\mathbf{K}^{e}_{beamfe} = \frac{EI}{L^{3}_{fe}}\begin{bmatrix} 12 & 6L_{fe} & -12 & 6L_{fe} \\ 6L_{fe} & 4L^{2}_{fe} & -6L_{fe} & 2L^{2}_{fe} \\ -12 & -6L_{fe} & 12 & -6L_{fe} \\ 6L_{fe} & 2L^{2}_{fe} & -6L_{fe} & 4L^{2}_{fe} \end{bmatrix},$$

$$\mathbf{M}^{e}_{beamfe} = \frac{\rho S L_{fe}}{420}\begin{bmatrix} 156 & 22L_{fe} & 54 & -13L_{fe} \\ 22L_{fe} & 4L^{2}_{fe} & 13L_{fe} & -3L^{2}_{fe} \\ 54 & 13L_{fe} & 156 & -22L_{fe} \\ -13L_{fe} & -3L^{2}_{fe} & -22L_{fe} & 4L^{2}_{fe} \end{bmatrix}, \quad (6)$$

where $L_{fe}$ is the length of the finite element. The global dynamic stiffness matrix is given by $\mathbf{D}_{beamfe} = \mathbf{K}_{beamfe} - \omega^{2}\mathbf{M}_{beamfe}$, where $\mathbf{K}_{beamfe}$ and $\mathbf{M}_{beamfe}$ are the global stiffness and the global mass matrices, respectively. They are obtained by the assembly of the stiffness and mass matrixes of the EB beam elements modeled by FE method. It is important to highlight that the dynamic stiffness of the all *j*th resonators, should be coupled in the correct DOFs of the $\mathbf{D}_{beamfe}$ and $\mathbf{D}_{beamse}$. The total number of the resonators along the beam is $n'N$, where $n'$ is the number of unit cells.

## 2.2 WSE and WFE methods

Considering a finite EB beam divided into a finite number of unit cells (the unit cells are meshed with an equal number of nodes on their left- and right-hand edges), see Fig. 1, one can obtain a dynamic stiffness of the unit cell, $\widetilde{\mathbf{D}}_{cell}$,obtained from the FE, $\widetilde{\mathbf{D}}_{cellfe}$, or SE, $\widetilde{\mathbf{D}}_{cellse}$, model. The $\widetilde{\mathbf{D}}_{cell}$ can be portioned and the dynamic equation of motion can be written as:

$$\begin{bmatrix} \widetilde{\mathbf{D}}_{ii} & \widetilde{\mathbf{D}}_{il} & \widetilde{\mathbf{D}}_{ir} \\ \widetilde{\mathbf{D}}_{li} & \widetilde{\mathbf{D}}_{ll} & \widetilde{\mathbf{D}}_{lr} \\ \widetilde{\mathbf{D}}_{ri} & \widetilde{\mathbf{D}}_{rl} & \widetilde{\mathbf{D}}_{rr} \end{bmatrix}\begin{Bmatrix} \mathbf{u}_{i} \\ \mathbf{u}_{l} \\ \mathbf{u}_{r} \end{Bmatrix} = \begin{Bmatrix} \mathbf{0} \\ \mathbf{F}_{l} \\ \mathbf{F}_{r} \end{Bmatrix}, \quad (7)$$

where $i$ represents the interior DOFs of the unit cell, $l$ and $r$ represent the left and right boundaries of the unit cell, respectively. The interior DOFs can be eliminated using the first row of Eq. (7) [20], which results in:

$$\mathbf{u}_{i} = \widetilde{\mathbf{D}}_{ii}^{-1}\left(\widetilde{\mathbf{D}}_{il}\mathbf{u}_{l} + \widetilde{\mathbf{D}}_{ir}\mathbf{u}_{r}\right). \quad (8)$$

Inserting Eq. (8) into Eq. (7) leads to:

$$\begin{bmatrix} \mathbf{D}_{ll} & \mathbf{D}_{lr} \\ \mathbf{D}_{rl} & \mathbf{D}_{rr} \end{bmatrix}\begin{Bmatrix} \mathbf{u}_{l} \\ \mathbf{u}_{r} \end{Bmatrix} = \begin{Bmatrix} \mathbf{F}_{l} \\ \mathbf{F}_{r} \end{Bmatrix} \therefore \mathbf{D}_{cell}\mathbf{u}_{cell} = \mathbf{F}_{cell}, \quad (9)$$

where $\mathbf{D}_{ll} = \widetilde{\mathbf{D}}_{ll} - \widetilde{\mathbf{D}}_{li}\widetilde{\mathbf{D}}_{ii}^{-1}\widetilde{\mathbf{D}}_{il}, \mathbf{D}_{rl} = \widetilde{\mathbf{D}}_{rl} - \widetilde{\mathbf{D}}_{ri}\widetilde{\mathbf{D}}_{ii}^{-1}\widetilde{\mathbf{D}}_{il}, \mathbf{D}_{lr} = \widetilde{\mathbf{D}}_{lr} - \widetilde{\mathbf{D}}_{li}\widetilde{\mathbf{D}}_{ii}^{-1}\widetilde{\mathbf{D}}_{ir}$, $\mathbf{D}_{rr} = \widetilde{\mathbf{D}}_{rr} - \widetilde{\mathbf{D}}_{ri}\widetilde{\mathbf{D}}_{ii}^{-1}\widetilde{\mathbf{D}}_{ir}$.

Equation (9), which relates the forces and the displacements on the two sides of the unit cell, is the starting point for the WFE [20] and WSE analysis. Note that $\mathbf{D}_{cell}$ can be obtained by FE method, $\mathbf{D}_{cellfe}$, or by SE method, $\mathbf{D}_{cellse}$. Thus, this is the difference between the WFE and WSE methods. Similar as section 2.1, it is important to highlight that the dynamic stiffness of the all *j*th resonators, $N$, on the unit cell should be coupled in the correct DOFs of the $\widetilde{\mathbf{D}}_{cellfe}$ and $\widetilde{\mathbf{D}}_{cellse}$. Here, it is not possible to couple in the correct DOFS of the $\mathbf{D}_{cellfe}$ and $\mathbf{D}_{cellse}$, *i.e.* after the condensation, because the resonators are not on the left and/or right side of the unit cell as usual. Thus, the coupling is done before the condensation.

One can reformulate Eq. (9) in terms of state vectors as:

$$\begin{Bmatrix} \mathbf{u}_{r} \\ -\mathbf{F}_{r} \end{Bmatrix} = \begin{bmatrix} -\mathbf{D}_{lr}^{-1}\mathbf{D}_{ll} & -\mathbf{D}_{lr}^{-1} \\ \mathbf{D}_{rl} - \mathbf{D}_{rr}\mathbf{D}_{lr}^{-1}\mathbf{D}_{ll} & -\mathbf{D}_{rr}\mathbf{D}_{lr}^{-1} \end{bmatrix}\begin{Bmatrix} \mathbf{u}_{l} \\ \mathbf{F}_{l} \end{Bmatrix} \therefore \mathbf{q}_{r} = \mathbf{T}\mathbf{q}_{l}, \quad (10)$$

where $\mathbf{T}$ is a symplectic [21] matrix and it is known as transfer matrix, $\mathbf{q}_r$ is the right state vector and $\mathbf{q}_l$ is the left state vector. The continuity of displacements and equilibrium forces at the boundary between cells $m$ and $m+1$, yields,

$$\begin{aligned}\mathbf{u}_l^{(m+1)} &= \mathbf{u}_r^{(m)},\\ \mathbf{F}_l^{(m+1)} &= -\mathbf{F}_r^{(m)}.\end{aligned} \tag{11}$$

Substituting Eq. (11) in Eq. (10), one can write:

$$\mathbf{q}_l^{(m+1)} = \mathbf{T}\mathbf{q}_l^{(m)}. \tag{12}$$

Invoking Floquet-Bloch's theorem [22–23], say:

$$\mathbf{q}_l^{(m+1)} = e^{\,\mu}\mathbf{q}_l^{(m)}, \tag{13}$$

where $\mu = -iKa$ is the attenuation constant. Substituting Eq. (13) in Eq. (12) leads to:

$$\mathbf{T}\mathbf{q}_l = e^{\,\mu}\mathbf{q}_l. \tag{14}$$

As pointed out by Zhong and Williams [21], direct calculation of the eigenvalue problem in Eq. (14) can lead to numerical ill-conditioning. According to Mencik [24], this ill-conditioning can be explained by the Bauer-Fike theorem [25], which says that the problem is that the eigenvector of $\mathbf{T}$ can be ill-conditioned. This can be explained as it is partitioned into displacement and force components, thus the values can be largely disparate. To solve this issue, Zhong and Williams [21] proposed a homogeneous generalized eigenvalue problem of the following form:

$$\begin{aligned}\mathbf{q}_l &= \begin{bmatrix}\mathbf{I}_n & \mathbf{0}\\ -\mathbf{D}_{ll} & -\mathbf{D}_{lr}\end{bmatrix}\begin{Bmatrix}\mathbf{u}_l\\ \mathbf{u}_r\end{Bmatrix} \therefore \mathbf{q}_l = \mathbf{L}\mathbf{w},\\ \mathbf{q}_r &= \begin{bmatrix}\mathbf{0} & \mathbf{I}_n\\ \mathbf{D}_{rl} & \mathbf{D}_{rr}\end{bmatrix}\begin{Bmatrix}\mathbf{u}_l\\ \mathbf{u}_r\end{Bmatrix} \therefore \mathbf{q}_r = \mathbf{N}\mathbf{w},\end{aligned} \tag{15}$$

where $\mathbf{I}_n$ is the $n$-dimensional unit matrix (identity matrix) and from Eq. (10), one can note that $\mathbf{T} = \mathbf{N}\mathbf{L}^{-1}$. Rewriting Eq. (14):

$$\mathbf{T}\mathbf{q}_l = e^{\,\mu}\mathbf{q}_l \therefore \mathbf{q}_r = e^{\,\mu}\mathbf{q}_l \;\; \therefore e^{\,\mu}\mathbf{L}\mathbf{w} = \mathbf{N}\mathbf{w}. \tag{16}$$

The solutions of Eq. (16) are denoted as $\left\{\left(e^{\,\mu_j}, \mathbf{w}_j\right)\right\}_j$, where $\{e^{\,\mu_j}\}_j$ are the eigenvalues and $\left\{\mathbf{w}_j\right\}_j$ are the eigenvectors associated with a given mode $j$. One can notice that each eigenvector of (14) can be obtained by $\mathbf{q}_{l\,j} = \mathbf{L}\mathbf{w}_j$. It can also be shown that $\left\{\left(e^{-\mu_j}, (\mathbf{J}\mathbf{L}\mathbf{w})_j\right)\right\}_j$ are also eigenvalues of Eq. (16) and left eigenvectors, respectively, because one can rewrite Eq. (16) as $e^{\,\mu}\mathbf{N}^{\mathrm{T}}(\mathbf{J}\mathbf{L}\mathbf{w}) = \mathbf{L}^{\mathrm{T}}(\mathbf{J}\mathbf{L}\mathbf{w}) \therefore (\mathbf{J}\mathbf{L}\mathbf{w})^{\mathrm{T}}(\mathbf{N} - e^{-\mu}\mathbf{L}) = 0$ [21].

Therefore, the $2n$ eigenvalues of the Eq. (16), when ordered appropriately, can be subdivided into two groups. The first corresponds to the waves travelling to the right, $e^{\mu_j}\ j = 1,2,\dots,n$ with $|e^{\mu_j}| < 1$ and the second corresponds to the waves travelling to the left, $e^{-\mu_j}\ j = 1,2,\dots,n$ with $|e^{-\mu_j}| > 1$. Note that to consider these hypotheses the substructure needs to be damped. If the substructure does not have damping, $\left|e^{\pm\mu_j}\right| = 1$ .

For the eigenvalues $\{e^{\,\mu_j}\}_j$ and $\{e^{\,-\mu_j}\}_j$ one can obtain the associated eigenvectors $\left\{\mathbf{q}_{l\,j}\right\}_j$ and $\left\{\mathbf{q}^*_{l\,j}\right\}_j$, respectively. Each eigenvector can be split into displacement and force components as $\mathbf{q}_{l\,j} = \begin{Bmatrix}\mathbf{u}_{l\,j}\\ \mathbf{F}_{l\,j}\end{Bmatrix}$ and $\mathbf{q}^*_{l\,j} = \begin{Bmatrix}\mathbf{u}^*_{l\,j}\\ \mathbf{F}^*_{l\,j}\end{Bmatrix}$. An important relation between the components of each eigenvector is $\mathbf{u}^*_{l\,j} = \mathfrak{R}\mathbf{u}_{l\,j}$ and $\mathbf{F}^*_{l\,j} = -\mathfrak{R}\mathbf{F}_{l\,j}$ [24], where $\mathfrak{R}$ is the diagonal symmetry transformation matrix. Tracking the frequency evolution of each wave mode is a crucial step of the WFE and WSE methods, for more details see Mencik [24].

To predict the harmonic response of a structure composed of $n'$ unit cells, one can write:

$$\mathbf{q}_l^{(1)} = \sum_{j=1}^{n} \mathbf{q}_{l\,j} \mathbf{Q}_j^{(1)} + \sum_{j=1}^{n} \mathbf{q}_{l\,j}^{*}\, e^{-n'\mu_j} \mathbf{Q}_j^{*(n')},$$

$$\mathbf{q}_r^{(n')} = \sum_{j=1}^{n} \mathbf{q}_{l\,j} e^{-n'\mu_j} \mathbf{Q}_j^{(1)} + \sum_{j=1}^{n} \mathbf{q}_{l\,j}^{*}\, \mathbf{Q}_j^{*(n')}, \tag{17}$$

where $\mathbf{q}_l^{(1)}$ is the state vector of the first node of the structure, $\mathbf{q}_r^{(n')}$ is the state vector of the last node of the structure and $\mathbf{Q}$ is the vector form of the modal amplitude. Equation (17) and the calculation of the modal amplitudes are discussed in [24].

## 2.3 TM method

The TM method is not new and it has it has its predecessors in the tabular methods which were successfully applied at a time when no automatic computer operated [26]. This method has been extensively used to solve periodic structures dynamics problems [12–13]. In this study, we do not apply the Floquet-Bloch's theorem [22–23] in TM method to obtain the band structure as other studies [12–13].

The transfer matrix relates the state vector of displacements and forces at a node with forces and displacement at a neighboring node, as represented by Eq. (12). Furthermore, the assembling to obtain the global matrix is done by propagating the transfer matrixes from the first unit cell to the last, $n'$th, unit cell. Thus, one can write:

$$\mathbf{T}_G = \mathbf{T}^{(n')} \ldots \mathbf{T}^{(2)} \mathbf{T}^{(1)} = \mathbf{T}^{n'}, \tag{18}$$

where $\mathbf{T}^{(k)}, k = 1,2, \ldots n'$, is the transfer matrix of the $k$th unit cell of the structure, $\mathbf{T} = \mathbf{T}^{(1)} = \cdots = \mathbf{T}^{(n')}$ and $\mathbf{T}_G$ is the global transfer matrix of the structure. The $\mathbf{T}^{(k)}$ matrix has internal elements as expressed in Eq. (10) and they can be obtained by $\mathbf{D}_{cellfe}$ or $\mathbf{D}_{cellse}$. In this study, we calculated $\mathbf{T}$ from $\mathbf{D}_{cellse}$. One can note that $\mathbf{D}_{cellse}$ already has the information of the resonators because, as explained before, the dynamic stiffness of the all $j$th resonators, $N$, attached in the unit cell should be coupled in the correct DOFs of the $\widetilde{\mathbf{D}}_{cellse}$.

Note that the global transfer matrix relates:

$$\mathbf{q}_r^{(n')} = \mathbf{T}_G \mathbf{q}_l^{(1)}. \tag{19}$$

Applying the boundary conditions, in this paper free-free beam, and considering no force and no moment applied in the right side of the beam, *i.e.* $\mathbf{F}_r^{(n')} = \mathbf{0}$, Eq. (19) can be written as:

$$\begin{bmatrix} -\mathbf{T}_G^{-1}{}_{lr} \mathbf{T}_{G\,ll} & \mathbf{T}_G^{-1}{}_{lr} \\ -\mathbf{T}_G^{-1}{}_{rr} \mathbf{T}_{G\,rl} & \mathbf{0} \end{bmatrix} \begin{Bmatrix} \mathbf{q}_l^{(1)} \\ \mathbf{q}_r^{(n')} \end{Bmatrix} = \mathbf{F}_l^{(1)} \begin{Bmatrix} \mathbf{1} \\ \mathbf{1} \end{Bmatrix}, \tag{20}$$

where $\mathbf{T}_{G\,ll}$, $\mathbf{T}_{G\,lr}$, $\mathbf{T}_{G\,rl}$, $\mathbf{T}_{G\,rr}$ are submatrices of $\mathbf{T}_G$ and $\mathbf{F}_l^{(1)}$ is the vector of force and moment of the first node of the structure. One problem related to the TM method is the numerical difficulties [26].

## 2.4 PWE and EPWE methods

The PWE and EPWE methods, also known as $\omega(k)$ and $k(\omega)$, are analytical methods to predict the band structure. The advantage of using the EPWE method is because the evanescent modes are obtained naturally and these modes are not ignored as well as by the PWE method. Hsue *et al.* [27] proved that the evanescent modes obtained by EPWE obey the Floquet-Bloch's theorem [22–23].

These methods applied to EM EB beam, considering $N$ SDOF force-only resonators attached in each unit cell, was developed by Xiao *et al.* [14]. For details of the mathematical formulation, see Xiao *et al.* [14].

We expanded the analysis of Xiao *et al.* [14] considering $N$ MDOF force-only resonators attached in each unit cell.

# 3 Results and Discussion

## 3.1 Multiple arrays of SDOF force-only resonators

The aluminum beam parameters and material properties are summarized in Table 1.

| Geometry/Property | Value |
|---|---|
| Unit cell length $(a)$ | 0.1 m |
| Beam length (for WSE, WFE, FE, SE and TM methods) $(L)$ | 0.5 m |
| Beam length (PWE and EPWE methods) $(L)$ | $\infty$ |
| Number of unit cells (for WSE, WFE, FE, SE and TM methods) $(n')$ | 5 |
| Cross section area $(S)$ | 4 x $10^{-4}$ $m^2$ |
| Young's modulus $(E)$ | 7 x $10^{10}$ Pa |
| Mass density $(\rho)$ | 2700 kg/$m^3$ |
| Loss factor of the beam $(\eta_b)$ | 0.01 |
| Poisson's ratio $(\upsilon)$ | 0.33 |
| Second moment of area $(I)$ | 1.3333 x $10^{-11}$ $m^4$ |

Table 1: Beam geometric parameters and material properties.

We consider an EM beam with five arrays of SDOF force-only resonators in the unit cell. The parameters of the resonators are: $\left\{\eta_j^{(1)}\right\} = \{0.05, 0.05, \ldots, 0.05\}$, $\left\{x_j^{(1)}\right\} = a\ x\ \{1, 2, \ldots, 5\}/6$ m, $\left\{\gamma_j^{(1)}\right\} = 0.5\ x\ \{1.4, 1.2, 1, 0.8, 0.6\}/5$, $m_j^{(1)} = \gamma_j^{(1)} \rho A a$, $\left\{f_j^{(1)}\right\} = \{160, 180, 200, 475, 500\}$ Hz and $k_j^{(1)} = m_j^{(1)} \left(\omega_j^{(1)}\right)^2$, $j = 1, 2 \ldots, 5$, where $\eta_j^{(1)}$ is the loss factor of the $j$th resonator, $x_j^{(1)}$ is the position of the $j$th resonator, $\gamma_j^{(1)}$ is the $j$th resonator mass ratio to the mass of the beam in each unit cell, the sum of all $\gamma_j^{(1)}$ is equal to 0.5 and $f_j^{(1)}$ is the resonance frequency of the $j$th resonator.

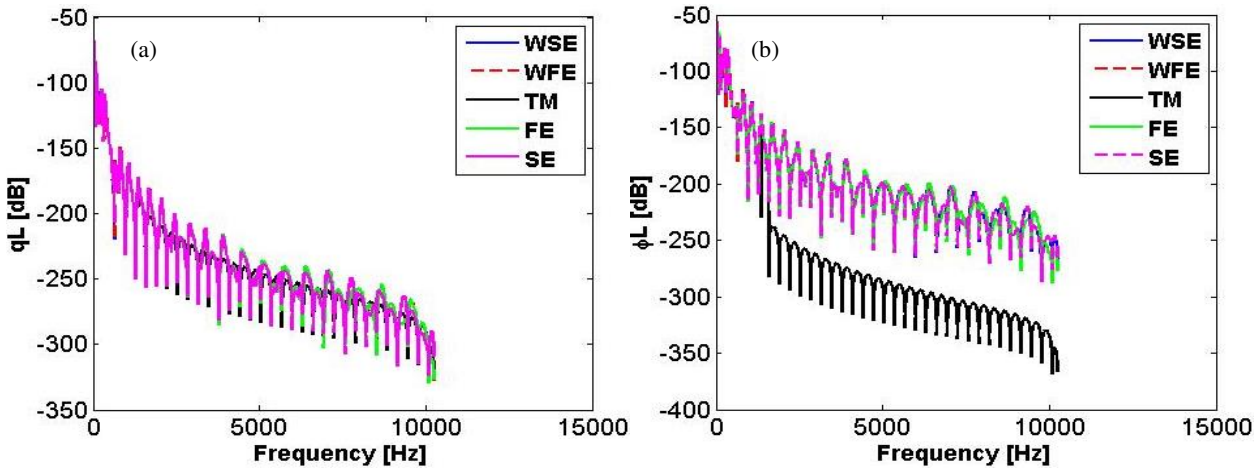

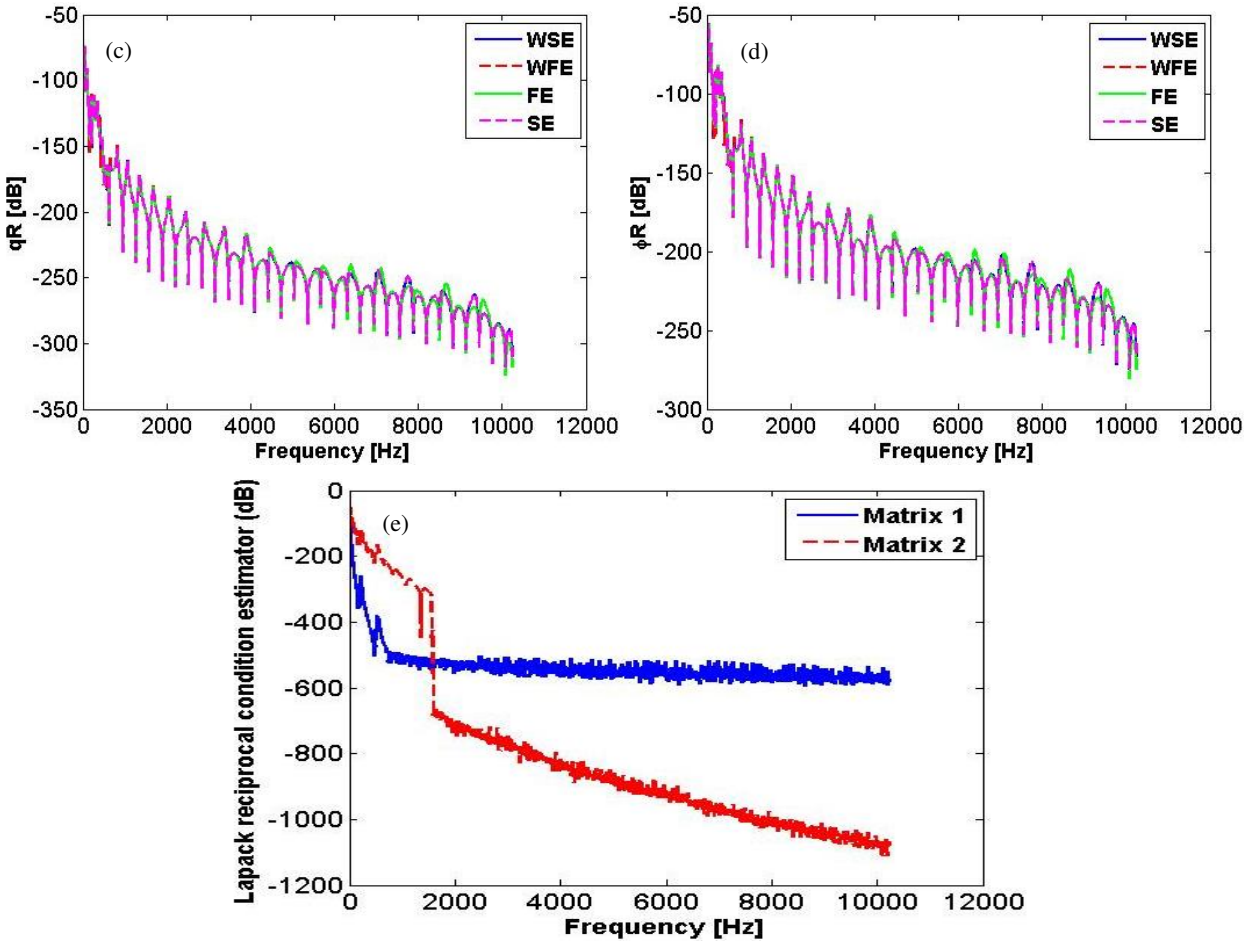


Figure 2: Displacement (a) and rotation (b) of the left side of the EM beam in frequency domain, displacement (c) and rotation (d) of the right side of the EM beam in frequency domain and the ill-conditioning (e) of the matrixes of the Eq. (19) and Eq. (20), called of matrix 1 and matrix 2, respectively.

The forced response of the EM beam was analyzed considering a free-free boundary condition and an excitation force as a cosine-shaped pulse only on the left side of the beam. Figure 2 (a-d) presents the displacement and the rotation of the left side and right side of beam in frequency domain. The ill-conditioning of TM method [26] can be observed in Fig. 2 (e) after 1345 Hz.

The ill-conditioning of the matrices in Eq. (19) and Eq. (20) increases with frequency. This ill-conditioning exists for the beam case mainly because of the evanescence waves and considering free-free boundary condition. Thus, we do not present the results of the TM method for the right side of the beam and for the rest of the results. One can observe from Fig. 2 (a-d) that WFE and FE do not converge with WSE and SE for higher frequencies. The convergence can be achieved increasing the number of finite elements of the unit cell.

In this investigation, we considered six finite and spectral elements per each unit cell, *i.e.* seven nodes per unit cell. Thus, the five arrays of SDOF force-only resonators are attached into the internal five nodes of the unit cell.

The displacement (a-c) and rotation (b-d) of the left side and right side of the beam in frequency domain are also illustrated in Figure (3) in a small range of frequency to see the LR band gaps and the Bragg-type band gap. The first Bragg frequency can be calculated using the Bragg condition $a = n''(\lambda/2)$ or $K_B a = n''\pi$, with $n'' = 1$ and for EB beam theory $K_B = \sqrt{2\pi f}\sqrt[4]{\rho A/EI}$:

$$f_{B_1} = \frac{1}{2\pi}\left(\frac{\pi}{a}\right)^2 \sqrt{\frac{EI}{\rho S}} \cong 461.77 \text{ Hz} \tag{21}$$

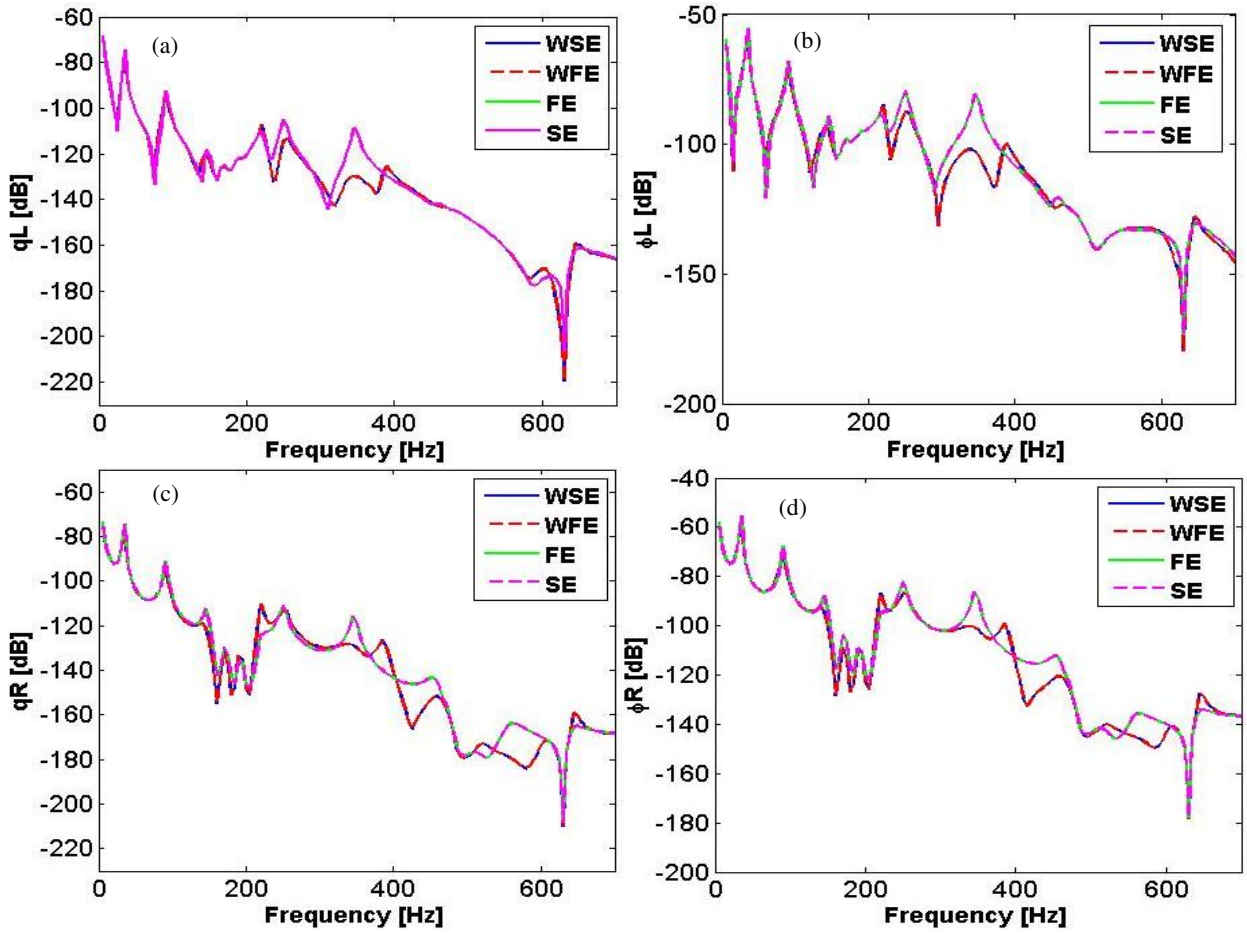


Figure 3: Displacement (a) and rotation (b) of the left side of the EM beam in frequency domain and displacement (c) and rotation (d) of the right side of the EM beam in frequency domain.

Figure (3) illustrates that WFE and WSE do not converge exactly with FE and SE on the resonant frequencies. Furthermore, the LR gaps and the Bragg-type gap are also observed. They can be better analyzed in the transmittance graphic and the attenuation performance is better analyzed in the elastic band structure of the beam.

Figure (4) and Fig. (5) show the displacement receptance and the rotation receptance of the beam, and the displacement transmittance and the rotation transmittance of the beam, respectively.

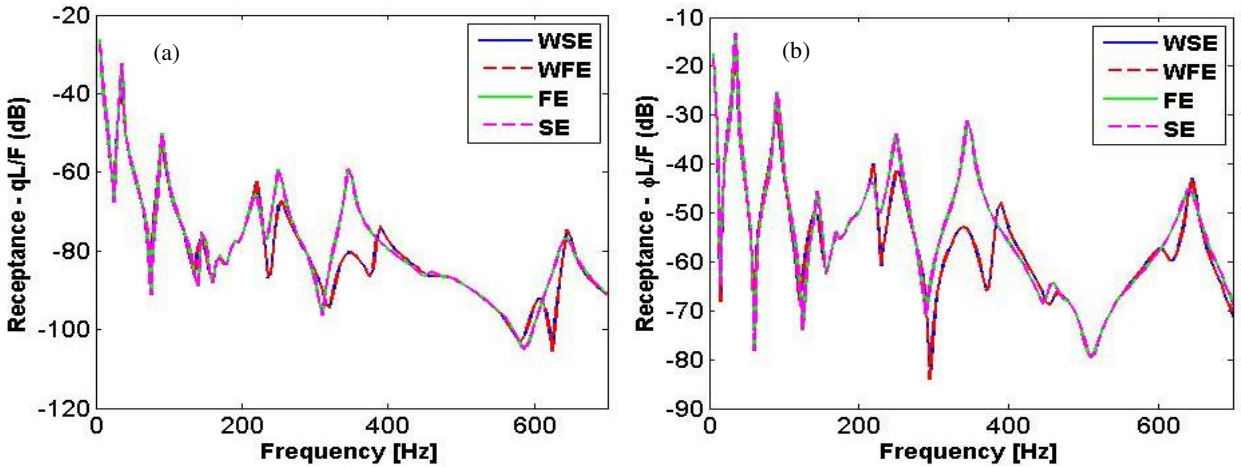

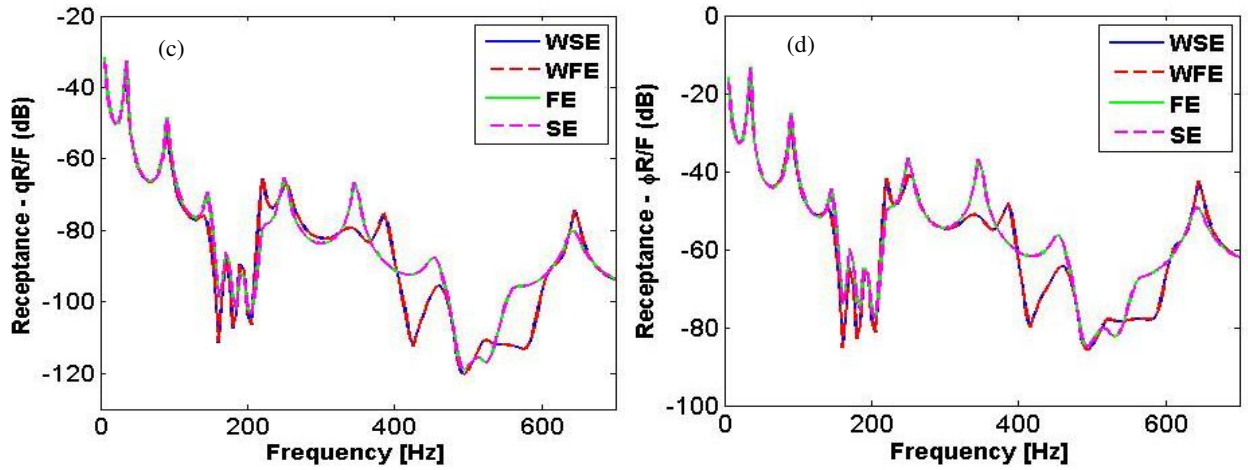


Figure 4: Displacement (a) and rotation (b) receptance of the left side of the EM beam and displacement (c) and rotation (d) receptance of the right side of the EM beam.

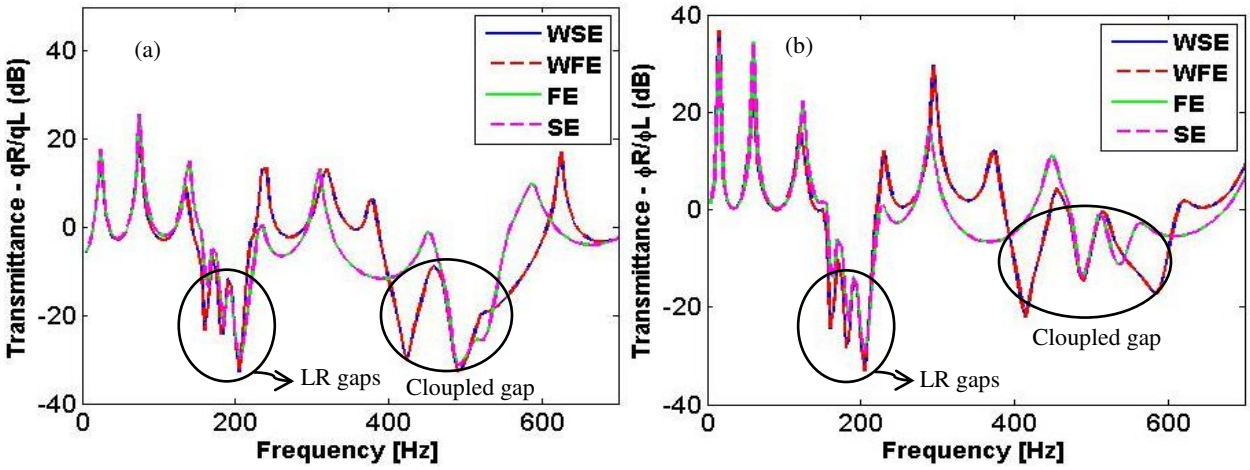


Figure 5: Displacement (a) transmittance and rotation (b) transmittance of the EM beam.

From Fig. 5 (a-b) it is possible to see the LR gaps on the resonant frequencies of $\{160, 180, 200\}$ Hz and it is also possible to see the coupling between the LR gaps on the resonant frequencies of $\{475, 500\}$ and the Bragg-type gap, $461.77$ Hz. The coupling between LR gaps and Bragg-type gap happens because the existence of resonators tuned near to the first Bragg frequency.

The coupling between the Bragg scattering mechanism and the LR mechanism is benefited by widening the gap [28]. The mathematics related to the band gap coupling can be found in Xiao et al. [29].

Figure 6 illustrates the elastic band structure using the WFE, WSE, PWE and EPWE. Figure 6 (a) shows the real part of the reduced Bloch wave vectors, $Ka/\pi$, using WFE, WSE and PWE methods and Figure 6 (b) shows the imaginary part of the reduced Bloch wave vectors using WFE, WSE and EPWE methods.

It is important to highlight that only the smaller imaginary part of the Bloch wave vectors, whose real part – $Re[K(\omega)]$ – lies inside the first Brillouin zone [30], *i.e.* $[-\pi/a\,, \pi/a]$, was considered using the EPWE method because it is the most accurate [31–33]. In addition, in PWE and EPWE calculations, we considered three plane waves in the Fourier series expansion and only the first eight bands are considered to plot the elastic band structure. In Figure 6, we only show the irreducible Brillouin zone (IBZ), $[0, \pi/a]$.

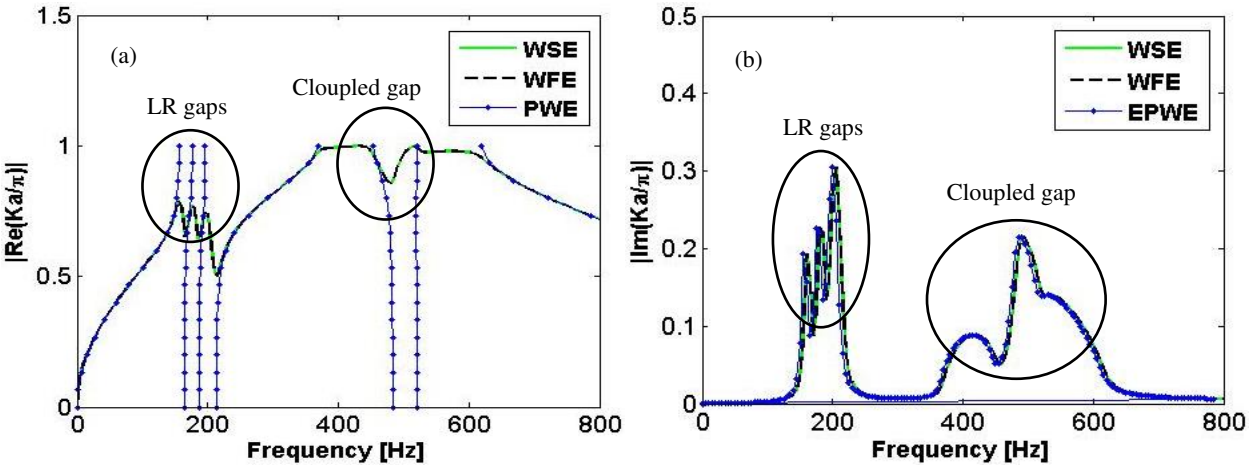


Figure 6: Elastic band structure of the EM beam with five arrays of SDOF force-only resonators. The real part of Bloch wave vectors (a) and the imaginary part of the Bloch wave vectors calculated (b).

From Fig. 6 (a-b) it is possible to see the LR gaps on the resonant frequencies of $\{160, 180, 200\}$ Hz and the coupling between the LR gaps on the resonant frequencies of $\{475, 500\}$ and the Bragg-type gap, 461.77 Hz, as discussed before. It is also possible to obtain the real part of the Bloch wave vector from the EPWE method as illustrated in Figure 7.

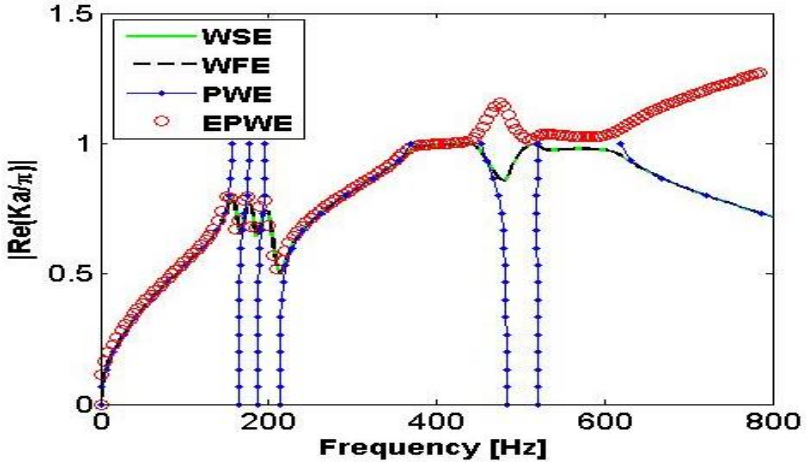


Figure 7: Elastic band structure of the EM beam with five arrays of SDOF force-only resonators. The real part of the Bloch wave vectors calculated.

From Figure 7, one can observe that the real part of the Bloch wave vectors estimated by the EPWE method increases with frequency even after the first Bragg frequency, thus one can compare WFE, WSE, PWE and EPWE methods in Figure 7 until the first Bragg frequency. In addition, the EPWE method is almost always used to estimate the imaginary part of the Bloch wave vectors.

## 3.2 Multiples arrays of MDOF force-only resonators

For multiple arrays of MDOF force-only resonators, we consider in each unit cell five arrays of 2DOF force-only resonators. The parameters of the resonators are: $\left\{\eta_j^{(1)}\right\} = \left\{\eta_j^{(2)}\right\} = \{0.05, 0.05, \ldots, 0.05\}$, $\left\{x_j^{(1)}\right\} = \left\{x_j^{(2)}\right\} = a\ x\ \{1, 2, \ldots, 5\}/6$ m, $\left\{\gamma_j^{(1)}\right\} = 0.5\ x\ \{1.4, 1.2, 1, 0.8, 0.6\}/5$, $\left\{\gamma_j^{(2)}\right\} = 0.5\ x\ \{1, 1, 1, 1, 1\}/5$, $m_j^{(1)} = \gamma_j^{(1)} \rho A a$, $m_j^{(2)} = \gamma_j^{(2)} \rho A a$, $\left\{f_{aj}^{(1)}\right\} = \{160, 275, 475, 500, 600\}$ Hz, $\left\{f_{aj}^{(2)}\right\} = \{70, 135, 185, 200, 320\}$ Hz, $k_j^{(1)} = m_j^{(1)} \left(\omega_{aj}^{(1)}\right)^2$, $k_j^{(2)} = m_j^{(1)} \left(\omega_{aj}^{(2)}\right)^2$, $j = 1, 2 \ldots, 5$, where $\eta_j^{(i)}$ is the loss factor of the $j$th resonator associated with the $i$th DOF, $x_j^{(i)}$ is the position of the $j$th

resonator associated with the *i*th DOF, $\gamma_j^{(i)}$ is the *j*th resonator mass ratio to the mass of the beam in each unit cell associated with the *i*th DOF, the sum of all $\gamma_j^{(i)}$ is equal to 0.5 and $f_{aj}^{(i)}$ are the frequencies used to calculate the resonator spring constant $k_j^{(i)}$ associated with the *i*th DOF. Note that to calculate the resonant frequencies of a 2DOF force-only resonator, one can write:

$$\left(\omega_j^{(1,2)}\right)^2 = \frac{k_j^{(1)}m_j^{(2)} + k_j^{(2)}m_j^{(1)} + k_j^{(2)}m_j^{(2)}}{2m_j^{(1)}m_j^{(2)}} \mp \frac{\sqrt{\left(k_j^{(1)}m_j^{(2)} + k_j^{(2)}m_j^{(1)} + k_j^{(2)}m_j^{(2)}\right)^2 - 4k_j^{(1)}k_j^{(2)}m_j^{(1)}m_j^{(2)}}}{2m_j^{(1)}m_j^{(2)}}, \tag{22}$$

where the resonant frequencies in Hz of the 2DOF *j*th resonator are $f_j^{(1,2)} = \sqrt{\left(\omega_j^{(1,2)}\right)^2}/2\pi$. Applying Eq. (22), the resonant frequencies of the five arrays of 2DOF force-only resonators are approximately $\left\{f_j^{(1,2)}\right\} = \{64.9, 120.9, 170.8, 172.7, 180.4, 254.9, 307.5, 515, 554.8, 754.2\}$ Hz.

Figure (8) shows the displacement transmittance and the rotation transmittance of the EM beam, respectively.

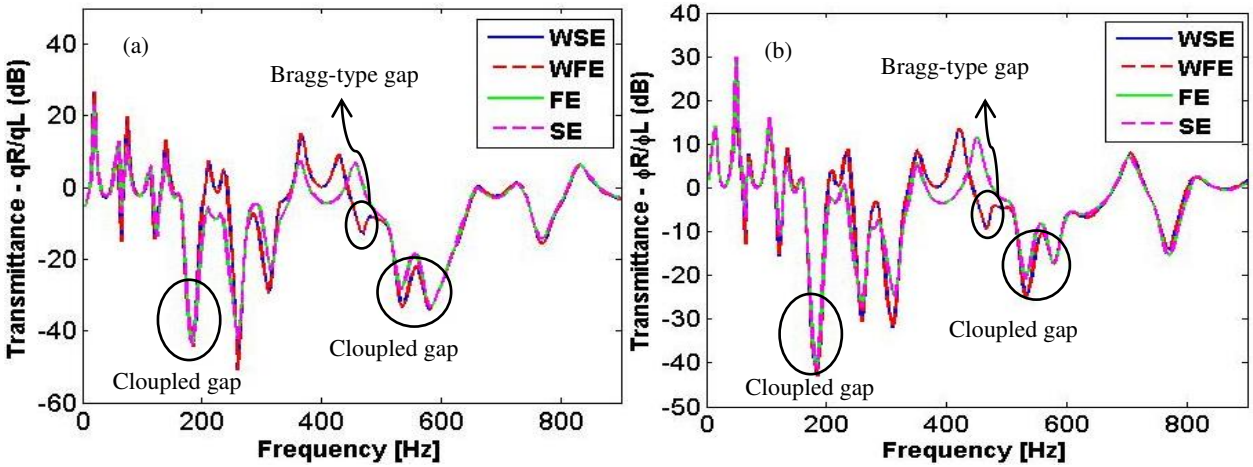


Figure 8: Displacement (a) transmittance and rotation (b) transmittance of the EM beam.

From Fig. 8, one can see the expected LR gaps, the first coupled gap formed by the coupling between three LR gaps, *i.e.* $\{170.8, 172.7, 180.4\}$ Hz, the Bragg-type gap and the second coupled gap formed by the coupling between two LR gaps, *i.e.* $\{515, 554.8\}$ Hz.

Figure 9 (a) shows the real part of the reduced Bloch wave vectors using WFE, WSE and PWE methods and Figure 9 (b) shows the imaginary part of the reduced Bloch wave vectors using WFE, WSE and EPWE methods. From Fig. 9 it is possible to see the same behavior as discussed in Fig. 8.

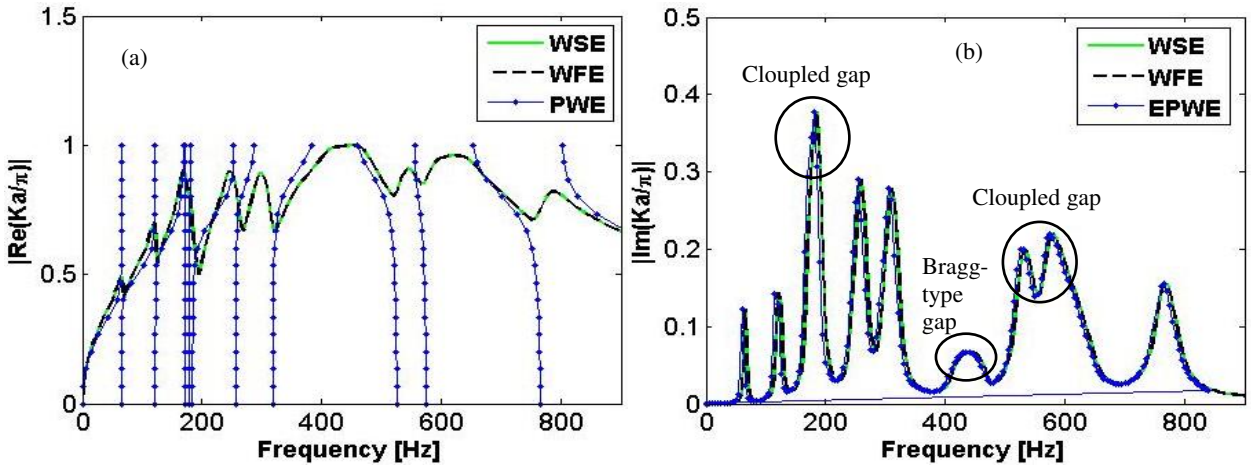


Figure 9: Elastic band structure of the EM beam with five arrays of 2DOF force-only resonators. The real part of Bloch wave vectors (a) and the imaginary part of the Bloch wave vectors calculated (b).

## 4 Conclusions

We have obtained the elastic band structure and the forced response for an EM EB beam with periodic five arrays of SDOF and MDOF LR force-only resonators. We used the WFE, FE, WSE, SE, TM, PWE and EPWE methods, however, the TM method diverges for higher frequencies because of the evanescence waves and the free-free boundary condition.

The EM beam with five arrays of SDOF force-only resonators presented a wide gap created by the coupling between the LR gaps and the Bragg-type gap. For the EM beam with five arrays of 2DOF force-only resonators, we create two wide gaps from the coupling between LR gaps.

The possibility of the coupling between LR gaps and Bragg-type gap with SDOF and MDOF force-only resonators enlarges the potential applications for vibration control.

## Acknowledgements

The authors gratefully acknowledge the Brazilian research funding agency FAPEMA and IFMA for their financial support of this investigation.

## References

[1] M.M. Sigalas, E.N. Economou, *Elastic waves in plates with periodically placed inclusions*, Journal of Applied Physics, Vol. 75, 1994, pp. 2845–2850.

[2] M.S. Kushwaha, P. Halevi, G. Martínez, L. Dobrzynski, B. Djafari-Rouhani, *Theory of acoustic band structure of periodic elastic composites*, Physical Review B, Vol. 49, No. 4, 1994, pp. 2313–2322.

[3] Z.-J. Yao, G.-L. Yu, Y.-S. Wang, Z.-F. Shi, *Propagation of bending waves in phononic crystal thin plates with a point defect*, International Journal of Solids and Structures, Vol. 46, No. 13, 2009, pp. 2571–2576.

[4] Y.-F. Wang, Y.-S. Wang, X.-X. Su, *Large bandgaps of two-dimensional phononic crystals with cross-like holes*, Journal of Applied Physics, Vol. 110, No. 113520, 2011, pp. 1–13.

[5] A. Arreola-Lucas, J. A. Franco-Villafañe, R. A. Méndez-Sánchez, *In-plane vibrations of a rectangular plate: Plane wave expansion modelling and experiment*, Journal of Sound and Vibration, Vol. 342, 2015, pp. 168–176.

[6] E.J.P. Miranda Jr., J.M.C. Dos Santos, *Flexural Wave Band Gaps in Metamaterial Elastic Beam*, *Proceedings of the 23rd ABCM International Congress of Mechanical Engineering*, *Rio de Janeiro*, *2015 December 6-11*, Brazil, pp. 1–8.

[7] V. Anjos, A. Arantes, *Phononic band structure in carbon microtube composites*, RSC Advances, Vol. 5, No. 15, 2015, pp. 11248–11253.

[8] E.J.P. Miranda Jr., J.M.C. Dos Santos, *Phononic Band Gaps in $Al_2O_3$/Epoxy Composite*, *Proceedings of the 60° Brazilian Ceramic Congress*, 2016 *May 15-18*, Águas de Lindóia, São Paulo, Brazil, pp. 1-10.

[9] R.H. Olsson III, I. El-Kady, *Microfabricated phononic crystal devices and applications*, Measurement Science and Technology, Vol. 20, No. 012002, pp. 1–13.

[10] Z. Liu, X. Zhang, Y. Mao, Y.Y. Zhu, Z. Yang, C.T. Chan, *Locally resonant sonic materials*, Science, Vol. 289, 2000, pp. 1734–1736.

[11] Y. Xiao, J. Wen, X. Wen, *Longitudinal wave band gaps in metamaterial-based elastic rods containing multi-degree-of-freedom resonators*, New Journal of Physics, Vol. 14, No. 033042, 2012, pp. 1–20.

[12] D. Yu, Y. Liu, G. Wang, H. Zhao, J. Qiu, *Flexural vibration band gaps in Timoshenko beams with locally resonant structures*, Journal of Applied Physics, Vol. 100, No. 124901, 2006, pp. 1–5.

[13] D. Yu, Y. Liu, H. Zhao, G. Wang, J. Qiu, *Flexural vibration band gaps in Euler-Bernoulli beams with locally resonant structures with two degrees of freedom*, Physical Review B, Vol. 73, No. 064301, 2006, pp. 1–5.

[14] Y. Xiao, J. Wen, X. Wen, *Broadband locally resonant beams containing multiple periodic arrays of attached resonators*, Physics Letters A, Vol. 376, 2012, pp. 1384–1390.

[15] Z. Wang, P. Zhang, Y. Zhang, *Locally resonant band gaps in flexural vibrations of a Timoshenko beam with periodically attached multioscillators*, Mathematical Problems in Engineering, Vol. 2013, No. 146975, 2013, pp. 1–10.

[16] Y. Xiao, J. Wen, D. Yu, X. Wen, *Flexural wave propagation in beams with periodically attached vibration absorbers: band-gap behavior and band formation mechanisms*, Journal of Sound and Vibration, Vol. 332, No. 4, 2013, pp. 867–893.

[17] T. Wang, Mei-Ping Sheng, Qing-Hua Qin, *Multi-flexural band gaps in an Euler-Bernoulli beam with lateral local resonators*, Physics Letters A, Vol. 380, No. 4, 2016, pp. 525–529.

[18] Y. Xiao, J. Wen, X. Wen, *Flexural wave band gaps in locally resonant thin plates with periodically attached spring–mass resonators*, Journal of Physics D: Applied Physics, Vol. 45, No. 19, 2012, 1–12.

[19] J.F. Doyle, *Wave Propagation in Structures: Spectral Analysis Using Fast Discrete Fourier Transforms*. Springer-Verlag, New York (1997), 2nd edition.

[20] D. Duhamel, B.R. Mace, M.J. Brennan, *Finite element analysis of the vibrations of waveguides and periodic structures,* Journal of Sound and Vibration, Vol. 294, 2006, pp. 205–220.

[21] W.X. Zhong, F.W. Williams, *On the direct solution of wave propagation for repetitive structures*, Journal of Sound and Vibration, Vol. 181, 1995, pp. 485–501.

[22] G. Floquet, *Sur les équations différentielles linéaires à coefficients périodiques*, *Annales scientifiques de l'École Normale Supérieure*, 12, 1883, pp. 47-88.

[23] F. Bloch, *Über die Quantenmechanik der Electron in Kristallgittern*, Zeitschrift für Physik, Vol. 52, 1928, pp. 550–600.

[24] J.-M. Mencik, *On the low- and mid-frequency forced response of elastic structures using wave finite elements with one-dimensional propagation*, Computers and Structures, , Vol. 88, 2010, pp. 674–689.

[25] G.J. Golub, C.F.V. Loan, *Matrix computations*. Baltimore/London. The Johns Hopkins University Press, 1996.

[26] R. Uhrig, *The transfer matrix method seen as one method of structural analysis among others,* Journal of Sound and Vibration, Vol. 4, No. 2, 1966, pp. 136–148.

[27] Y.C. Hsue, A.J. Freeman, B.Y. Gu, *Extended plane-wave expansion method in three-dimensional anisotropic photonic crystals*, Physical Review B, Vol. 72, No. 195118, 2005, pp. 1–10.

[28] D. Yu, J. Wen, H. Zhao, Y. Liu, X. Wen, *Vibration reduction by using the idea of phononic crystals in pipe-conveying fluid,* Journal of Sound and Vibration, Vol. 318, 2008, pp. 193–205.

[29] Y. Xiao, B.R. Mace, J. Wen, X. Wen, *Formation and coupling of band gaps in a locally resonant elastic system comprising a string with attached resonators,* Physical Letters A, Vol. 375, 2011, pp. 1485–1491.

[30] L. Brillouin, *Wave Propagation in Periodic Structures.* Dover Publications, New York (1946).

[31] V. Romero-García, J.V. Sánchez-Pérez, L.M. Garcia-Raffi, *Evanescent modes in sonic crystals: Complex dispersion relation and supercell approximation*, Journal of Applied Physics, Vol. 108, No. 044907, 2010, pp. 1-6.

[32] V. Romero-García, J.V. Sánchez-Pérez, S. Castiñeira-Ibáñez, L.M. Garcia-Raffi, *Evidence of evanescent Bloch waves in phononic crystals*, Applied Physics Letters, Vol. 96, No. 124102, 2010, pp. 1-3.

[33] V. Romero-García, J.V. Sánchez-Pérez, L.M. Garcia-Raffi, *Propagating and evanescent properties of double-point defects in sonic crystals*, New Journal of Physics, Vol. 12, No. 083024, 2010, pp. 1-14.

# APPENDIX G – Full Paper in Conference Proceedings

# FLEXURAL WAVE BAND GAPS IN A MULTI-RESONATOR ELASTIC METAMATERIAL THIN PLATE

Miranda Júnior, E.J.P.[a,b], Ferreira, A.H.R.[a] and Dos Santos, J.M.C.[a]

[a] *University of Campinas, UNICAMP-FEM-DMC-LVA, Mendeleyev Street, 200, 13083970, Campinas, SP, Brazil.*
[b] *Federal Institute of Education, Science and Technology of Maranhão, IFMA-CCH-NIB-DEP, Afonso Pena Street, 174, 65010030, São Luís, MA, Brazil.*
*E-mail of the corresponding author: edson.jansen@ifma.edu.br*

**ABSTRACT**
During the last few decades many researches have been interested in the field of wave propagation in periodic composite systems known as phononic crystals. Recently, a new type of phononic crystal was proposed, namely locally resonant phononic crystal, also known as elastic metamaterial. The main difference between phononic crystals and elastic metamaterials is that the latter present locally resonant band gaps arising in the vicinity of local resonators natural frequencies while Bragg-type band gaps typically occur at wavelengths of the order of the unit cell size. We investigate theoretically the band structure of flexural waves propagating in an elastic metamaterial thin plate. The classical theory of thin plate, Kirchhoff-Love theory, is considered. We study the influence of periodic arrays of multiple degrees of freedom local resonators in square and triangular lattices. The plane wave expansion and the extended plane wave expansion methods, also known as $\omega(\mathbf{k})$ and $\mathbf{k}(\omega)$, respectively, are used to solve the governing equation of motion for a thin plate. The locally resonant band gaps for square and triangular lattices present almost the same attenuation for all examples analysed. However, the square lattice presents broader Bragg-type band gaps with higher attenuation than triangular lattice. An elastic metamaterial plate with attached double periodic arrays of S-DOF resonators and with attached single periodic array of 2-DOF resonator tuned at the same frequencies, 102 hz and 283 Hz, presents different attenuation performance for locally resonant and Bragg-type band gaps. We find the coupling between locally resonant band gaps for resonators tuned at 70 Hz and 102 Hz. The application of a multi-resonator elastic metamaterial thin plate enlarges its potential for vibration control.

**KEYWORDS:** elastic metamaterial thin plate, flexural wave band gaps, multiple degrees of freedom, vibration control.

## 1. INTRODUCTION

Over the last decades, artificial composites known as phononic crystals (PCs), consisting of a periodic array of scatterers (inclusions) embedded in a host medium (matrix), have been quite studied [1, 2, 3, 4, 5, 6, 7, 8, 9]. They have received renewed attention because they exhibit band gaps where the mechanical (elastic or acoustic) wave propagation is forbidden. The physical origin of phononic and photonic band gaps can be understood at micro-scale using the classical wave theory to describe the Bragg and Mie resonances, respectively, based on the scattering of mechanical and electromagnetic waves propagating within the crystal [10].
In PC investigation, the band gap formation is based on the Bragg scattering mechanism, whose frequency location is governed by the Bragg law $a = n(\lambda/2), (n = 1, 2, \ldots)$ where $a$ is the lattice parameter of periodic system, and $\lambda$ is the wavelength in host material. Bragg law implies that it is difficult to achieve a low-frequency Bragg-type band gap for small size PCs. Difficulties to create PCs with low frequency band gaps for small sizes instigated researchers to explore others dissipative mechanisms together with periodicity effect. In 2000, Liu and co-workers [11] proposed a locally resonant PC, also known as elastic metamaterial (EM), containing an array of localized resonant structures. This resonance-type band gaps were obtained in a frequency range two orders of magnitude lower than that given by the Bragg limit. Locally resonant band gaps arise on the vicinity of local resonator natural frequency while Bragg-type band gaps typically occur at wavelengths of the order of unit cell size.

EM have been proposed as acoustic barriers [12, 13], vibration isolators [14] and noise suppression devices [15, 16] with emphasis on low frequency applications. There are various types of elastic structures being investigated containing an array of local resonators, such as rods [17, 18, 19], beams [20, 21, 22, 23, 24, 25, 26, 27, 28, 29, 30, 31, 32], plates [33, 34, 35, 36, 37, 38, 39] and shells [40]. These local resonators can be modelled by spring-mass resonators of S-DOF [17, 20, 21, 23, 24, 25, 28, 29, 33, 34, 35, 36, 38, 40] or M-DOF [18, 19, 22, 26, 27, 30, 31, 32, 37, 41, 42].

The main purpose of this paper is to investigate the elastic band structure, also known as dispersion diagram, of flexural waves propagating in an EM thin plate with multiple periodic arrays of attached multiple degrees of freedom (M-DOF) resonators, considering square and triangular lattices. Kirchhoff-Love plate theory [43, 44] is applied for thin plate modelling. The plane wave expansion (PWE) [1, 2] and extended plane wave expansion (EPWE) [45, 46, 47, 48, 49, 50, 51] methods, also known as $\omega(\mathbf{k})$ and $\mathbf{k}(\omega)$, respectively, are used to predict the complex band structure of the EM thin plate.

### 1.1. Elastic Metamaterial Thin Plate Modelling

PWE and EPWE are semi-analytical methods used to predict the band structure of PCs and EMs. The advantage of using the EPWE method is because the evanescent modes are obtained naturally and these modes are not ignored as well as the PWE method. In contrast to the PWE method, which assumes that $k$ is real ($\mathbf{k}$ is the Bloch wave vector, also known as wavenumber, and $k = ||\mathbf{k}||$), EPWE method is not restricted from the start to the first Brillouin [52] zone [48]. Hsue and co-workers [47] proved that the evanescent modes obtained by EPWE obey the Floquet-Bloch's theorem [53, 54]. Xiao and co-workers [35] developed the PWE and EPWE formulations applied to EM thin plate with multiple periodic arrays of attached S-DOF local resonators. We expanded the formulation of Xiao *et al.* [35] for an EM thin plate with multiple periodic arrays of attached M-DOF resonators. However, this formulation will be published by the authors in due course. For details of PWE and EPWE formulations applied to an EM thin plate with S-DOF resonators, see Xiao *et al.* [35].

Figure 1 shows an infinite plate with multiple periodic arrays of attached S-DOF spring-mass local resonators for square $(a)$ and triangular $(b)$ lattices, and its irreducible Brillouin zone (in shaded region) $(c)$, $(d)$, respectively. The IBZ points in Figure 1 ($c$-$d$) are $\Gamma$ $(0,0)$, X $(\pi/a,0)$ and M $(\pi/a,\pi/a)$ for square lattice and $\Gamma$ $(0,0)$, X $(4\pi/3a,0)$ and M $(\pi/a,\pi/\sqrt{3}a)$ for triangular lattice. Triangular lattice is a type of hexagonal lattice. There are three variations of hexagonal lattice: triangular, honeycomb (or graphite) and Kagomé lattices [57].

In order to deal with an EM thin plate, an appropriate conditions for the validity of thin plate theory can be assumed $h < \lambda/6$ [55] or $kh \ll 1$, $h/a \ll 1$ [56], where $\lambda = 2\pi/k$ and $h$ is the plate thickness.

### 1.2. Simulated Examples

To verify the PWE and EPWE methods formulated with Kirchhoff-Love plate theory and to demonstrate its capacity of calculating the complex band structure of an infinity EM thin plate with attached periodic array of M-DOF local resonators, simulated examples are performed in this section. It is important to highlight that we apply a criterion for tracking the frequency evolution of wave modes when EPWE method is used. We choose the model assurance criterion (MAC) for estimating the correlation among wave shapes. This criterion is based on the hermitian scalar product and it is useful for very low frequencies [58]. For all PWE and EPWE calculations from now on, 81 plane waves are used in the Fourier series expansion. This resulted in a good convergence.

The EM plate geometry and material properties are shown in Table 1. They are chosen to be the same as used by Xiao *et al.* [35] for the simplest case (EM thin plate with attached single periodic array of S-DOF local resonator), in order to facilitate comparisons. The local resonators are localized on the middle of unit cell for all simulated

Table 1 – Metamaterial plate geometry and material properties.

| Geometry/Property | Value |
|---|---|
| Lattice parameter ($a$) | 0.1 m |
| Unit cell area for square lattice ($S = a^2$) | 0.01 m$^2$ |
| Unit cell area for triangular lattice ($S = a^2\sqrt{3}/2$) | 0.0087 m$^2$ |
| Thickness ($h$) | 0.002 m |
| Young's modulus ($E$) | $70 \times 10^9$ Pa |
| Mass density ($\rho$) | 2700 kg/m$^3$ |
| Structural damping ($\eta$) | 0.01 |
| Poisson's ratio ($\nu$) | 0.3 |

examples. The influence of resonator position will be discussed in a further publication. Each resonator has stiffness

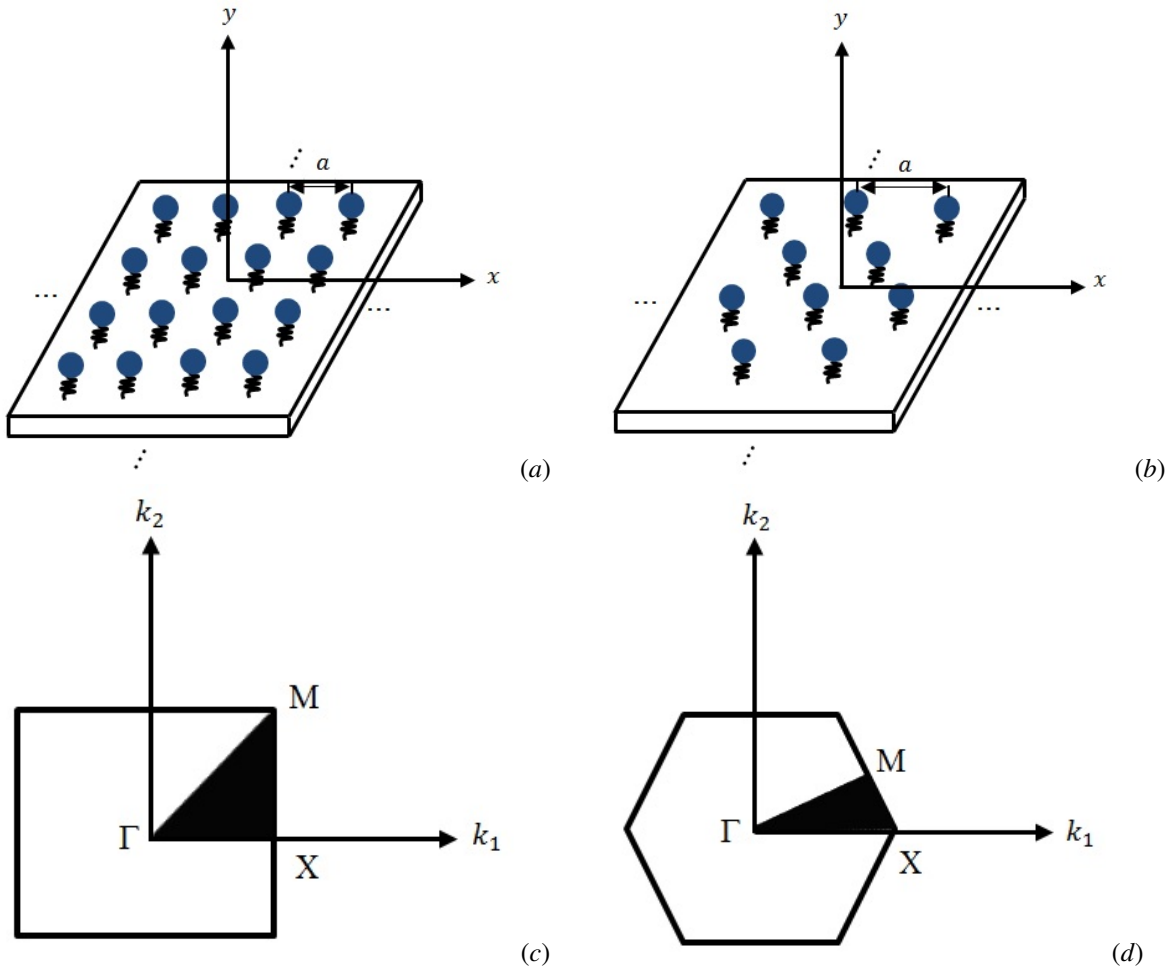


Figure 1 – Infinite elastic metamaterial plate with multiple periodic arrays of attached S-DOF resonators for $(a)$ square and $(b)$ triangular lattices. The irreducible Brillouin zone (in shaded region) for $(c)$ square and $(d)$ triangular (d) lattices.

$k_j^{(i)}$ and a mass $m_j^{(i)}$, where $j = 1,2,\ldots,N$ is the index related to the $j$-th resonator and $i = 1,2,\ldots,\bar{N}$ is the index related to the $i$-th DOF in the $j$-th resonator.

### 1.2.1. *Metamaterial plate with attached single periodic array of S-DOF resonator*

The S-DOF local resonator has a natural frequency $f_1^{(1)} = 300$ Hz, mass $m_1^{(1)} = \gamma_1^{(1)} \rho S a$, where $\gamma_1^{(1)} = 0.5$ is the ratio of resonator mass to the plate unit cell mass. The resonator stiffness is calculated by $k_1^{(1)} = m_1^{(1)}(2\pi f_1^{(1)})^2(1 + i\eta_1^{(1)})$, where $\eta_1^{(1)} = 0.05$ is the resonator damping, also known as loss factor.

Figure 2 $(a$-$b)$ shows the real band structure of the EM thin plate for square $(a)$ and triangular lattices $(b)$ calculated by PWE method. This band structure for square lattice agrees with the results of Xiao and co-workers [35]. We plot the real band structure in the three principal symmetry directions of the IBZ. The plots are given in terms of frequency in Hz versus the real part of the reduced Bloch wave vector defined as $\mathbf{k}a/2\pi$. One complete band gap is found around the resonant frequency of 300 Hz for both lattices. This band gap is known as locally resonant band gap.

The Bragg-type gap is predicted by Bragg's law along different directions, $a = n(\lambda/2\cos\phi)$, with $n \in \mathbb{Z}$. For a thin plate, the first Bragg frequency, $n = 1$, is given by:

$$f_{B_1} = \frac{1}{2\pi}\left(\frac{\pi}{a\cos\phi}\right)^2\sqrt{\frac{D}{\rho h}} = \frac{1}{2\pi}\left\{\frac{\pi}{a\cos[\arctan(k_2/k_1)]}\right\}^2\sqrt{\frac{D}{\rho h}}, \tag{1}$$

where $k_1$ and $k_2$ are the Bloch wave vector components on the $x$ and $y$ directions, respectively, and $D = Eh^3/12(1-\nu^2)$ is the plate bending stiffness.

The first Bragg frequency for square lattice, along ΓX direction ($\phi = 0°$), calculated by Eq. (1) is 484 Hz and it can be observed in Fig. 2 $(a)$. This Bragg-type band gap creates a directional band gap along ΓX direction. Along

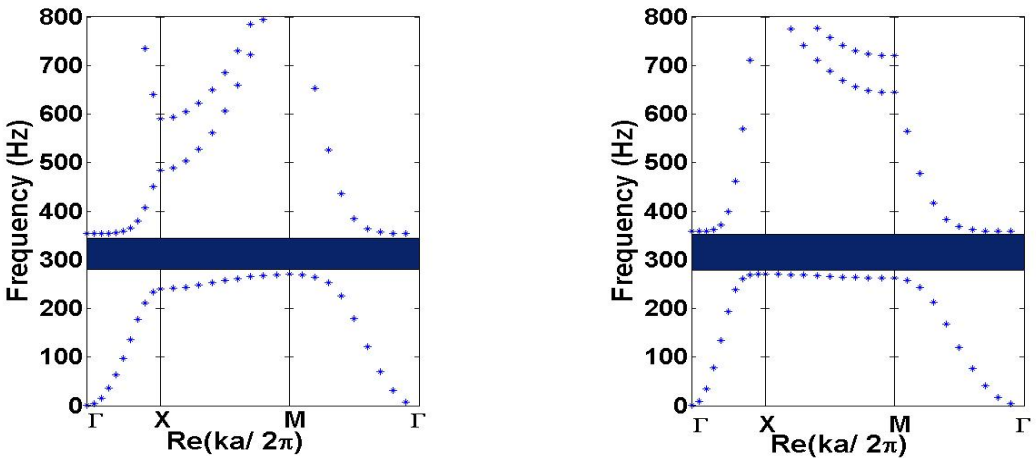


Figure 2 – Real band structure of EM thin plate for $(a)$ square and $(b)$ triangular lattices with $f_1^{(1)} = 300$ Hz.

MΓ direction ($\phi = 45°$) in Fig. 2 $(a)$, the first Bragg frequency is 968 Hz. However, along XM direction we have a variation of $\phi$, thus $f_{B_1}$ varies. For triangular lattice, the first Bragg frequency along MΓ direction ($\phi = 30°$) is 645.4 Hz and a directional band gap is opened up, as illustrated in Fig. 2 $(b)$.
Fig. 3 compares the real band structure of square and triangular lattices. We observe that the triangular lattice presents a broader complete band gap than square lattice. The bandwidth for triangular lattice is 89.4 Hz while the bandwidth for square lattice is 84.3 Hz.

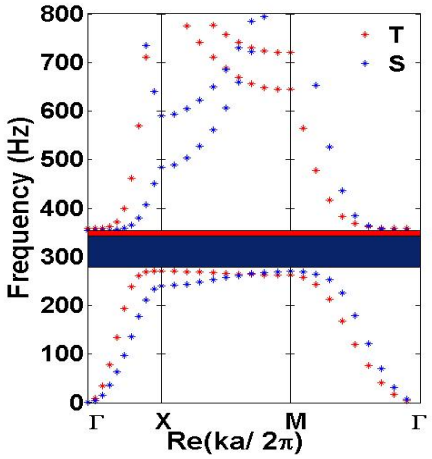


Figure 3 – Comparison of real band structures of EM thin plate for square (S) and triangular (T) lattices with $f_1^{(1)} = 300$ Hz.

Figure 4 $(a$-$b)$ illustrates the imaginary band structure for the square and for triangular lattices, respectively, calculated by EPWE method, considering $f_1^{(1)} = 300$ Hz. The attenuation is related to the imaginary part of the Bloch wave vector by $\mu = \mathrm{Im}\{k\}a$.
In Figure 4 $(a$-$b)$, we consider only the smallest positive imaginary part of the reduced Bloch wave vector (lowest component whose real part of the reduced Bloch wave vector lies inside and around the IBZ is the most accurate), since it represents the least rapidly decaying wave (evanescent Bloch wave [49, 50, 51]) that carries energy the farthest [35]. The imaginary band structure for the square lattice in Figure $(a)$ agrees with Xiao and co-workers [35] results. From Figure 4 $(a$-$b)$, it can be seen the locally resonant and the Bragg-type band gaps for square and triangular lattices in different directions. These results complement the real band structure for the square and for triangular lattices illustrated in Figure 3 $(a$-$b)$.
Figure 5 compares the attenuation performance of square and triangular lattices. The attenuation related to the triangular lattice is little higher than square lattice. However, the attenuation of the Bragg-type band gap is higher

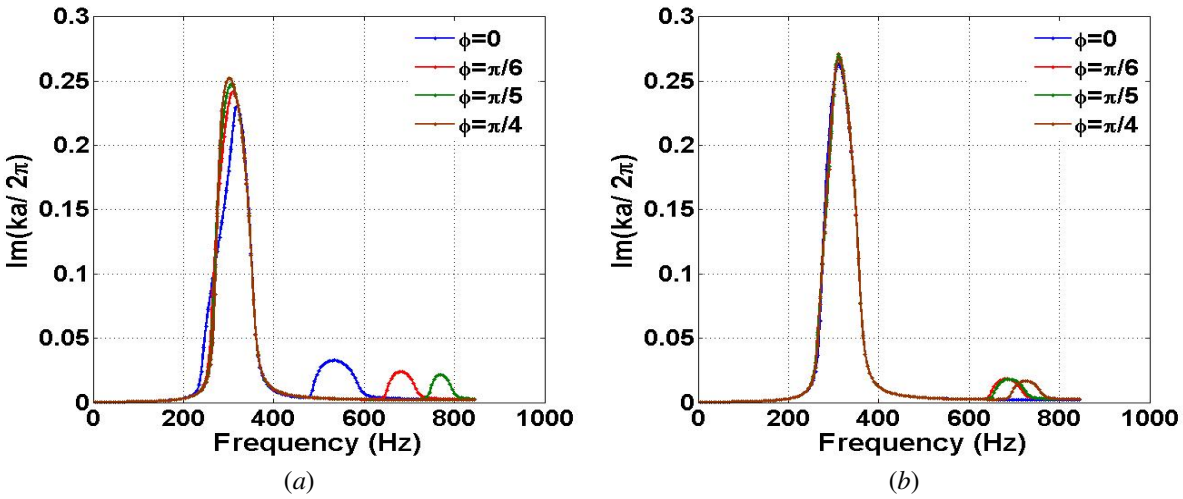


Figure 4 – Imaginary elastic band structures of EM thin plate for $(a)$ square and $(b)$ triangular lattices with $f_1^{(1)} = 300$ Hz.

for square lattice. The locally resonant band gap for triangular lattice do not vary with $\phi$, differently from square lattice.

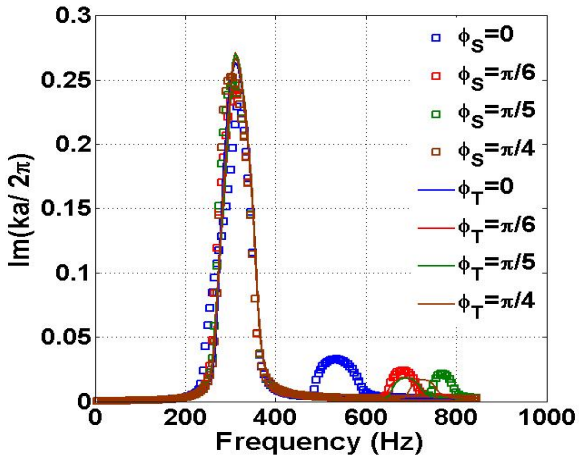


Figure 5 – Comparison of imaginary band structures of EM thin plate for square ($\phi_S$) and triangular ($\phi_T$) lattices with $f_1^{(1)} = 300$ Hz.

### 1.2.2. *Metamaterial plate with attached multiple periodic arrays of S-DOF resonators*

The S-DOF local resonators parameters are $f_j^{(1)} = \{283, 102\}$ Hz, $\gamma_j^{(1)} = \{0.6, 0.4\}$, $m_j^{(1)} = \gamma_j^{(1)} \rho S a$, $\eta_j^{(1)} = 0.05$ and $k_j^{(1)} = m_j^{(1)}(2\pi f_j^{(1)})^2(1 + i\eta_j^{(1)})$, where $j = 1, 2$. The sum of all resonator mass ratio to the mass is equal to 0.5, the same of EM plate with attached single periodic array of S-DOF resonator.

Figure 6 $(a$-$b)$ shows the real band structure of the EM thin plate with attached double periodic arrays of S-DOF resonators for square $(a)$ and triangular $(b)$ lattices. It can be seen the locally resonant band gaps on the natural frequencies (283 Hz and 102 Hz). The resonator with natural frequency 283 Hz opened up the broadest complete band gap for both lattices. The band gap related to the natural frequency 283 Hz is broader for square lattice than triangular lattice, differently from EM plate with attached single periodic array of S-DOF resonator (see Figure 3).

Figure 7 $(a$-$b)$ illustrates the imaginary band structure for the square $(a)$ and for triangular $(b)$ lattices, respectively, considering $f_j^{(1)} = \{283, 102\}$ Hz. It can be seen the attenuation performance of the two locally resonant and the Bragg-type band gaps for square and triangular lattices in different directions. The highest attenuation is related to the resonator with 283 Hz for both lattices.

Figure 8 compares the attenuation performance of square and triangular lattices. The square and triangular lattices

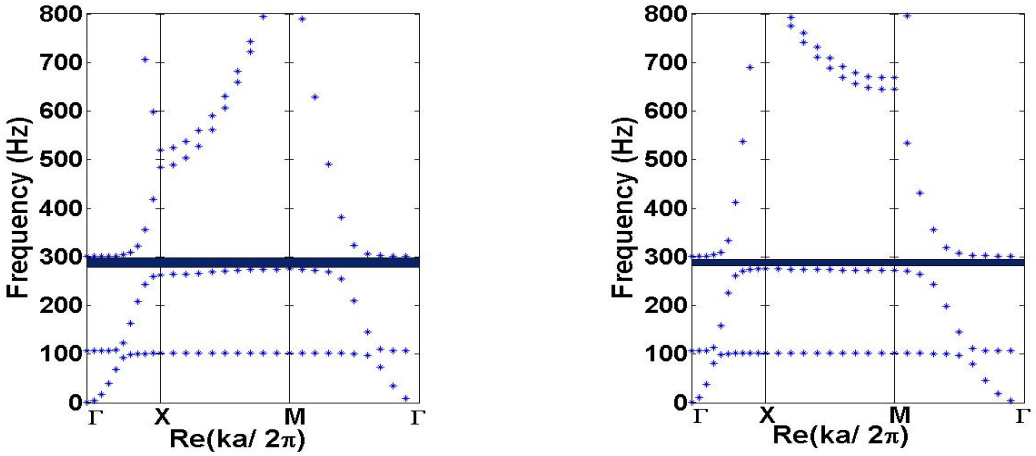


(a) (b)

Figure 6 – Real band structure of EM thin plate with attached double periodic arrays of S-DOF resonators for $(a)$ square and $(b)$ triangular lattices with $f_j^{(1)} = \{283, 102\}$ Hz.

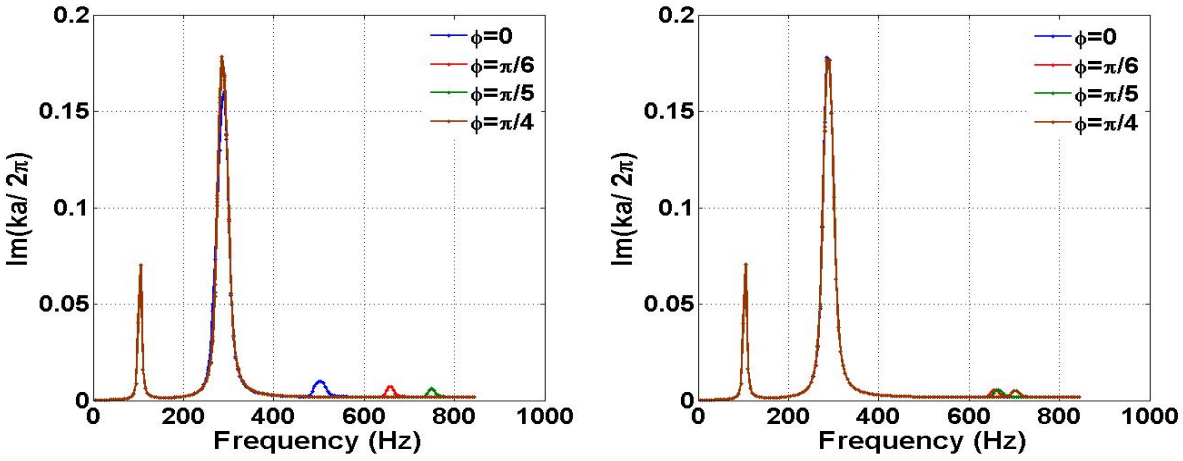


(a) (b)

Figure 7 – Imaginary band structures of EM thin plate with attached double periodic arrays of S-DOF resonators for $(a)$ square and $(b)$ triangular lattices with $f_j^{(1)} = \{283, 102\}$ Hz.

present almost the same attenuation performance on the locally resonant band gaps and the attenuation related to the Bragg-type band gap is higher for square lattice.

One can note that the locally resonant and Bragg-type band gaps of EM plate with attached single periodic array of S-DOF resonator presents higher attenuation and are broader than the band gaps of EM plate with attached multiple periodic arrays of S-DOF resonators.

### 1.2.3. *Metamaterial plate with attached single periodic array of M-DOF resonator*

We consider an EM plate with attached single periodic array of 2-DOF resonator. The 2-DOF resonator parameters are $\gamma_1^{(i)} = \{0.5, 0.5\}$, $m_1^{(i)} = \gamma_1^{(i)} \rho Sa$, $k_1^{(1)} = m_1^{(1)}(2\pi \times 160)^2(1 + i\eta_1^{(1)})$, $k_1^{(2)} = m_1^{(2)}(2\pi \times 180)^2(1 + i\eta_1^{(2)})$ and $\eta_1^{(i)} = \{0.05, 0.05\}$, where $i = 1, 2$. The resonator frequencies are calculated by:

$$\omega_1^{(i)^2} = \frac{(k_1^{(1)}m_1^{(2)} + k_1^{(2)}m_1^{(1)} + k_1^{(2)}m_1^{(2)}) \mp \sqrt{(k_1^{(1)}m_1^{(2)} + k_1^{(2)}m_1^{(1)} + k_1^{(2)}m_1^{(2)})^2 - 4k_1^{(1)}k_1^{(2)}m_1^{(1)}m_1^{(2)}}}{2m_1^{(1)}m_1^{(2)}}, \qquad (2)$$

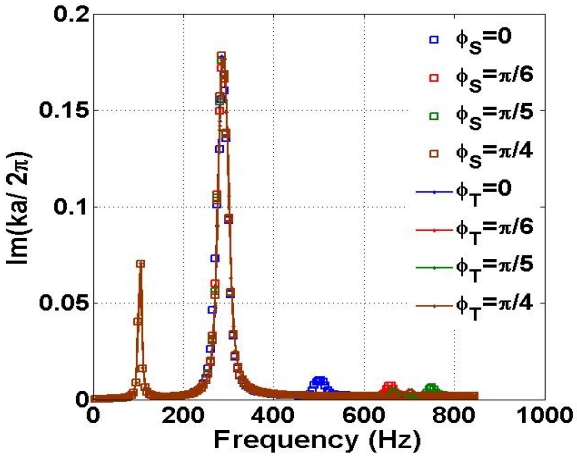


Figure 8 – Comparison of imaginary elastic band structures of EM thin plate with attached double periodic arrays of S-DOF resonators for square ($\phi_S$) and triangular ($\phi_T$) lattices with $f_j^{(1)} = \{283, 102\}$ Hz.

where $\omega_1^{(i)} = 2\pi f_1^{(i)}$, which results $f_1^{(i)} = \{102, 283\}$ Hz. We choose the same natural frequencies of the EM plate with attached double periodic arrays of S-DOF resonators in order to compare.
Figure 9 $(a\text{-}b)$ shows the real band structure of the EM thin plate with attached single periodic array of 2-DOF resonator for square $(a)$ and triangular $(b)$ lattices. The locally resonant band gap related to $f_1^{(2)} = 283$ Hz is

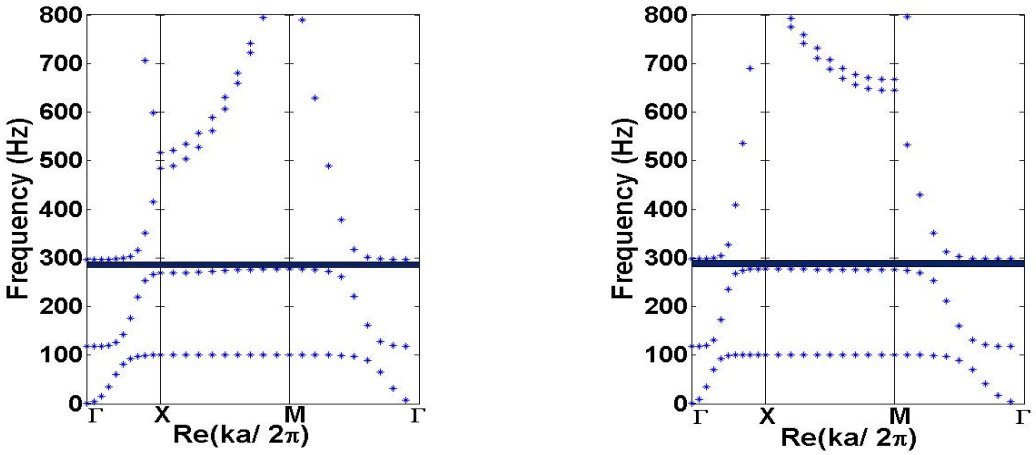


Figure 9 – Real band structure of EM thin plate with attached single periodic array of 2-DOF resonator for $(a)$ square and $(b)$ triangular lattices with $f_1^{(i)} = \{102, 283\}$ Hz.

broader than the band gap related to $f_1^{(1)} = 102$ Hz. Besides, the locally resonant band gap related to $f_1^{(2)} = 283$ Hz is broader for triangular lattice than square lattice, differently from the behaviour in Figure 6.
Figure 10 $(a\text{-}b)$ illustrates the imaginary band structure for the square and for triangular lattices, respectively. One can see that the higher attenuation is associated with the first natural frequency, 102 Hz, differently from the behaviour illustrated in Figure 7.
Figure 11 compares the attenuation performance of square and triangular lattices. The square and triangular lattices present almost the same attenuation performance on the locally resonant band gaps.
Figure 12 shows the imaginary band structure of an EM thin plate comparing two cases analysed: (I) with attached double periodic arrays of 1-DOF resonators ($\phi_{1\text{DOF}}$) and (II) with attached single periodic array of 2-DOF resonator ($\phi_{2\text{DOF}}$). Both cases consider $f_j^{(1)} = \{283, 102\}$ Hz and $f_1^{(i)} = \{102, 283\}$ Hz. We can observe that the case (II) presents the highest attenuation on 102 Hz for both lattices. The case (I) presents higher attenuation than case (II) on 283 Hz, however, this attenuation is still lower than the attenuation on 102 Hz for case (I). The attenuation of

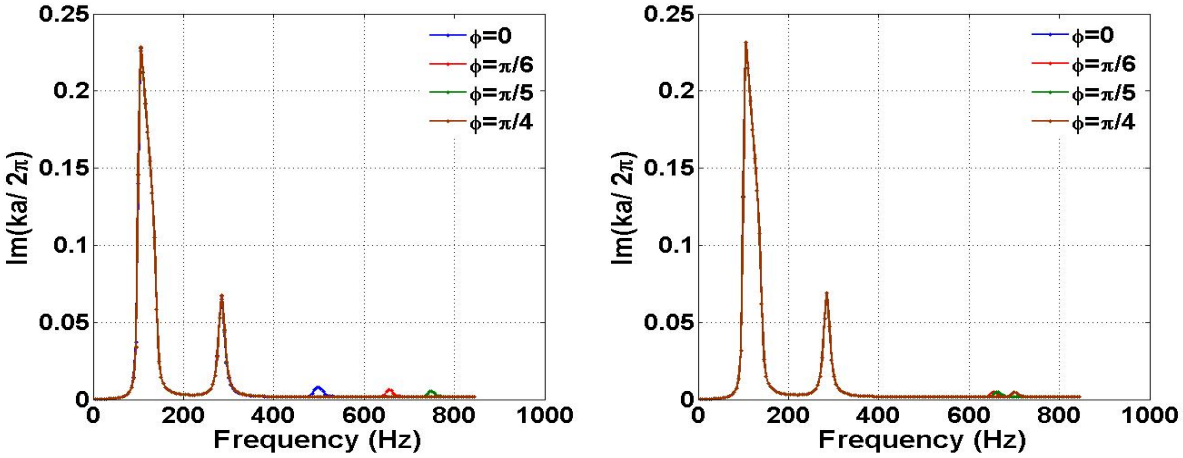


Figure 10 – Imaginary band structures of EM thin plate with attached single periodic array of 2-DOF resonator for $(a)$ square and $(b)$ triangular lattices with $f_1^{(i)} = \{102, 283\}$ Hz.

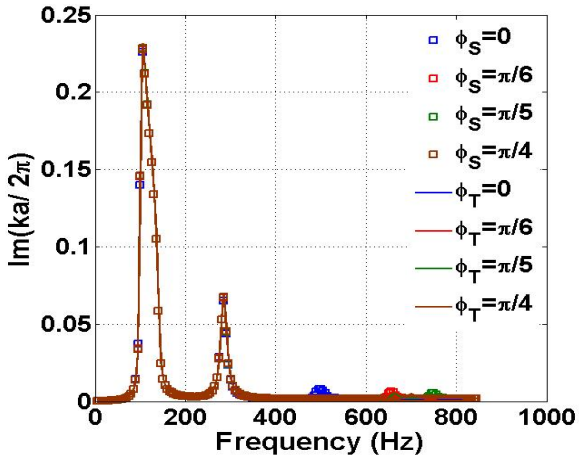


Figure 11 – Comparison of imaginary band structures of EM thin plate with attached single periodic array of 2-DOF resonator for square ($\phi_S$) and triangular ($\phi_T$) lattices with $f_1^{(i)} = \{102, 283\}$ Hz.

the Bragg-type band gaps is little higher for case (I) than case (II).

### 1.2.4. *Metamaterial plate with attached multiple periodic arrays of M-DOF resonators*

We consider an EM plate with attached double periodic arrays of 2-DOF resonators. The 2-DOF resonators parameters are $\gamma_j^{(i)} = \{0.5, 0.5, 0.5, 0.5\}$, $m_j^{(i)} = \gamma_j^{(i)} \rho S a$, $k_1^{(1)} = m_1^{(1)}(2\pi \times 160)^2(1 + i\eta_1^{(1)})$, $k_1^{(2)} = m_1^{(2)}(2\pi \times 180)^2(1 + i\eta_1^{(2)})$, $k_2^{(1)} = m_2^{(1)}(2\pi \times 100)^2(1 + i\eta_2^{(1)})$, $k_2^{(2)} = m_2^{(2)}(2\pi \times 300)^2(1 + i\eta_2^{(2)})$ and $\eta_j^{(i)} = \{0.05, 0.05, 0.05, 0.05\}$. The resonator frequencies are calculated by Eq. (1), which give $f_1^{(1)} = 102$ Hz, $f_1^{(2)} = 283$ Hz, $f_2^{(1)} = 70$ Hz and $f_2^{(2)} = 430.5$ Hz.

Figure 13 $(a\text{-}b)$ illustrates the real band structure of the EM thin plate with attached double periodic arrays of 2-DOF resonators for square $(a)$ and triangular lattices $(b)$. We observe four locally resonant band gaps associated with each natural frequency.

Figure 14 $(a\text{-}b)$ illustrates the imaginary band structure for the square and for triangular lattices, respectively. One can see that the highest attenuation is associated with the first natural frequencies, 70 Hz and 102 Hz, similar to the behaviour illustrated in Figure 10. Besides, the locally resonant band gaps on 70 Hz and 102 Hz start coupling. The band gap associated with 430.5 Hz have almost no attenuation.

Figure 15 compares the attenuation performance of square and triangular lattices. The square and triangular lattices

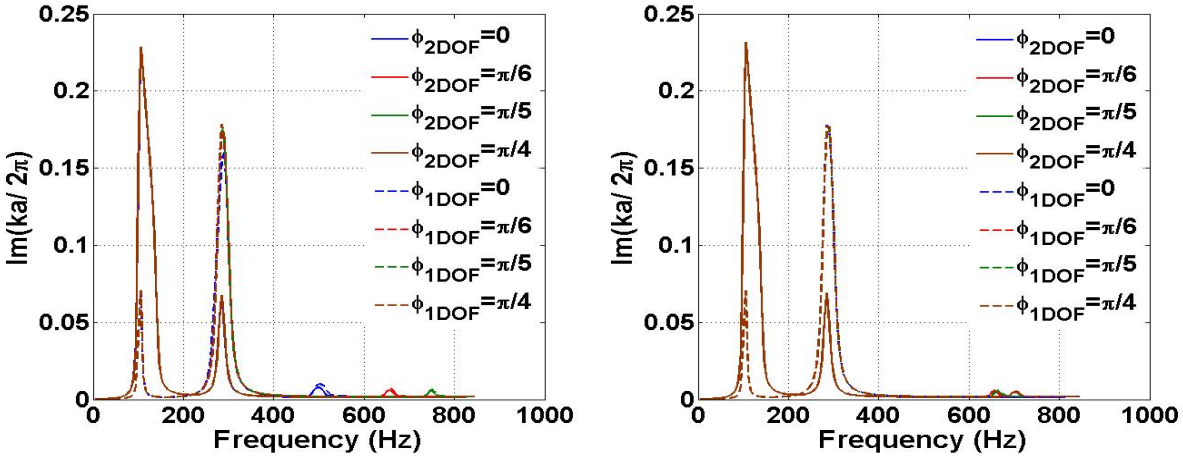


(*a*) (*b*)

Figure 12 – Comparison of imaginary band structures of EM thin plate with attached double periodic arrays of 1-DOF resonators ($\phi_{1\text{DOF}}$) and with attached single periodic array of 2-DOF resonator ($\phi_{2\text{DOF}}$) for $(a)$ square and $(b)$ triangular lattices, considering $f_j^{(1)} = \{283, 102\}$ Hz and $f_1^{(i)} = \{102, 283\}$ Hz.

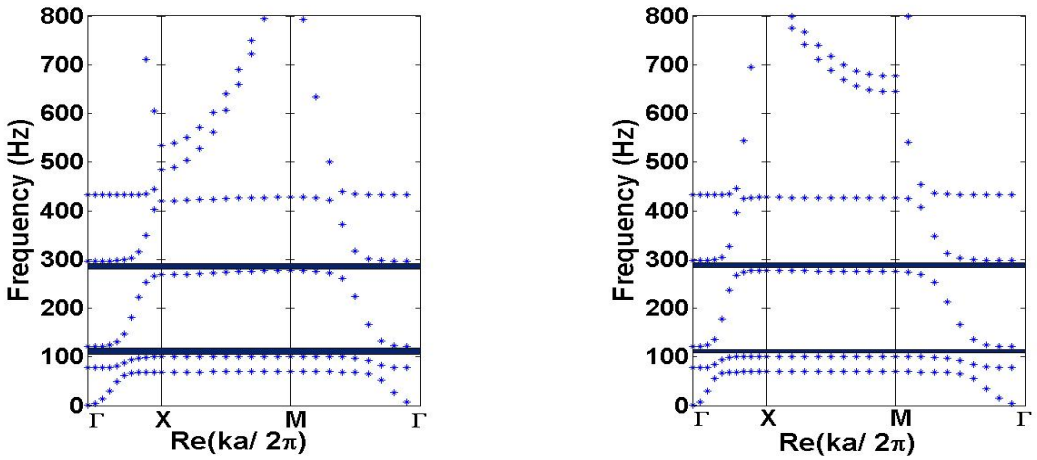


(*a*) (*b*)

Figure 13 – Real band structure of EM thin plate with attached double periodic arrays of 2-DOF resonators for $(a)$ square and $(b)$ triangular lattices with $f_1^{(i)} = \{102, 283\}$ Hz and $f_2^{(i)} = \{70, 430.5\}$ Hz.

present almost the same attenuation performance on the locally resonant band gaps.

## 2. CONCLUSION

We obtain the complex band structure for a multi-resonator EM thin plate with periodic arrays of MDOF resonators, considering square and triangular lattices. We consider four cases: (1) EM plate with attached single periodic array of S-DOF resonator, (2) EM plate with attached double periodic arrays of S-DOF resonators, (3) EM plate with attached single periodic array of 2-DOF resonator and (4) EM plate with attached double periodic arrays of 2-DOF resonators. The PWE and EPWE methods are used to find the real and imaginary band structures, respectively.
The locally resonant band gaps present almost the same attenuation for both lattices. However, the square lattice present broader Bragg-type band gaps with higher attenuation than triangular lattice for all cases. We compare cases (2) and (3), considering resonators tuned at the same frequencies 102 Hz and 283 Hz. An inverse behaviour is observed. In this comparison, the highest locally resonant band gap attenuation is observed for case (3) on 102 Hz. The case (4) presents almost no attenuation on 430.5 Hz and a coupled band gap between 70 Hz and 102 Hz is opened up.
The formation of locally resonant and the Bragg-type band gaps in a multi-resonator EM thin plate enlarges the

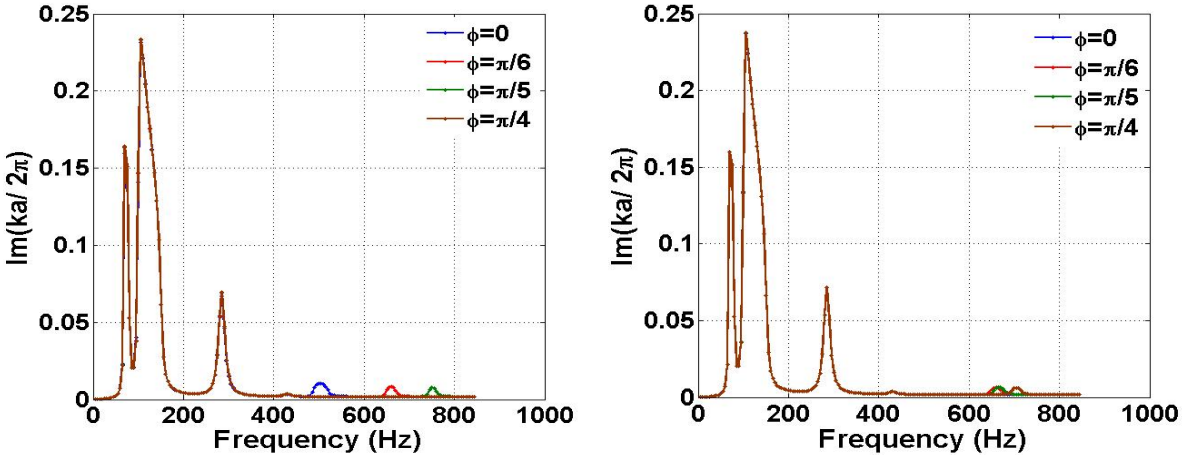


(*a*) (*b*)

Figure 14 – Imaginary band structures of EM thin plate with attached double periodic arrays of 2-DOF resonators for $(a)$ square and $(b)$ triangular lattices with $f_1^{(i)} = \{102, 283\}$ Hz and $f_2^{(i)} = \{70, 430.5\}$ Hz.

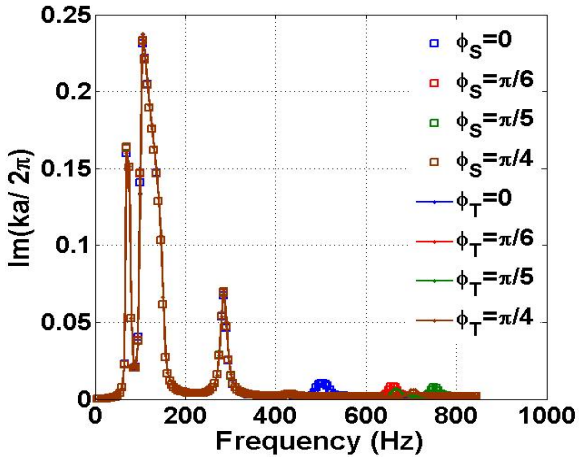


Figure 15 – Comparison of imaginary band structures of EM thin plate with attached double periodic arrays of 2-DOF resonators for square ($\phi_S$) and triangular ($\phi_T$) lattices with $f_1^{(i)} = \{102, 283\}$ Hz and $f_2^{(i)} = \{70, 430.5\}$ Hz.

engineering applications for vibration management.

**ACKNOWLEDGEMENTS**

The authors gratefully acknowledge the Brazilian research funding agency FAPEMA and IFMA for their financial support of this investigation.

**REFERENCES**

[1] Sigalas, M.M., Economou, E.N., "Elastic and Acoustic Wave Band Structure", Journal of Sound and Vibration, 158(2), 1992, pp. 377-382.

[2] Kushwaha, M.S., Halevi, P., Martínez, G., "Theory of Acoustic Band Structure of Periodic Elastic Composites", Physical Review B, 49, 1994, pp. 2313-2322.

[3] Pennec, Y., Vasseur, J.O., Djafari-Rouhani, B., Dobrzyński, L., Deymier, P.A., "Two-Dimensional Phononic Crystals: Examples and Applications", Surface Science Reports, 65, 2010, pp. 229-291.

[4] Huang, J., Shi, Z., "Attenuation Zones of Periodic Pile Barriers and its Application in Vibration Reduction for Plane Waves", Journal of Sound and Vibration, 332, 2013, pp. 4423-4439.

[5] Yu, K., Chen, T., Wang, X., "Band Gaps in the Low-Frequency Range Based on the Two-Dimensional Phononic Crystals Plates Composed of Rubber Matrix with Periodic Steel Stubs", Physica B, 416, 2013, pp. 12-16.

[6] Anjos, V., Arantes, A., "Phononic Band Structure in Carbon Microtube Composites", RSC Advances, 5, 2015, pp. 11248-11253.

[7] Miranda Júnior, E.J.P., Dos Santos, J.M.C., "Flexural Wave Band Gaps in Metamaterial Elastic Beam", Proceedings of the 23rd ABCM International Congress of Mechanical Engineering (COBEM2015), Rio de Janeiro, Brazil, December 2015, pp. 1-8.

[8] Miranda Júnior, E.J.P., Dos Santos, J.M.C., "Flexural Wave Band Gaps in $Al_2O_3$/Epoxy Composite Rectangular Plate Using Mindlin Theory", Proceedings of the 3rd Brazilian Conference on Composite Materials (BCCM-3), Gramado, Brazil, August 2016, pp. 1-8.

[9] Miranda Júnior, E.J.P., Dos Santos, J.M.C., "Elastic Wave Band Gaps in a Two-Dimensional Magnetoelectroelastic Phononic Crystal", Revista Interdisciplinar de Pesquisa em Engenharia, 2(13), 2016, pp. 13-26.

[10] Olsson III, R.H., El-Kady, I., "Microfabricated Phononic Crystal Devices and Applications", Measurement Science and Technology, 20(012002), 2009, pp. 1-13.

[11] Liu, Z., Zhang, X., Mao, Y., Zhu, Y.Y., Yang, Z., Chan, C.T., Sheng, P., "Locally Resonant Sonic Materials", Science, 289(5485), 2000, pp. 1734-1736.

[12] Ho, K.M., Cheng, C.K., Yang, Z., Zhang, X.X., Sheng, P., "Broadband Locally Resonant Sonic Shields", Applied Physics Letters, 83(26), 2003, pp. 5566-5568.

[13] Yang, Z., Dai, H.M., Chan, N.H., Ma, G.C., "Acoustic Metamaterial Panels for Sound Attenuation in the 50-1000 Hz Regime", Applied Physics Letters, 96(041906), 2010, pp. 1-3.

[14] Casadei, F., Beck, B.S., Cunefare, K.A., Ruzzene, M., "Vibration Control of Plates through Hybrid Configurations of Periodic Piezoeletric Shunts", Journal of Intelligent Material Systems and Structures, 23(10), 2012, pp. 1169-1177.

[15] Casadei, F., Dozio, L., Ruzzene, M., Cunefare, K.A., "Periodic Shunted Arrays for the Control of Noise Radiation in an Enclosure", Journal of Sound and Vibration, 329(18), 2010, pp. 3632-3646.

[16] Xiao, Y., Wen, J., Wen, X., "Sound Transmission Loss of Metamaterial-Based Thin Plates with Multiple Subwavelength Arrays of Attached Resonators", Journal of Sound and Vibration, 331(25), 2012, pp. 5408-5423.

[17] Wang, G., Wen, X., Wen, J., Liu, Y., "Quasi-One-Dimensional Periodic Structure with Locally Resonant Band Gap", Journal of Applied Mechanics, 73(1), 2005, pp. 167-170.

[18] Xiao, Y., Wen, J., Wen, X., "Longitudinal Wave Band Gaps in Metamaterial-Based Elastic Rods Containing Multi-Degree-of-Freedom Resonators", New Journal of Physics, 14(033042), 2012, pp. 1-20.

[19] Nobrega, E.D., Gautier, F., Pelat, A., Dos Santos, J.M.C., “Vibration Band Gaps for Elastic Metamaterial Rods Using Wave Finite Element Method”, Mechanical Systems and Signal Processing, 79, 2016, pp. 192-202.

[20] Wang, G., Wen, J., Wen, X., “Quasi-One-Dimensional Phononic Crystals Studied Using the Improved Lumped-Mass Method: Application to Locally Resonant Beams with Flexural Wave Band Gap”, Physical Review B, 71(104302), 2005, pp. 1-5.

[21] Yu, D., Liu, Y., Wang, G., Zhao, H., Qiu, J., “Flexural Vibration Band Gaps in Timoshenko Beams with Locally Resonant Structures”, Journal of Applied Physics, 100(124901), 2006, pp. 1-5.

[22] Yu, D., Liu, Y., Zhao, H., Wang, G., Qiu, J., “Flexural Vibration Band Gaps in Euler-Bernoulli Beams with Locally Resonant Structures with Two Degrees of Freedom”, Physical Review B, 73(064301), 2006, pp. 1-5.

[23] Liu, Y., Yu, D., Li, L., Zhao, H., Wen, J., Wen, X., “Design Guidelines for Flexural Wave Attenuation of Slender Beams with Local Resonators”, Physics Letters A, 362(5-6), 2007, pp. 344-347.

[24] Xiao, Y., Wen, J., Wen, X., “Broadband Locally Resonant Beams Containing Multiple Periodic Arrays of Attached Resonators”, Physics Letters A, 376(16), 2012, pp. 1384-1390.

[25] Raghavan, L., Phani, A.S., “Local Resonance Bandgaps in Periodic Media: Theory and Experiment”, Journal of Acoustical Society of America, 134(3), 2013, pp. 1950-1959.

[26] Wang, M.Y., Wang, X., “Frequency Band Structure of a Locally Resonant Periodic Flexural Beams Suspended with Force-Moment Resonators”, Journal of Physics D: Applied Physics, 46(255502), 2013, pp. 1-8.

[27] Wang, Z., Zhang, P., Zhang, Y., “Locally Resonant Band Gaps in Flexural Vibrations of a Timoshenko Beam with Periodically Attached Multioscillators”, Mathematical Problems in Engineering, 2013(146975), 2013, pp. 1-10.

[28] Xiao, Y., Wen, J., Yu, D., Wen, X., “Flexural Wave Propagation in Beams with Periodically Attached Vibration Absorbers: Band-Gap Behavior and Band Formation Mechanisms”, Journal of Sound and Vibration, 332(4), 2013, pp. 867-893.

[29] Casadei, F., Bertoldi, K., “Wave Propagation in Beams with Periodic Arrays of Airfoil-Shaped Resonating Units”, Journal of Sound and Vibration, 333(24), 2014, pp. 6532-6547.

[30] Wang, M.Y., Choy, Y.T., Wan, C.W., Zhao, A.S., “Wide Band-Gaps in Flexural Periodic Beams with Separated Force and Moment Resonators”, Journal of Vibration and Acoustics, 137(6), 2015, pp. 1-6.

[31] Wang, T., Sheng, M.-P., Qin, Q.-H., “Multi-Flexural Band Gaps in an Euler-Bernoulli Beam with Lateral Local Resonators", Physics Letters A, 380(4), 2016, pp. 525-529.

[32] Miranda Júnior, E.J.P., Dos Santos, J.M.C., “Flexural Wave Band Gaps in an Elastic Metamaterial Beam with Periodically Attached Spring-Mass Resonators”, Proceedings of ISMA2016, Leuven, Belgium, September 2016, pp. 2099-2113.

[33] Sun, C.-Y., Hsu, J.-C., Wu, T.-T., “Resonant Slow Modes in Phononic Crystal Plates with Periodic Membranes”, Applied Physics Letters, 97(031902), 2010, pp. 1-3.

[34] Oudich, M., Senesi, M., Assouar, M.B., Ruzenne, M., Sun, J.-H., Vicent, B., Hou, Z., Wu, T.-T., “Experimental Evidence of Locally Resonant Sonic Band Gap in Two-Dimensional Phononic Stubbed Plates”, Physical Review B, 84(165136), 2011, pp. 1-6.

[35] Xiao, Y., Wen, J., Wen, X., “Flexural Wave Band Gaps in Locally Resonant Thin Plates with Periodically Attached Spring-Mass Resonators”, Journal of Physics D: Applied Physics, 45(19), 2012, pp. 1-12.

[36] Claeys, C.C., Vergote, K., Sas, P., Desmet, W., “On the Potential of Tuned Resonators to Obtain Low-Frequency Vibrational Stop Bands in Periodic Panels”, Journal of Sound and Vibration, 332, 2013, pp. 1418-1436.

[37] Peng, H., Pai, P.F., Deng, H., “Acoustic Multi-Stopband Metamaterial Plates Design for Broadband Elastic Wave Absorption and Vibration Suppression”, International Journal of Mechanical Sciences, 103, 2015, pp. 104-114.

[38] Song, Y., Feng, L., Wen, J., Yu, D., Wen, X., “Analysis and Enhancement of Flexural Wave Stop Bands in 2D Periodic Plates”, Physics Letters A, 379, 2015, pp. 1449-1456.

[39] Miranda Júnior, E.J.P., Dos Santos, J.M.C., “Flexural Wave Band Gaps in Elastic Metamaterial Thin Plate”, Proceedings of the IX Mechanical Engineering Brazilian Congress, Fortaleza, August 2016, pp. 1-10.

[40] Thorp, O., Ruzzene, M., Baz, A., “Attenuation of Wave Propagation in Fluid-Loaded Shells with Periodic Shunted Piezoeletric Rings”, Smart Materials and Structures, 14, 2005, pp. 594-604.

[41] Huang, G.L., Sun, C.T., “Band Gaps in a Multiresonator Acoustic Metamaterial”, Journal of Vibration and Acoustics, 132(3), 2010, pp. 1-6.

[42] Huang, G.L., Sun, C.T., “Metamaterial-Based Broadband Elastic Wave Absorber”, Journal of Intelligent Material Systems and Structures, 21(5), 2010, pp. 517-528.

[43] Kirchhoff, G., “Über das Gleichgewicht und die Bewegung einer Elastischen Scheibe”, Journal für die reine und Angewandte Mathematik, 40, 1850, pp. 51-88.

[44] Love, A.E.H., “The Small Free Vibrations and Deformation of a Thin Elastic Shell”, Philosophical Transactions of the Royal Society A, 179, 1888, pp. 491-546.

[45] Hsue, Y.-C., Yang, T.-J., “Contour of the Attenuated Length of an Evanescent Wave at Constant Frequency within a Band Gap of Photonic Crystal”, Solid State Communications, 129, 2004, pp. 475-478.

[46] Hsue, Y.-C., Yang, T.-J., “Applying a Modified Plane-Wave Expansion Method to the Calculations of Transmittivity and Reflectivity of a Semi-Infinite Photonic Crystal”, Solid State Communications, 70(016706), 2004, pp. 1-6.

[47] Hsue, Y.-C., Freeman, A.J., “Extended Plane-Wave Expansion Method in Three-Dimensional Anisotropic Photonic Crystals”, Physical Review B, 72(195118), 2005, pp. 1-10.

[48] Laude, V., Achaoui, Y., Benchabane, S., Khelif, A., “Evanescent Bloch Waves and the Complex Band Structure of Phononic Crystals”, Physical Review B, 80(092301), 2009, pp. 1-4.

[49] Romero-García, V., Sánchez-Pérez, J.V., Castiñeira-Ibáñez, S., Garcia-Raffi, L.M., “Evidences of Evanescent Bloch Waves in Phononic Crystals”, Applied Physics Letters, 96(124102), 2010, pp. 1-3.

[50] Romero-García, V., Sánchez-Pérez, J.V., Castiñeira-Ibáñez, S., Garcia-Raffi, L.M., “Evanescent Modes in Sonic Crystals: Complex Dispersion Relation and Supercell Approximation”, Journal of Applied Physics, 108(044907), 2010, pp. 1-6.

[51] Romero-García, V., Sánchez-Pérez, J.V., Garcia-Raffi, L.M., “Propagating and Evanescent Properties of Double-Point Defects in Sonic Crystals”, New Journal of Physics, 12(083024), 2010, pp. 1-14.

[52] Brillouin, L., “Wave Propagation in Periodic Structures”, New York/USA, Dover Publications, 1946.

[53] Floquet, G., “Sur les Équations Différentielles Linéaires à Coefficients Périodiques”, Annales Scientifiques de L’École Normale Supérieure, France, 12, 1883, pp. 47-88.

[54] Bloch, F., “Über die Quantenmechanik der Electron in Kristallgittern”, Zeitschrift für Physik, 52, 1928, pp. 555-600.

[55] Fahy, F., Gardonio, P., “Sound and Structural Vibration: Radiation, Transmission and Response”, 2nd edition, UK, Oxford: Academic Press, pp. 656.

[56] Yao, Z.-J., Yu, G.-L., Wang, Y.-S., Shi, Z.-F., “Propagation of Bending Waves in Phononic Crystal Thin Plates with a Point Defect”, International Journal of Solids and Structures, 46, 2009, pp. 2571-2576.

[57] Dyogtyev, A.V., Sukhoivanov, I.A., De La Rue, R.M., “Photonic Band-Gaps Maps for Different Two Dimensionally Periodic Photonic Crystal Structures”, Journal of Applied Physics, 107(013108), 2010, pp. 1-7.

[58] Mencik, J.-M., “On the Low- and Mid-Frequency Forced Response of Elastic Structures Using Wave Finite Elements with One-Dimensional Propagation”, Computers and Structures, 88, 2010, pp. 674-689.

# APPENDIX H – Implemented Codes

## H.1 MATLAB® codes

### H.1.1 PWE code for 1D phononic crystal rods

```
1
2  clc; clear all; close all;
3
4  im=sqrt(-1);
5  nmax=10;
6  neig=2*nmax+1;                          % Number of
       Eigenvalues to keep
7  n1=(-nmax:nmax);                        % Number of plane
       waves = length(n1);
8
9  Ba=.01;                                 % Base for material A
10 Bb=Ba;                                  % Base for material B
11 Ha=.01;                                 % Height for material
       A
12 Hb=.01;
13 La=.05;                                 % Length for material
       A
14 Lb=.02;
15 Lc=La+Lb;                               % Unit cell length
16 f=La/Lc;                                % Filling fraction
17 rhoa=2730;                              % Density of material
       A
18 rhob=1180;
19 Sa=Ba*Ha;                               % Cross section area
       of material A
20 Sb=Bb*Hb;
21 alfaa=rhoa*Sa;
22 alfab=rhob*Sb;
23 Ea=77.6*10^9;
24 Eb=4.35*10^9;
25 gammaa=Ea*Sa;
26 gammab=Eb*Sb;
27
28 [nx,nxp]=meshgrid(n1,n1);
```

```
29 kro_del_ggp=eye(length(n1));
30 G_Gp=(2*pi/Lc)*(nx-nxp);                    % Reciprocal lattice
       vector
31 fG_Gp=f.*sinc((nx-nxp)*f);                  % Structure function
32
33 alfam=alfaa*f+alfab*(1-f);
34 delalfa=alfaa-alfab;
35 alfamc=alfam.*kro_del_ggp+delalfa.*(1-kro_del_ggp).*fG_Gp;
           % Fourier coefficient
36
37 gammam=gammaa*f+gammab*(1-f);
38 delgamma=gammaa-gammab;
39 gammamc=gammam.*kro_del_ggp+delgamma.*(1-kro_del_ggp).*fG_Gp;
        % Fourier coefficient
40
41 i=1;
42 for kx=-pi/Lc:2*pi/Lc/30:pi/Lc
                                        % First Brillouin Zone
43     Gx=2*pi/Lc*diag(n1);
44     M=(kx*eye(length(n1))+Gx)*gammamc*(kx*eye(length(n1))+Gx);
45     N=alfamc;
46     omega=eig(M,N);
47     omega=sort((omega));
48     freqs(:,i)=sqrt(real(omega(1:neig))).*Lc./2./pi;
49     i=i+1;
50 end
51
52 figure
53 for idx=1:neig % idx=1:neig
54     plot((-pi/Lc:2*pi/Lc/30:pi/Lc)*Lc/pi,real(freqs(idx,:))*1/
          Lc,'.-')
55     hold on
56 end
57 xlabel('\Re(ka/ \pi)','FontSize',22,'FontWeight','bold')
58 ylabel('Frequency (Hz)','FontSize',22,'FontWeight','bold')
59 set(gca,'FontSize',24,'FontWeight','bold')
60 grid on
```

### H.1.2 PWE code for a 2D sonic crystal with circular inclusions and square lattice

```
1
2  clc; clear all; close all;
3
4  num_Eigenvals=15;
5  nmax=10;
6  n1=(-nmax:nmax);
7  n2=(-floor((2*nmax+1)^2/2):floor((2*nmax+1)^2/2));
8
9  lat_a=.022;                                          % Lattice
       parameter
10 f=0.274;                                             % Filling
       fraction
11 ro=sqrt(f/pi*lat_a^2);                               %
     Inclusion radius, considering square lattice
12
13 pa=7800;                                             % Density
       of inclusion
14 pb=1.2;                                              % Density
       of matrix
15 cla=6100;                                            %
     Longitudinal speed of sound in inclusion
16 clb=343;
17 c11a=cla^2*pa;                                       % Elastic
       constant of inclusion
18 c11b=clb^2*pb;
19
20 delp=(pa^-1)-(pb^-1);
21 pm=(pa^-1)*f+(pb^-1)*(1-f);
22 delc11=(c11a^-1)-(c11b^-1);
23 c11m=(c11a^-1)*f+(c11b^-1)*(1-f);
24
25 nx_arr=repmat(n1,1,2*nmax+1);
26 ny_arr=round(n2/(2*nmax+1));
27 [nx,nxp]=meshgrid(nx_arr,nx_arr);
28 [ny,nyp]=meshgrid(ny_arr,ny_arr);
29 fill=ones(1,length(nx_arr));
```

```
30 fillt=diag(fill);
31
32 Gx=2*pi/lat_a*nx;
33 Gxp=2*pi/lat_a*nxp;
34 Gy=2*pi/lat_a*ny;
35 Gyp=2*pi/lat_a*nyp;
36 G_Gp=sqrt(4*pi*f*((nx-nxp).^2+(ny-nyp).^2))+fillt;
37 fG_Gp=2*f*besselj(1,G_Gp)./G_Gp;                    % Structure function for circular inclusion in a square lattice
38
39 kro_del_ggp=(nxp==nx) & (nyp==ny);
40 pmc=pm.*kro_del_ggp+delp.*(1-kro_del_ggp).*fG_Gp;   % Fourier coefficient
41 c11mc=c11m.*kro_del_ggp+delc11.*(1-kro_del_ggp).*fG_Gp; % Fourier coefficient
42
43     for kyind=1:3
44         onoff=1;
45         for kx=.05:2*pi/lat_a/20:pi/lat_a
46             if kyind==1
47                 kxt=kx;
48                 kx=pi/lat_a-kx;
49                 ky=kx;
50             elseif kyind==2
51                 kxt=kx;
52                 ky=0;
53             elseif kyind==3
54                 kxt=kx;
55                 ky=kx;
56                 kx=pi/lat_a;
57             end
58             Q=pmc.*(((kx+Gx)).*((kx+Gxp)))+pmc.*(((ky+Gy)).*((ky+Gyp)));
59             R=c11mc;
60             A=R\Q;
61             [a,b]=eig(A);
62             g=find(b~=0);
63             eigs=(sort(b(g)));
```

```
64              eigs(1:num_Eigenvals);
65              k=repmat(kxt,1,num_Eigenvals)*lat_a/(2*pi);
66              min(b(g));
67              if onoff==1
68                  omega=[real(sqrt(eigs(1:num_Eigenvals)))']/(2*
                        pi);
69                  karr=[k];
70                  if kyind==1
71                      omegafull=[real(sqrt(eigs(1:num_Eigenvals))
                            )']/(2*pi);
72                      karrfull=[k];
73                  end
74                  onoff=0;
75              else
76                  omega=[omega,real(sqrt(eigs(1:num_Eigenvals)))
                        '*1/(2*pi)];
77                  karr=[karr,k];
78                  omegafull=cat(1,omegafull,...
79                      real(sqrt(eigs(1:num_Eigenvals)))'*1/(2*pi)
                            );
80                  karrfull=cat(1,karrfull,k);
81              end
82          end
83          if kyind==1
84              myfig=figure;
85              ymax=max(omega);
86              subplot(1,3,1)
87              b1=plot(karr,omega,'*');
88              ax1=gca;
89              po=get(gca,'position');
90              set(gca,'YLim',[0,ymax]);
91              set(gca,'XLim',[0,.5]);
92              set(gca,'FontSize',22,'FontWeight','bold')
93              set(gca,'nextplot','add');
94              left_side=po(1);
95              set(gca,'xtick',[]);
96              width=po(3);
97              right_side=left_side+width;
98              set(gca,'xticklabel',{});
```

```
99          ylabel('Frequency (Hz)','FontSize',24,'FontWeight',
                'bold');
100     elseif kyind==2
101         subplot(1,3,2)
102         b2=plot(karr,omega,'*');
103         po=get(gca,'position');
104         po(1)=right_side;
105         ax2=gca;
106         set(gca,'nextplot','add');
107         set(gca,'position',po);
108         set(gca,'YLim',[0,ymax]);
109         set(gca,'XLim',[0,.5]);
110         set(gca,'xtick',[]);
111         set(gca,'xticklabel',{});
112         set(gca,'yticklabel',{});
113         left_side=po(1);
114         width=po(3);
115         right_side=left_side+width;
116         set(gca,'xticklabel',{});
117     elseif kyind==3
118         subplot(1,3,3)
119         b3=plot(karr,omega,'*');
120         po=get(gca,'position');
121         po(1)=right_side;
122         ax3=gca;
123         set(gca,'nextplot','add');
124         set(gca,'position',po);
125         set(gca,'xtick',[]);
126         set(gca,'xticklabel',{});
127         set(gca,'yticklabel',{});
128         set(gca,'YLim',[0,ymax]);
129         set(gca,'XLim',[0,.5]);
130         left_side=po(1);
131         width=po(3);
132         right_side=left_side+width;
133         set(gca,'xticklabel',{});
134         text(-1,-.035*ymax,'M','FontSize',22,'FontWeight','
                bold');
135         text(-.52,-.035*ymax,'\Gamma','FontSize',22,'
```

```
                FontWeight','bold');
136             text(-0.02,-.035*ymax,'X','FontSize',22,'FontWeight
                ','bold');
137             text(.43,-.035*ymax,'M','FontSize',22,'FontWeight',
                'bold');
138         end
139     end
```

# ANNEXE A – Periodic Systems

In this annexe, it is presented a brief review of basic fundamentals of 2D periodicity (A.1), wave propagation in periodic systems (A.2) and band gap formation mechanisms (A.3). A special attention is given for 2D periodic structures, since they are the subject of this thesis herewith 1D periodic structures, and their theory is more general than for 1D.

## A.1 Geometric properties

The idea of periodic systems or crystal structures is associated with lattice and basis concepts. The crystal structure illustrated in Figure A.1 is formed by adding a basis to every lattice point (Kittel, 2004).

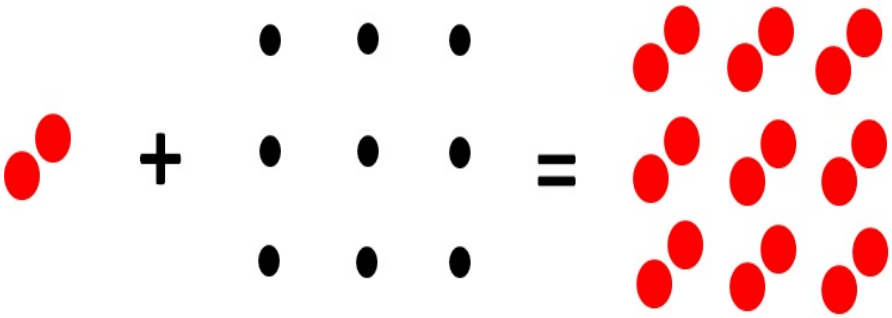

Figure A.1: An example of a crystal structure with its basis and lattice points of the lattice.

A particular lattice $\bar{\mathbf{r}}$ in $\mathbb{R}^n$ is defined in such a way that the periodic system is equally observed from any point of the lattice, that is the system is invariant under translations and, sometimes, under rotations. From group theory, it has been proved that there is a unique 1D periodic system, five 2D and fourteen 3D different Bravais lattices (García, 2010). Figure A.2 illustrates examples of artificial crystals, for instance PnCs with 1D, 2D and 3D periodicity.

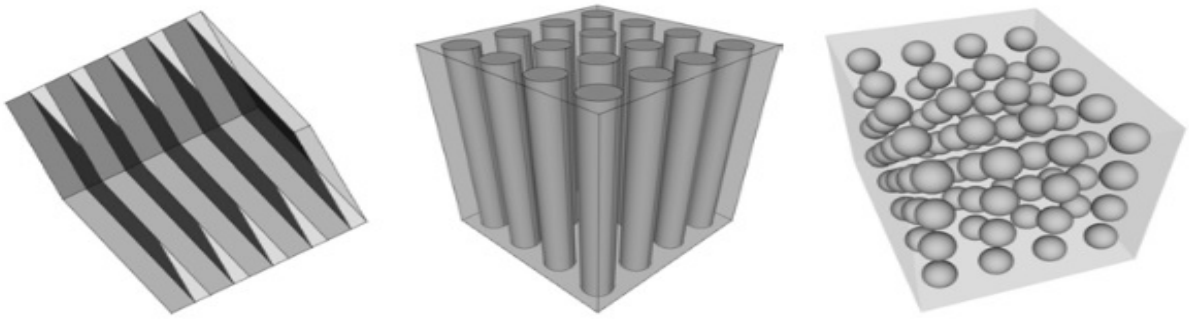

Figure A.2: Artificial crystals with 1D, 2D and 3D periodicity (Laude, 2015).

The lattice of a periodic system is defined as:

$$\bar{\mathbf{r}} = \sum_{i=1}^{n} z_i \mathbf{a}_i, \tag{A.1}$$

where $z_i \in \mathbb{Z}$ and $\mathbf{a}_i$ are the primitive translation vectors of the lattice. The parallelepiped formed by $\mathbf{a}_i$ is known as primitive cell (a type of unit cell). There is always a lattice point per unit cell. The Wigner–Seitz cell is an example of a primitive cell, which is a unit cell containing exactly one lattice point. It is the locus of points in real space that are closer to that lattice point than to any of the other lattice points.

In order to proceed further with the Fourier analysis, there is the reciprocal lattice in reciprocal space (also known as momentum space or $\mathbf{k}$-space), which is related to the direct lattice (Bravais lattice) in direct space (real space). Reciprocal lattice is a basic definition in Solid State Physics for better understanding of the physical properties of periodic systems. The primitive cell in reciprocal space is called Brillouin zone (Brillouin, 1946). Thus, a Brillouin zone is defined as a Wigner-Seitz primitive cell in the reciprocal lattice (Kittel, 2004). Primitive cell vectors in the reciprocal lattice are defined from direct lattice vectors as:

$$\mathbf{b}_i = 2\pi \frac{\varepsilon_{ijk}\mathbf{a}_j \times \mathbf{a}_k}{\mathbf{a}_1 \cdot (\mathbf{a}_2 \times \mathbf{a}_3)}, \tag{A.2}$$

where $\varepsilon_{ijk}$ is the completely anti-symmetric Levi-Civita symbol, also known as permutation symbol, and it is 1 if $(i,j,k)$ is an even permutation of $(1,2,3)$, -1 if it is an odd permutation, and 0 if any index is repeated. Any linear combination $\mathbf{g} = \sum_{i=1}^{n} \mu_i \mathbf{b}_i$, with $\mu_i \in \mathbb{Z}$, gives a lattice point in the reciprocal space, where $\mathbf{g}$ is known as reciprocal lattice vector. In addition, the primitive vectors on reciprocal and real spaces have the following orthogonality relation $\mathbf{a}_i \cdot \mathbf{b}_j = 2\pi\delta_{ij}$, where $\delta_{ij} = 0$ if $i \neq j$ or $\delta_{ij} = 1$ if $i = j$ is the Kronecker delta.

Every periodic system has two lattices associated with it, that is the real and reciprocal lattices. The reciprocal lattice is a lattice in the Fourier space related to the crystal. An interesting analogy is that the diffraction pattern of a crystal is a map of its reciprocal lattice, whereas a microscope image, if it can be resolved in fine enough scale, is a map of the crystal structure in real space (Kittel, 2004).

Figure A.3 illustrates some examples of lattices for 2D PnCs, *i.e.*, square (a), rectangular (b), triangular (c), honeycomb (d) and Kagomé (e) lattices. The first irreducible Brillouin zone (FIBZ) of these lattices is also illustrated in Figure A.3 (f-j). The FIBZ is the first Brillouin zone (FBZ) reduced by all of the symmetries in the lattice point group (crystal point group). In Figure A.3, note that $a$ is lattice parameter for square, triangular, honeycomb and Kagomé lattices, whereas $a_1$ and $a_2$ are lattice parameters for rectangular lattice.

The FIBZ points in Figure A.3 (f-j) are $\Gamma$ $(0,0)$, X $(\pi/a,0)$ and M $(\pi/a,\pi/a)$ for square lattice, $\Gamma$ $(0,0)$, X $(\pi/a_1,0)$, M $(\pi/a_1,\pi/a_2)$ and K $(0,\pi/a_2)$, with $a_1 > a_2$, for rectangular lattice, $\Gamma$ $(0,0)$, X $(4\pi/3a,0)$ and M $(\pi/a,\pi/\sqrt{3}a)$ for triangular lattice, $\Gamma$ $(0,0)$, X $(4\pi/3\sqrt{3}a,0)$ and M $(\pi/\sqrt{3}a,\pi/3a)$ for honeycomb lattice, and $\Gamma$ $(0,0)$, X $(2\pi/3a,0)$ and M $(\pi/2a,\pi/2\sqrt{3}a)$ for Kagomé lattice.

The primitive vectors in real space are defined for square lattice, $\mathbf{a}_i = a\mathbf{e}_i$ $(i = 1,2)$, rectangular lattice, $\mathbf{a}_1 = a_1\mathbf{e}_1$, $\mathbf{a}_2 = a_2\mathbf{e}_2$, triangular lattice, $\mathbf{a}_1 = a\mathbf{e}_1$, $\mathbf{a}_2 = \frac{a}{2}\mathbf{e}_1 + \frac{a\sqrt{3}}{2}\mathbf{e}_2$, hon-

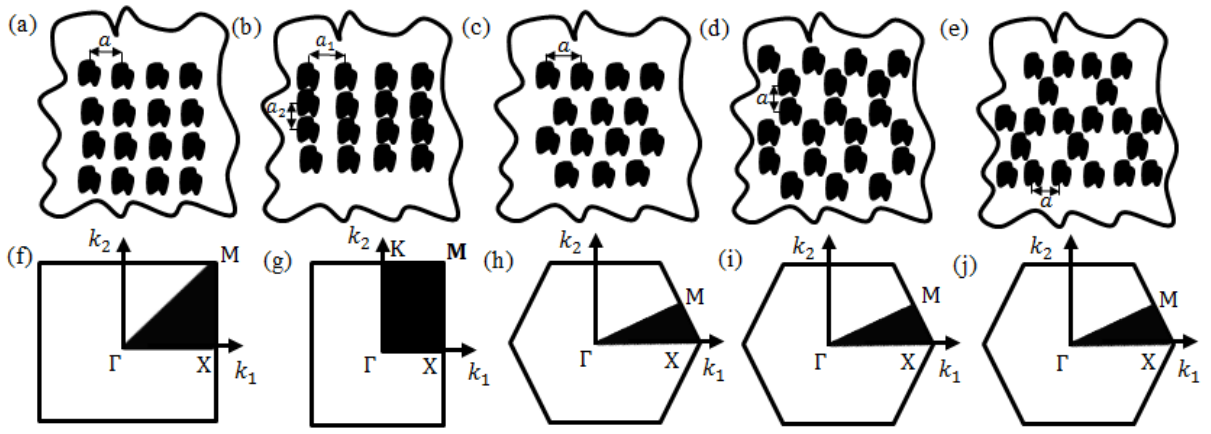


Figure A.3: Transverse cross section of the 2D PnC with (a) square, (b) rectangular, (c) triangular, (d) honeycomb and (e) Kagomé lattices. The first irreducible Brillouin zone, in shaded region, for (f) square, (g) rectangular, (h) triangular, (i) honeycomb and (j) Kagomé lattices.

eycomb lattice, $\mathbf{a}_1 = \frac{a\sqrt{3}}{2}\mathbf{e}_1 + \frac{3a}{2}\mathbf{e}_2$, $\mathbf{a}_2 = -\frac{a\sqrt{3}}{2}\mathbf{e}_1 + \frac{3a}{2}\mathbf{e}_2$ and Kagomé lattice, $\mathbf{a}_1 = a\mathbf{e}_1 + a\sqrt{3}\mathbf{e}_2$, $\mathbf{a}_2 = -a\mathbf{e}_1 + a\sqrt{3}\mathbf{e}_2$, where $\mathbf{e}_i$, $i = 1,2$, are the basis vectors in real space. The reciprocal lattice vector, $\mathbf{g}$, calculated for square, rectangular, triangular, honeycomb and Kagomé lattices is expressed by $\mathbf{g}_{m,n} = \frac{2\pi}{a}(m\mathbf{e}_1 + n\mathbf{e}_2)$, $\mathbf{g}_{m,n} = 2\pi(\frac{m}{a_1}\mathbf{e}_1 + \frac{n}{a_2}\mathbf{e}_2)$, $\mathbf{g}_{m,n} = \frac{2\pi}{a}[m\mathbf{e}_1 + \frac{(-m+2n)}{\sqrt{3}}\mathbf{e}_2]$, $\mathbf{g}_{m,n} = \frac{2\pi}{a\sqrt{3}}[(m-n)\mathbf{e}_1 + \frac{(m+n)}{\sqrt{3}}\mathbf{e}_2]$ and $\mathbf{g}_{m,n} = \frac{\pi}{a}[(m-n)\mathbf{e}_1 + \frac{(m+n)}{\sqrt{3}}\mathbf{e}_2]$, $m, n \in \mathbb{Z}$, respectively. The vector $\mathbf{g}_{m,n}$ is two-dimensional because it is considered 2D periodicity.

Another important concept for 2D PnCs is the filling fraction, defined as $\bar{f} = \frac{S_A}{S_C}$ for square, rectangular and triangular lattices, where $S_A$ and $S_C = ||\mathbf{a}_1 \times \mathbf{a}_2||$ are the cross section areas of inclusion and unit cell. For honeycomb and Kagomé lattices, the filling fraction can be defined as $\bar{f} = \frac{2S_A}{S_C}$ and $\bar{f} = \frac{3S_A}{S_C}$, respectively, since they have two and three inclusions per unit cell. The PnC inclusions in Figure A.3 (a-e) are arbitrary, but they can be, for instance, in Figure A.4 – circular (a), hollow circular (b), square (c) and rotated square with a 45° angle of rotation with respect to the *x* and *y* axes (d). For hollow circular inclusion, Figure A.4 (b), grey region represents the same material of matrix.

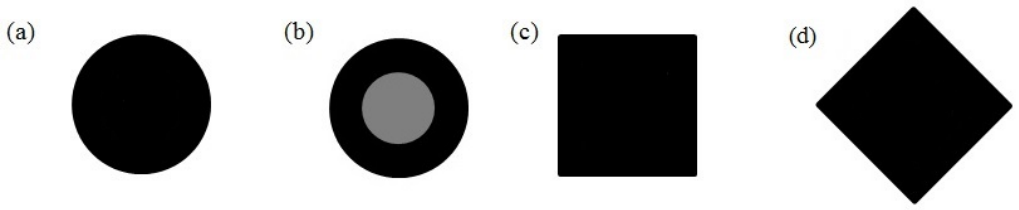


Figure A.4: Transverse cross section of the PnC inclusions: (a) circular, (b) hollow circular, (c) square and (d) rotated square with a 45° angle of rotation with respect to the *x*, *y* axes.

## A.2 Wave propagation

The basis of periodic structure study, from a mathematical point of view, was pioneered by Floquet (1883). He proposed analytical solutions for ordinary differential equations with periodic coefficients. Until 1887, only discrete models of periodic structures composed of regular lattices of springs connected to point masses had been considered. Later, Bloch (1928) extended the results presented by Floquet (1883) for the 1D spatial periodicity to the 3D case (Silva, 2015).

Schrödinger equation in quantum mechanics, Maxwell equations in electromagnetism, vectorial equation of Navier-Cauchy for elasticity and wave equation in acoustics present the same type of solution when they are solved for periodic system (García, 2010). Floquet-Bloch's theorem affirms that the eigenfunctions of the wave equation for a periodic potential are the product of a plane wave times a function with the same periodicity of the crystal (Kittel, 2004). Considering 2D periodicity and wave propagation in the $xy$ plane ($k_3 = 0$), one can write (hereafter omitting frequency dependence):

$$u_i(\mathbf{r}) = e^{j\mathbf{k}\cdot\mathbf{r}} u_{i_\mathbf{k}}(\mathbf{r}), \tag{A.3}$$

where $u_i(\mathbf{r})$ ($i$ = 1,2,3) is the elastic displacement, $\mathbf{r} = x\mathbf{e}_1 + y\mathbf{e}_2$, $x, y \in \mathbb{R}$, is the 2D spatial vector, $u_{i_\mathbf{k}}(\mathbf{r})$ is the Block wave amplitude and note that $u_{i_\mathbf{k}}(\mathbf{r}) = u_{i_\mathbf{k}}(\mathbf{r} + \bar{\mathbf{r}})$, $u_i(\mathbf{r} + \bar{\mathbf{r}}) = u_i(\mathbf{r})e^{j\mathbf{k}\cdot\bar{\mathbf{r}}}$, where $e^{j\mathbf{k}\cdot\bar{\mathbf{r}}}$ is known as Floquet-Bloch periodic boundary condition. The Bloch wave vector, also known as wave number, is defined as $\mathbf{k} = \bar{u}\mathbf{b}_1 + \bar{v}\mathbf{b}_2$, where $\bar{u}$,$\bar{v} \in \mathbb{Q}$ are the symmetry points within the FIBZ in reciprocal space, or we may write $\mathbf{k} = k_1\mathbf{e}_1 + k_2\mathbf{e}_2$, $k_1, k_2 \in \mathbb{R}$ are the point coordinates within the FIBZ for reciprocal space in Figure A.3 (f-j).

The equations that describe the elastic waves in an transversely isotropic infinite solid, considering 2D problem, $\partial/\partial x_3 = 0$, and linear media (small deformation theory), are given by Navier-Cauchy equations in frequency domain:

$$-\omega^2\rho u_i = \nabla\cdot(c_{66}\nabla u_i) + \nabla\cdot(c_{66}\frac{\partial\mathbf{u}}{\partial x_i}) + \frac{\partial}{\partial x_i}[(c_{11} - 2c_{66})\nabla\cdot\mathbf{u}], \tag{A.4}$$

$$-\omega^2\rho u_3 = \nabla\cdot(c_{44}\nabla u_3), \tag{A.5}$$

where $\rho$ is the density, $c_{66} = \frac{1}{2}(c_{11} - c_{12})$, $\nabla = (\partial/\partial x_1)\mathbf{e}_1 + (\partial/\partial x_2)\mathbf{e}_2$, $\mathbf{u} = u_1\mathbf{e}_1 + u_2\mathbf{e}_2$, and $c_{11}, c_{12}, c_{44}, c_{66}$ are the elastic constants of stiffness tensor using Voigt notation. In Eq. (A.4), there are implicit the longitudinal ($c_l$) and transverse ($c_t$) sound velocities, hence longitudinal-transverse vibrations (XY modes) remain coupled. Furthermore, these vibration directions are related to the displacements $u_1$ and $u_2$. In Eq. (A.5), the transverse vibration (Z modes) is in $z$ direction, perpendicular to $xy$ plane, and it is associated with $u_3$. XY modes are also known as pressure and vertically polarised shear modes – P-SV modes, and Z modes as horizontally polarised shear modes – SH modes (Barnell, 2014). Equations (A.4) and (A.5) represent a non-dispersive wave propagation of bulk waves in a infinite medium, since phase velocity does not

depend on frequency, thus all harmonic waves travel at the same velocity, that is group velocity is equal to phase velocity. For more details of bulk wave propagation, see Graff (1975).

The wave propagation described by Eqs. (A.4) and (A.5) starts to become dispersive whether a inhomogeneous medium is considered, for instance the 2D PnC illustrated in Figure A.3 with periodically inclusions embedded in a matrix. For 2D PnCs, one can note that $c_{11} = c_{11}(\mathbf{r})$, $c_{12} = c_{12}(\mathbf{r})$, $c_{66} = c_{66}(\mathbf{r})$ and $c_{44} = c_{44}(\mathbf{r})$. Furthermore, in order to handle sonic crystals (SnCs), *i.e.*, the acoustic case of PnCs, hence, for instance, periodically solid inclusions embedded in a fluid matrix, the wave equation can be written as:

$$-\omega^2 c_{11}^{-1} = \nabla \cdot (\rho^{-1} \nabla p), \tag{A.6}$$

where $p = p(\mathbf{r})$ is the acoustic pressure in frequency domain. Equation A.6 is known as Helmholtz equation and it is used to analyse acoustic wave problems. In addition, Eq. (A.6) can be obtain from Eq. (A.4) rewritten as:

$$-\omega^2 \rho \mathbf{u} = \nabla \cdot (c_{66} \nabla u_i) + \nabla \cdot (c_{66} \frac{\partial \mathbf{u}}{\partial x_i}) + \nabla[(c_{11} - 2c_{66}) \nabla \cdot \mathbf{u}], \tag{A.7}$$

remembering that $c_t$ is zero in fluids and considering that $\nabla \times \rho \mathbf{u} = 0$ and $\rho \mathbf{u} = \nabla p$. Equation (A.6) is more suitable neglecting inclusion shear rigidity (Kushwaha and Halevi, 1997). In addition, it must be highlighted that Eq. (A.6) is valid only whether waves propagating through a SnC can be regarded as purely longitudinal as long as coupling of shear elastic waves inside the inclusions to acoustic waves in the matrix can be completely ignored (Laude, 2015).

When other effects are present in PnCs, such as piezoelectricity and/or piezomagnetism, the wave propagation becomes more complex, because constitutive relations change, since these effects must be regarded.

## A.3 Band gaps

Band gaps can be defined as ranges of frequency where there are no propagating Bloch waves. In these frequency ranges, there are only evanescent Bloch waves. Bloch wave vector is complex for evanescent waves. The imaginary part of Bloch wave vector is especially significant, since it describes the exponential decay or amplification of the evanescent wave. The transmission through a finite length PnC or MM at frequencies within a band gap range is governed by exponentially decaying evanescent waves (Laude, 2015).

There are basically two types of band gaps – locally resonant and Bragg-type. In this thesis, band gaps are classified as partial, complete and full. Partial band gap is valid for at least one direction in $\mathbf{k}$-space, but not necessarily for others. A band gap is considered as complete when it is opened up for all values of $\mathbf{k}$ inside the FBZ. A full band gap is a complete band gap that is opened up for all polarization modes, and thus for all possible waves in the periodic structure. Bragg-type band gaps can be partial, complete and full, however, locally-resonant

band gaps are always complete band gaps if the coupling (between propagating wave and the vibration excited in the resonator) does not vanish for any direction of propagation (Laude, 2015).

The most common and historically first invoked physical mechanism of band gap formation is Bragg interference. Bragg scattering occurs at every periodic plane of scatterers inside the periodic structure. Bragg-type band gaps can be created anytime a forward and a backward propagating Bloch waves are phase matched, *i.e.*, when they would have degenerated modes in the band structure space $(\mathbf{k},\omega)$ if they did not couple (Laude, 2015). The destructive interference of waves creates the band gaps (Armenise *et al.*, 2010). Some important parameters that influence the Bragg-type band gap widths are the PnC lattice, material properties, unit cell geometry, filling fraction, among others.

The limitation of PnCs and SnCs is that only Bragg-type band gaps are created, thus it is not possible of achieving low-frequency band gaps for small lattice parameters. This can be overcome with the locally resonant band gaps opened up by MMs. Achaoui *et al.* (2013) studied the propagation of surface acoustic waves in 2D locally resonant PnCs with a random array of pillars and with a periodic structure. It was shown that the locally resonant in the low frequency range is almost independent of periodicity and resilient to randomness, while the Bragg-type band gap disappears with the random array.

Considering local resonance in EMs, there is the possibility of a part of the incoming wave energy to be trapped in the resonator for some time before it is radiated away to all permitted propagation modes. Local resonance principle can be viewed as a classical analog of Fano resonance, *i.e.*, as the coupling of a continuum of propagating waves with a localized resonant state (Laude, 2015).